TURBULENCE-CHEMISTRY INTERACTIONS FOR LEAN PREMIXED FLAMES

A Dissertation
Presented to
The Academic Faculty

by

Debolina Dasgupta

In Partial Fulfillment
of the Requirements for the Degree
Doctor in Philosophy in the
School of Aerospace Engineering

Georgia Institute of Technology
December 2018

TURBULENCE-CHEMISTRY INTERACTIONS FOR LEAN PREMIXED FLAMES

Approved by:

Dr. Tim Lieuwen, Advisor
School of Aerospace Engineering
Georgia Institute of Technology

Dr. Suresh Menon
School of Aerospace Engineering
Georgia Institute of Technology

Dr. Wenting Sun
School of Aerospace Engineering
Georgia Institute of Technology

Dr. Joseph Oefelein
School of Aerospace Engineering
Georgia Institute of Technology

Dr. Carsten Sievers
School of Chemical and Biomolecular Engineering
Georgia Institute of Technology

Date Approved:[September 20, 2018]

To my parents

ACKNOWLEDGEMENTS

It takes a full village for a successful completion of a PhD. It has been no different for me and I was blessed to have a wonderful bunch of people always ready to pick me up from each and every slump I faced.

First and foremost, I would like to thank my advisor Tim Lieuwen. Without his guidance, support and patience, none of this would be a reality. He is truly one of the best advisors a graduate student could ask for. I have learnt so much from him over the last 4 years; not just in my academic and scientific pursuits but also as a human being. It has truly been a delight to work with him over the last 4 years. I would also like to sincerely thank Wenting Sun for helping me understand and strengthen my knowledge of chemical kinetics and for always being available for discussions and improvements in what I was doing. I would also like to thank Dr. Suresh Menon, Dr. Joseph Oefelein and Dr. Carsten Sievers who agreed to be a part of my defense committee.

I am also eternally grateful to Dr. Marc Day from Lawrence Berkeley National Lab for all the help and support that I received from him. Without his assistance, it would be much harder to wade through the labyrinth of codes for the solver and the development and application of the post-processing tools. I would also like to sincerely thank Dr. Andy Aspden from Newcastle University for the numerous physics discussions and brainstorming sessions to come up with novel ideas for analysis.

I was lucky to be surrounded by a bunch of great people at the combustion lab. Without Nick Magina and Luke Humphrey, my initial years at Tech would have looked

markedly different. From numerous random discussions to the coffee breaks to helping get a footing of the life at Tech, they have been a constant source of encouragement and "wisdom". It is really hard for me to put into words what my friendship with Hanna Ek, has meant to me over the years. She has been a constant support and believed in me more than I have believed in myself. I truly believe I have gained a friend for life. The last four years have definitely been better with Vedanth Nair. All the technical discussions and numerous rants about work and life during extended breaks will truly be missed. The Combustion Lab group of Subodh Adhikari, Sai Kaza, Athanasios Moshos, Tim Cook and Alex Miller have truly been amazing to engage with and I doubt I will ever find a bunch of people with whom I can have lengthy conversations about the oddest of topics. This list would be incomplete without Dan Fries, Matt Sirignano, Chris Douglas and Nick Rock who have always been a delight to share space with and engage in conversations about science and "other" things. Also I am confident that the lab is in good hands with the newer graduate students Sukruth Somappa, Tony John and Raghul Manosh Kumar. It was a pleasure to share space with the superb research engineers Vishal Acharya, Ben Emerson and David Wu. I am eternally grateful to Vishal who made computing resources available whenever I needed them and also for the umpteen long exchange of ideas. I am yet to meet another person like Ben Emerson who has always shown infinite patience for everyone and had an open door policy whenever there were any problems. Even though we never shared lab space, I would also like to thank Alberto Amato who was my predecessor and found time sitting in Italy to guide me through the first two months to align me with codes he developed which made my settling in that much easier. I would also like to thank Sampath Adusumilli, Nishant Jain, Edwin Goh, Sheng Wei, Tom Pritchard, Brandon Sforzo, Gina

Magnotti, Henderson Johnson for being a part of this wonderful workplace I am happy to call my second home in Atlanta.

Atlanta also gave me a bunch of friends who became my family over the years. It is hard to imagine what my life would be without my amazing roommate, Eisha Nathan and I am glad I don't have to. Thank you for being my family away from home. This list is incomplete without mentioning Vinh Nguyen, Pushparghyadeb Kuila, Clayton Greer, Sarah Beth Nelius , Ye and Stephanie Locks. Cheers to all the good times we've shared from Savannah to candy poker to Christmas Karaoke!

Last but not the least I would like to give a big thank you to my parents, Utpal Kumar Dasgupta and Debjani Dasgupta who have always been my pillars of strength. They have supported me through thick and thin and made me who I am today. They have been patient and selfless and have taught me what unconditional love means. This is as much my success as it is theirs. My grandparents have been an integral part of this journey as well. My grandmother, Parvati Dasgupta overcame her inhibitions of technology so that she could FaceTime and iMessage me miles away and keep giving me a small taste of home every day. Even though my other grandparents may not be around, I hope I have made them proud with my accomplishments and there isn't a single day I don't miss them.

Finally, I would like to acknowledge the funding from AFOSR (contract#FA9550-16-1-0442). This work used computational resources of charge# TG-CTS160017 under Project PI Dr. Vishal Acharya at the Extreme Science and Engineering Discovery Environment (XSEDE), which is supported by National Science Foundation grant number ACI-1548562.

TABLE OF CONTENTS

LIST OF TABLES

LIST OF FIGURES

LIST OF SYMBOLS AND ABBREVIATIONS

T_{ad}	Adiabatic flame temperature
D_T	Artificial Diffusivity constant
ω_i	Chemical source term for species, i
τ_{chem}	Chemical time scale
$\mathbb{K}_C$	Curvature
ρ	Density
s_d	Displacement speed
ν	Dynamic Viscosity
ϕ	Equivalence ratio
τ_{ext}	Extinction residence time
κ_{ext}	Extinction stretch rate
$\overrightarrow{v_F}$	Flame propagating speed
$\vec{u}$	Flow-field velocity
τ_{flow}	Flow time scale
$\dot{q}$	Heat release rate

l	Integral length scale
Ka	Karlovitz number
η	Kolmogorov length scale
S_L	Laminar Flame speed
l_o	Laminar Flame thickness
Le	Lewis number
D_i	Mass diffusivity of species, i
Y_i	Mass fraction of species, i
R_{mix}	Mixture Gas constant
$c_{p_{mix}}$	Mixture specific heat constant
k_{mix}	Mixture thermal conductivity
α_{mix}	Mixture thermal diffusivity
X_i	Mole fraction of species, i
W_i	Molecular weight of species, i
$\vec{n}$	Normal
p	Pressure

$\mathbb{k}_1, \mathbb{k}_2$	Principal curvatures
$\bar{c}$	Progress variable
RR_k	Reaction rate of reaction, k
τ_{res}	Residence time
Re	Reynolds number
K_S	Tangential Strain
T	Temperature
ε	Turbulent kinetic energy dissipation
u'	Turbulence intensity velocity RMS
T^u	Unburnt reactant temperature
S_{L_O}	Unstretched laminar flame speed
R_u	Universal Gas constant
Ω	Volume of prism

SUMMARY

Stricter regulations in emissions for pollutants such as NO_x and greenhouse gases such as CO_2 has led to the development of cleaner combustion systems. Lean premixed combustion is an attractive avenue for gas turbine combustion systems. Premixing the fuel and oxidizer for leaner compositions leads to reduced combustion temperature and hence lower emissions. Due to the nature of turbulence and combustion, these systems are characterized by a large set of time, length and velocity scales due to the nature of turbulence and combustion. A significant effort has been made to understand this interaction of turbulence with combustion for different fuels, compositions and inlet conditions. Even though there are a lot of open questions in turbulent combustion, strides have been made in understanding flame-flow interactions and its impact on flame structure and propagation speeds which in turn has led to the development of closure models required by Large eddy simulations and Reynolds averaged Navier-Stokes equations.

Of all the interactions, turbulence-chemistry interactions are the least understood primarily due to the difficulty in obtaining responses for a large number of species from laser diagnostics and stiffness of the equations for simulations which leads to very small time steps leading to high computational costs. It is essential to understand this interaction as it can directly lead to alteration of flame structures and fundamental quantities of a reacting mixture such as auto-ignition times and blow-off behavior. Even though experimentally studying turbulence-chemistry interactions and its underlying physics is still difficult, improvements in computational resources has allowed the usage of detailed

chemical mechanisms for direct numerical simulations which can resolve all time and length scales.

Understanding turbulence-chemistry interactions for different fuels is the primary focus of this thesis. This is accomplished by analyzing datasets for turbulent flames with a canonical "flame-in-a-box" configuration with increasing turbulent intensities for premixed hydrogen/air, methane/air and n-dodecane/air flames. These results are compared with computations of unstretched flames, stretched flames and perfectly stirred reactors. The analysis is broadly divided into two categories:

a) Understanding the impact of increased turbulence on the overall chemical pathways through a "global" analysis.
b) From a modeling perspective, understanding the impact of turbulence on the chemical flame structure through a "local" analysis.

First, a "global" analysis of different metrics to quantify pathways is analyzed. These metrics include heat release and key species consumption and production pathways. An integration based method is developed to analyze multi-dimensional data i.e. 3D turbulent flames, 1D unstretched and stretched flames and 0D perfectly stirred reactors. For the "global" analysis the integrated values are averaged across the flame surface for the turbulent flames and compared with integrated values from unstretched and stretched flames along with point data from perfectly stirred reactors for all the three fuels considered. The "global" data for turbulent flames is also conditioned on local topology and fuel consumption to analyze feature specific chemical pathways for the different metrics and compared with their global counterpart.

Second, a “local” analysis of the reaction rates, heat release and fuel consumption based on conditional means is performed for the turbulent flames to understand the effect of turbulence on the chemical flame structure. These results are compared with the equivalent 1D profiles obtained from unstretched and highly stretched flames (close to extinction). This comparison is essential to see if the variation in the reaction rates with increasing turbulence can be represented using simple laminar models such as unstretched and stretched flames. The development of laminar flamelet libraries for LES and RANS uses the results from these simplified models for tabulation. It is, hence, useful to gain insight into conditions where they perform well and conditions where the model may break down.

Third, simplified transport models are compared to explain the changes in the reaction rate profiles obtained from the “local” analysis. The models tested include mixture-averaged transport (a common model for species transport in DNS, LES and RANS), unity Lewis number transport and mixture-averaged transport with an artificial constant diffusivity (which can mimic increased turbulence diffusivity with increasing turbulence intensities).

The results show a striking similarity in the pathways for stretched flames, perfectly stirred reactors and turbulent flames for hydrogen and methane, and between stretched flames and turbulent flames for n-dodecane flames. The variation in results between the turbulent flames and perfectly stirred reactors for n-dodecane flames is attributed to thermal effects. Local conditioning of the global results reveals changes in chemical pathways within different topologies and fuel consumption for all three fuels. Even though the dominant reactions are fairly invariant to the effects of turbulence, reactions of

secondary importance show a much stronger sensitivity to increasing turbulence intensities which may not be captured by the laminar flames. A "local" analysis reveals that the turbulent flame profiles are well bounded by the stretched flame calculations for all three fuels. This analysis also reveals an increased low temperature activity for hydrogen flames and reduced low temperature activity for the n-dodecane flames. The methane profiles do not show a significant change at lower temperatures. Even though the stretched flame calculations bound the turbulent flame profiles, these laminar calculations cannot explain the behavior of the turbulent flames with increasing turbulence intensities. Thus, a transport model comparison is performed to illustrate the effect of turbulence on the flame profiles. Increasing turbulence leads to two-fold effect on the flame: an increased stretch due to increased wrinkling and increased diffusivity and hence altered transport. For $Le<1$ flames, the effect of stretch supersedes the effect of increased diffusivity whereas for $Le\approx1$, diffusivity plays a stronger role. However, for $Le>1$ flames, both stretch and increased diffusivity drive the characteristics of the turbulent flames. In general, the behavior of the flames may not tend to unity Lewis number (unless the global Lewis number is close to unity).

The results presented in this thesis provide further insight into the physics of turbulence-chemistry interactions and its impact on the reaction rates and the dominant pathways. Additionally, it sets stage for the development of improved and simplified closure models for turbulence-chemistry interactions which can be used for LES and RANS.

CHAPTER 1. INTRODUCTION

1.1 Motivation

Turbulent premixed combustion has been a focus of research due to its extensive applications in internal combustion engines and gas turbines. Stricter regulations on emissions (NO_x, unburnt hydrocarbons, smoke, CO) and concerns over the effects of greenhouse gases (primarily CO_2) on global warming has led to significant research in the design and development of the next generation of combustors. Quintessential to this development is the improvement in the fundamental understanding of the characteristics and dynamics of these flames.

Typically, these new combustion technologies employ turbulent lean premixed flames. In premixed combustion, the fuel and oxidizer are mixed as homogenously as practical. This mixture can either auto-ignite or be ignited using an external source (such as a spark plug). The higher flow rates, required for the operation of these engines, lead to turbulent flows within the combustors introducing many interesting and challenging flow fields within these combustors. In addition, lean combustion (i.e. less fuel compared to stoichiometric proportions) is an excellent candidate that leads to lower emissions under appropriate conditions[1].

Turbulent combustion research encompasses many challenging and interesting phenomena. Turbulent flows introduce a spectrum of length, time and velocity scales. Turbulent kinetic energy is produced at the larger scales which cascades into the smaller scales leading to a strong coupling of these scales. Every flow is characterized by a large

scale, typically an integral length (and time) scale, which is a representation of the geometry of the problem. Additionally, the smallest scales in the spectrum correspond to the Kolmogorov scales, which are isotropic, following Kolmogorov's hypothesis and have universal features under all flow conditions[2]. Combustion, similar to turbulent flows, is a multi-scale non-linear problem comprised of reaction and diffusion processes. For a laminar premixed flame, the larger length scale corresponds to the flame thickness and a corresponding time scale related by the flame thickness and the propagation speed of the flame. Combustion chemistry, comprised of thousands of reactions, occurs over time scales that cover several orders of magnitude. Additionally, the involvement of numerous species introduces a multitude of diffusive time scales. A combination of turbulence and combustion thus involves the interaction of a collection of physical phenomena occurring at different length/time scales making it a rich area of research.

Many aspects of turbulent combustion still remain an open area of research. For example, flame-turbulence interaction focusses on understanding the effects of turbulence on flame wrinkling and flame structure through the effects of curvature and tangential straining[3-7]. Flame-flame interaction focusses on transient events when two flames (for example, two flames propagating towards each other, or a pocket and main flame interaction) interact with each other and variations in the flow field around these flames[8-11]. Finally, turbulence-chemistry interaction investigates the effect of increasing turbulence intensities on the response of the reactions and how these reactions can in turn alter the flame structure[12-14]. The primary motivation of this thesis is to understand this latter interaction and hence is discussed in detail in the next section.

1.2 Turbulence-Chemistry interactions

The effect of turbulence on chemistry can manifest itself in two ways. The first way is through an indirect method wherein the flame structure can alter the chemical reactions locally. For laminar flames, the diffusive fluxes are governed by the molecular transport of species and heat. However, increasing turbulence intensities leads to increased rates of scalar transport through increased turbulence diffusivity. This, in conjunction with the molecular transport rates can lead to an overall higher diffusion rates. These changes can in turn lead to an altered flame structure affecting macroscopic quantities of interest such as flame thickness and propagation speed. The chemical reactions, which are a strong function of the local species concentrations and temperature, are thus indirectly altered to respond to the modified flame profile.

The second way is a more direct response of the chemical reactions to turbulence. This can occur due to the alteration in the chemical pathways through a sequence of elementary reactions. The chemical pathways for simple fuels such as hydrogen and methane are well established[1, 15, 16]. To illustrate, Figure 1.1(a) depicts a network diagram for the production and consumption of different species and radicals involved in the oxidation of lean hydrogen/air reactants for $\phi = 0.4$ at $T^u = 298K$ and $p = 1atm$ to water (H_2O), as predicted by Li et al's[17] kinetic mechanism. It can be seen, for example, most of the fuel (81%) directly forms water (81%) through the reaction, $H_2+OH \rightarrow H_2O+H$. The rest of the fuel is indirectly converted to water through the H and OH radicals via different reactions such as $H+OH+M \rightarrow H_2O+M$, $HO_2+OH \rightarrow H_2O+O_2$. Figure 1.1(b) shows a schematic of the simplified connection diagram of the species/radicals formed in the CH_4 oxidation as predicted by GRIMech 3.0[18] for $\phi = 0.7$ at $T^u = 298K$ and $p = 1atm$. The

percentages show how much of a given species is converted to another species. The indicated values are calculated using the integrated reaction rates for the reactions involved in the mechanism. For example, most of the fuel (99.2%) is converted to the methyl radical (CH_3). The dominant path then breaks into three branches, as 48.3%, 22.4%, and 10.8% of CH_3 is converted to CH_2O, CH_2, and CH_3O, respectively. The diagram clearly shows that the basic chemical pathway for methane oxidation in laminar flames consists of breaking down of methane into the methyl radical, eventually leading to the formation of CO_2 through CH_2O, HCO and CO [16].

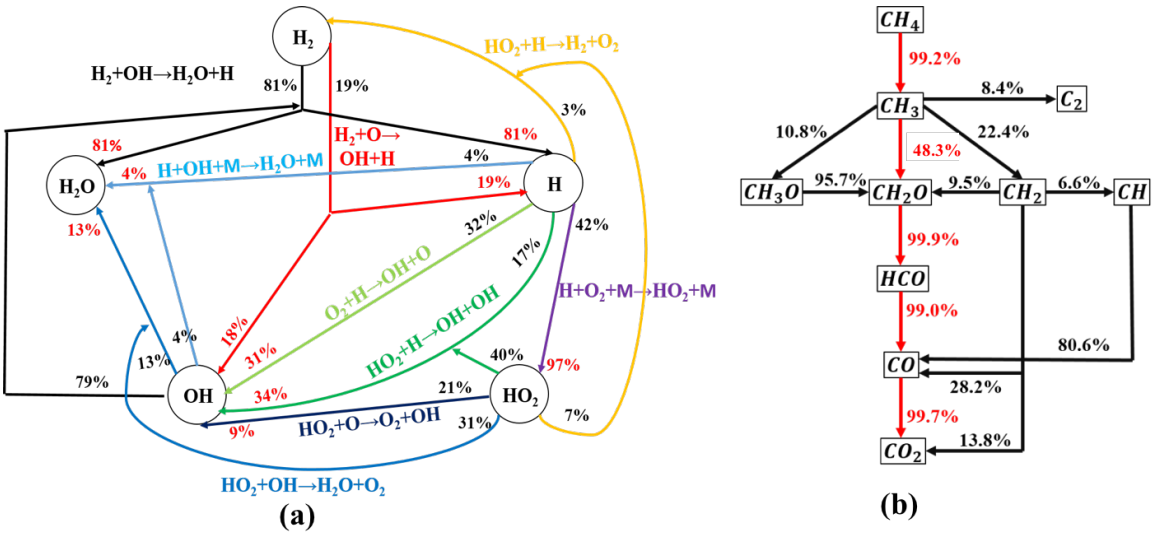

Figure 1.1. Chemical pathway for the oxidation of (a) hydrogen using Li et al. mechanism [14] (b) methane using GRI Mech 3.0[15] for unstretched laminar flames

Even for unstretched laminar flames, multiple different pathways for fuel oxidation can be observed. In a turbulent environment, the temperature field and the concentration fields of various major and intermediate species can be significantly different from a laminar flame. This raises an essential question for turbulent flames:

Are the relative contributions of different reactions altered in a turbulent flame relative to their laminar counterpart?

This question is particularly significant given that kinetic mechanisms are generally validated and benchmarked with measured data from canonical laminar flames, such as bomb reactors or steady laminar flames[19]. In addition, flamelet modeling approaches generally use libraries developed from laminar calculations for unstretched and stretched flames by solving the flamelet equations [20] and it is essential to understand their validity in describing chemistry in highly turbulent flow fields. Thus, a second important question to be addressed is:

To what extent do flamelet libraries built on laminar calculations capture the whole chemistry picture in turbulent flames?

After gaining insight into turbulence-chemistry interactions through the above two questions, the final question address is:

Can we use simplified models for turbulence-chemistry interactions rooted in the physics of the interaction to understand the changes observed?

1.3 Current Work

The scope of the current work is to investigate the effects of turbulence on the chemical pathways for lean premixed flames. This is accomplished by analyzing data obtained from direct numerical simulations for three different fuels: hydrogen, methane and *n*-dodecane. The 3D data is compared with results obtained from simplified laminar

models of unstretched premixed flames, stretched premixed flames and perfectly stirred reactors.

Chapter 2 considers in details the relevant background and literature review for the subsequent analysis. First, a detailed discussion about the potential mechanisms for turbulence-chemistry interactions is given. This is followed by a description of the turbulent premixed combustion regime. Different chemistry models prevalent for modeling turbulence-chemistry interactions are discussed. Finally, previous works looking at the influence of turbulence on chemistry are reviewed.

Chapter 3 reviews the details of the numerical procedures utilized for the data analysis. First, a concise description of the low Mach number code is given followed by a detailed description of the post-processing techniques used for data reduction and the inlet conditions for the different cases considered. Next, details of the laminar calculations for the different model reactors are discussed.

Chapter 4 discusses the results obtained for the "global" analysis (integrated and averaged across the flame) of the chemical pathways using multiple metrics. This is followed by an analysis of these metrics conditioned on local features (such as curvature, fuel consumption).

Chapter 5 examines the results obtained for a "local" analysis. Conditional means obtained from DNS are compared and contrasted with their laminar counterpart for different metrics (heat release, reaction rates).

Chapter 6 attempts to understand the results obtained from the "local" analysis using altered transport models. Firstly, the transport models implemented are discussed. This is followed by a detailed discussion of the impacts of altered transport on the reaction rates for the different fuels.

Chapter 7 closes this work with a summary highlighting the key observations and contributions of the work. This is followed by a scope of future work with the relevant unanswered questions.

CHAPTER 2. BACKGROUND AND LITERATURE REVIEW

This chapter discusses the relevant background and literature review relevant to the understanding of the work presented in the subsequent chapters. First, the potential mechanisms that can lead to significant turbulence-chemistry interactions are discussed. Following this, a discussion of premixed turbulent combustion and the regime diagram is provided to discuss the interaction of turbulence length/time scales with flame relevant length/time scales. Next, a discussion of simplified turbulence-chemistry models used in Large-Eddy simulations and Reynolds Averaged Navier-Stokes is provided. Finally, a review of the current body of work focusing on turbulence-chemistry interactions and its impact on the flame and its dynamics is discussed.

2.1 Mechanisms of turbulence-chemistry interactions

2.1.1 Flame stretch

All flames, whether laminar or turbulent, can experience flame stretch. Flame stretch, κ is defined as the fractional rate of change of the area, A of an infinitesimal element on the surface. This is pictorially depicted in Figure 2.1 and is defined as:

$$\kappa = \frac{1}{A}\frac{dA}{dt} \tag{2.1}$$

The expression given in 2.1 can be manipulated using vector geometry to take the form:

$$\frac{1}{A}\frac{dA}{dt} = \frac{\partial u_{t_1}}{\partial t_1} + \frac{\partial u_{t_2}}{\partial t_2} + (\vec{u}.\vec{n})\nabla.\vec{n} \tag{2.2}$$

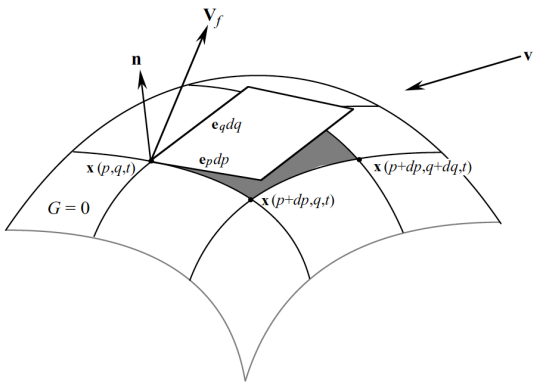

Figure 2.1. Schematic of a surface element with velocity V_f and unit normal n in a flow field of velocity v. Adapted from Law and Sung [21].

The coordinate system is defined in Figure 2.2. The expression 2.2 can also be expressed as:

$$\frac{1}{A}\frac{dA}{dt} = -\vec{n}\,.\nabla \times (\vec{u} \times \vec{n}) + (\vec{u}.\vec{n})\nabla.\vec{n} \tag{2.3}$$

where $\vec{u}$ is the flow velocity and $\vec{n}$ is the unit normal to the surface. For a premixed flame surface which propagates normal to itself, $(\vec{u}.\vec{n})$ is replaced with $(\overrightarrow{v_F}.\vec{n}) = (\vec{u}.\vec{n}) - S_L$ where $\overrightarrow{v_F}$ is the flame surface velocity and S_L is the laminar speed of propagation. The expression, $-\vec{n}\,.\nabla \times (\vec{u} \times \vec{n})$, is called hydrodynamic stretch and represents the stretching of the surface by tangential velocity and is represented as $\nabla_t.u_t$. The curvature of a surface, $\mathbb{K}_C$, is given by $-\nabla.\vec{n}$. Positive curvature corresponds to the center of curvature in products i.e. convex towards reactants. Thus, the term $(\overrightarrow{v_F}.\vec{n})\nabla.\vec{n}$ is the stretch due to curvature and flame movement.

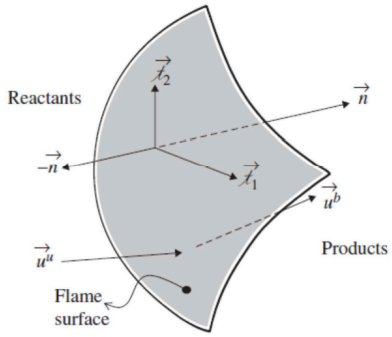

Figure 2.2. Coordinate system schematic for flame stretch derivation. Adapted from Lieuwen[22].

Equation 2.3 can be manipulated to distinctly illustrate the effects of flow non-uniformities and flame surface curvature as:

$$\kappa = -\vec{n}\vec{n}: \nabla \vec{u} + \nabla . \vec{u} - S_L \nabla . \vec{n} = -\frac{\partial u_n}{\partial n} + \nabla . \vec{u} + S_L \mathbb{K}_C \tag{2.4}$$

where, $\partial u_n / \partial n$ represents the gradient of the normal component of the velocity, u_n in the normal direction. A combination of the first two terms in Equation 2.4 is called tangential strain (K_S) and it represents the effect of spatial velocity gradients on flame stretch. Additionally, since the flame is typically defined as an iso-surface, S_L can be replaced with s_d, the displacement velocity of the surface. Thus, flame stretch is given by:

$$\kappa = K_S + s_d \mathbb{K}_C \tag{2.5}$$

For an unstretched laminar flame, the flame structure with the convective and diffusive fluxes is shown in Figure 2.3.

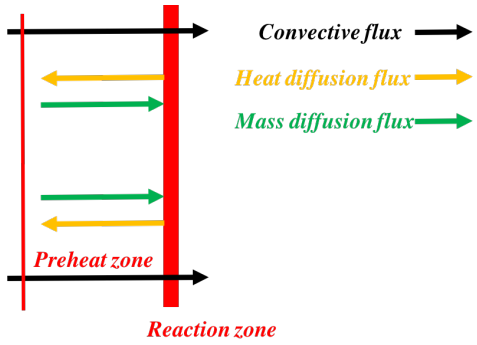

Figure 2.3. Schematic of unstretched laminar flame with fluxes

Unstretched laminar flames are flat and hence $\mathbb{K}_C = 0$. Additionally, the flow is uniform with no tangential velocity leading to $K_S = 0$. Thus, these flames are unstretched. A stagnation flame is a good example for stretched flames wherein $K_S \neq 0$ since $u_t \neq 0$. These flames are flat and hence $\mathbb{K}_C = 0$. These flames, thus, experience stretch only due to flow non-uniformities. A schematic for stagnation flames is shown in Figure 2.4(right). Another example of stretched flames is a Bunsen tip which is shown in Figure 2.4(left). For such flames, the tip is curved and hence $\mathbb{K}_C \neq 0$.

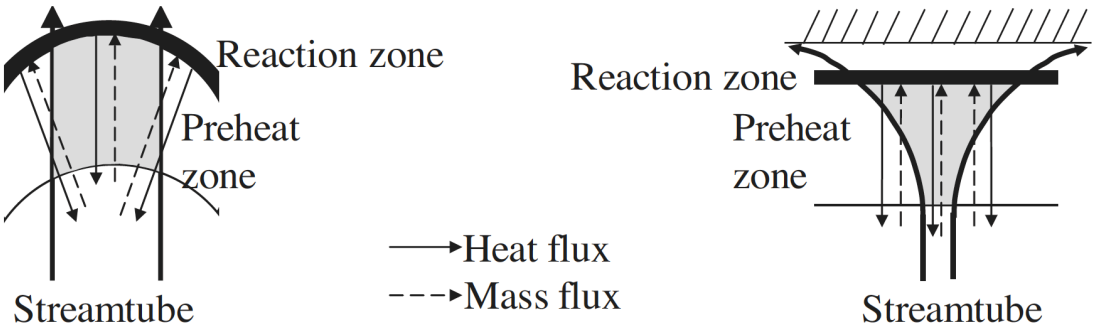

Figure 2.4. Schematic for stretched flames with misaligned fluxes. Adapted from Lieuwen[22].

To understand why stretch modifies the flame structure, firstly, a control volume is defined such that the sides are defined using streamlines. This leads to diffusive fluxes of heat and mass in and out of the control volume but no convective transfer through the sides of the control volume. Stretch manifests itself through the misalignment between the diffusive and the convective fluxes. The flame is a source for heat and a sink for reactants. For the curved flame(Figure 2.4(left)), the heat diffuses into the control volume leading to focusing of the heat whereas, the reactants diffuse out of the control volume leading to their defocusing. Reaction intermediates can also diffusive into or out of the control volume depending on their region of existence. For the stagnation flames(Figure 2.4(right)), heat is lost or defocused from the control volume and reactants are gained or focused into the control volume.

Additionally, how much more (or less) heat is lost compared to reactant gain is dictated by the Lewis number of the reactants, given by the ratio of thermal diffusivity to mass diffusivity. For example, if $Le < 1$ (or >1), thermal diffusivity is smaller (or greater) than mass diffusivity. As a result, the control volume loses less (or more) heat compared to mass. Preferential diffusion of species can also take place, given the existence of multiple species with varying diffusivity. For example, hydrogen, a light species, has a much higher diffusivity compared to other species such as oxygen, nitrogen etc. As a result, it will have higher diffusive fluxes in or out of the control volume. All these phenomena together can, in turn, change the local concentrations of scalars i.e. species mass fractions and temperature leading to altered reaction rates.

The mean curvature, $\mathbb{K}_C$ and Gaussian curvature of a surface can be used to calculate the principal curvatures, $\mathbb{k}_1, \mathbb{k}_2 (\mathbb{k}_2 < \mathbb{k}_1)$ such that $\mathbb{K}_C = \mathbb{k}_1 + \mathbb{k}_2$. Based on the signs of $\mathbb{k}_1, \mathbb{k}_2$, elements can be spherical ($\mathbb{k}_1 \mathbb{k}_2 > 0$), cylindrical ($\mathbb{k}_1 \mathbb{k}_2 = 0$) or saddle point ($\mathbb{k}_1 \mathbb{k}_2 < 0$). Figure 2.5 shows the three dimensional space afforded by $\mathbb{k}_1, \mathbb{k}_2, K_S$.

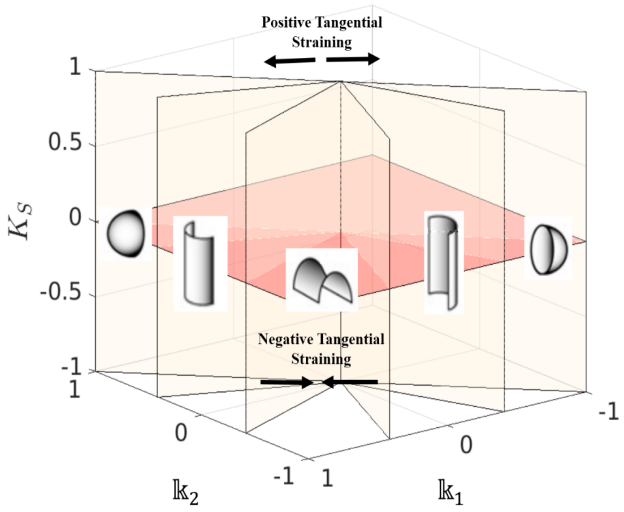

Figure 2.5. Illustration of potential iso-surface curvature and strain combinations.

Turbulent "flame", typically identified with an iso-surface (to associate strain and curvature with), can, in general, be highly curved and strained and portray these multiple topologies. The solution spaces of turbulent flames may not uniformly occupy all regions in this volume. This is because strain and curvature of the chosen iso-surface are correlated with each other[5, 23]. Additionally, the displacement speed of the iso-surface is also correlated with strain and curvature[4, 23-25]. Typical joint PDFs between these quantities is shown in Figure 2.6.

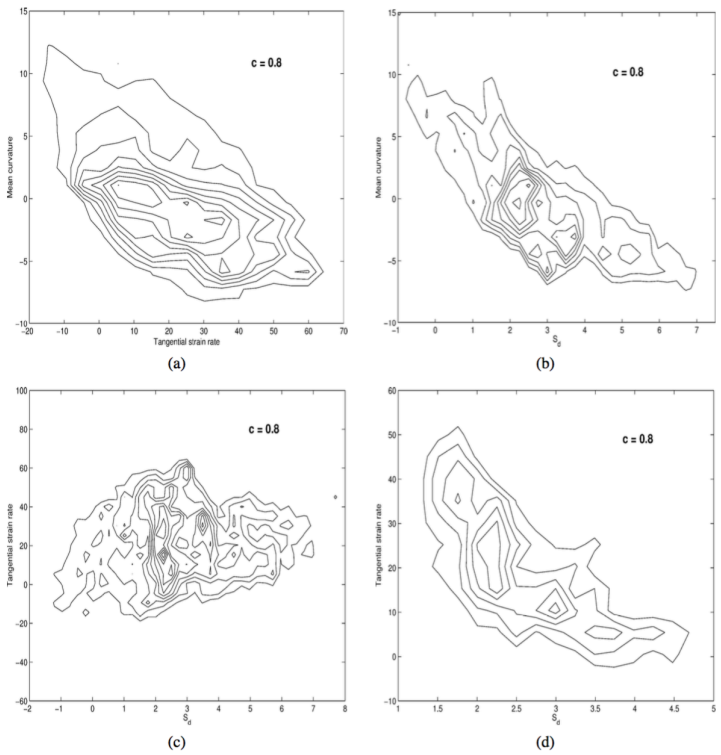

Figure 2.6. Contours of joint pdfs of tangential strain rate, mean curvature, and displacement speed on the isosurface at c = 0.8, close to the location of maximum reaction rate. (a) Joint pdf of tangential strain rate and mean curvature. (b) Joint pdf of displacement speed and curvature. (c) Joint pdf of displacement speed and tangential strain rate. (d) Conditional joint pdf of displacement speed and tangential strain rate taken at zero curvature. Joint pdf magnitudes decrease from the center to the circumference. Adapted from Chakraborty and Cant[7].

A strong negative correlation can be seen between the mean curvature and tangential strain in Figure 2.6(a). A negative correlation between the displacement speed and curvature can also be observed in Figure 2.6(b). In general, the tangential strain and displacement speed seem uncorrelated(Figure 2.6(c)). However, when the joint PDF is conditioned at zero curvature, a negative correlation can be seen for tangential strain and displacement speed. As mentioned earlier, the iso-surface used to identify the "flame" is definition specific and each of these surfaces can have different responses for curvature, tangential straining and displacement speeds[4, 7, 24]. Additionally, even for the same progress variable, surfaces

corresponding to different iso-values can give significantly different correlation[26]. This is shown in Figure 2.7. At smaller values of progress variables, tangential strain and curvature seem uncorrelated. However, at higher values of progress variable, a negative correlation can be seen.

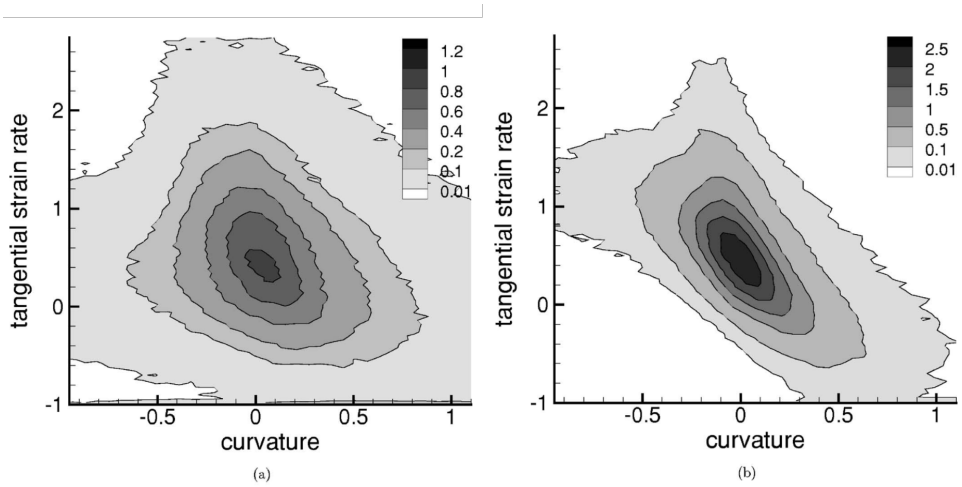

Figure 2.7. The joint PDFs of the curvature and the tangential strain rate term for (a) the ensemble with 0.05<C<0.15 and (b) the ensemble with 0.4<C<0.8. Adapted from Kim and Pitsch[26]

Turbulent distortions of the flamelet introduce a large number of potential combinations and topologies for flame stretch and each topology can respond differently by focusing and defocusing scalars as discussed earlier. This can strongly affect the local reaction rates through species concentrations and temperature dependencies. This has been explicitly observed wherein faster diffusing species such as H, H_2 correlate strongly with curvature. Slower reactive species such as CO are correlated strongly with tangential strain but not curvature[3].

2.1.2 Unsteady response

A second mechanism which effects the relative contributions of different reactions in turbulent flames is due to unsteady kinetic and diffusive effects. One can define a chemical time $\tau_{chem,i}$ and an associated Karlovitz number, Ka_i associated with the i-th reaction as:

$$Ka_i = \tau_{chem,i}\,\kappa \tag{2.6}$$

Different reactions have different characteristic chemical times and their instantaneous rates and relative roles in the overall oxidation and heat release pathway may be altered in cases where the response of one or more reactions to unsteady stretch is not quasi-steady, i.e., Ka_i~O (1)[3, 4, 27, 28]. Different portions of the flame i.e. the preheat zone and the reaction zone can respond different to the unsteady stretch leading to altered species concentrations upstream of and within the two zones. This is demonstrated in Figure 2.8, wherein the response of the consumption speed (representative of the reaction zone) and flame speed (representative of the flame preheat zone) to unsteady straining are drastically different. The consumption speed response is insensitive with increasing frequency whereas the flame speed shows increased response with increasing frequency suggesting altered response of different zones within the flame structure.

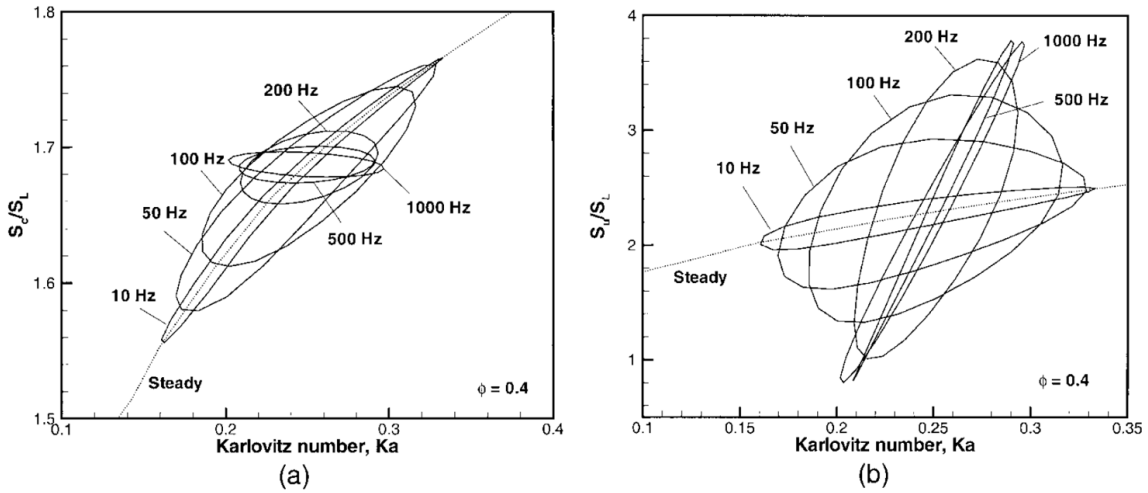

Figure 2.8. Response of (a) Sc and (b) Su to laminar Karlovitz number, Ka for different frequencies. Adapted from Im and Chen[28].

In addition, even in cases where all reactions are quasi-steady, local radical concentrations may not be at quasi-steady values due to diffusive time lags. For example, slower species are more susceptible to unsteady strain rate effects which can lead to altered reaction response for reactions containing these species [3, 4, 28].

2.1.3 Stirring effect

A third mechanism through which turbulence can modify the contributions of different reactions, relative to laminar flames, is through the "stirring" action of small scale eddies within the flamelet, introducing spatially differentiated convective transport of species along the flamelet. Increasing turbulence intensities introduces smaller energetic scales which can penetrate into the flame and lead to altered scalar concentrations. The effect of these eddies is further discussed in the next section wherein the different regimes of premixed turbulent combustion are explored.

2.2 Turbulent premixed combustion regime diagram

Turbulence introduces a spectrum of time, length and velocity scales. Thus, the characteristics of turbulent flames can be significantly different based on the turbulence intensities. The classification for these premixed turbulent flames is represented using the Borghi diagram shown in Figure 2.9. The x-axis of the diagram is given by the ratio of the turbulent integral length scale l to the flame thickness, l_o. The y-axis is given by the ratio of turbulent intensity, u' to the unstretched laminar flame speed, S_{L_O}.

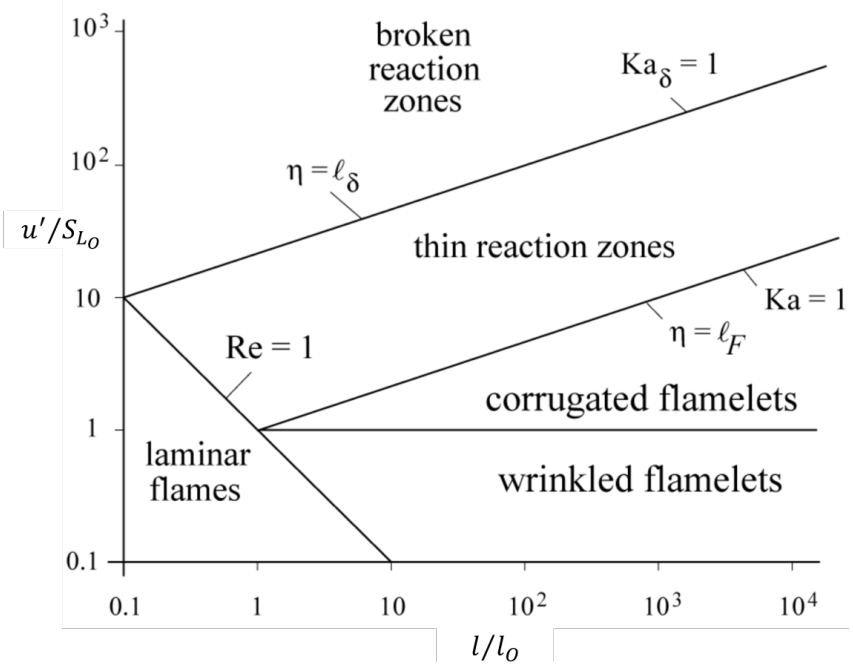

Figure 2.9. Borghi diagram for turbulent premixed combustion. The classification depends on ratio of velocity scales and length scales[29, 30].

Karlovitz number (*Ka*) is a non-dimensional number used to characterize turbulent flames and appears in the Borghi diagram to mark different limits. It is the ratio of a characteristic chemical time scale, τ_{chem} associated with the flame and a turbulent flow time scale, τ_{flow} i.e. $Ka = \tau_{chem} / \tau_{flow}$.

The laminar flame regime is characterized by flow perturbations much smaller than the laminar flame speed or integral length scales much smaller than the flame thickness and is typically characterized by a Reynolds number, $Re \leq 1$. Any turbulent fluctuations are overwhelmed by the viscous diffusion. The unstretched and stretched flames such as Bunsen flames, stagnation flames discussed above fall into this category.

In the wrinkled flamelet regime, the turbulence intensities are lower than the flame speed and hence large wrinkles formed are damped by the flame propagation. Also, the integral length scale is much larger than the flame thickness and hence cannot interrupt the internal processes and structure of the flame.

In the corrugated flamelet regime, the flame thickness is still smaller than the integral length scale leading to an undisrupted flame structure similar to laminar flames. The upper limit for this ratio is when the Kolmogorov length scale, η (which is the smallest turbulence scale) is of the same order as the flame thickness. However, the turbulence intensities are now larger than the laminar flame speed. This leads to highly wrinkled and folded flames wherein the wrinkles are formed faster than they can be smoothened. Pockets of reactants in products and vice-versa may be observed in this regime. Highly stretched flames may extinguish in this region due to hydrodynamic straining[22].

The thin reaction zone regime is also known as the thickened flamelet regime. The lower bound of this regime is given by $Ka_\eta = 1$ where the Karlovitz number is defined by the ratio of the overall flame time scale to the Kolmogorov time scale for the turbulent flow i.e. $Ka_\eta = \tau_{chem} / \tau_\eta$. The upper bound of this regime is given by $Ka_\delta = 1$ where the Karlovitz number is defined by the ratio of the reaction zone time scale to the Kolmogorov

time scale. In this limit, the smaller energetic scales are of the same order as the reaction zone thickness but are smaller than the preheat zone thickness and can penetrate into this zone leading to convective stirring of scalars internally which, in turn, disrupts the preheat zone structure. Thus, the quasi-steady, laminar flame structure is lost and laminar flamelet concepts cannot be applied directly[22, 31]. However, the smaller scales are still larger or of the same order as the reaction zone and hence, not small enough to penetrate into this zone, leading to an undisrupted and thin reaction zone but a thickened preheat region. $Ka_\eta = 1$ line is also known as the Klimov-William limit and quasi-steady laminar flames extinguish in this limit. The smaller eddies with high hydrodynamic strain, however, cannot quench the flame since they diffuse out in the preheat region due to comparable viscous dissipation time scales and Kolmogorov time scales in these regions [22, 32-34]. Most practical combustion devices are operated in this regime since mixing is enhanced at higher Karlovitz numbers leading to higher heat release and shorter combustion times.

In the broken reaction zone, the smaller turbulent scales are smaller than the reaction zone leading to $Ka_\delta > 1$ and can potentially penetrate into the reaction zone. This in turn leads to a broken reaction zone wherein the "flame" resembles a well-stirred reactor. The mixing is faster than chemistry which can lead to local extinction. Practical combustion devices are not operated in this region since this can cause noise, instabilities and global extinction.

Even though this diagram depicts well-defined regions, these estimates are theoretical. Generally, thin flamelets can exist at Karlovitz number higher than the Klimov-Williams limit. Similarly, thickened flamelets can exist in regions that are theoretically marked broken reaction zone.

All the datasets analyzed in this work fall into the thin reaction zone and on the boundary between the thin reaction zone and broken reaction zone.

2.3 Comparing stretched flames and turbulent flames

A common practice in understanding the behavior of turbulent flames is to perform detailed analysis of stretched flames and extrapolate that knowledge to the dynamics of turbulent flames. Stagnation flames are typical configurations used for this comparison[25, 35, 36]. These are flat flames and are, thus, subjected to only tangential straining which leads to flame stretch.

A topology analysis of turbulent flames using probability density functions suggest the mean curvature of the flames is close to zero with longer tails towards negative curvature for hydrocarbons flames and positive curvature for hydrogen flames. The strain rate PDF has a positive mean with finite probability for negative straining (for example in [3, 37, 38]). This is shown in Figure 2.10 for methane/air flames. As long as the curvature response is linear and there is a slight correlation between curvature and strain, the effects of curvature will average away in the mean leaving only strain effects[23]. Thus, for averaged statistics, stagnation flames with no curvature and positive straining should be able to represent turbulent flame characteristics.

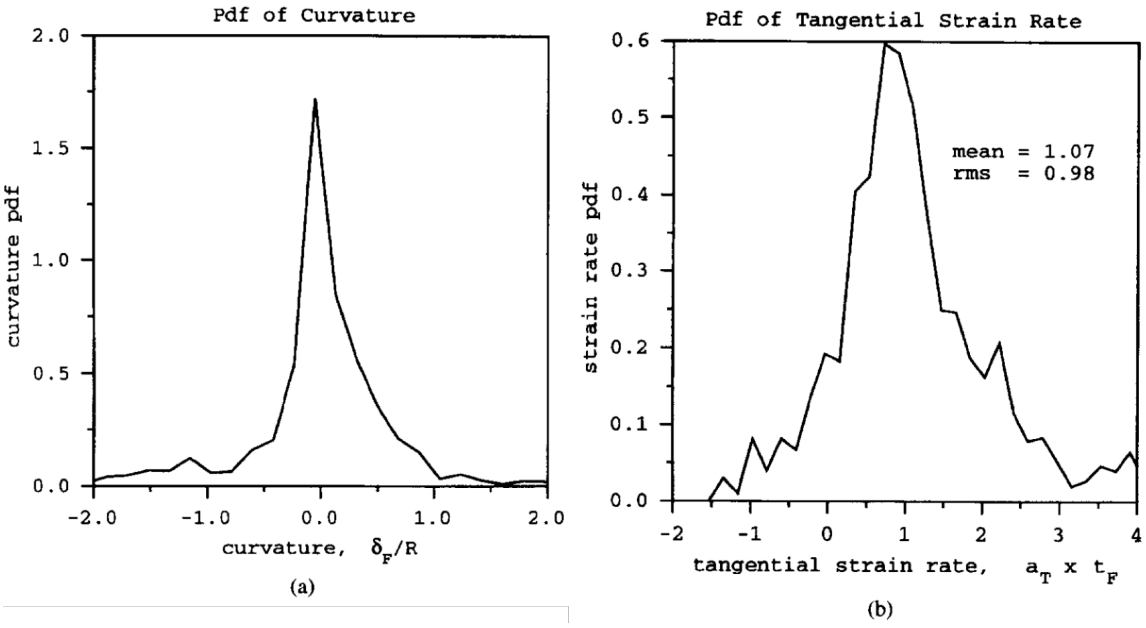

Figure 2.10. Probability density function of (a) curvature and (b) tangential strain rate. Curvature and tangential strain rate are normalized by the flame thickness and inverse of a flame time respectively. Adapted from Echekki and Chen[3]

The two common configurations of comparison are the reactant-to-reactant and the reactant-to-product configuration. For the reactant-to-reactant configuration, reactants are introduced from two nozzles leading to twin flames with an impermeable stagnation plane at the center. For the reactant-to-product configuration, the reactant from one nozzle is stagnated against hot adiabatic products from the other nozzle leading to a permeable stagnation flame. Though an extensive analysis does not exist to identify the ideal configuration, studies have shown that the two models provide similar results in the low stretch regime. At higher stretch rates, there are quantitative deviations in their predictions of quantities such as flame speed but both the models capture the qualitative changes well[36]. For this work, the reactant-to-reactant configuration is chosen. This configuration allows for the extinction of the flame at high stretch rates leading to regions of "low" and "high" stretch w.r.t the extinction stretch rate.

2.4 Review of turbulence-chemistry models for premixed flames

A significant body of work for DNS, LES and RANS uses single-step chemistry to understand and predict flame dynamics (for example, see [6, 39, 40]). However, to completely understand the structure of turbulent flames and for better predictions in emissions, it is essential to utilize detailed chemistry. Typically, for LES and RANS, the thermochemical state is described by a reaction progress variable such as temperature or a product mass fraction using which the other relevant species mass fractions can be obtained. The governing equation for the progress variable needs closure models for filtered chemical reaction rate, filtered rate of molecular transport and sub-grid model for the turbulent transport [41, 42].

One of the simplified model for reaction rate is an algebraic model called the Eddy Break-Up model(EBU) model[43] which assumes that the chemistry is fast and the mean reaction rate is determined by the mean turbulent mixing rate. Even though this is computationally inexpensive, this does not include information about detailed chemistry.

Another approach based on laminar flames are thickened flame models[44, 45]. The flame thickness is scaled by a factor keeping the flame speed constant and can be resolved on the LES mesh. Detailed chemistry can be incorporated into this model while generating the flame structure and this model has been used extensively.

G-equation modeling has been used extensively in RANS for numerous applications[46] and has been extended for use in LES[47]. The modeling philosophy for the G-equation is opposite of the previous model and it treats the “flame” as a propagating surface with zero flame thickness. A comparison between the two in given in Figure 2.11

However, this approach requires a closure model for turbulent burning velocity which is not trivial and does not have a universal form[41].

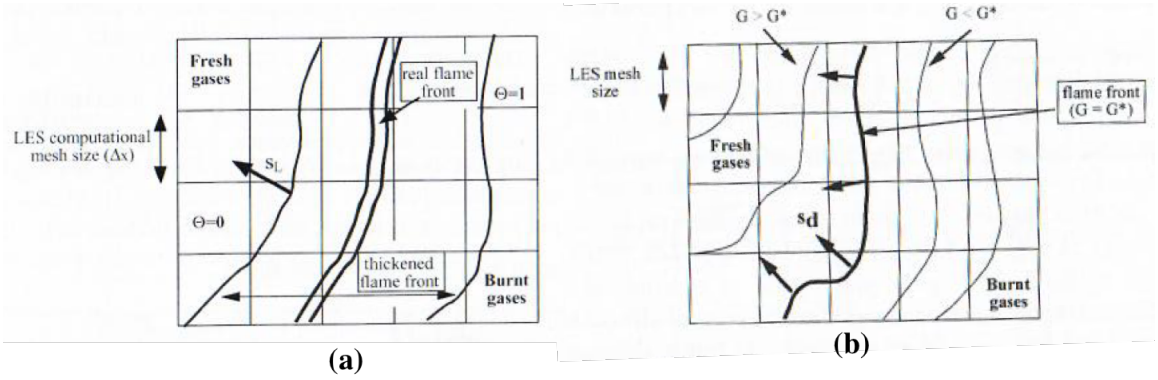

Figure 2.11. (a) Thickened flame approach (b) Flame front and G field with G=G* as the given surface. Adapted from Poinsot and Veynante[41].

Another popular approach is flame surface density(FSD) modeling[48, 49]. FSD is defined as the flame surface area per unit volume. Algebraic expressions can relate the reaction rate with the FSD. FSD can be modeled using algebraic expressions or balance equations. It can also be obtained from filtered laminar flamelets or from experimental data which account for complex chemistry with filtered reactions rates[50, 51].

Conditional moment closure (CMC) approach has been successfully used for non-premixed flames and has been extended to premixed flames with a reaction progress variable as a conditioning variable[52]. This approach solves balance equations for conditional species mass fractions and can be considered as an extension of FSD formulation for multiple surfaces.

Flamelet libraries, another popular approach, can be precomputed using detailed chemistry and can store quantities such as mean reaction rates, burning rates as a function

of a reaction progress variables such as temperature and inlet conditions. These tables can include quantities that affect flame stretch such as strain and curvature. These look-up tables can then be used to find the derived quantities as a function of these independent quantities. This method tends to be computationally expensive.

An alternate to this approach is the Flamelet Generated Manifold (FGM) [20] and Flamelet Prolongation of Intrinsic Low-Dimensional Manifold (FPI)[53] methods. These approaches involve a set of flamelet equations with the inclusion of strong stretch effects. The manifold is constructed using 1D laminar flamelets and can be used in subsequent flame simulations. The dimensionality of this manifold is determined by the number of controlling variables which is dependent on the application. For example, product and reactant mass fractions can be controlling variables with the minor species solved from the manifold rather than governing equations.

Probability density function models use PDF's to describe the averaged variables. Two classes of PDF approaches exist to describe the chemical closure. The first approach utilizes information of a given number of moments to close the source terms and is referred to as the presumed PDF approach. The PDF shape of certain variables (typically progress variables) is assumed and parameterized using the mean and variance[54, 55]. The other dependent variables are calculated using these assumed PDF shapes. The second approach involves solving an evolution equation for the PDF[56, 57]. The chemical source term directly depends on chemical variables and do not need to modelled and thus, this approach can handle complex chemistry easily.

Most of the methods discussed here intend to resolve the flame structure and heavily rely on laminar calculations for the chemical source terms and hence it is important to contrast and compare laminar flame chemistry with turbulent flame chemistry to understand if laminar flames can truly portray the whole picture for turbulent flames.

2.5 Turbulence-chemistry interactions

The effect of turbulence on the flame structure has been an active research area first through simplified asymptotic analysis [30, 31] followed by experiments and simulations[58, 59]. With improved diagnostics and computing resources, it has been possible to gain significant insight into turbulence-flame interactions. For example, a significant effort has been invested in understanding the effect of turbulence on propagation speeds[4, 9, 60], how they are affected for different Lewis number flames[9, 23] and its dependence on flame topology and flow properties[6]. Understanding the effect of turbulence on the flame structure and its transition from thin reaction zone to the distributed zone has also been of interest[37, 61-63].

However, body of literature focusing on understanding the physics of turbulence-chemistry interactions is fairly new and has been facilitated by the improvement in computational resources allowing for the inclusion of detailed chemistry over a simplified one-step chemistry in direct numerical simulations[59, 64].

Early analysis for oxidation pathway for hydrocarbon fuels suggests local variations in the oxidation pathways for turbulent flames. For example, Day et al.[65] performed 2D DNS of methane/air flames with varying hydrogen content. They noted three different regions of the flame front (a) intense burning regions with positive curvature, (b)

weak burning regions with negative curvature (c) large scale flame folding regions (Regions where H_2 consumption is zero but C_2 hydrocarbon concentrations are high (shown in Figure 2.12). They investigated corresponding changes in C and C_2 kinetic pathways for each of these regions. The C pathway via CH_3O increased from 4.2% in region (a) to 7.7% in region (b) to 11.8% in region (c). The C_2 pathway shifted from 2.7% to 3.8% to 5.1% in regions (a), (b) and (c) respectively.

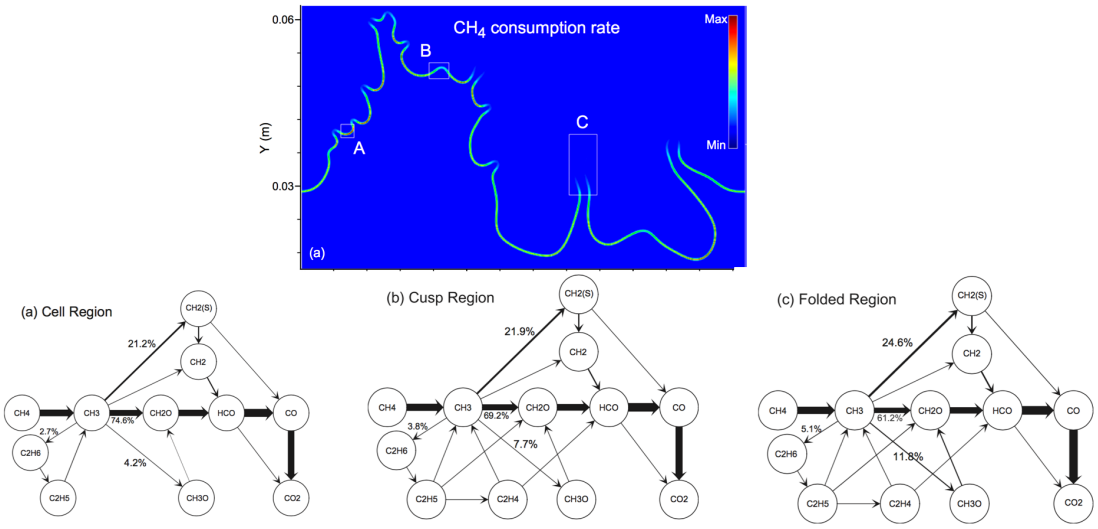

Figure 2.12. (above) Methane consumption rate from typical flame snapshot and (below) C pathway diagram for the three indicated regions. Adapted from Day et al.[65]

One noted effect of turbulence on chemistry is increased low temperature activity for different reactions[12, 14, 66]. For example, for H_2/Air flames, Aspden et al.[12] observed a decorrelation between heat release and fuel consumption in regions of high curvature (shown in Figure 2.13) due to reactions $H+O_2(+M)\rightarrow HO_2(+M)$, $HO_2+H\rightarrow OH+OH$ and $HO_2+OH\rightarrow H_2O+O_2$. These reactions do not involve H_2 (and hence fuel consumption) and contribute most of the heat released in regions of negative curvature.

Overall, the lower temperature regions (T < 992K) show a 7 times higher heat release compared to high temperature regions from *Ka*=1 to *Ka*=36. This can be attributed to the higher radical pool in these regions with increasing *Ka.*

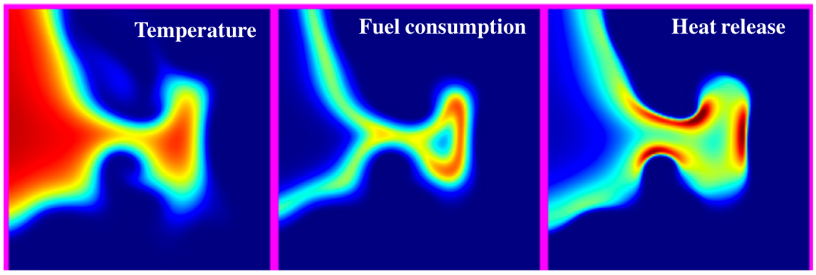

Figure 2.13. Zoomed in slices for temperature, fuel consumption, heat release for a high Karlovitz H2/Air flame. Red regions correspond to a higher value of the quantities. Adapted from Aspden et al.[12]

Carlsson et al.[14, 66] also observed changes in the low temperature region with increasing turbulence for CH_4/Air and H_2/Air flames. They noted a factor of 2-3 increase in heat release in these regions (T < 800K for CH_4 and T < 600K for H_2) compared to 1D laminar flames shown in Figure 2.14.

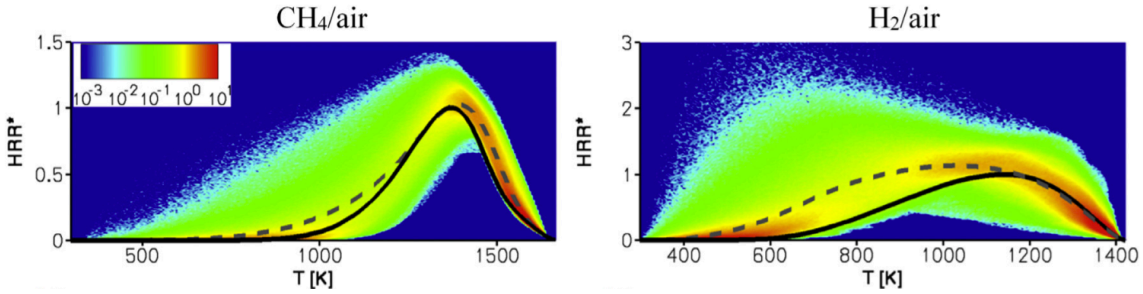

Figure 2.14. JPDF for normalized heat release for CH_4/Air (left) and H_2/Air(right) as a function of temperature. The dotted line corresponds to the DNS conditional mean and the solid line corresponds to an unstretched laminar flame profile. Adapted from Carlsson et al.[14].

Increasing turbulence intensities reduce the effective diffusive time scales leading to higher concentration of H radicals in the low temperature regions. This, in turn, promotes the reaction rates for $H+O_2(+M)\rightarrow HO_2(+M)$ and $H+CH_2O\rightarrow HCO+H_2$ leading to higher heat release at low temperatures for these flames.

Another common effect of turbulence on the flame structure is a thickening of the preheat zone[38, 67-70]. Compensation for this altered flame structure leads to an altered species response which can affect the reactions. For example, in methane flames, Aspden et al.[67] observed a shift of the species profiles towards a unity Lewis number profile from an unstretched laminar flame profile with increasing turbulence intensities suggesting a decreased effect of molecular diffusion over turbulent diffusion. Turbulence transports all scalars i.e. heat and species at the same rate, leading to equivalent turbulent thermal and mass diffusivity and hence a unity turbulent Lewis number. Specifically, reactants seemed unaffected. However, products and stable intermediates had elevated concentrations in the preheat zone as shown in Figure 2.15. A similar observation was found for n-dodecane flames wherein extensive thickening of thermal profiles was noted with stronger variations in fuel fragment formed from pyrolysis at temperatures lower than heat release[68].

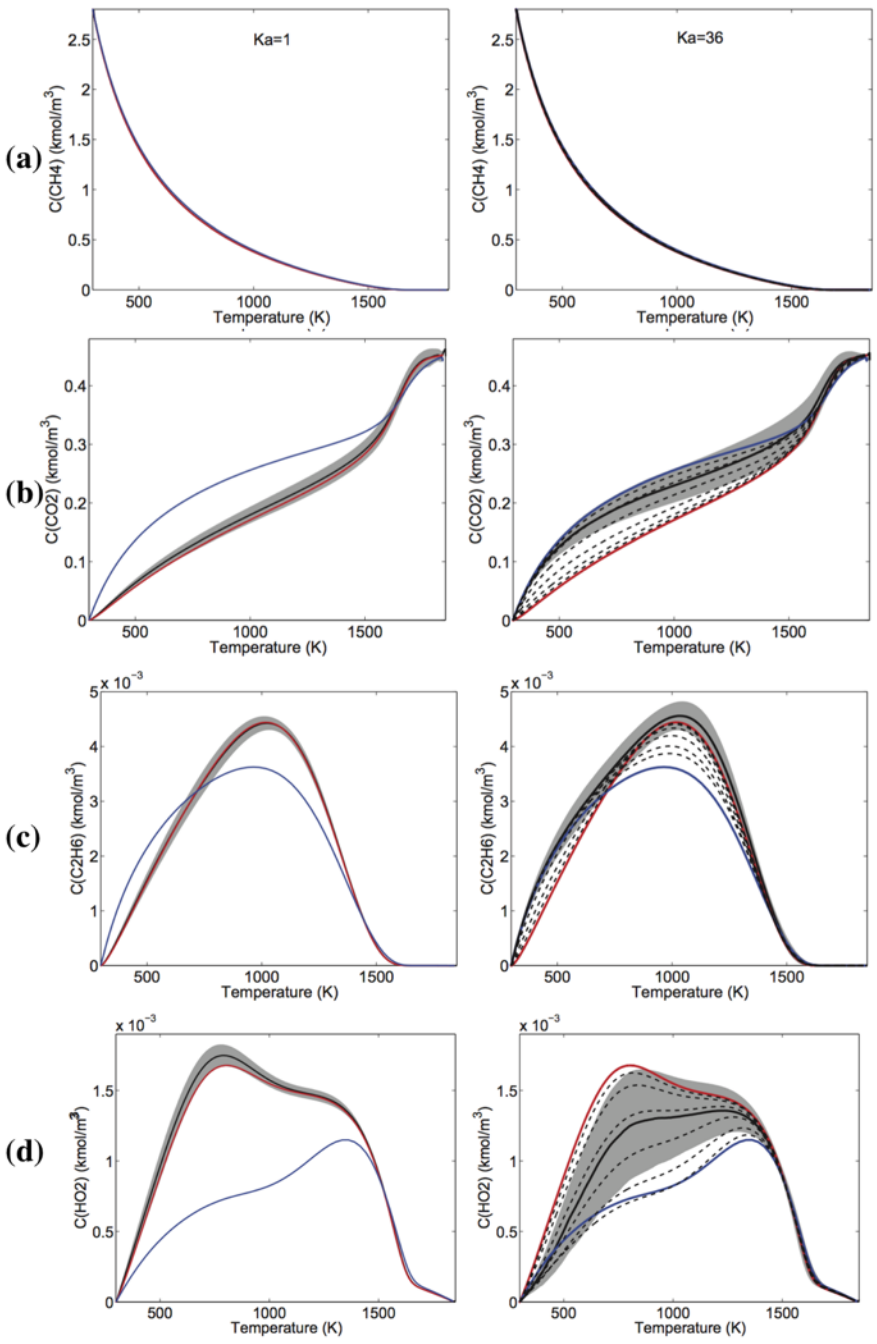

Figure 2.15. Conditional means of molar concentrations of (a) CH_4 (b) CO_2 (c) C_2H_6 (d) HO_2 for low (left) and high(right) turbulence intensities. Adapted from Aspden et al. [67]. The black line denotes the DNS conditional mean, red line denotes the unstretched laminar profile and the blue line denotes unstretched laminar flame profile with unity Lewis number transport.

Savard et al.[13] observed a similar response for n-heptane flames where the low temperature profiles aligned with unity Lewis number profiles whereas the high temperature profile deviates from the unity Lewis flamelet due to a reduced local Karlovitz number since the Kolmogorov length scale increases through the flame. For the same datasets, Lapointe et al.[71] compared the three dominant fuel consumption reactions for n-heptane and observed ~1-3% change between the turbulent and laminar cases. They also compared two high heat release reactions: $CH_3+O \rightarrow CH_2O+H$, $HCO+H \rightarrow CO+H_2$ and noted a 0-1% change in their contributions to the total heat release suggesting no significant effect of turbulence on chemistry. In general, experiments and DNS have observed the broadening of important species layers which play a key role in oxidation such as OH and CH_2O which can modify the reaction pathways in different zones of the flame[72, 73].

Overall, some of the key relevant findings focus on the influence of turbulence on the flame structure namely, increased low temperature heat release, thickening of the preheat zone, movement of the species profiles towards unity Lewis number. Little work exists to identify the direct influence of turbulence on chemistry through the disturbance of chemical pathways. Additionally, most of the turbulent and laminar flame comparisons involve unstretched flames as the laminar model. There exists limited systematic comparison between laminar stretched flames and turbulent flames. This work has two primary objectives; one, to quantify the disturbance of the chemical pathways through a "global" analysis and two, to compare the turbulent chemical flame structure with the corresponding laminar stretched and unstretched flame to identify regimes of good (and poor) agreement through a "local" analysis. This work also extends the "local" analysis to identify the factors controlling the agreement.

CHAPTER 3. NUMERICAL PROCEDURES

Three different simulations are used for answering the questions raised in Chapter 1; namely direct numerical simulations for three dimensional turbulent flames, PREMIX[74] for unstretched laminar flames, OPPDIF[75] for stretched counter-flow flames and PSR[76] for perfectly stirred reactors. Problem setup and post-processing of the data obtained from all simulations is discussed below.

3.1 Direct numerical simulations

3.1.1 Low Mach number Code

The reacting Navier-Stokes equations are solved using a low Mach number approximation[77-79] which allows acoustics waves to propagate out of the system at infinite speed. This is a good assumption when the flow velocities within the domain are much smaller than the speed of sound. Under these assumptions, the resulting set of equations is given by:

$$\frac{\partial \rho}{\partial t} + \nabla.(\rho\vec{u}) = 0 \tag{3.1}$$

$$\frac{\partial(\rho\vec{u})}{\partial t} + \nabla.(\rho\vec{u}\vec{u}) = -\nabla\pi + \nabla.\vec{\tau} + \rho\vec{F} \tag{3.2}$$

$$\frac{\partial(\rho Y_i)}{\partial t} + \nabla.(\rho Y_i\vec{u}) = \nabla.(\rho D_i \nabla Y_i) + \rho\omega_i \tag{3.3}$$

$$\frac{\partial(\rho h)}{\partial t} + \nabla.(\rho h\vec{u}) = \nabla.(k\nabla \mathrm{T}) + \sum_i \nabla.(\rho h_i D_i \nabla Y_i) \tag{3.4}$$

where, ρ is the density, $\vec{u}$ is the velocity field, π is the perturbation pressure field, $\vec{\tau}$ is the stress tensor, $\vec{F}$ is a long wavelength forcing term which is used to maintain turbulence inside the domain, Y_i is the mass fraction of the *i*th species, D_i is the diffusivity of species *i,* $\rho\omega_i$ is the source term for species *i* and is calculated from the chemical reactions*,* h is the mixture enthalpy, k is the thermal conductivity, T is the temperature and h_i is the enthalpy for species *i*. Diffusion is modeled using the mixture-averaged approximation and neglects Soret and Dufour effects[80]. In the low-Mach number simulations, π satisfies $\pi/p_o \sim O(Ma^2)$ where p_o is the ambient pressure and Ma is the Mach number. Additionally, all thermodynamic quantities are independent of π. The ideal equation of state supplements the above set of equations to solve the flow field and is given as:

$$p_o = \rho R_{mix} T = \rho R_u T \sum_i \frac{Y_i}{W_i} \tag{3.5}$$

Where R_{mix} is the mixture gas constant, R_u is the universal gas constant and W_i is the molecular weight of species *i*.

The numerical framework is established by Day and Bell [81]wherein the code implements an operator-split formulation to computationally decouple the chemistry from the flow properties. These set of equations discretely conserve species and enthalpy with a correction constraint to prevent the solution drifting too far away from the equation of state. A Godunov-type upwind advection algorithm is used for computing advection

derivatives[82]. Low Mach number simulation leads to decreased stiffness allowing the time steps to be governed by the flow time scales resulting in larger time steps. The source term and species diffusion occur at much smaller time scales compared to the flow time scale and are calculated at smaller time steps implicitly. The implementation details can be found in Almgren et al.[83, 84]. This integration algorithm achieves second order accuracy in time and space.

3.1.2 Domain description

The simulations are performed for a canonical "flame-in-a-box" configuration. A schematic of the domain is shown in Figure 3.1.

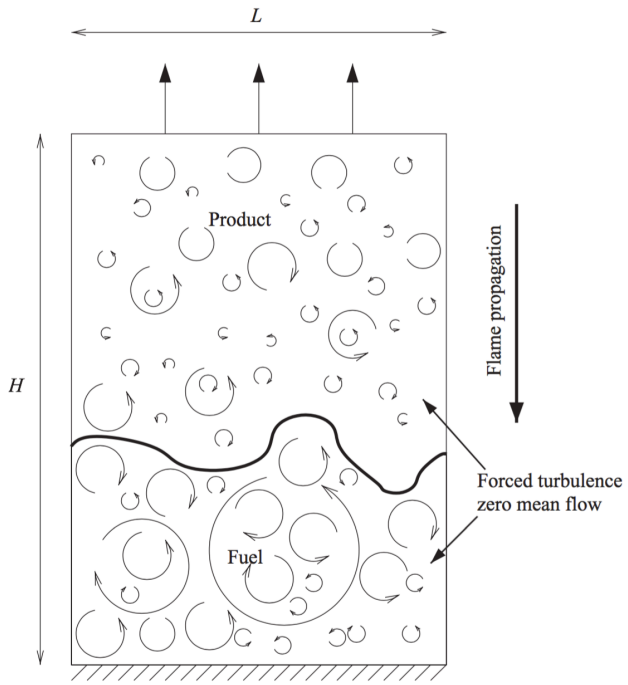

Figure 3.1. Schematic of the flow domain. Adapted from Aspden et al.[62].

A flame is simulated with cold reactants beneath hot products leading to a downward propagating flame. Periodic lateral boundary conditions with outflow at the top and free-

slip fixed wall at the bottom of the domain are specified. Typically, a high aspect ratio domain (1:1:8) is specified allowing enough length for flame propagation to reach a statistically stationary state allowing for further post-processing of the data without any transient information.

For all the data sets analyzed here, the inlet temperature, T^u is 298K and the pressure, p_o is 1 atm. The pressure p_o is maintained a constant in space and time establishing an "open" domain.

3.1.3 Initialization of the problem

The forcing term in the momentum equation as mentioned in 3.1.1 maintains the turbulence within this domain. This approach has been established in Aspden et al. [85, 86] and has certain advantages over the inflow boundary conditions. For example, the turbulence levels are maintained in this approach, opposed to decaying turbulence. The latter approach warrants regulated inflow flow rates which, in turn, can lead to instabilities particularly at higher inlet velocities[62]. Typically, the turbulence is first established and allowed to evolve till it is well-developed inside the box.

A flat flame is obtained using PREMIX[74] using the same pressure, inlet temperature, composition and chemistry as the different cases considered. This flame (the initial velocity field) is interpolated onto the three-dimensional domain as a flat flame and is allowed to evolve till it becomes statistically steady. The integral length scales of the turbulence are maintained as the same order of magnitude as the flame thickness and allows to inspect the effect on intense turbulence on the flame and its structure.

3.1.4 Grid resolution

The grid resolution is driven by two length scales: resolution of the flame thickness and the Kolmogorov scales. The flame is typically resolved using ~25-30 grid points[62] which is sufficient to resolve the flame structure (i.e. chemical and thermal profiles). The Kolmogorov scale is estimated as $\eta = (\nu^3/\varepsilon)^{1/4}$ where ν is the viscosity and ε is the dissipation of the turbulent kinetic energy as is given by $\varepsilon = u'^3/l$ where u' is the turbulence intensity and l is the integral length scale. The resolution is chosen based on an effective Kolmogorov length scale calculated from the simulation as detailed in Aspden et al.[86].

Adaptive mesh refinement(AMR) is employed for increased resolution around the flame leaving a courser domain elsewhere. The simulations are run on a coarser mesh without refinement till steady state followed by refinement of the mesh to collect data. Details of the procedure can be found in Aspden et al.[62].

3.1.5 Post-processing

A reference isosurface is needed to associate the local curvature, stretch values and the flame normal. The reference isosurface can be defined using any progress variable that monotonically increases through the flame from reactants to products and the "flame" is identified with a particular value for the chosen variable. In the analysis considered here, temperature is chosen as the progress variable with a given value for temperature identifying the "flame" iso-surface.

Spatial integration of reaction rates and species consumption rates are defined over volumes whose lateral surfaces are normal to this reference surface. The normal is defined by the temperature gradient i.e. $\vec{n} = \nabla T$. This defines a local coordinate parallel to integral curves of the local temperature gradient, as shown in Figure 3.2.

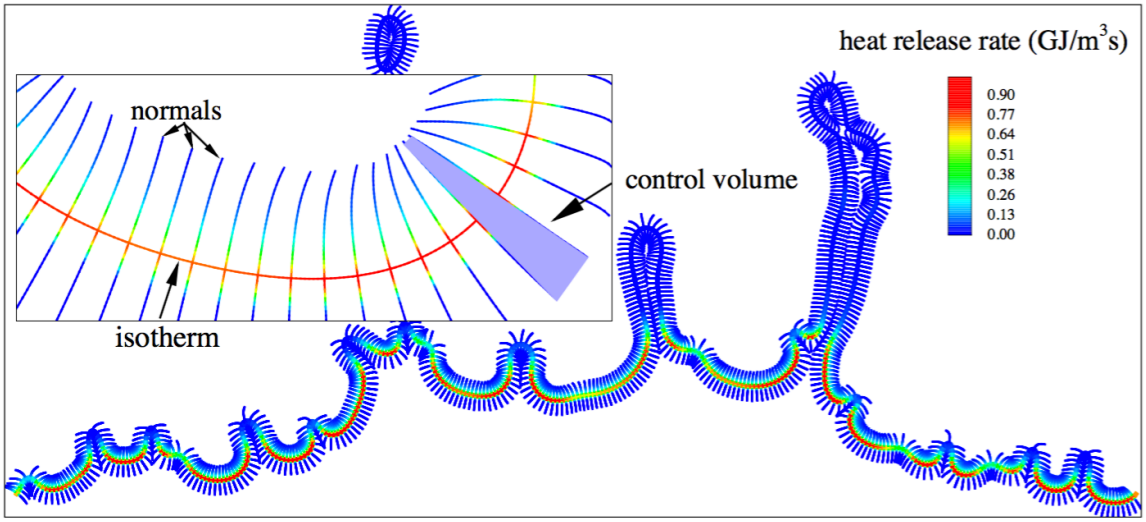

Figure 3.2. Illustration of an isotherm with normals for a two-dimensional hydrogen/air lean premixed flame. Adapted from Gao et al. [87]

Tessellation of the iso-surface is performed to extract a triangulated surface using a marching cubes algorithm[37] and decimation of this surface is performed using QSlim[88] which ensures no poorly formed triangles are extracted. The data is then mapped onto these integral curves as shown in the inset of Figure 3.3 along with the tessellated surface.

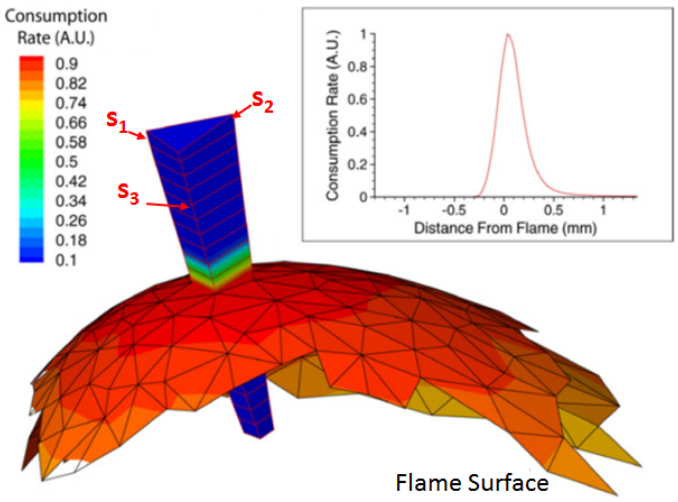

Figure 3.3. Prism shaped volume, Ω, constructed using curves s_j locally normal to the temperature isotherms; the inset plot shows a typical variation of $\dot{\omega}_{fuel}$ along s_j. Adapted from Day et al.[37]

Finally, quantities such as fuel consumption, reactions rates, heat release can be integrated within these volumes leading to a "point" representation at every point on the iso-surface given by:

$$\overline{RR_k}(\vec{x}, t) = \frac{\int RR_k(\vec{x}, t)\, d\Omega}{A_{ref}} \tag{3.6}$$

where, RR_k is the reaction rate of the kth reaction and is a function of space and time and A_{ref} is the intersection area of the reference iso-surface with the volume, Ω.

3.1.6 Data sets

Multiple data sets spanning different fuels generated using the above code are analyzed to understand turbulence-chemistry interactions. For each fuel, multiple turbulence intensities are computed. The increasing turbulence intensities are characterized by a flame Karlovitz number which is a ratio of chemical time scales and a flow time scale. For turbulent flames, this definition reduces to:

$$Ka_F{}^2 = \left(\frac{u'}{S_{L_o}}\right)^3 \left(\frac{l}{l_o}\right) \tag{3.7}$$

where S_{L_o} is the unstretched laminar flame speed and l_o is the thermal flame thickness for the unstretched laminar flame. The Borghi diagram below shows the different cases considered for hydrogen, methane and n-dodecane. For the simulations, the ratio of length scales is maintained as a constant. u' controls the turbulence intensities with higher values corresponding to higher turbulence intensities.

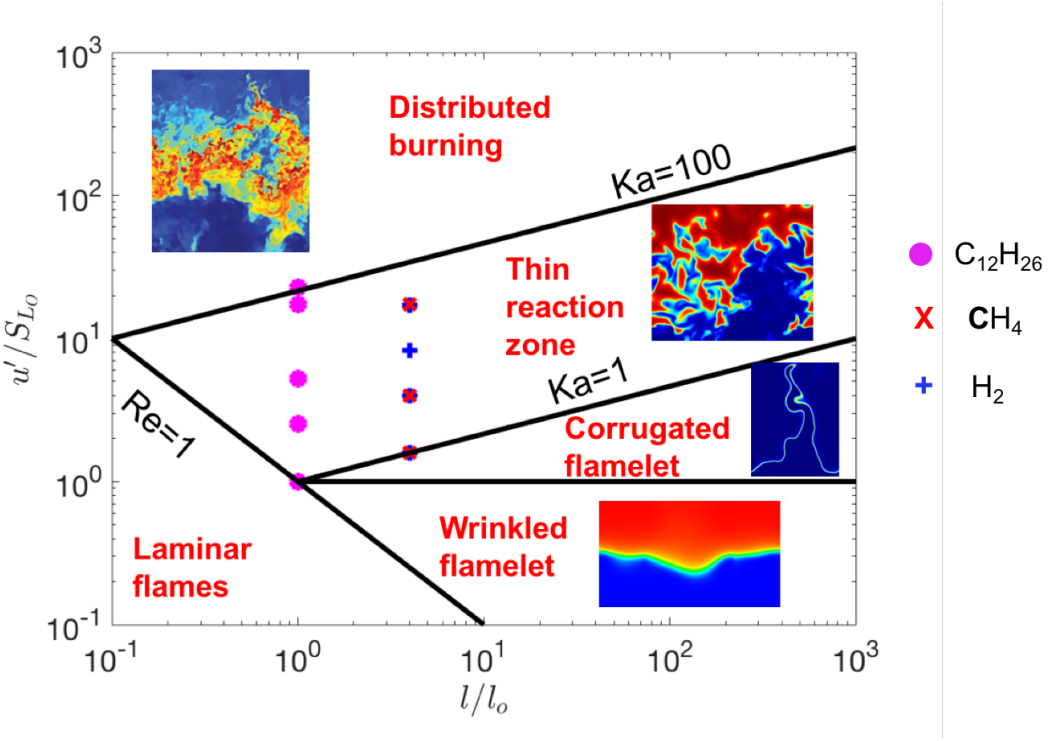

Figure 3.4. Borghi diagram summary of datasets.

3.1.6.1 Hydrogen

The key inlet conditions for the hydrogen/air datasets are summarized in Table 3.1. For hydrogen flames, the unstretched laminar flame speed is represented by a freely-propagating flame speed since thermo-diffusive instability leads to a faster speed of propagation[12].

Table 3.1. Inlet conditions for hydrogen/air flames. Adapted from Aspden et al.[12]

Equivalence ratio, ϕ	0.4
Inlet temperature, T^u	298K
Pressure, p	1 atm
Freely propagating flame speed, S_F	47 cm/s
Laminar Flame thickness, l_O	410μm

The reaction kinetics, thermodynamic properties and transport coefficients are calculated using Li et al. [17] chemical model with 9 species and 21 reactions. Table 3.2 below summarizes the different turbulent flame cases considered.

Table 3.2. Summary of cases for H_2/Air flames

Case	$u'(m/s)$	u'/S_F	l/l_0	Ka_F
A	0.75	1.6	4	1
B	1.9	4.0	4	4
C	3.9	8.3	4	12
D	8.2	17.0	4	36

3.1.6.2 Methane

The key inlet conditions for the hydrogen/air datasets are summarized in Table 3.3.

Table 3.3. Inlet conditions for methane/air flames. Adapted from Aspden et al.[67]

Equivalence ratio, ϕ	0.7
Inlet temperature, T^u	298K
Pressure, p	1 atm
Unstretched laminar flame speed, S_{L_O}	18.9 cm/s
Laminar Flame thickness, l_O	$600\mu m$

The reaction kinetics, thermodynamic properties and transport coefficients are calculated using GRIMech 3.0 [18] (with nitrogen chemistry removed) chemical model with 35 species and 217 reactions.

Table 3.4 below summarizes the different turbulent flame cases considered.

Table 3.4. Summary of cases for CH_4/Air flames

Case	$u'(m/s)$	u'/S_{L_O}	l/l_0	Ka_F
A	0.299	1.59	4	1
B	0.754	4.0	4	4
D	2.27	17.3	4	36

3.1.6.3 n-dodecane

The key inlet conditions for the hydrogen/air datasets are summarized in Table 3.5.

Table 3.5. Inlet conditions for n-dodecane/air flames. Adapted from Aspden et al.[68]

Equivalence ratio, ϕ	0.7
Inlet temperature, T^u	298K
Pressure, p	1 atm
Unstretched laminar flame speed, S_{L_O}	22.6 cm/s
Laminar Flame thickness, l_O	$520\mu m$

The reaction kinetics, thermodynamic properties and transport coefficients are calculated using You et al. [89] chemical model with 56 species and 289 reactions. This is a reduced mechanism for n-dodecane. A sensitivity study was performed to compare this mechanism with other larger mechanisms (Luo et al.[90], Narayanswamy et al.[91]) for laminar models which is presented in Appendix A. Even though there were quantitative variations in the pathways for different metrics, the qualitative behavior of the reactions remained consistent across all mechanisms.

Table 3.6 below summarizes the different turbulent flame cases considered.

Table 3.6. Summary of cases for n-$C_{12}H_{26}$/Air flames

Case	$u'(m/s)$	u'/S_{L_O}	l/l_0	Ka_F
A	0.226	1.0	1	1
B	0.570	2.52	1	4
C	1.18	5.25	1	12
D	2.47	17.3	1	36
E	5.12	22.7	1	108

3.2 Unstretched laminar flames

The unstretched laminar flame calculations are performed using the PREMIX module in CHEMKIN[74].

3.2.1 Problem initialization

Table 3.7 summarizes the key parameters set for the calculations to ensure proper resolution of the solution.

Table 3.7. Summary of key parameters for unstretched laminar flame calculations

Parameter	Value
Solution curvature, CURV	0.001
Solution gradient, GRAD	0.001
Inlet radial velocity	0

This leads to a typical number of 8000-12000 grid points for the convergence of unstretched laminar flame speed value. In all the cases, the inlet temperature, pressure and composition is similar to the inlet conditions considered for the direct numerical simulations discussed in Section Data sets. Convergence tests for the three fuels are detailed in Appendix C.

3.3 Stretched flame calculations

The stretched flame calculations are performed using OPPDIF[75] module in CHEMKIN.

3.3.1 Domain description

The opposed flow configuration is sketched in Figure 3.5. Two nozzles with the same inlet conditions are initialized leading to a twin flame configuration with the stagnation plane at the center plane. The distance between the two nozzles is 2 cm with the center plane at 1 cm.

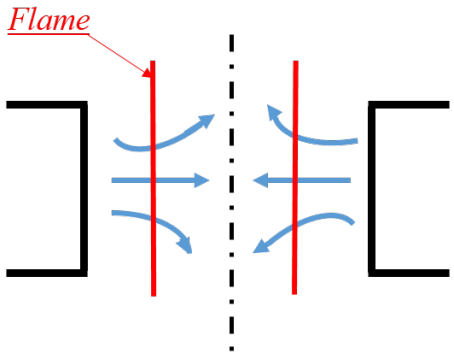

Figure 3.5. Opposed flow configuration for twin flames

3.3.2 Problem initialization

Table 3.8 summarizes the key parameters used for the stretched flame calculations.

Table 3.8. Summary of key parameters for stretched flame calculations.

Parameter	Value
Solution curvature, CURV	0.01
Solution gradient, GRAD	0.01
Inlet radial velocity	0

Typically, the simulations are initialized with an inlet axial velocity slightly higher than the corresponding unstretched laminar flame speed. 10 continuations are performed between the inlet axial velocity and the final targeted axial velocity. Continuations refine the solution progressively leading to an eventual resolution of 6000-10000 grid points for every case considered. The stretch rate, κ, is given by the maximum value of $-du/dx$ between the inlet and the first minima in the axial velocity profile where u is the axial velocity. A typical velocity profile with the velocity gradient is plotted in Figure 3.6.

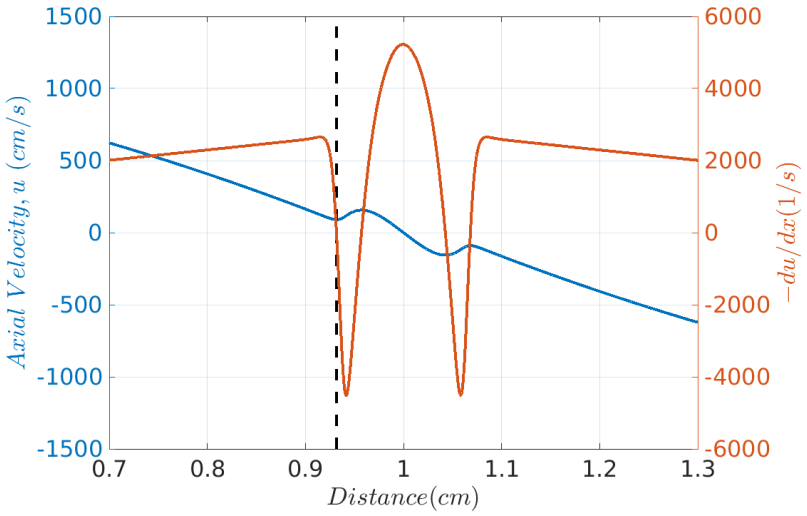

Figure 3.6. Variation of axial velocity(blue) and - du/dx(orange) with distance.

Extinction calculations are run to calculate the maximum stretch rate and the corresponding inlet axial velocity that the premixed flame sees before extinction. Table 3.9 tabulates the inlet velocities and extinction stretch rates for three fuels considered. Appendix D details the inlet conditions and the corresponding stretch rates chosen for the different fuels.

Table 3.9. Results for stretched flame calculations

	H_2/Air	CH_4/Air	n-$C_{12}H_{26}$/Air
Inlet conditions	ϕ=0.4, 298K, 1atm	ϕ=0.7, 298K, 1atm	ϕ=0.7, 298K, 1atm
Inlet velocities	284 - 4730 cm/s	30 – 605 cm/s	25 – 121 cm/s
Extinction stretch rate, κ_{ext}	10170 1/s	1213 1/s	244 1/s

3.4 Perfectly stirred reactors

The perfectly stirred reactor calculations are performed using the PSR[76] module in CHEMKIN.

3.4.1 Problem Initialization

The reactors initial temperature is set at 1000K. The inlet conditions for the reactors and the computed residence time are tabulated in Table 3.10.

Table 3.10. Results for perfectly stirred reactors

	H_2/Air	CH_4/Air	n-$C_{12}H_{26}$/Air
Inlet conditions	ϕ=0.4, 298K, 1atm	ϕ=0.7, 298K, 1atm	ϕ=0.7, 298K, 1atm
Extinction residence time, τ_{ext}	0.08ms	0.17ms	0.17ms

CHAPTER 4. CHEMICAL PATHWAYS - A GLOBAL ANALYSIS

Different metrics can be used to assess the degree to which chemical pathways are altered in turbulent flames. These include (1) fraction of heat release rate associated with a given reaction, (2) fraction of species production/consumption associated with a given reaction, (3) mole fraction of species/radicals at a given progress variable. These metrics can also be calculated at a fixed point in space and time, spatially integrated, or conditioned on progress variables or topological features (e.g., positive or negative curvature).

4.1 Equations for analysis

As discussed in Section 3.1.5, the reaction rates can be integrated within the prismatic volumes using the equation:

$$\overline{RR_k}(\vec{\mathrm{x}},\mathrm{t}) = \frac{\int RR_k(\vec{x},t)\, d\Omega}{A_{ref}} \tag{4.1}$$

This quantity can be used to calculate area averaged means over the entire flame surface or conditioned on local features.

4.1.1 Global analysis equations(DNS)

The area averaged mean is calculated as:

$$\overline{RR_k} = \frac{\sum_{j=1}^{j=N} RR_k(\vec{x},t)|_j A_{ref,j}}{\sum_{j=1}^{j=N} A_{ref,j}} \tag{4.2}$$

Where N is the number of points on the surface. An area-weighted mean ensures that high values of the quantities occurring over smaller areas on the surface does not lead to higher values of the averaged values which can skew the mean.

The heat release contribution of the individual reactions, $\overline{\dot{q}_k}$ is then calculated as:

$$\overline{\dot{q}_k} = \overline{RR_k}\left(\Delta h_f^o\big|_{reac} - \Delta h_f^o\big|_{prod}\right) \tag{4.2}$$

Where, $\Delta h_f^o\big|_{reac}$ is the formation enthalpy of reactants and $\Delta h_f^o\big|_{prod}$ of the products of the given reaction. Similarly, the rate of formation/consumption of species, *i* in reaction *k*, a is defined as:

$$\overline{\dot{\omega}_{\iota,k}} = \overline{RR_k}\left(\nu''_{i,k} - \nu'_{i,k}\right) \tag{4.3}$$

where a generalized reaction is written as $\nu'_{i,k}M_i \rightarrow \nu''_{i,k}M_i$. The reaction rate, $\overline{RR_k}$ can be <0 or >0. If $\overline{RR_k} < 0$, then the reverse reaction from the mechanism is used for the analysis.

The net heat release is:

$$\bar{\dot{q}} = \sum_k \overline{\dot{q}_k} \tag{4.4}$$

The net production of species, *i* is given as:

$$\overline{\dot{\omega}_{\iota,p}} = \sum_k \overline{\dot{\omega}_{\iota,k}} \tag{4.5}$$

Here if the reaction k, forms species, i then $\overline{\dot{\omega}_{\iota,k}} > 0$ else $\overline{\dot{\omega}_{\iota,k}} = 0$. Similarly, the net consumption is given as:

$$\overline{\dot{\omega}_{\iota,c}} = \sum_{k} \overline{\dot{\omega}_{\iota,c}} \tag{4.6}$$

Here if the reaction, k consumes species, i then $\overline{\dot{\omega}_{\iota,k}} < 0$ else $\overline{\dot{\omega}_{\iota,k}} = 0$. The subscript *p* and *c* denote production and consumption respectively. The values obtained in Equation 4.4-4.6 are used for normalizing the values obtained in Equation 4.2 and 4.3.

4.1.2 Progress-variable conditioned equations(DNS)

The mean fuel consumption, $\overline{\dot{\omega}}_{fuel}$ can be calculated as shown in Equation 4.7 by integrating $\dot{\omega_{fuel}}$ over the volume Ω. The direction of propagation, Z is divided into 200 points between the lowest (Z_{min}) and the highest point (Z_{max}). The cumulative fuel consumption is then calculated along this direction and normalized by the total fuel consumption in the volume. A typical profile for the fuel consumption is shown Figure 4.1.

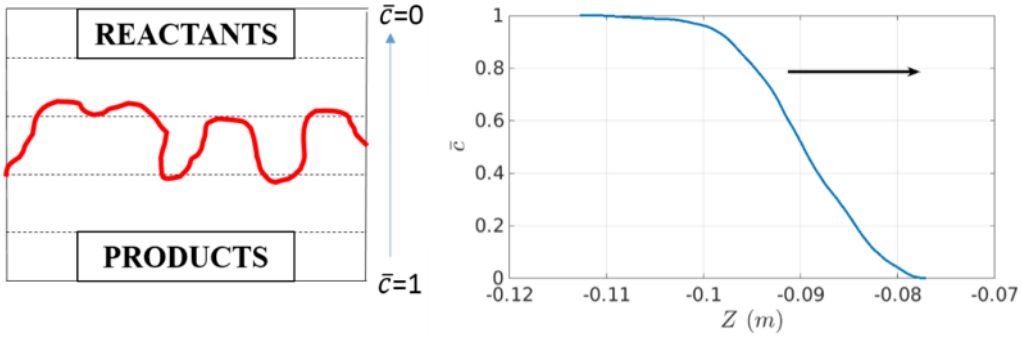

Figure 4.1. (left) Illustration of progress variable, $\bar{c}$. (right) Mapping of physical space to progress variable. The arrows denote the direction of propagation.

Progress variable, $\overline{c_i}$, at a location, Z_i, is defined as:

$$\overline{c_i} = \frac{\sum_{Z_i<Z<Z_{max}} \overline{\dot{\omega}}_{fuel}}{\sum \overline{\dot{\omega}}_{fuel}} \tag{4.7}$$

The location, $\bar{c} = 0$, corresponds to unburnt reactants.

The heat release contribution of the individual reactions, $\overline{\dot{q}_k}$ at a certain progress variable $\bar{c}_i$, at every point on the reference surface is defined as:

$$\overline{\dot{q}_k(x,y)}\big|_{\bar{c}_i} = \overline{RR_k(x,y)}\big|_{\bar{c}_i}\left(\Delta h_f^o\big|_{reac} - \Delta h_f^o\big|_{prod}\right) \tag{4.8}$$

Similarly, the rate of formation/consumption of species, i in reaction k, at a certain progress variable $\bar{c}_i$, at every point on the reference surface is defined as:

$$\overline{\dot{\omega}_{i,k}(x,y)}\big|_{\bar{c}_i} = \overline{RR_k}(x,y)|_{\bar{c}_i}\left(\nu''_{i,k} - \nu'_{i,k}\right) \tag{4.9}$$

where a generalized reaction is written as $\nu'_{i,k}M_i \rightarrow \nu''_{i,k}M_i$. The reaction rate, $\overline{RR_k}(x,y)$ can be <0 or >0. If $\overline{RR_k}(x,y) < 0$, then the reverse reaction from the mechanism is used for the analysis.

The area-weighted average heat release at a certain progress variable $\bar{c}_i$ can then be computed as:

$$\overline{\dot{q}_k}|_{\bar{c}_i} = \frac{\sum_{j=1}^{j=N} \overline{\dot{q}_k}(x,y)|_{\bar{c}_i} A_{ref,j}}{\sum_{j=1}^{j=N} A_{ref,j}} \tag{4.10}$$

and, the area weighted $\overline{\dot{\omega}_{\iota,k}}\big|_{\bar{c}_i}$ as:

$$\overline{\dot{\omega}_{\iota,k}}\big|_{\bar{c}_i} = \frac{\sum_{j=1}^{j=N} \overline{\dot{\omega}_{\iota,k}}(x,y)\big|_{\bar{c}_i} A_{ref,j}}{\sum_{j=1}^{j=N} A_{ref,j}} \tag{4.11}$$

where N is the number of points on the reference isosurface that fall within the progress variable bracket considered. $\overline{\dot{\omega}_{\iota,k}}\big|_{\bar{c}_i} > 0$ implies that species, i is produced by reaction, k.

The net heat release at $\bar{c}_i$ is:

$$\bar{\dot{q}}|_{\bar{c}_i} = \sum_k \overline{\dot{q}_k}|_{\bar{c}_i} \tag{4.12}$$

The net production of species, i at $\bar{c}_i$ is given as:

$$\overline{\dot{\omega}_{\iota,p}}\big|_{\bar{c}_i} = \sum_k \overline{\dot{\omega}_{\iota,k}}\big|_{\bar{c}_i} \tag{4.13}$$

Again if the reaction k, forms species, i then $\overline{\dot{\omega}_{\iota,k}} > 0$ else $\overline{\dot{\omega}_{\iota,k}} = 0$. Similarly, the net consumption is given as:

$$\overline{\dot{\omega}_{\iota,c}}\big|_{\bar{c}_i} = \sum_k \overline{\dot{\omega}_{\iota,k}}\big|_{\bar{c}_i} \tag{4.14}$$

Here if the reaction, k consumes species, i then $\overline{\dot{\omega}_{\iota,k}} < 0$ else $\overline{\dot{\omega}_{\iota,k}} = 0$. The subscript p and c denote production and consumption respectively. The values obtained in Equations 4.12-4.14 are used for normalizing the values obtained in Equations 4.10 and 4.11.

4.1.3 Curvature conditioned equations(DNS)

Different topological elements can be defined based on the principal curvatures of the iso-surface i.e. $\mathbb{k}_1$ and $\mathbb{k}_2$ ($\mathbb{k}_2 < \mathbb{k}_1$) as discussed earlier and are shown in Figure 4.2.

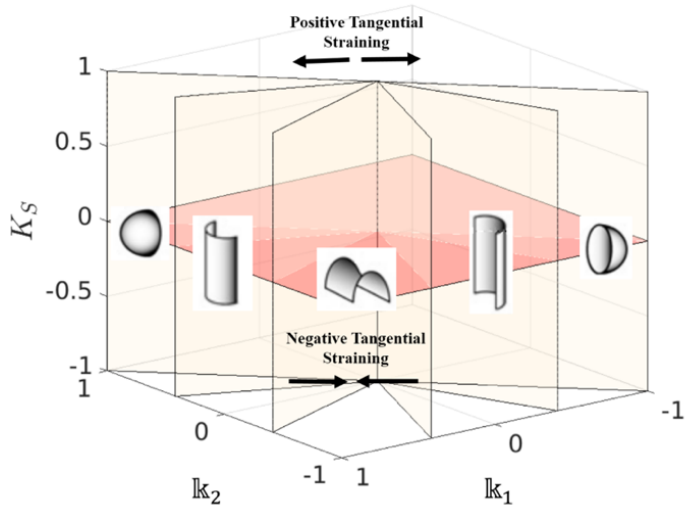

Figure 4.2. Illustration of potential iso-surface curvature and stretch combinations.

The principal curvatures are calculated from the mean curvature $\mathbb{K}_C$ and the Gaussian curvature, G as:

$$\mathbb{k}_1, \mathbb{k}_2 = \mathbb{K}_C \pm \sqrt{\mathbb{K}_C{}^2 + G} \tag{4.15}$$

$\mathbb{k}_2\mathbb{k}_1 > 0$, forms spherical elements, $\mathbb{k}_2\mathbb{k}_1 = 0$ forms cylindrical elements and $\mathbb{k}_2\mathbb{k}_1 < 0$ forms saddle point elements. Additionally, the spherical elements can be positively curved or negatively curved. Positively curved elements have center of curvature in products whereas the negatively curved elements have center of curvature in reactants.

The heat release contribution of the individual reactions, $\overline{\dot{q}_k}|_{\bar{e}_i}$ and consumption/formation rate, $\overline{\dot{\omega}_{\iota,k}}\big|_{\bar{e}_i}$ within a given element $\bar{e}_i$, at on the reference surface are calculated similar to Equations 4.10-4.11. The net heat release $\bar{\dot{q}}|_{\bar{e}_i}$, the net production of species, *i*, $\overline{\dot{\omega}_{\iota,p}}\big|_{e_i}$, the net consumption of species, *i*, $\overline{\dot{\omega}_{\iota,p}}\big|_{e_i}$ at $\bar{e}_i$ are calculated similar to Equations 4.12-4.14.

4.1.4 Stretched flames equations

Net heat release and reaction rates are computed from OPPDIF results by integrating the heat release and reaction rate profiles in the axial direction:

$$\bar{\dot{q}}_k = \sum_{j=1}^{j=N} \dot{q_{k,J}} dx_j \ , \quad \bar{\dot{q}} = \sum_k \overline{\dot{q}_k} \tag{4.16}$$

$$\overline{\dot{R}R_k} = \sum_{j=1}^{j=N} R\dot{R}_{k_J} dx_j \tag{4.17}$$

$\overline{\dot{\omega}_{\iota,k}}$ can be calculated from $\overline{\dot{R}R_k}$ as outlined in Equation 4.3. $\overline{\dot{\omega}_{\iota,p}}$ and $\overline{\dot{\omega}_{\iota,c}}$ are computed similar to Equation 4.5 and 4.6 respectively.

4.2 Hydrogen

This section discussed the global and conditioned results for the hydrogen/air premixed flames.

4.2.1 "Flame" surface visualization

The flame surface is defined using a temperature iso-value. This iso-value is chosen from unstretched laminar calculations. Figure 4.3 below plots the heat release rate and fuel consumption as a function of temperature for premixed H_2/Air flames with the same inlet conditions as the DNS data set.

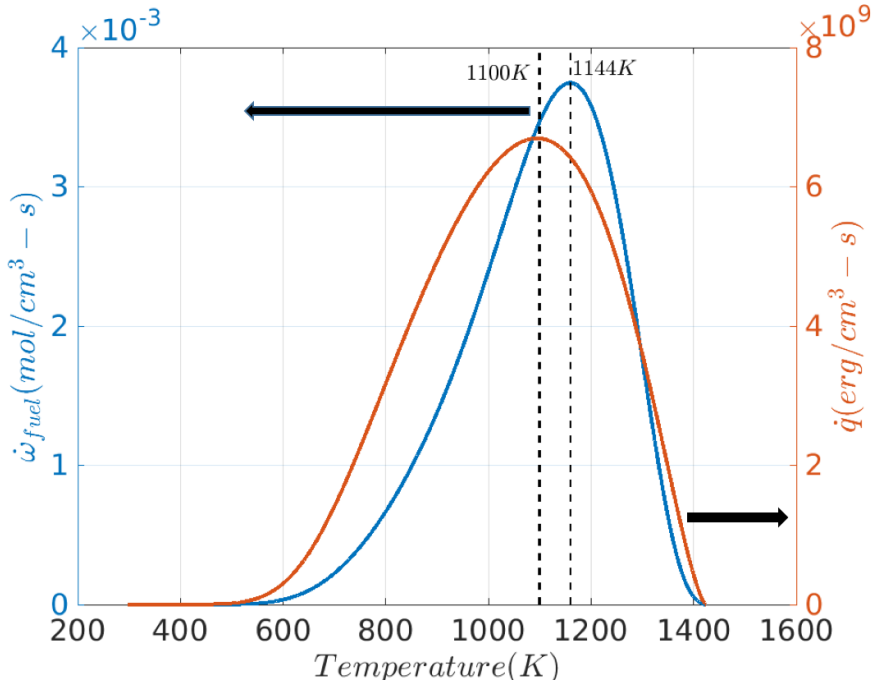

Figure 4.3. Variation of fuel consumption and heat release rate as a function of temperature for H_2/Air flames with ϕ=0.4, T^u=298K, p=1atm.

The peak heat release and fuel consumption occur at 1100K and 1144K respectively. These values are close to each other and the isotherm corresponding to the peak fuel consumption is chosen. A higher temperature iso-surface is, in general, continuous with holes or pockets since the turbulent cases lie within the thin reaction zone regime. This is an important feature for the surface to obtain well-defined normals calculated from temperature gradients and its divergence.

4.2.2 Data Visualization

Slices of temperature and some key reactions for hydrogen/air flames are shown in Figure 4.4. The formation of the cellular flame due to thermo-diffusive instability can be observed at the leading edge of the flame for *Ka*=1. With increasing Karlovitz number, the appearance of finer structures on the flame front can be seen and it is hard to clearly observe the cellular burning. For all the flames, the leading edge of the flame burns strongly compared to the rest of the flame which can be observed from the elevated temperatures. Temperatures higher than adiabatic temperatures (T_{ad}~1426K) can be seen at the leading edge. This is a common observation for these thermo-diffusively unstable flames. The reaction front remains thin across all turbulence intensities. This can be observed from the reaction rate slices for two important reactions. With increasing turbulence, the reaction rates are elevated at the leading edge of the flame as well.

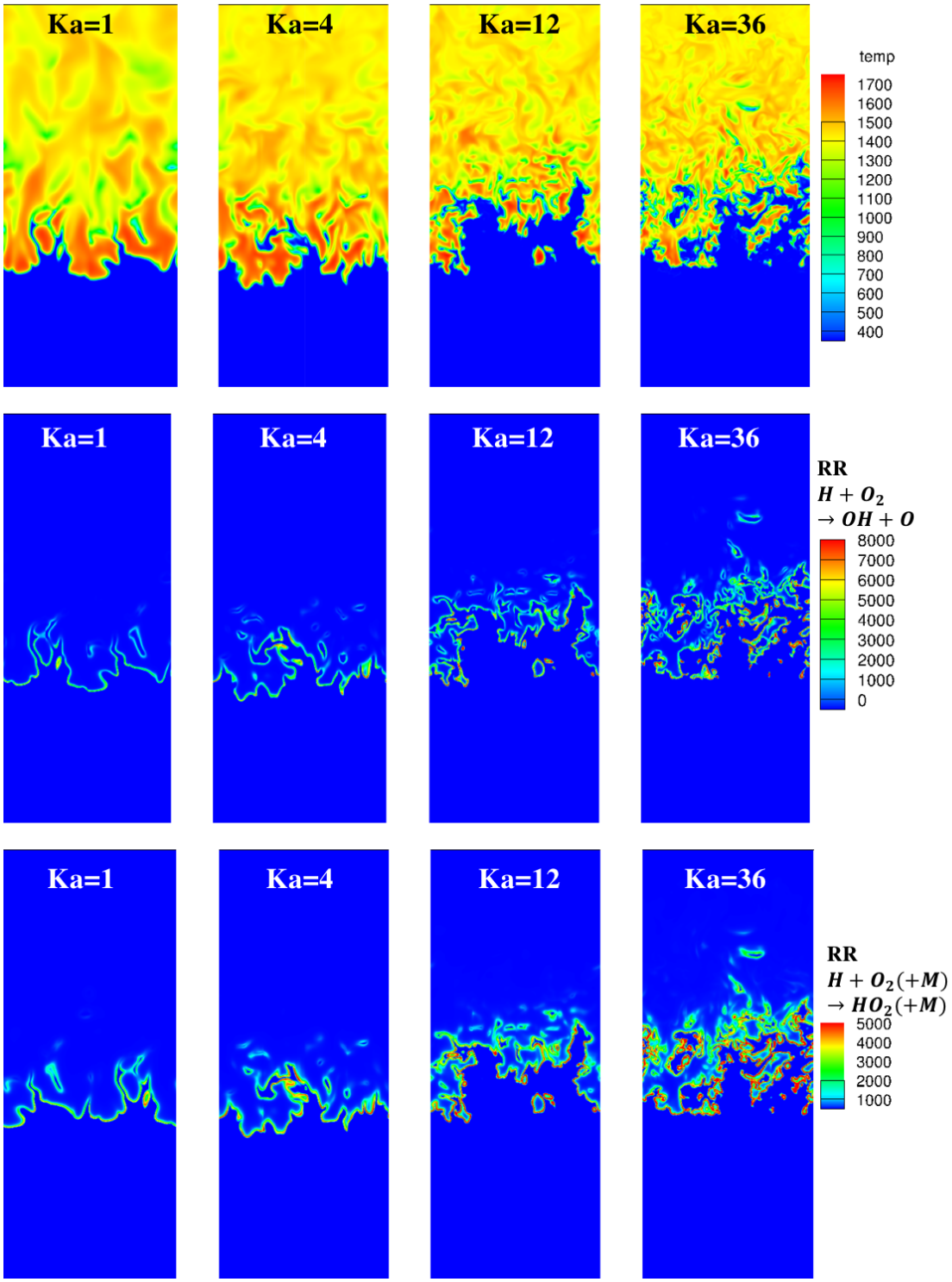

Figure 4.4. Slices of temperature(top), $H+O_2 \rightarrow OH+O$ reaction rate (center) and $H+O_2(+M) \rightarrow HO_2(+M)$ reaction rate(bottom). The slices are constructed using the x=0 and y=0 plane using the fact of periodic lateral boundary conditions.

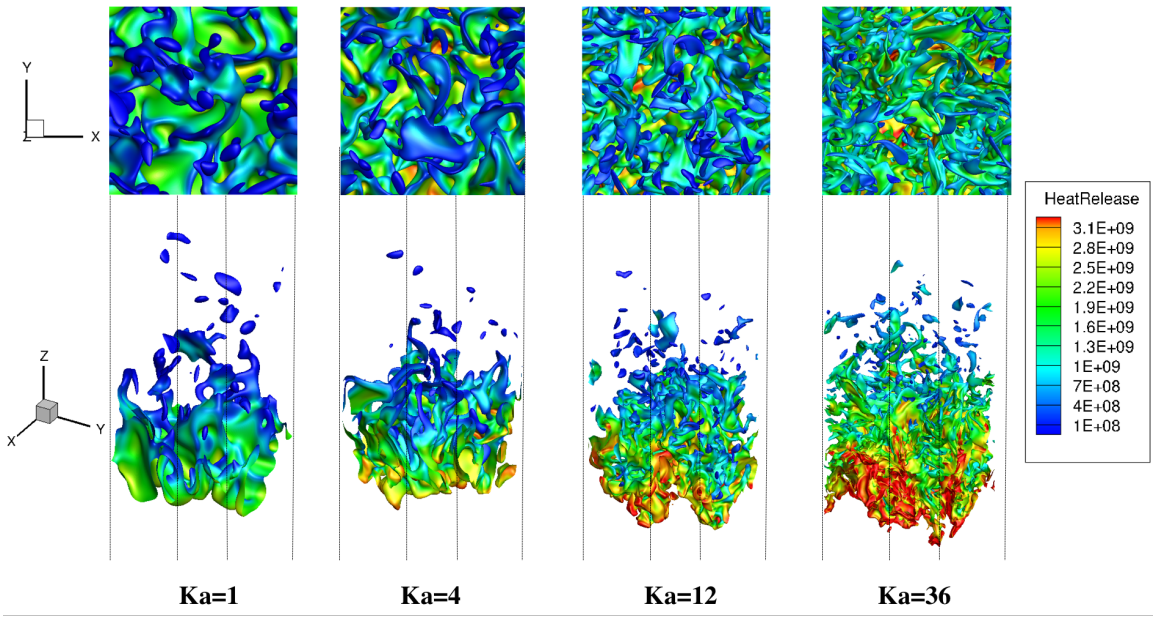

Figure 4.5. Isotherm, T_{ref} = 1144 K(colored by heat release). (Top) X-Y slices of the flame surface (bottom) 3D view of the flame surface. The rectangular domain is shown in black lines.

As discussed in the previous section, the flame is defined by the 1144K isotherm. Figure 4.5 shows the isotherm, T_{ref} = 1144 K (colored by local values of the heat release) for the cases considered. Significant wrinkling of the flame with increasing turbulence can be observed in the figure. Higher heat release at the leading edge of the flame compared to the rest of the flame can be observed. Also increased heat release with increasing turbulence at this leading edge can be seen. These flames, even though highly wrinkled, have a flamelet like structure. This can be seen in Figure 4.6 wherein the fuel consumption and heat release are plotted as a function of a progress variable (defined based on temperature).

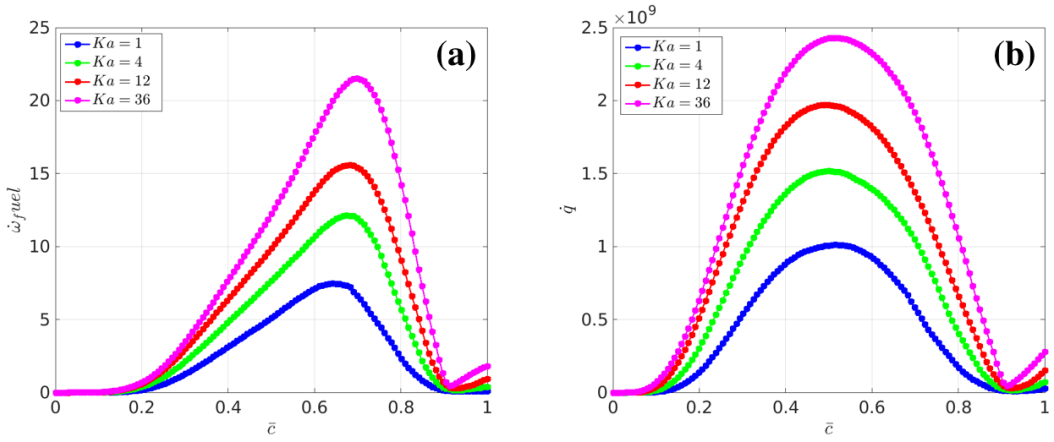

Figure 4.6. Variation of (a) fuel consumption and (b) heat release along a progress variable through the flame for different turbulence intensities for hydrogen flames.

4.2.3 Global analysis

First the fractional heat release pathways are considered for the laminar and turbulent flames. Figure 4.7(a) plots the heat release (normalized by the total heat release for each case) associated with the given reactions as a function of normalized stretch rate, κ/κ_{ext} and normalized residence time, τ_{ext}/τ_{res}, for the laminar flame reference cases. Results are shown for the largest magnitude exothermic and endothermic reactions (the other reaction steps that are not shown contribute an additional ~10% of the total heat release). The figure shows that $H+O_2(+M) \rightarrow HO_2(+M)$ is the dominant heat release reaction and that its relative importance changes only modestly with stretch, there being about an 11% difference from its unstretched value and its value at κ/κ_{ext} =0.4. Note also the striking similarity of the PSR results with the stretched flamelet calculation.

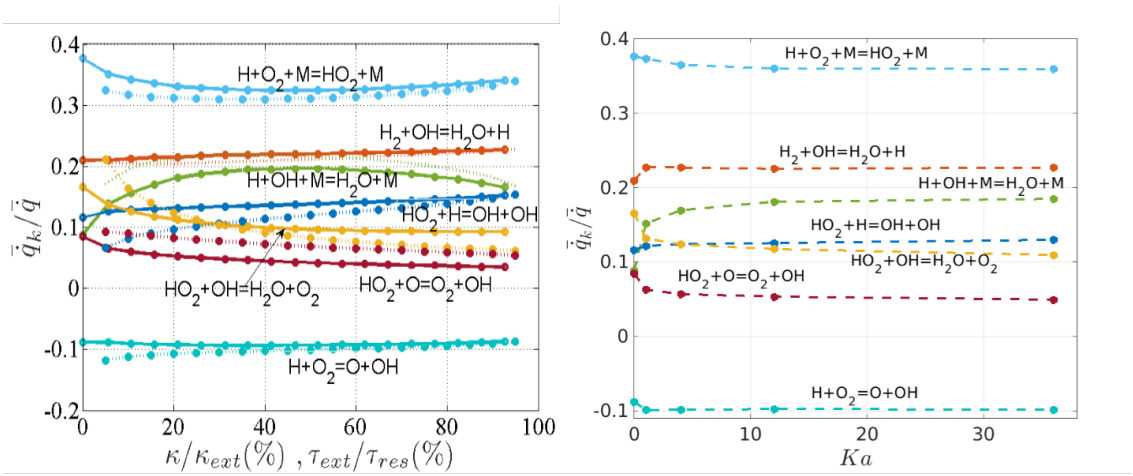

Figure 4.7. Dependence of fractional heat release associated with different reactions upon (a) stretch (OPPDIF, solid line) and residence time (PSR, dotted line) and (b) Karlovitz number (DNS)

Similarly, the next two most important reactions are H_2+OH→H_2O+H and H+OH+M→H_2O+M, showing maximum changes of 10 and 120% respectively. This latter reaction has the largest fractional change of relative heat release of all these reactions. In general, the PSR results are quite similar to the OPPDIF results for all the reactions, with a maximum deviation of ~20% for the range of residence times calculated.

Figure 4.7 (b) shows the same analysis for the turbulent flames (where *Ka*=0 denotes the laminar, unstretched value). Turning to the individual reactions and comparing reactions side by side with the laminar results, note the strong similarity in both the relative significance of the different reactions, as well as their quantitative contributions to the heat release. In particular, the two exothermic reactions, H+O_2(+M)→HO_2(+M) and H_2+OH→H_2O+H, are dominant in the laminar and turbulent case. There is some shift in relative significance of the HO_2+OH→H_2O+O_2, HO_2+O→O_2+OH and

$H+OH+M \rightarrow H_2O+M$ reactions, mirroring the laminar results. The biggest change in relative roles with *Ka* are the $H+OH+M \rightarrow H_2O+M$ and $HO_2+H \rightarrow OH+OH$ reactions.

The relative roles of different reactions in producing reaction intermediates are considered, focusing on H, OH, and HO_2 production. The integrated reaction rates are obtained as shown in Equations 4.2 and 4.17 for DNS and OPPDIF respectively. The consumption/production of a radical/species can then be calculated using the stoichiometric coefficients of the reaction as shown in Equation 4.3. This consumption (or production) of a radical by a given reaction is normalized by the total consumption (or production) of this radical by all reactions as given by Equations 4.5 and 4.6 respectively. Figure 4.8 shows the consumption/production of these radicals from DNS and OPPDIF. The consumption of H (shown in Figure 4.8(a)) is dominated by the reaction $H+O_2+M \rightarrow HO_2+M$ and the trend resembles the heat release plot shown earlier of the same reaction. There is a change of ~16% from the unstretched value to $\kappa/\kappa_{ext}=0.4$ for the OPPDIF case and ~14% change from *Ka*=0 to *Ka*=36 for the DNS. The next two dominant consumers of the H radical are $H+O_2 \rightarrow O+OH$ and $HO_2+H \rightarrow OH+OH$. These are nearly insensitive to changes in stretch with maximum changes of 10% and 16%, respectively, over the entire range of stretch. The DNS shows even lower sensitivity of increasing turbulence with ~3% and ~5% changes in the consumption between *Ka*=1 and *Ka*=36. The reaction $H+OH+M \rightarrow H_2O+M$ shows the maximum change with stretch and Karlovitz number. The H consumption by this reaction almost doubles relative to its laminar unstretched value, similar to the heat release results for this reaction.

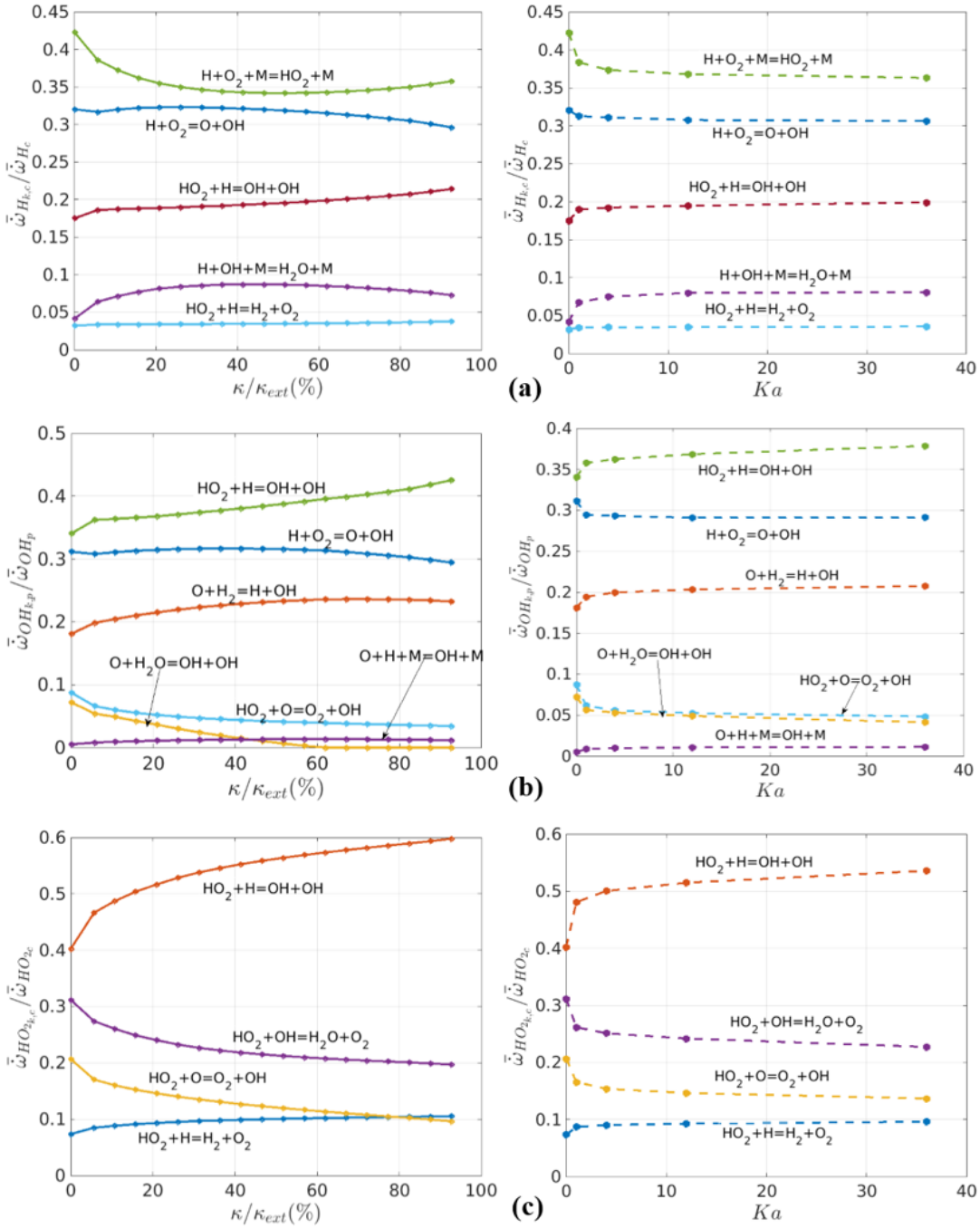

Figure 4.8. Dependence of normalized (a) H consumption (b) OH production (c) HO_2 consumption by different reactions upon κ (left) and *Ka* (right)

The reaction $HO_2+H \rightarrow OH+OH$ produces the maximum OH (shown in Figure 4.8(b)). The OH production rate increases with increasing κ and *Ka* demonstrating a change of ~20% and ~8% between the unstretched laminar value and $\kappa/\kappa_{ext}=0.97$ for the stretched flames and *Ka*=36 for the turbulent flames respectively. The production of OH by the reactions $H+O_2 \rightarrow O+OH$, $O+H_2 \rightarrow H+OH$, $HO_2+O \rightarrow O_2+OH$ and $O+H_2O \rightarrow OH+OH$ varies by 3%, 14%, 40% and 100% respectively for the entire range of stretch. The change is high for $O+H_2O \rightarrow OH+OH$ because this reaction reverses its direction for higher stretch values and thus, OH is consumed and not produced. However, these reactions show negligible changes from *Ka*=1 to *Ka*=36.

HO_2 consumption shows some significant changes with stretch and turbulence as demonstrated in Figure 4.8(c). The dominant consumer of HO_2 is $HO_2+H \rightarrow OH+OH$. The HO_2 consumption is augmented by 50% and 32% with increasing κ and *Ka* respectively. This consumption reduces by ~33% and ~50% for $HO_2+OH \rightarrow H_2O+O_2$ and $HO_2+O \rightarrow OH+O_2$ respectively from $\kappa/\kappa_{ext}=0$ and $\kappa/\kappa_{ext}=0.97$. The reduction is ~25% and ~40% respectively from *Ka*=0 to *Ka*=36. It can be observed that the consumption of HO_2 by $HO_2+H \rightarrow OH+OH$ increases. This chain branching reaction suppresses the chain termination reaction $HO_2+OH \rightarrow H_2O+O_2$ and chain propagation reaction $HO_2+O \rightarrow O_2+OH$.

From these results, it is clear that the strong turbulence has little effect on the integrated chemical pathways in these lean-hydrogen flames. While there are some quantitative shifts, these differences are quite modest, particularly for the dominant reactions.

4.2.4 Global analysis conditioned on curvature

This section shows how the role of different reactions vary with topological features. Figure 4.2 shows five different topological regions (concave/convex spherical elements, concave/convex cylindrical elements, and saddle points) conditioned on the two principal components of curvature, $\mathbb{k}_1$ and $\mathbb{k}_2$. The fraction of heat release associated with the dominant reactions, conditioned on these five regions is shown in Figure 4.9. Burning rates are enhanced for lean H_2-air flames, and so the dominant heat release occurs in the spherical positively stretched elements, followed by positively stretched cylindrical elements, saddle points, then negatively stretched cylindrical elements, with the least heat release coming from negatively stretched spherical elements. This general trend would be expected, but it is interesting how the differences in relative contributions diminish with increasing Karlovitz number. For example, the contribution of positively stretched spherical elements drops by ~11% for $H+OH+M \rightarrow H_2O+M$, ~20% for $H+O_2+M \rightarrow HO_2+M$ and $H_2+OH \rightarrow H_2O+H$ between Ka=0 and 36. The relative contributions of the negatively curved spherical elements increase by ~200% from Ka=1 to Ka=36 for $H+OH+M \rightarrow H_2O+M$, ~50% for $H+O_2+M \rightarrow HO_2+M$ and ~90% for $H_2+OH \rightarrow H_2O+H$. This is likely an unsteady effect, as the burning rate sensitivity to stretch decreases with increasing frequency of the stretch fluctuations.

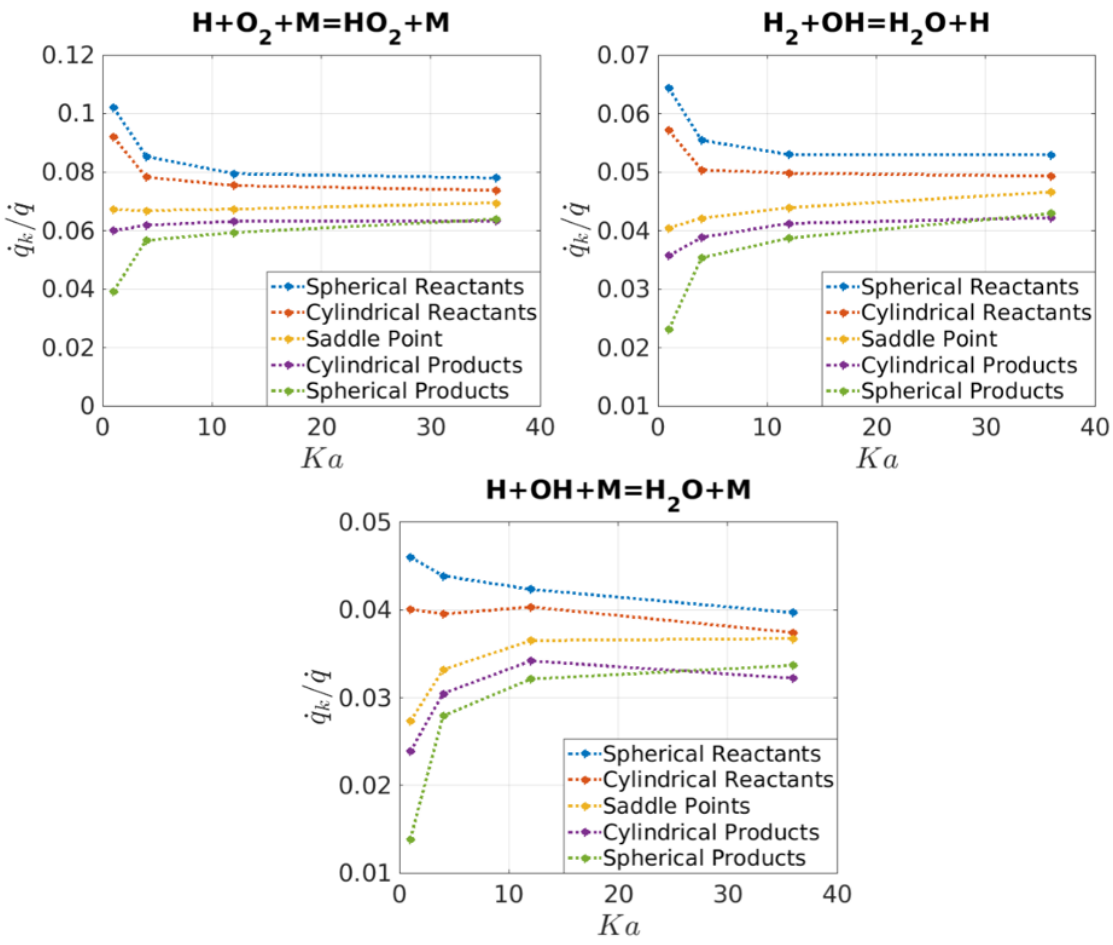

Figure 4.9. Dependence of the fractional heat release of a given reaction in each of the five topological elements upon *Ka*. The heat released by a given reaction within an element is normalized by the total heat released at the given *Ka*.

4.2.5 Global analysis conditioned on progress variable

This section considers similar metrics as the previous one, but focuses on spatial integrals between specific progress variables. Low progress variable values will necessarily be associated with more positively curved flame segments, due to their proximity to the leading edge of the front. As such, systematic differences in averaged stretch rates and curvature exist at different progress variables.

The relative contributions of different reactions to heat release are calculated by taking the area weighted average of the heat release given by Equation 4.10 normalized by the total heat release given by Equation 4.12. Progress variable conditioned heat release for some selected reactions are shown in Figure 4.10– the blue line shows the same spatially integrated value shown in Figure 4.7 , while the green, red and cyan lines show $0.095 \leq \bar{c} \leq 0.105$, $0.495 \leq \bar{c} \leq 0.505$ and $0.695 \leq \bar{c} \leq 0.705$ respectively.

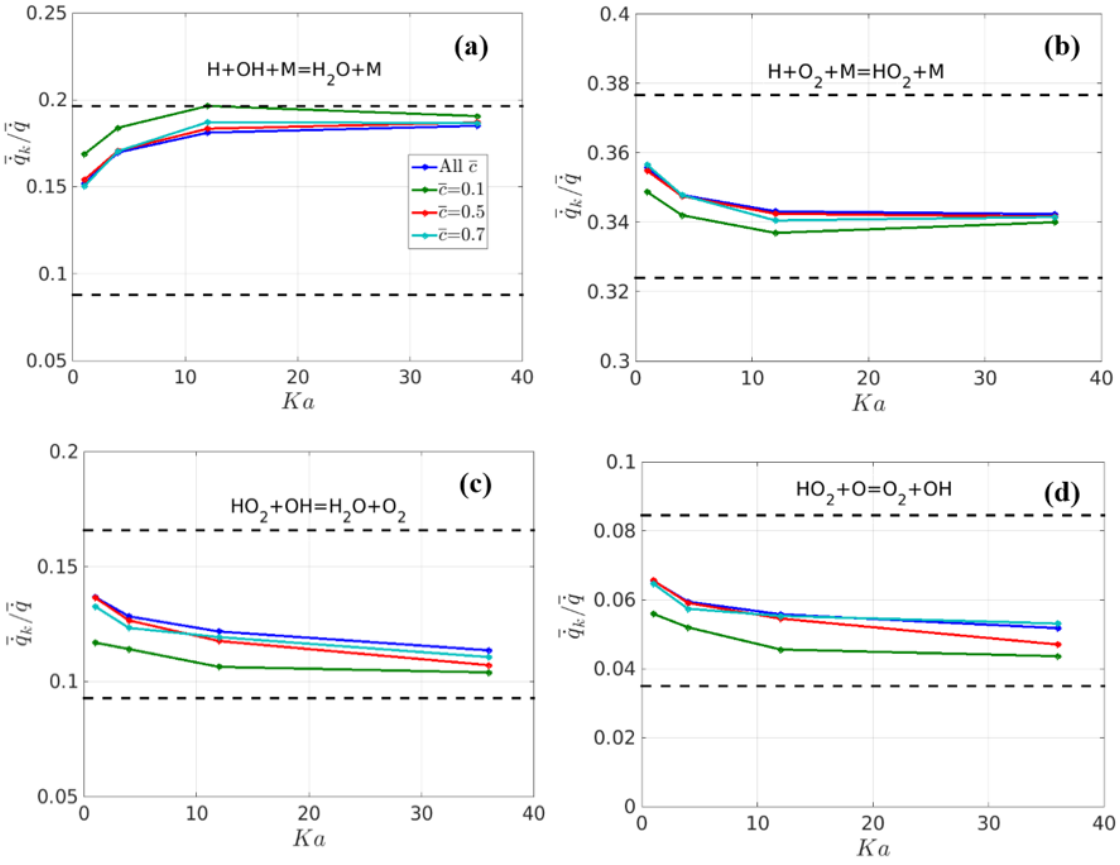

Figure 4.10. Progress variable conditioned heat release for (a) H+OH+M→H_2O+M (b) H+O_2+M→HO_2+M (c) HO_2+OH→H_2O+O_2 (d) HO_2+O→O_2+OH; (Blue: All $\bar{c}$, Green: $\bar{c}$ = 0.1, Red: $\bar{c}$ = 0.5, Cyan: $\bar{c}$ = 0.7). Dashed horizontal lines denote range of values from OPPDIF calculations.

Again, quantitative differences exist, but they are modest. Moreover, the results conditioned on $\bar{c}$ = 0.5 and 0.7 are quite close to the spatially averaged ones. The biggest differences occur at the leading edge of the brush, $\bar{c}$ =0.1. The dashed lines in the figures represent the OPPDIF bounds for these reactions, showing significantly larger ranges for the laminar, stretched flame calculations. Figure 4.11 and Figure 4.12 show corresponding plots for the H and OH radical, also showing little change.

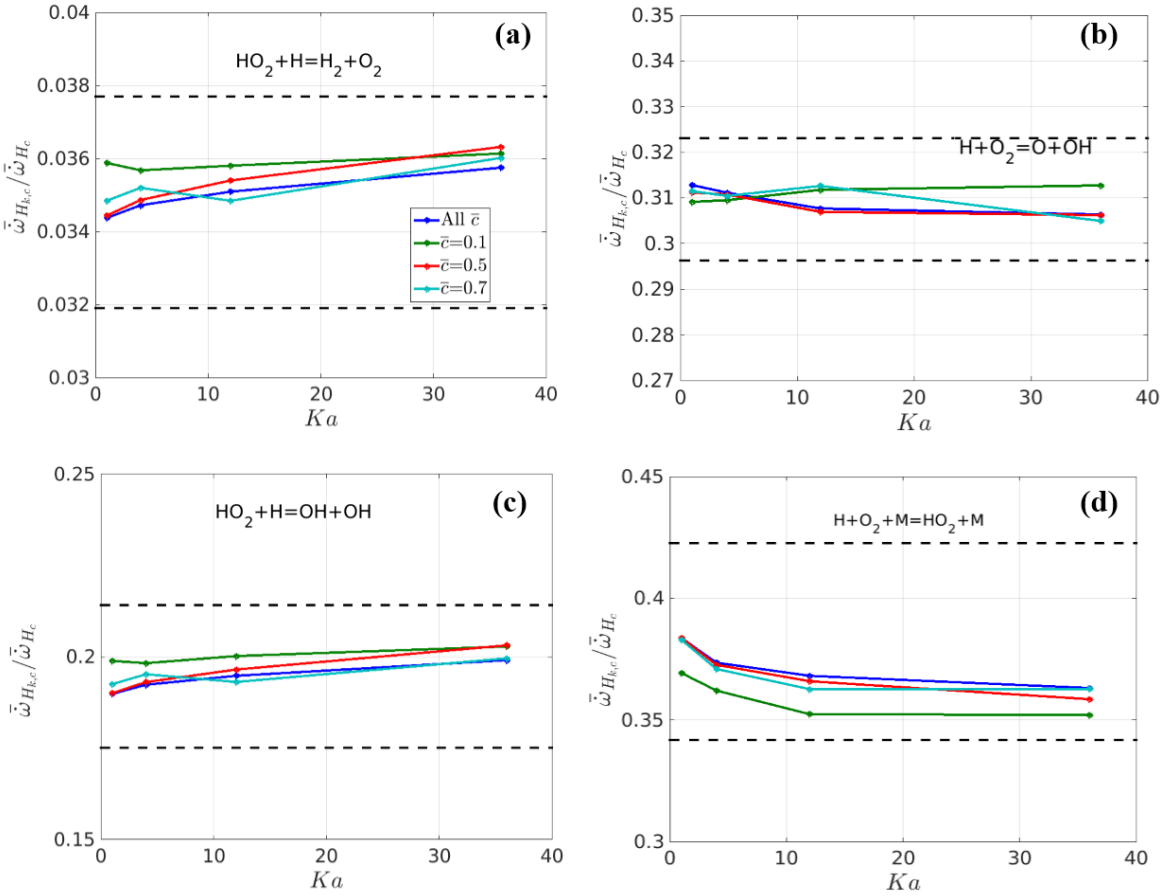

Figure 4.11. Progress variable conditioned H consumption for (a) HO_2+H→OH+OH (b) H+O_2→O+OH (c) HO_2+H→H_2+O_2 (d) H+O_2+M→HO_2+M; (Blue: All $\bar{c}$, Green: $\bar{c}$ = 0.1, Red: $\bar{c}$ = 0.5, Cyan: $\bar{c}$ = 0.7). Dashed horizontal lines denote range of values from OPPDIF calculations.

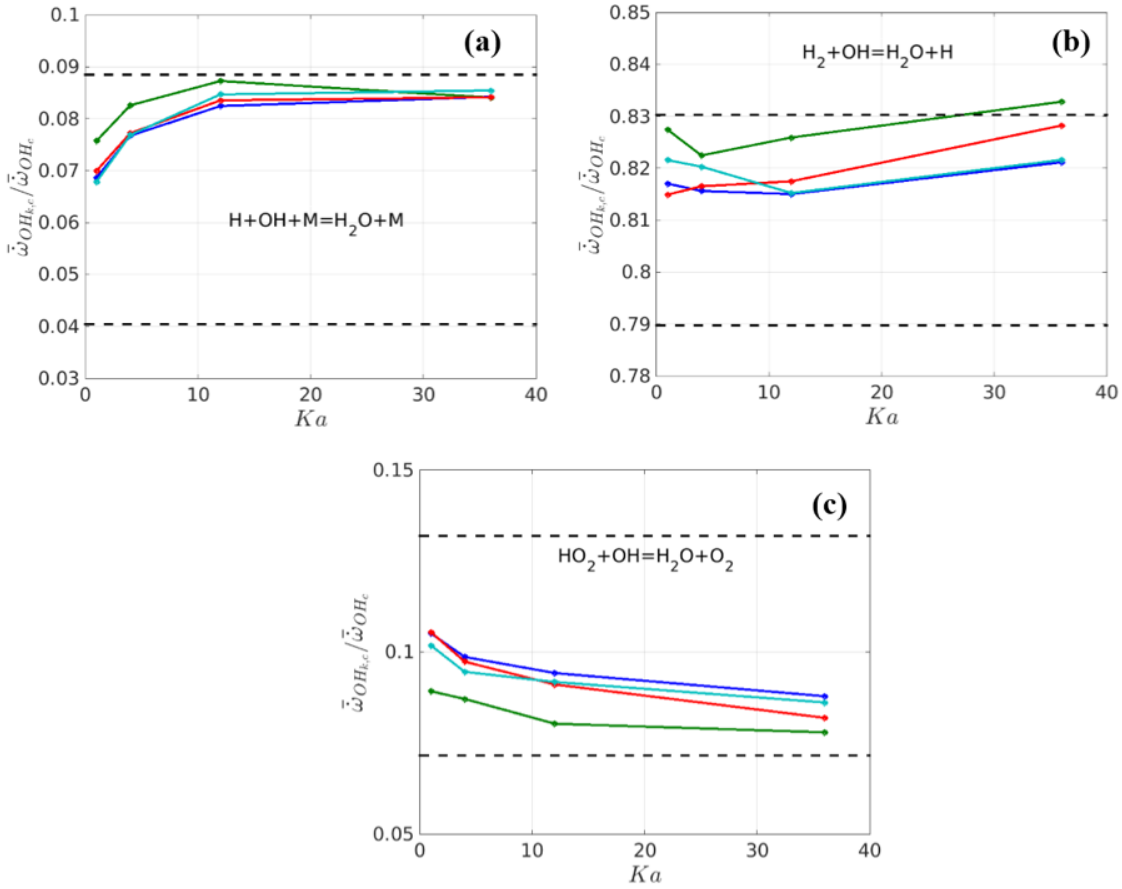

Figure 4.12. Progress variable conditioned OH consumption for (a) H+OH+M→H_2O+M (b) H_2+OH→H_2O+H (c)HO_2+OH→H_2O+O_2; (Blue: All $\bar{c}$, Green: $\bar{c}$ = 0.1, Red: $\bar{c}$ = 0.5, Cyan: $\bar{c}$ = 0.7). Dashed horizontal lines denote range of values from OPPDIF calculations.

4.3 Methane

This section discussed the global and conditioned results for the methane flames.

4.3.1 "Flame" surface definition

Figure 4.13 plots the variation of fuel consumption rate and heat release rate for unstretched laminar flames.

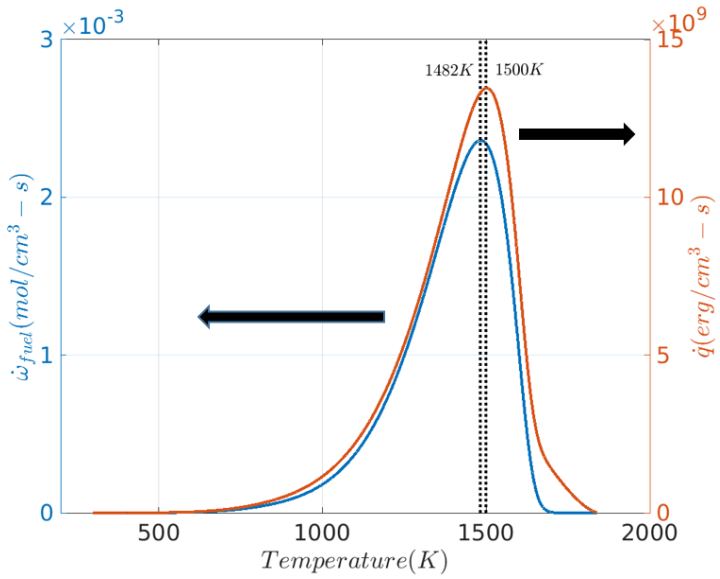

Figure 4.13. Variation of fuel consumption and heat release rate as a function of temperature for CH_4/Air flames with ϕ=0.7, T^u=298K, p=1atm.

The peak temperature for heat release and fuel consumption is 1500K and 1482K respectively. These two values are very close and the isotherm corresponding to the peak fuel consumption is chosen to define the "flame" surface.

4.3.2 Data Visualization

Slices of temperature and some key reactions for methane/air flames are shown in Figure 4.14. Similar to hydrogen flames, appearance of finer scale structures can be seen with increasing turbulence intensities. For the lower turbulence intensities, the "flame" remains thin and can be seen as a "discontinuity" between reactants and products. However, for the higher turbulence intensity case, there appears to be a broadening of the flame. This thickening for methane flames due to preheat zone thickening has been observed by Aspden et al.[67]. The broadening of the reaction zones for some of the reactions can be noted as well. For example, the reaction rate slice for $HO_2+OH \rightarrow H_2O+O_2$ shows slightly broadened regions of existence compared to the lower Karlovitz cases. However, some other reactions such as $CH_3+O \rightarrow CH_2O+H$ occur within a thin reaction zone. This can be seen in the reaction rate slices shown in Figure 4.14(bottom).

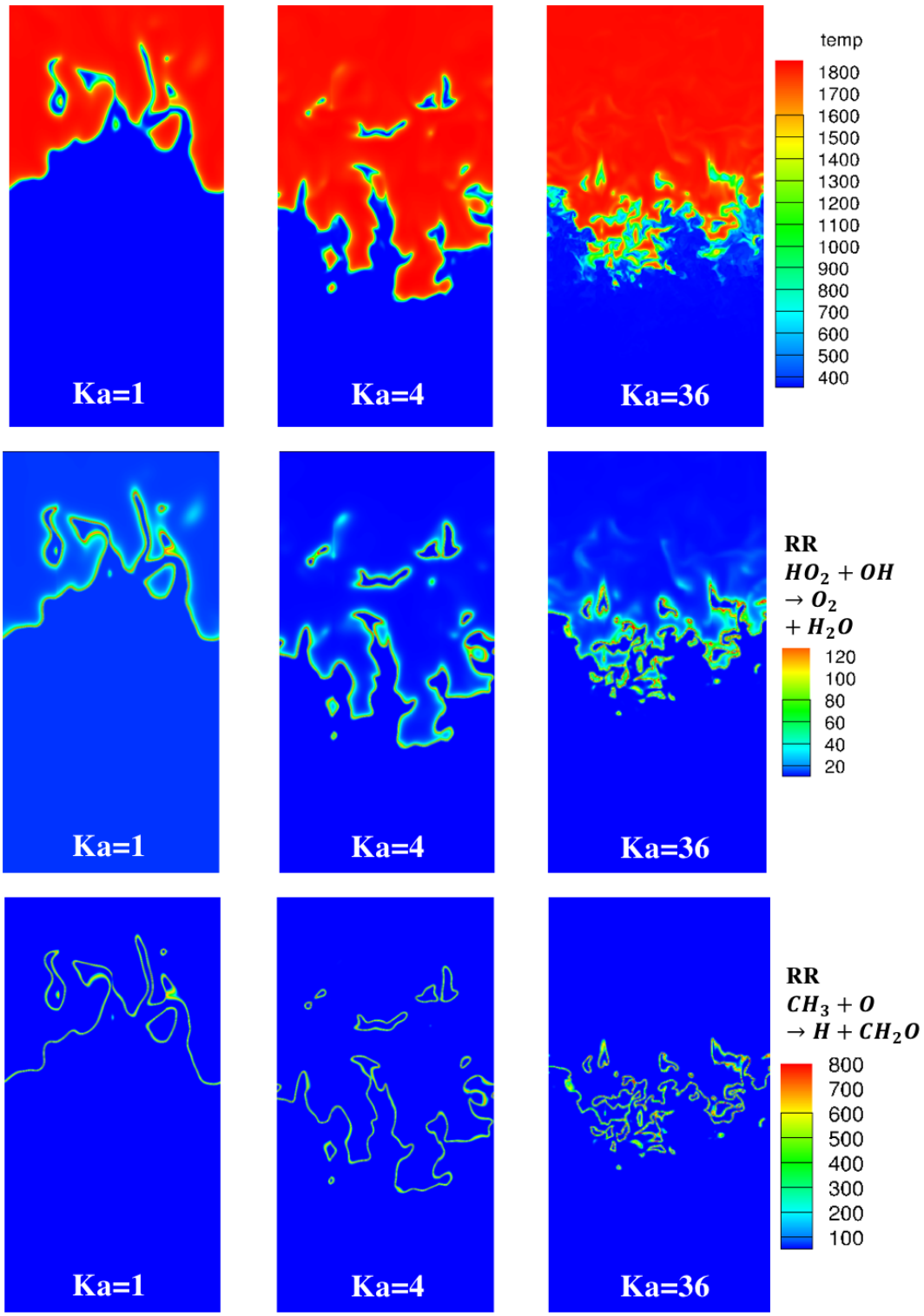

Figure 4.14. Slices of temperature(top), $HO_2 + OH \rightarrow H_2O + O_2$ reaction rate (center) and $CH_3 + O \rightarrow CH_2O + H$ reaction rate(bottom). The slices are constructed using the x=0 and y=0 plane using the fact of periodic lateral boundary conditions.

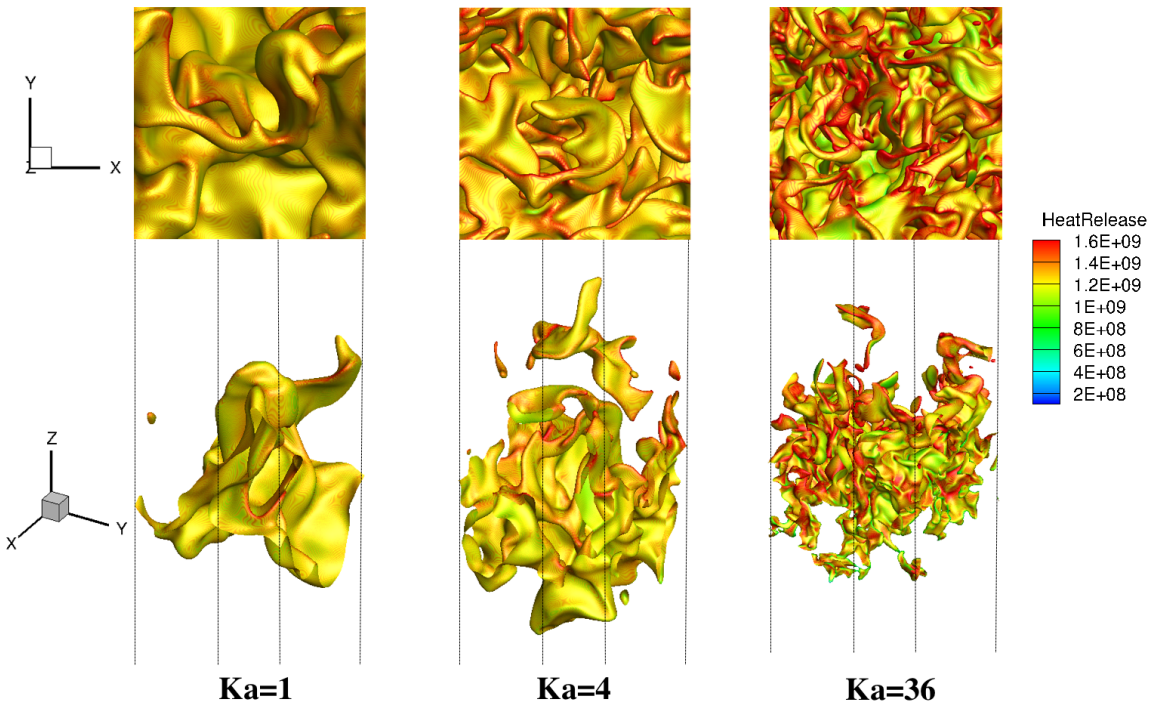

Figure 4.15. Isotherm, T_{ref} = 1482 K(colored by heat release). (Top) X-Y slices of the flame surface (bottom) 3D view of the flame surface. The rectangular domain is shown in black lines.

As discussed in the previous section, the flame is defined by the 1482K isotherm. Figure 4.15 shows the isotherm, T_{ref} = 1482 K (colored by local values of the heat release) for the cases considered. Significant wrinkling of the flame with increasing turbulence can be observed in the figure. Relatively higher heat release can be observed closer to the products side of the flame (reactants are at the bottom and products on the top in Figure 4.15). Even though these "flames" appear highly wrinkled, they maintain their flamelet-like structure. This can be seen in Figure 4.16 wherein the fuel consumption and heat release are plotted as a function of a progress variable (defined based on temperature). The value of the progress variable is zero for reactants and one for products.

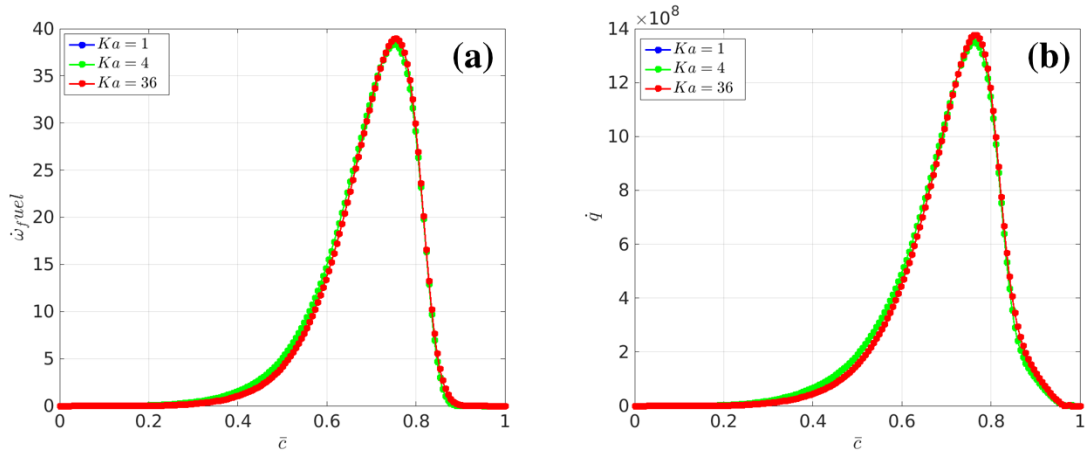

Figure 4.16. Variation of (a) fuel consumption and (b) heat release along a progress variable through the flame for different turbulence intensities for methane flames.

Typically, as expected the fuel consumption and heat release increase, reach a maximum at a given value of the progress variable and then decrease to zero in the products.

4.3.3 Global analysis

First, the global heat release is considered. The heat released by a given reaction at a given condition of stretch, residence time or turbulence intensity (*Ka* =0 corresponds to unstretched laminar flames values) is normalized by the total heat released at that specific condition. Figure 4.17 below plots this normalized heat release for the 5 most dominant heat release reactions. First, note that the dominant reactions remain essentially the same for the DNS, the PSR, and the stretched, premixed flame. Specifically, $O+CH_3 \rightarrow H+CH_2O$ is the dominant heat release reactions (except at high residence times or low stretch). Its contribution to heat release increases by ~45% with decreasing residence time, by ~27% with increasing stretch and ~9% with increasing turbulence.

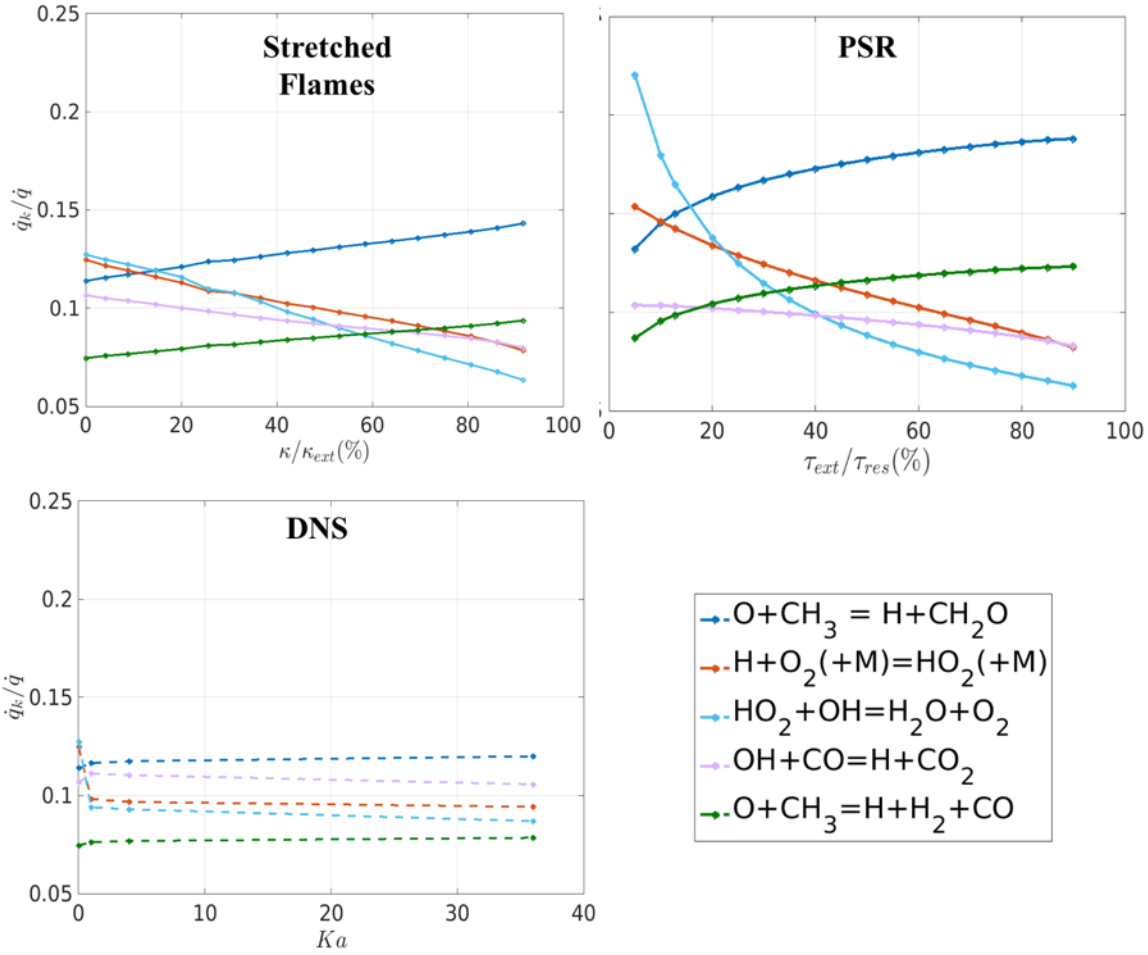

Figure 4.17. Variation of normalized heat release for the 5 dominant heat release reactions with Karlovitz number (DNS), stretch (OPPDIF) and residence time (PSR)

The second dominant heat release reaction for DNS is CO+OH→H+CO_2. However, its contribution to heat release for stretched flames and for perfectly stirred reactors ranks fourth. Its contribution to heat release decreases by ~9% with increasing turbulence, by ~27% with increasing stretch and ~18% with decreasing residence time. The third and fourth dominant reactions are H+O_2(+M)→HO_2(+M) and HO_2+OH→H_2O+O_2 respectively, which show a similar decreasing trend as the previous reaction. These two reactions have the largest fractional change of ~25% and ~30%, respectively between *Ka*=0

and *Ka*=36. $O+CH_3 \rightarrow H+H_2+CO$ is the second dominant reactions for the laminar flame models at high stretch or low residence times but is the fifth dominant reaction for the DNS.

Second, the DNS shows significantly less sensitivity than the laminar calculations. Specifically, the reaction $HO_2+OH \rightarrow H_2O+O_2$ changes the most for the DNS, decreasing by ~8% as Ka increases from 1 to 36. In contrast, the maximum change for the stretched laminar flame is ~50% and ~72% for the PSR for the same reaction. This relative insensitivity is probably a manifestation of unsteady effects.

The variation of some key species' consumption and production is next analyzed. Figure 4.18 shows the variation for species and radicals involved in the formation of CO_2. The OPPDIFF results and the DNS results are plotted for comparison. All the consumption plots in Figure 4.18 show little variation with increasing turbulence intensity and stretch. For turbulent flames, however, some additional reactions play a role. For example in Figure 4.18(a) the reaction $2CH_3 \rightarrow H+C_2H_5$ is a consumer of the methyl radical whereas the reverse reaction is preferred for laminar flames. A similar observation is made for CH_2O consumption with the reaction $H+CH_2O(+M) \rightarrow CH_3O(+M)$.

The hydrogen species/radicals are considered next. Figure 4.19 plots the variation of HO_2 consumption, HO_2 production and OH consumption with *Ka* (DNS, left) and stretch (OPPDIF, right).

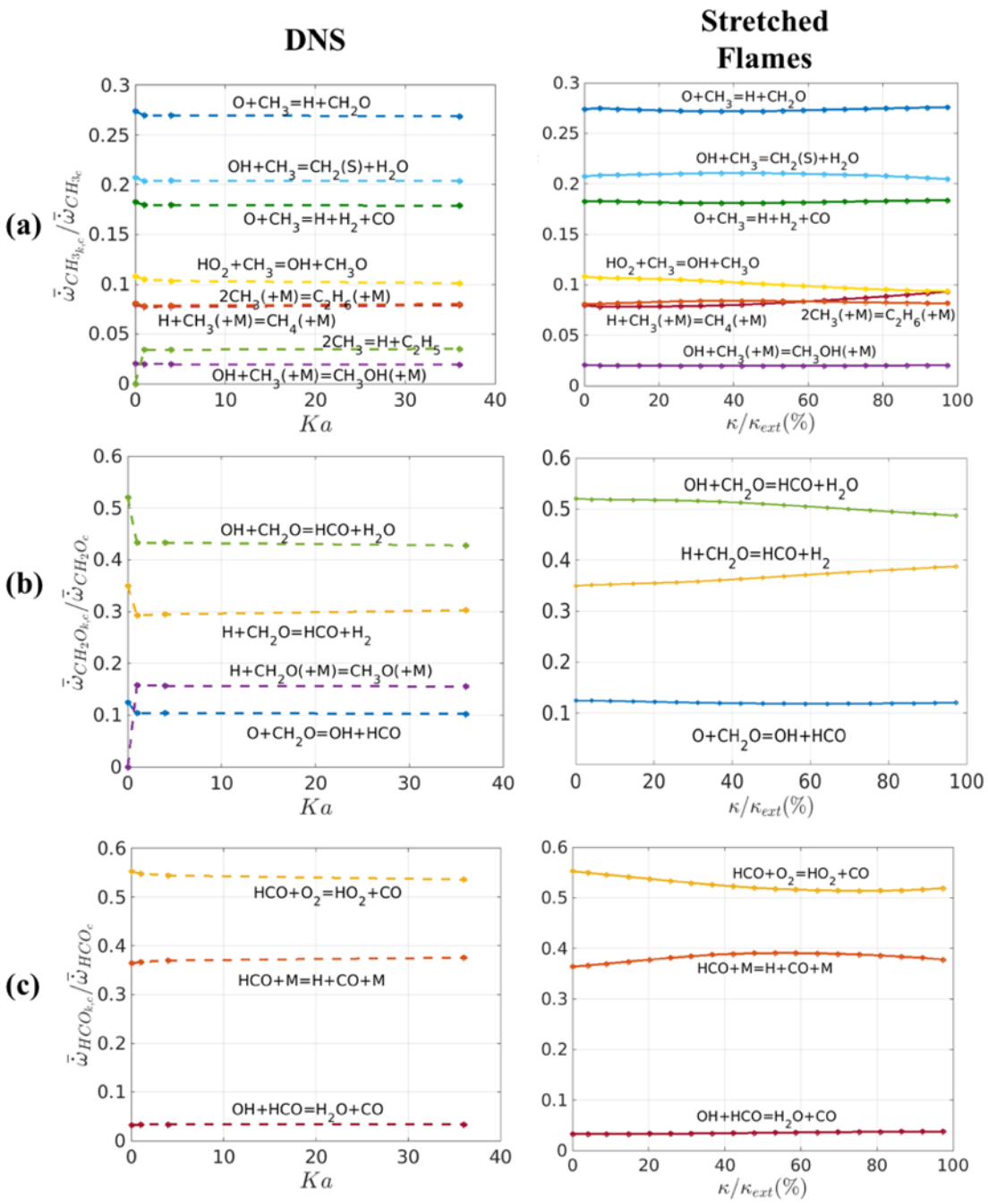

Figure 4.18. Variation of radicals/species consumption with *Ka* (DNS, left) and stretch (OPPDIF, right) for (a) CH_3 consumption (b) CH_2O consumption and (c) HCO consumption.

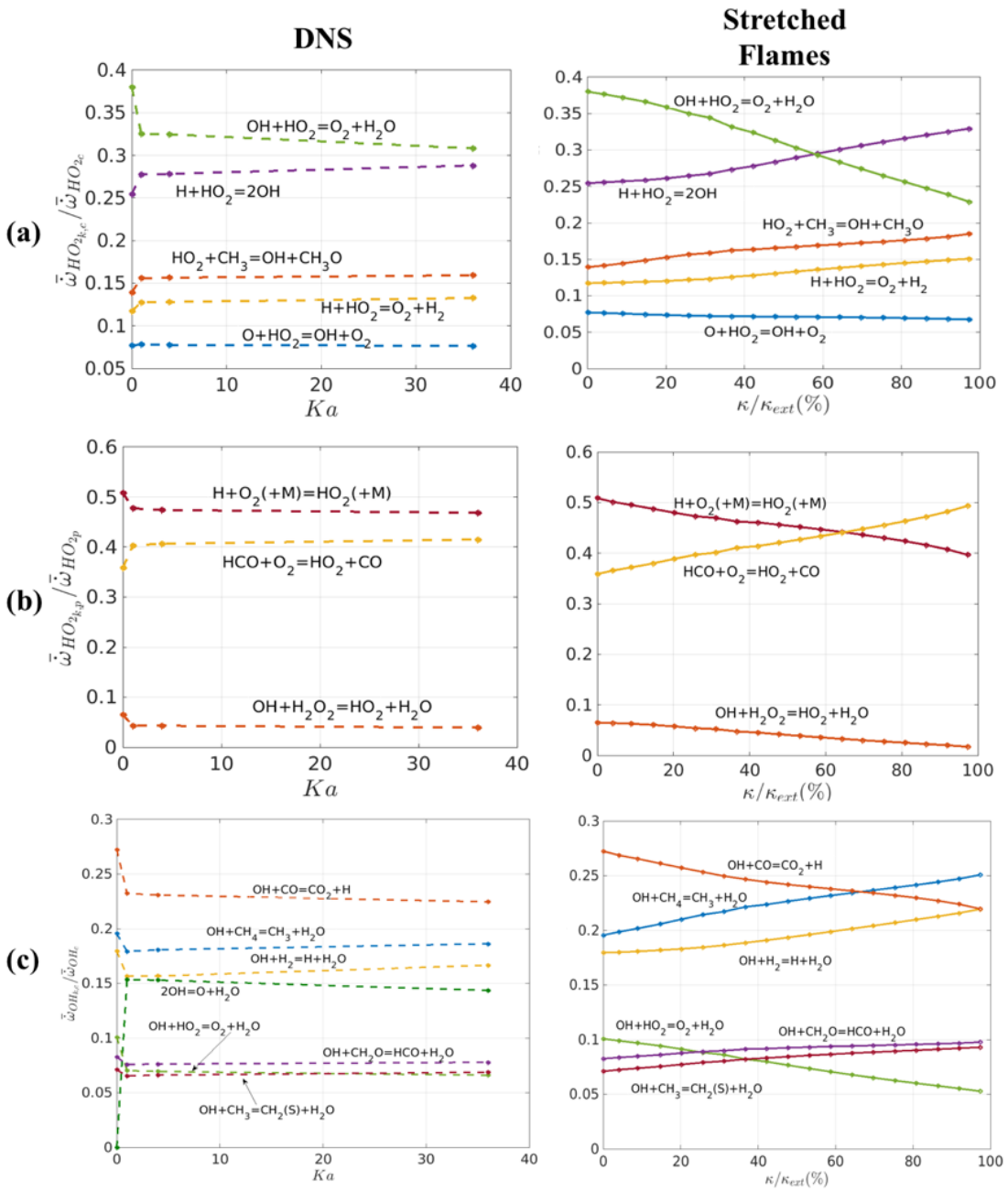

Figure 4.19. Variation of radicals/species consumption with *Ka* (DNS, left) and stretch (OPPDIF, right) for (a) HO_2 consumption (b) HO_2 production and (c) OH consumption

In Figure 4.19(a,b,c right) it can be observed that increasing stretch changes the dominant reaction consuming HO_2 ,producing HO_2 and consuming OH with increasing

stretch. For HO_2 consumption the dominant reaction changes from $OH+HO_2 \rightarrow O_2+H_2O$ to $H+HO_2 \rightarrow 2OH$. This implies that with increasing stretch the chain branching reaction is enhanced over the chain termination reaction creating an increased radical pool of OH. The HO_2 production's dominant reaction, around the same stretch transition point, changes from $H+O_2(+M) \rightarrow HO_2(+M)$ to $HCO+O_2 \rightarrow HO_2+CO$. The OH consumption is also affected around this transition point which is seen by the shift of the dominant reaction from $OH+CO \rightarrow CO_2+H$ to $OH+CH_4 \rightarrow CH_3+H_2O$. These transitions are however, not seen for the turbulent flames but the changes remain qualitatively similar in the low-moderate stretch regions.

4.3.4 Global analysis conditioned on curvature

Having considered the relative roles of different reactions averaged over the entire flame, this section considers a more local evaluation of this issue by conditioning results on curvature. A familiar effect of turbulence on the flame is surface wrinkling. This can in turn alter the reaction rates and hence $\bar{\dot{q}}_k$ and $\overline{\dot{\omega}}_k$. , for stretch sensitive flames.

Figure 4.20 plots the fractional contribution to heat release of each of the elements with increasing turbulence intensity. Even though the heat released varies with turbulence, the normalization enables an effective comparison between all the elements eliminating the changes in the actual values.

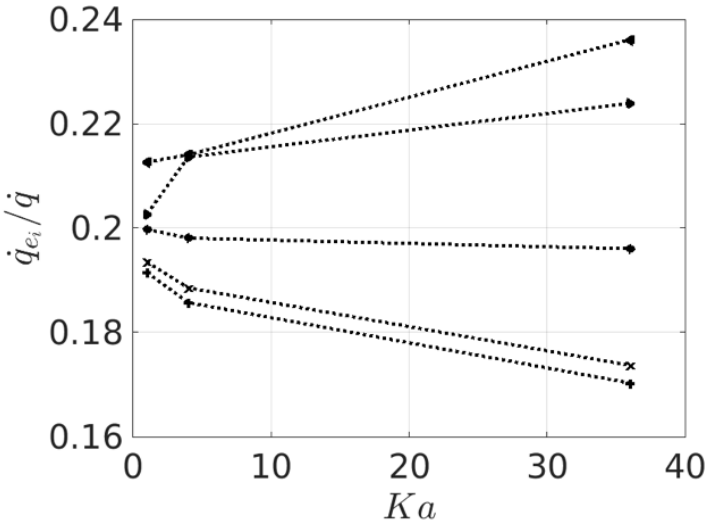

Figure 4.20. Variation of fractional heat release within each element with Karlovitz number. (.▲:Spherical negatively curved, .◄:Cylindrical negatively curved, .●:Saddle points, +:Spherical positively curved, .x: Cylindrical positively curved)

Figure 4.21 plots the heat released by 6 dominant reactions. The heat release is normalized by the total heat released by all the reactions within a certain element. It can be seen that the same 6 reactions dominate the heat release in all 5 elements. However, there is some change in the relative roles of three different reactions for the two positive elements, while they do not for the negatively curved ones. However, the most dominant reaction changes from $O+CH_3 \rightarrow H+CH_2O$ in the positively curved and saddle point elements to $OH+CO \rightarrow CO_2+H$ in the negatively curved elements. A higher fuel consumption by the reaction $OH+CH_4 \rightarrow CH_3+H_2O$ in the positively curved elements leads to a higher concentration of CH_3 and hence an increased reaction rate (and heat release) for reactions consuming CH_3 such as $O+CH_3 \rightarrow CH_2O+H$ and $O+CH_3 \rightarrow CO+H_2+H$. This in turn leads to reduced CH_4(and hence CH_3) concentrations in the negatively curved elements reducing the reaction rates of the above mentioned two reactions. As a result, the reaction of $OH+CO \rightarrow CO_2+H$ takes over as the dominant heat release reaction for these

elements as illustrated in Figure 4.21(c)-(d). The heat release contributions in the positively curved elements show the maximum variation with turbulence intensities. For example, the heat release contribution decreases by ~50% for the reactions $OH+CO \rightarrow CO_2+H$, $OH+HO_2 \rightarrow O_2+H_2O$ and $H+O_2(+M) \rightarrow HO_2(+M)$ in these elements. The chemical pathways seem fairly invariant to increasing turbulence intensity in the negatively curved (convex towards products) elements. It can also be noted that the reaction $HCO+O_2 \rightarrow HO_2+CO$ has a higher heat release than $HO_2+OH \rightarrow H_2O+O_2$ at higher turbulence intensities (i.e. Ka=36) than at Ka=1 for the positively curved elements (Figure 4.21 (a) and Figure 4.21(b)). The dominant heat release reaction does not change for the positively curved elements. The major change observed is the shift of the second dominant heat release reaction from $OH+CO \rightarrow H+CO_2$ at lower turbulence intensities (Ka=1, 4) to $O+CH_3 \rightarrow H+H_2+CO$ at higher turbulence intensities (Ka = 36). The ordering of the other reactions is similar to the global trends shown in Figure 4.17.

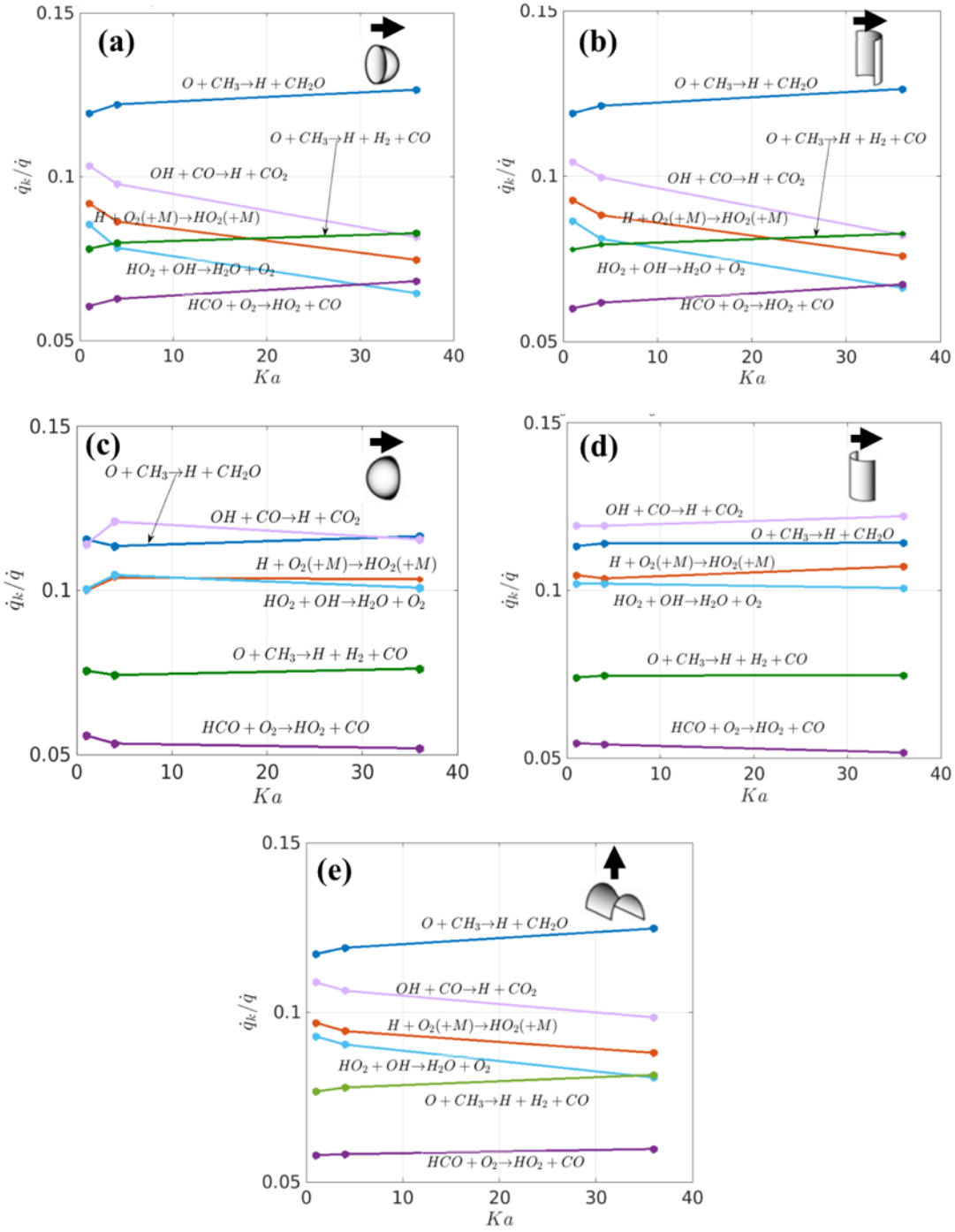

Figure 4.21. Normalized heat release by the dominant reactions in (a) Spherical positively curved elements (b) Cylindrical positively curved elements (c) Spherical negatively curved elements (d) Cylindrical negatively curved elements and (e) Saddle point elements.

To better understand the shift in dominant heat release reaction from positively to negatively curved elements, the consumption rates of selected species are plotted in Figure 4.22.

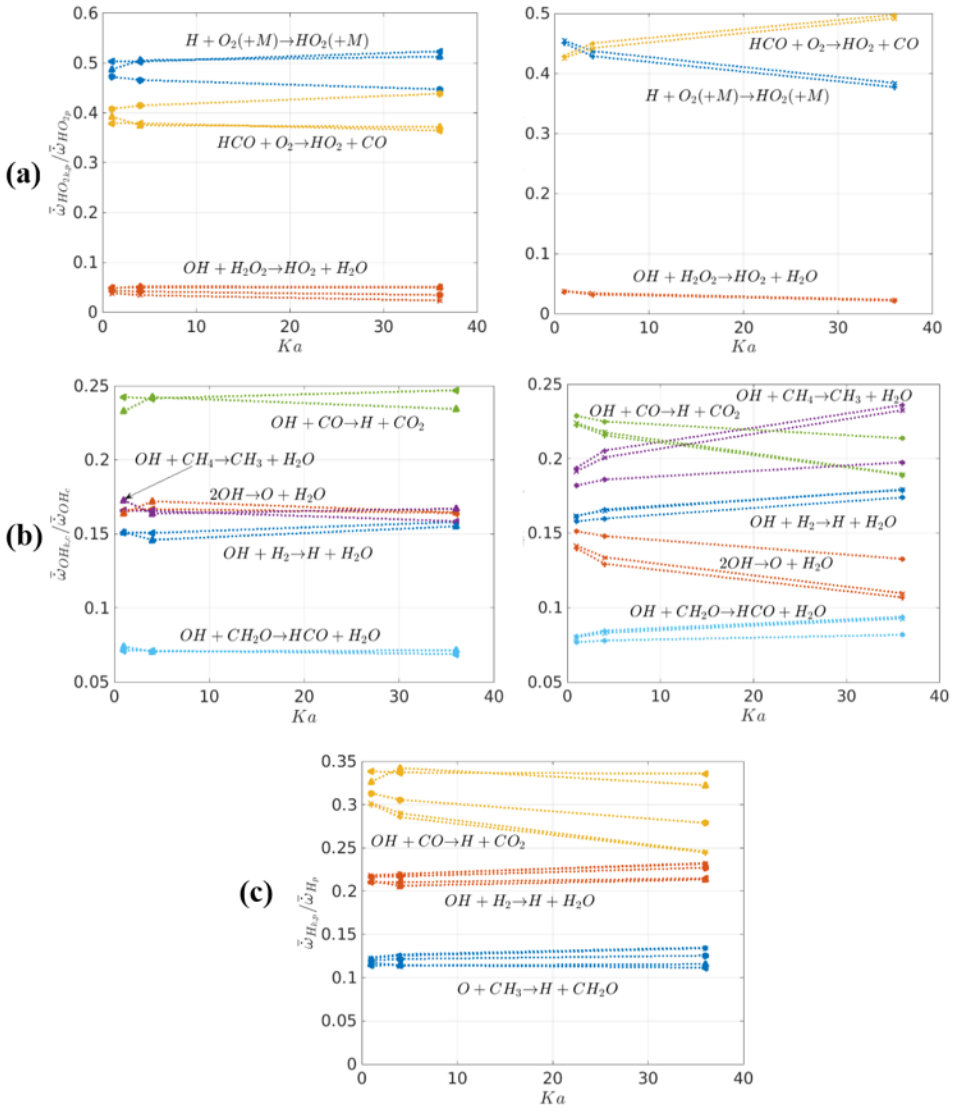

Figure 4.22. Normalized (a) HO_2 production (b) OH consumption and (c) H production by the dominant reactions for the different elements; (.▲:Spherical negatively curved, .◀:Cylindrical negatively curved, .●:Saddle points, +:Spherical positively curved, .x: Cylindrical positively curved).

It can be seen in Figure 4.22(a), the reaction $H+O_2(+M)\rightarrow HO_2(+M)$ is the dominant producer of HO_2 in the negatively curved elements, saddle points and in the positively curved elements at lower turbulence intensities (*Ka*=1). At higher turbulence intensities, $HCO+O_2\rightarrow HO_2+CO$ takes over as the dominant producer of HO_2 for the positively curved elements. The HO_2 production in the saddle points follow trends similar to the negatively curved elements as seen in Figure 4.22(a, left). These 2 reactions also show the maximum change (~20%) with increasing turbulence intensities for the positively curved elements. It can be noted that its contribution to HO_2 production at higher turbulence intensities (*Ka*=36) is comparable to $H+O_2(+M)\rightarrow HO_2(+M)$ in the saddle points. Figure 4.22(b) plots the variation of OH consumption with turbulence intensities in the different elements. $OH+CO\rightarrow H+CO_2$ is the dominant consumer of OH for the negatively curved elements and for saddle points, positively curved elements at lower turbulence intensities (*Ka*=1). At higher turbulence intensities, the CH_4 decomposition (fuel consumption) reaction of $OH+CH_4\rightarrow CH_3+H_2O$ is the higher consumer of OH radicals with a 25% increased consumption with increasing turbulence intensities. In the negatively curved element, the reactions $OH+CH_4\rightarrow CH_3+H_2O$, $2OH\rightarrow O+H_2O$ and $OH+H_2\rightarrow H+H_2O$ have comparable OH consumption rates that are fairly invariant with increasing turbulence intensities. However, for the positively curved elements and saddle points there is increased OH consumption (~20%) by the reaction $OH+H_2\rightarrow H+H_2O$ (3^{rd} dominant consumer) and decreased OH consumption (~15%) by $OH+CO\rightarrow H+CO_2$ and $2OH\rightarrow O+H_2O$ (4^{th} dominant consumer). Figure 4.22(c) plots the H production variation. The H production chemistry remains the same across all 5 elements showing a maximum variation of ~15% for the positively curved elements.

4.3.5 Global analysis conditioned on progress variable

This section considers similar metrics as the previous one focusing on integrated metrics between specific progress variables. Figure 4.23 plots the normalized heat release variation at different $\bar{c}$.

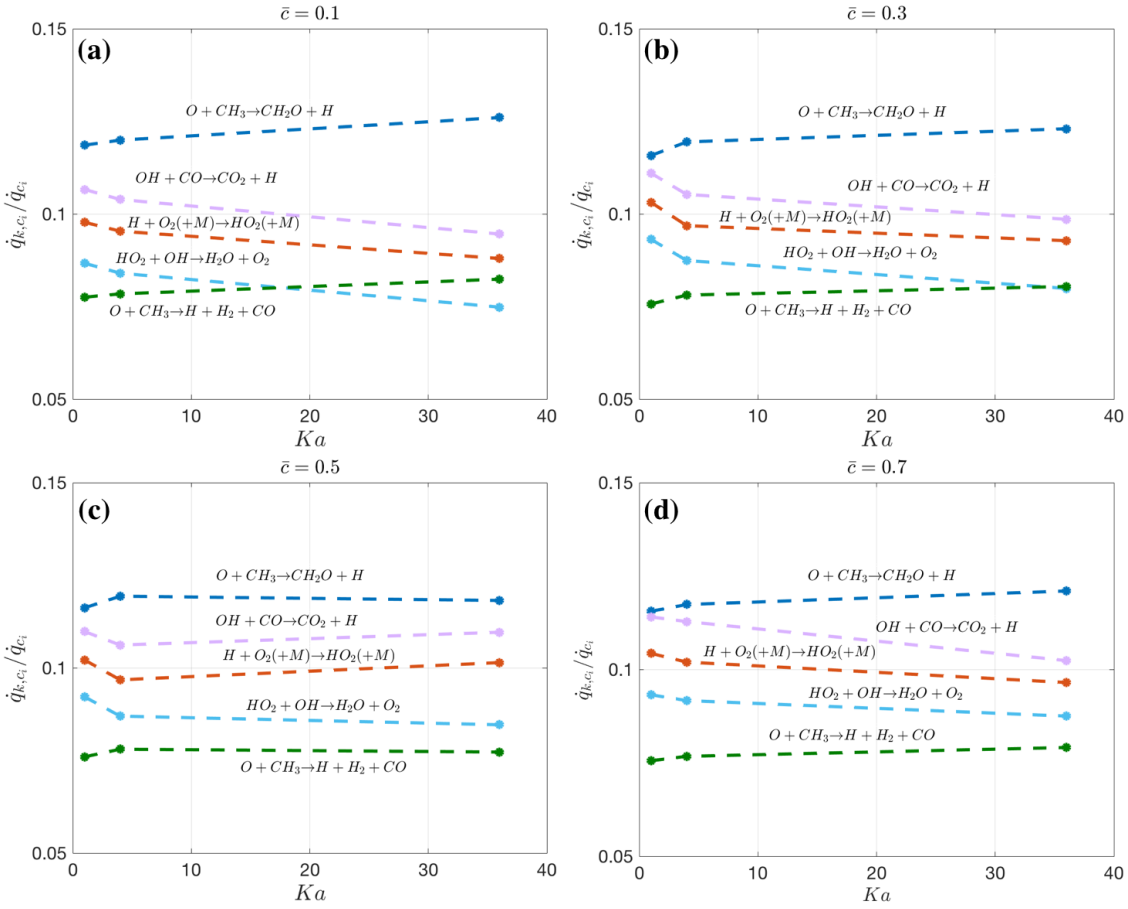

Figure 4.23. Variation of normalized heat release at (a)$\bar{c} = 0.1$ (b) $\bar{c} = 0.3$ (c) $\bar{c} = 0.5$ (d) $\bar{c} = 0.7$.

Overall the same dominant heat release reactions can be observed at different $\bar{c}$. Changes with turbulence are slightly pronounced at progress variables closer to the leading edge of the flame. For example, the contribution of the reaction OH+CO→H+CO_2 to heat release decreases by ~25% at $\bar{c} = 0.1$ and ~20% at $\bar{c} = 0.3$ with increasing turbulence

compared to a ~9% for the overall flame. Similarly, the contribution of the reaction $O+CH_3 \rightarrow CH_2O+H$ increases by about ~5% at $\bar{c} = 0.1$ between Ka=1 and Ka=36 compared to a ~2% change for the overall flame between Ka=1 and Ka=36. At the leading edge of the flame i.e. at $\bar{c} = 0.1$ the reactions $O+CH_3 \rightarrow CO+H_2+H$ takes over from $HO_2+OH \rightarrow H_2O+O_2$ as the 4th dominant heat release reaction at higher Ka. These two reactions have comparable contributions to heat release at higher Ka for $\bar{c} = 0.3$. The heat release variations for $\bar{c} = 0.5,0.7$ behave similar to its global counterpart. For example, the reaction, $O+CH_3 \rightarrow CH_2O+H$ changes by ~9% for the global characteristics. This change is between 7-12% for the progress variables away from the leading edge of the flame. The higher sensitivity of the reaction $H+O_2(+M) \rightarrow HO_2(+M)$ as identified from the global analysis is prevalent at all progress variables with a pronounced increase at the leading edge of the flame. The change in the contribution of this reaction varies between ~20-50% at different progress variables compared to the ~25% change seen from the global characteristics.

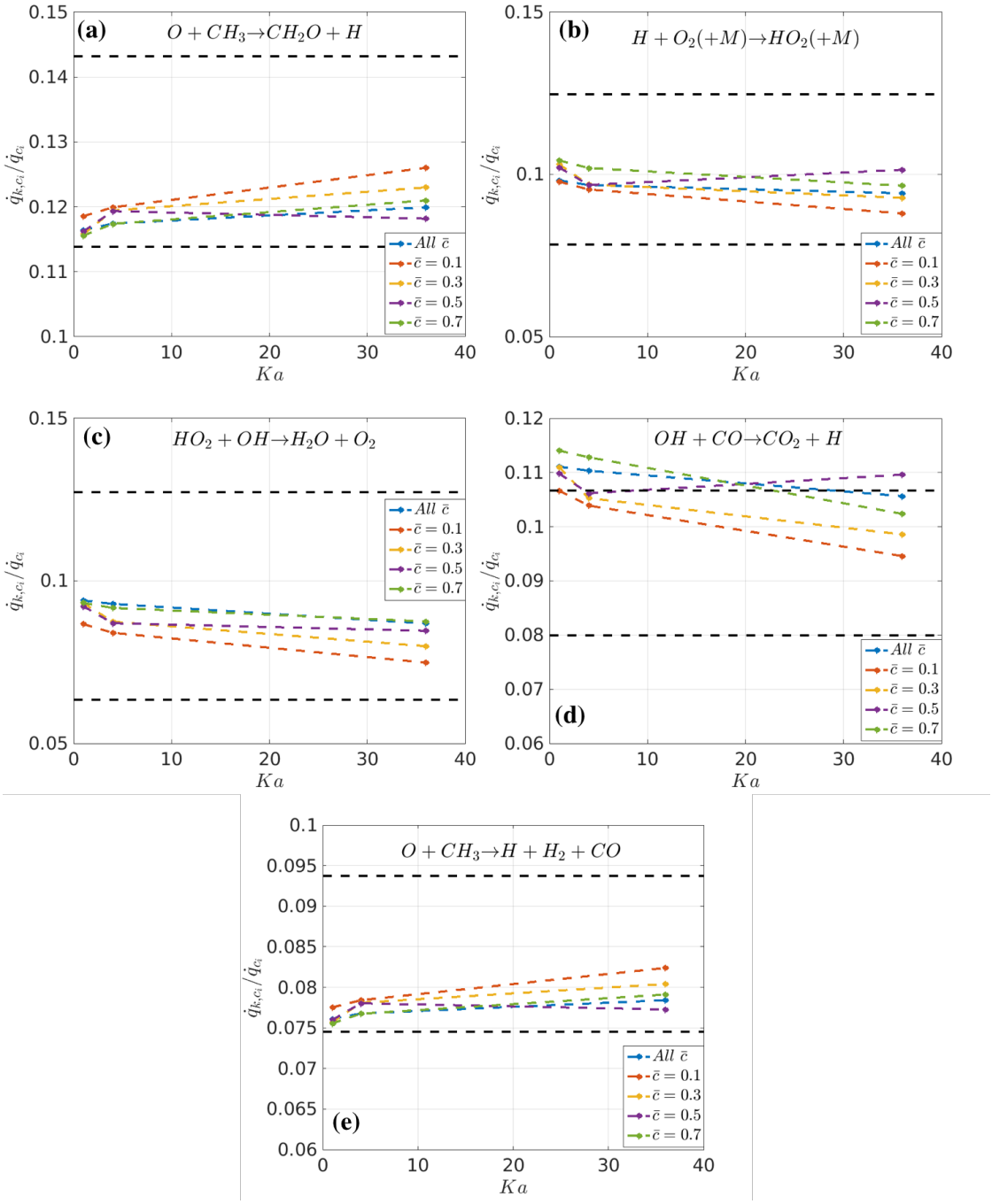

Figure 4.24. Progress variable conditioned heat release for (a)O+CH₃→CH₂O+H (b) H+O₂(+M)→HO₂(+M) (c) HO₂+OH→O₂+H₂O (d) OH+CO→CO₂+H (e) O+CH₃→CO+H₂+H ; (Blue: All $\bar{c}$, Orange: $\bar{c}$ = 0.1, Yellow: $\bar{c}$ = 0.3, Purple: $\bar{c}$ = 0.5, Green: $\bar{c}$ = 0.7). Dashed horizontal lines denote range of values from OPPDIF calculations.

In general, from Figure 4.24 it can be observed that the laminar calculations bound the quantitative contributions of the reactions except for $OH+CO \rightarrow CO_2+H$ wherein the heat release contributions at lower Ka lies outside the laminar bounds. With increasing turbulence intensity, the contribution of this reactions decreases and falls within the laminar bounds. Overall, the variations are not significant as highlighted by the limited range on the y-axis of all the plots. The variation across progress variables (i.e. from $\bar{c} = 0.1$ to $\bar{c} = 0.7$) for all the reactions is of the order of ~10-13% with the maximum variation of ~20% for $OH+CO \rightarrow CO_2+H$. In general, the means from the global characteristics lie closer to $\bar{c} = 0.5,0.7$ with the leading edge showing the most significant changes for all the reactions. For example, the reactions $HO_2+OH \rightarrow H_2O+O_2$ shows a ~40% decrease with increasing turbulence intensities from Ka=1 to Ka=36 for $\bar{c} = 0.1$ whereas this change is ~10% between Ka=1 and Ka=36 for the global mean.

The consumption and production pathways of selected species are shown in Figure 4.25. The same dominant reactions as the global characteristics are identified for HO_2 consumption, production and OH consumption. For all these species, interesting characteristics are observed for the two progress variables; one closer to the leading edge of the flame and the other closer to the trailing edge of the flame. For example, at Ka=36, OH consumption by $OH+CO \rightarrow CO_2+H$ and $OH+CH_4 \rightarrow CH_3+H_2O$ become comparable at $\bar{c} = 0.1$. This behavior is similar to the stretched flame behavior shown in Figure 4.19(c) wherein with increasing stretch $OH+CH_4 \rightarrow CH_3+H_2O$ takes over from $OH+CO \rightarrow CO_2+H$ as the dominant OH consumer.

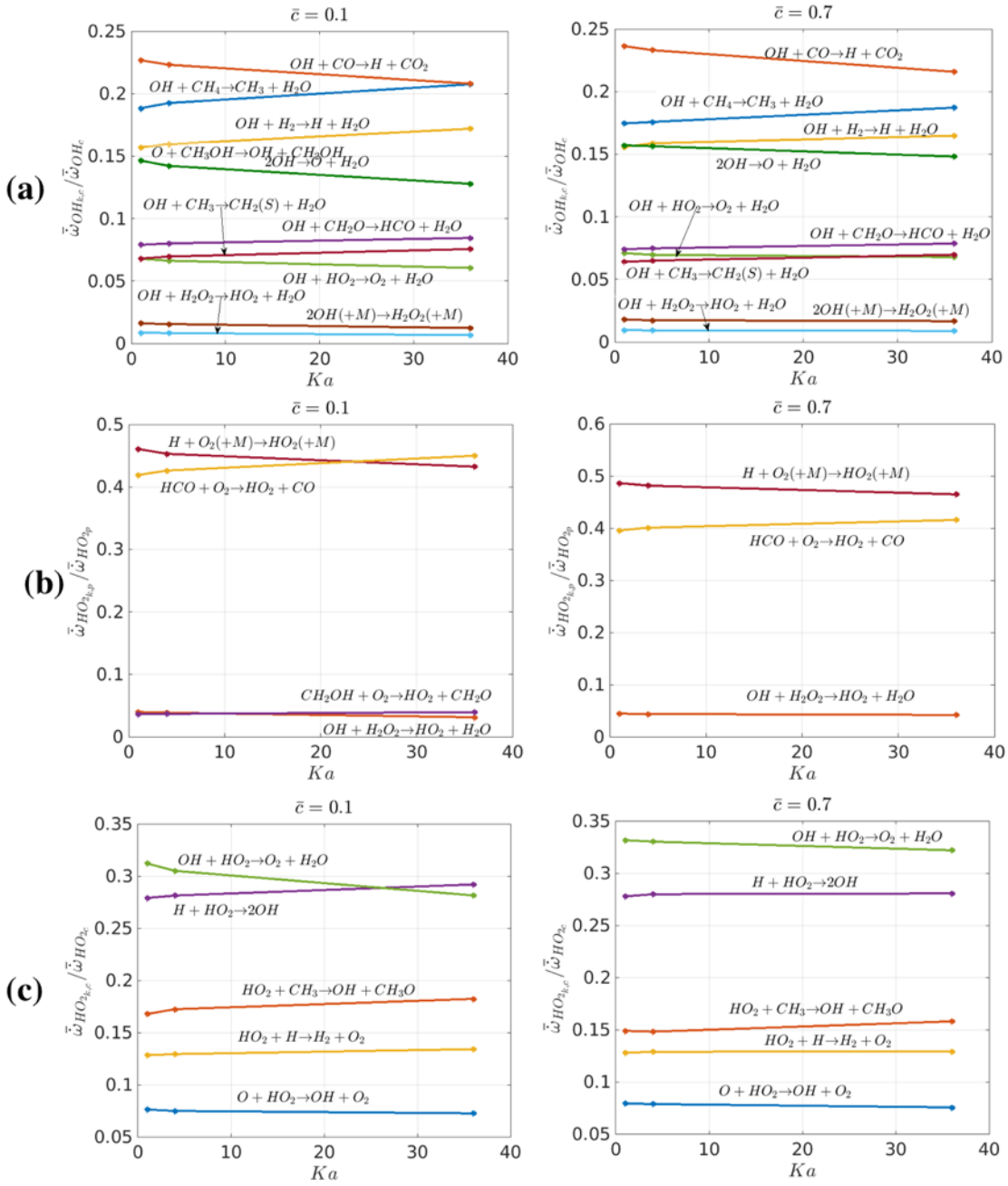

Figure 4.25. Normalized contribution of reactions for (a) OH consumption (b) HO_2 production (c) HO_2 consumption for $\bar{c} = 0.1$ (left), 0.7(right).

This strong resemblance of pathways to stretched flames can be observed for HO_2 production and consumption in Figure 4.19(b) and (c) with Figure 4.25(b) and (c) respectively. For example, with increasing turbulence intensities, $HCO+O_2 \rightarrow HO_2+CO$

becomes the dominant HO_2 producing reaction over $H+O_2(+M) \rightarrow HO_2(+M)$ with ~13% increase in its contribution. Similarly, at lower turbulence intensities, $OH+HO_2 \rightarrow O_2+H_2O$ is the dominant HO_2 consuming reaction and its contribution decreases by ~6% with increasing turbulence. However, the chain branching reaction of $H+HO_2 \rightarrow 2OH$ is the dominant reaction with its contribution increasing by ~10% at higher turbulence intensities. This behavior is consistent with the trends shown for stretched flames with increasing stretch rates. Thus, a striking similarity is seen in the pathways between stretched flames and progress variables closer to the leading edge of the flame. Progress variables closer to the trailing edge of the flame are well represented by the pathways at $\bar{c} = 0.7$. These pathways are very similar in characteristics and behavior to the global characteristics for the DNS cases. For example, $OH+CO \rightarrow CO_2+H$ is the dominant OH consuming reaction for both cases and changes by ~6% for the global characteristics and ~13% at $\bar{c} = 0.7$ between Ka=1 to Ka=36. Similarly, for HO_2 production, the percentage change in $H+O_2(+M) \rightarrow HO_2(+M)$ with increasing turbulence intensities is ~4% at $\bar{c} = 0.7$ and ~2% for global characteristics.

Overall, the leading edge of the flame which is primarily composed of positively curved elements shows pathways very similar to highly stretched flames with increasing turbulence intensities. Away from the leading edge, the pathways resemble the global characteristics wherein a significant contribution comes in from the negatively curved elements.

4.4 n-dodecane

This section discusses the global and conditioned results for the n-dodecane flames.

4.4.1 "Flame" surface definition

Figure 4.26 plots the variation of heat release rate and fuel consumption for unstretched laminar flames.

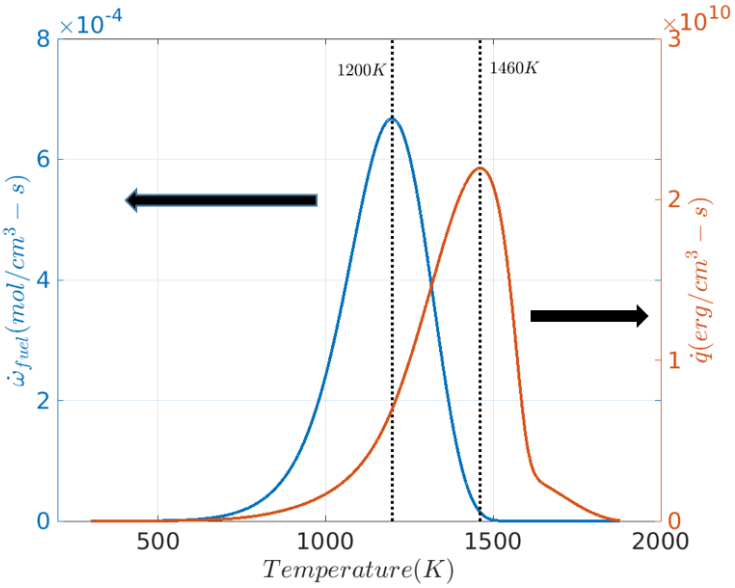

Figure 4.26. Variation of fuel consumption and heat release rate as a function of temperature for $nC_{12}H_{26}$/Air flames with ϕ=0.7, T^u=298K, p=1atm.

The peak temperature for heat release and fuel consumption is 1460K and 1200K respectively. For n-dodecane/air flames, pyrolysis is the first step in fuel oxidation wherein the fuel is broken down into smaller fragments. The eventual oxidation to CO_2, H_2O and heat release occurs at higher temperatures. The isotherm corresponding to peak heat release is chosen to define the iso-surface. Again, a higher temperature iso-value forms a well-connected surface with well-defined normals.

4.4.2 Data Visualization

Slices of temperature and some key reactions for n-dodecane/air flames are shown in Figure 4.27.

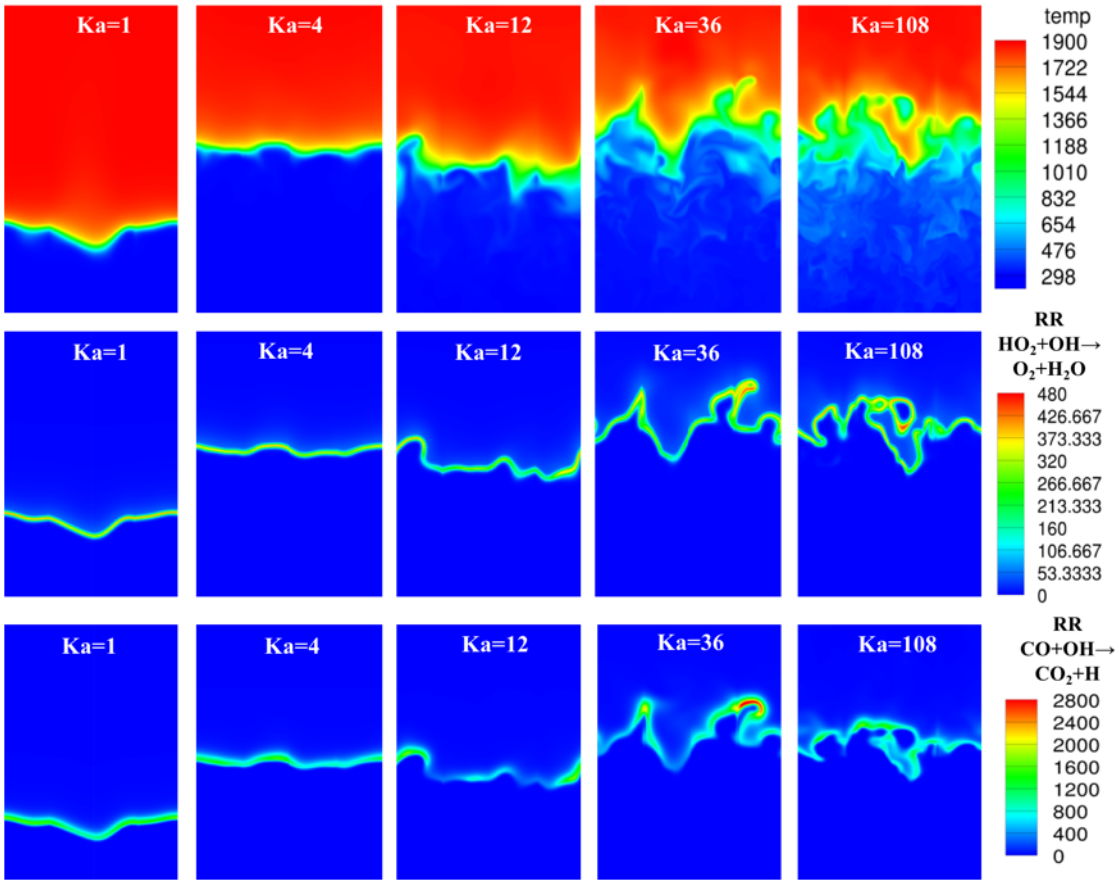

Figure 4.27. Slices of temperature(top), $HO_2+OH \rightarrow O_2+H_2O$ reaction rate (center) and $CO+OH \rightarrow CO_2+H$ reaction rate(bottom). The slices are constructed using the x=0 and y=0 plane using the fact of periodic lateral boundary conditions.

The clear thickening of the flame with increasing turbulence intensity, which has been established in literature[13, 68], can be observed from the temperature slices. For the lower Ka cases, the flame is thin and slightly wrinkled. With increased turbulence intensities, the temperature region between 800-1300K starts broadening suggesting penetration of the

eddies in the preheat zone. With further increase in turbulence, the further spatial broadening of the preheat zone can be observed. Even though there is a significant spatial variation in temperature, certain reactions still have a thin zone of reaction. For example, it can be observed that the reaction $HO_2+OH \rightarrow O_2+H_2O$ occurs within a thin reaction zone even at higher Ka. However, certain other reactions mimic the temperature broadening leading to broadened reaction zones. This can be seen for the reaction $CO+OH \rightarrow CO_2+H$ which has a broadened reaction zone with increasing turbulence intensities with a pronounced effect at Ka=108.

As discussed in the previous section, the flame is defined by the 1460K isotherm. Figure 4.28 shows the isotherm, T_{ref} = 1460 K (colored by local values of the heat release) for the cases considered.

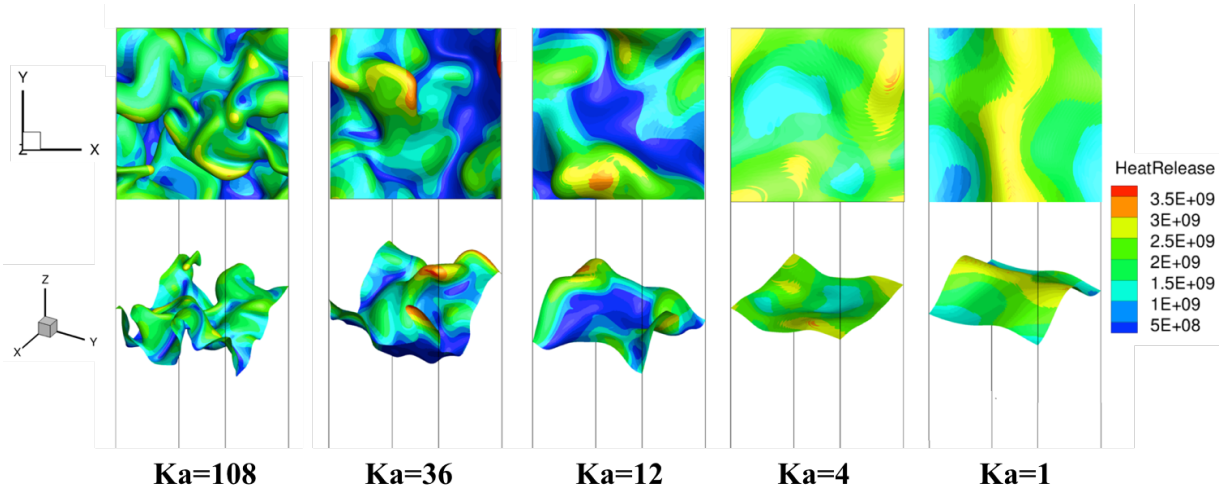

Figure 4.28. Isotherm, T_{ref} = 1460 K(colored by heat release). (Top) X-Y slices of the flame surface (bottom) 3D view of the flame surface. The rectangular domain is shown in black lines.

The increased wrinkling of the flame with increasing turbulence is apparent from Figure 4.28. A wider range of heat release occurs over the highly wrinkled surfaces at the

higher turbulence levels of Ka=36,108 compared to Ka=1,4. Increased local curvature (positive or negative) leads to focusing and defocusing of scalars which directly affects the local reaction rates and hence heat release. The flames maintain their flamelet-like structure which is observed in the plot for heat release and fuel consumption as function of a temperature based progress variable.

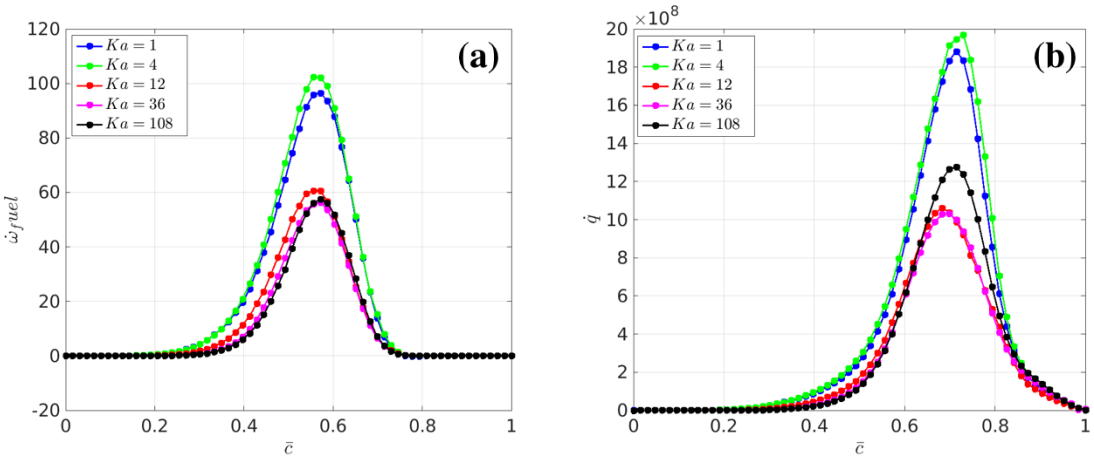

Figure 4.29. Variation of (a) fuel consumption and (b) heat release along a progress variable through the flame for different turbulence intensities for n-dodecane flames.

$\bar{c}$=0 corresponds to reactants and $\bar{c}$=1 corresponds to products. The fuel consumption and heat release increase from zero to a maximum at a given progress variable and decreases to zero on the products side.

4.4.3 Global analysis

Figure 4.30 plots the variation of normalized heat release for stretched flames, PSR and DNS.

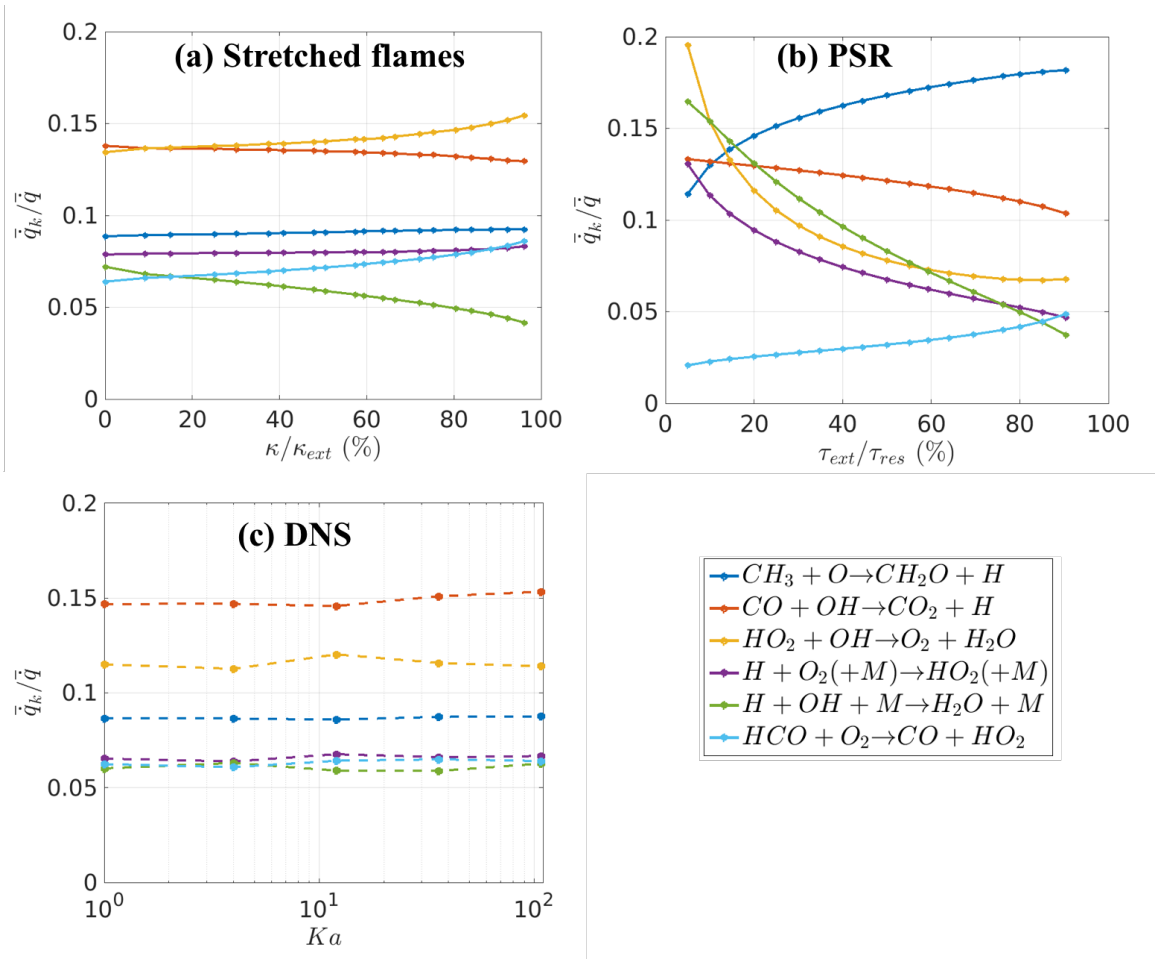

Figure 4.30. Variation of normalized heat release with (a) increasing stretch and (b) decreasing residence time and (c) increasing turbulence intensities using You et al.[89]'s mechanism.

Starting with Figure 4.30(a) and (b), the first observation is that the same set of dominant heat release reactions appear for both the reference calculations. However, there are differences in sensitivity to κ and τ_{res}, as well as in the dominant reaction at a given point, between the two reference calculations. For example, the reaction of HO_2+OH→O_2+H_2O increases with κ with a maximum variation of ~8%. The same reaction decreases with decreasing residence time by ~65% for the PSR. Similarly, the reaction of CH_3+O→CH_2O+H is fairly invariant to increasing stretch, changing by ~1%

from κ/κ_{ext}=0 to $\kappa/\kappa_{ext} = 0.97$. The contribution of the same reaction increases by ~50% with decreasing residence time. This observation is very different from that observed in the case of lighter fuels, such as hydrogen and methane discussed in Sections 4.2 and 4.3, wherein the variation between the stretched flame and the PSR results was within ~20%.

Considering next the turbulent flame results in Figure 4.30(c), the plot shows that the dominant heat release reactions identified from DNS are the same dominant reactions as seen for stretched flames and PSR. The ordering and behavior of the reactions more closely resembles those of stretched flames. Overall, however, the results show almost no change of the reactions contributions with *Ka*. For example, the variation in normalized heat release for the dominant heat release reaction, $CO+OH \rightarrow CO_2+H$, with increasing turbulence intensities is ~6% between Ka = 1 and Ka = 12. The difference between the unstretched laminar case and the Ka=108 case is ~2%. Similarly, the maximum variation for the second dominant heat release reaction, $HO_2+OH \rightarrow O_2+H_2O$, is ~5% between Ka=1 and Ka=12.

Having considered heat release, another metric that can be used to assess turbulence effects on chemical pathways is radical formation or destruction rates. Figure 4.31 plots the fractional consumption of the high temperature radicals, CH_3 (left) and HCO (right), for the DNS and model reactor/flame calculations.

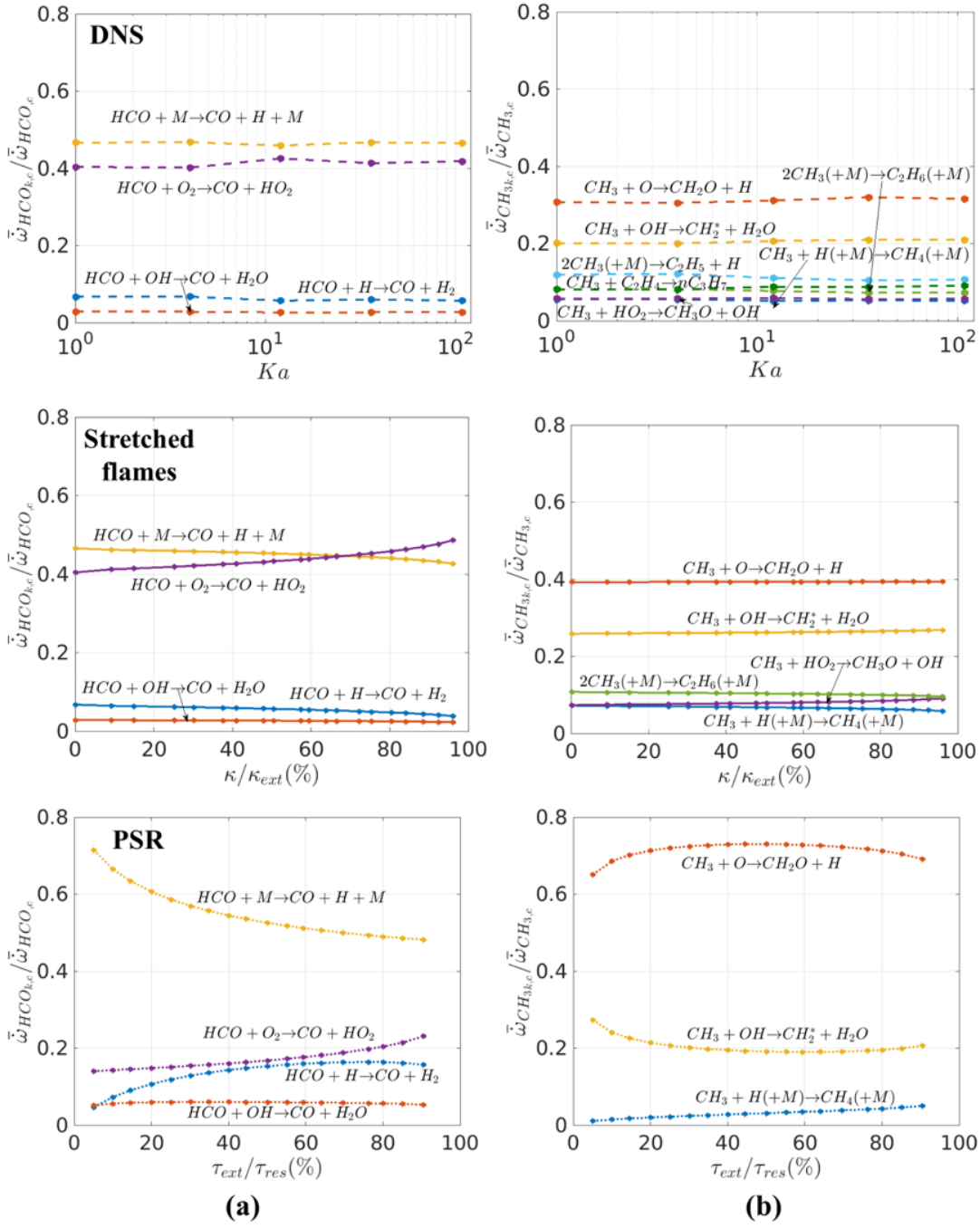

Figure 4.31. Dependence of normalized consumption rates for (a) HCO and (b) CH_3 upon Karlovitz number (top), stretch rate (center) and residence time (bottom)

Significant quantitative variation of consumption rates via these reactions is observed between the two configurations. All the dominant HCO-consuming reactions

form CO, as seen in Figure 4.31(a). For stretched flames, $HCO+O_2 \rightarrow CO+HO_2$ surpasses $HCO+M \rightarrow CO+H+M$ as the dominant HCO-consuming reaction at high stretch rates. These two reactions are also the most dominant HCO consumers for perfectly stirred reactors. These reactions also have similar directional sensitivity to stretch/residence time for both models. For example, HCO consumption via the reaction, $HCO+M \rightarrow CO+H+M$, decreases by ~8% from κ/κ_{ext}=0 to $\kappa/\kappa_{ext} = 0.97$ and by ~32% from τ_{ext}/τ_{res}=0.05 to $\tau_{ext}/\tau_{res} = 0.91$. Similarly, the normalized rate of HCO consumption by $HCO+O_2 \rightarrow CO+HO_2$ increases by ~20% from κ/κ_{ext}=0 to $\kappa/\kappa_{ext} = 0.97$ and by ~65% from τ_{ext}/τ_{res}=0.05 to $\tau_{ext}/\tau_{res} = 0.91$.

The two dominant CH_3-consuming reactions are $CH_3+O \rightarrow CH_2O+H$ and $CH_3+OH \rightarrow CH_2^*+H_2O$. These two reactions account for almost ~65% and ~90% of the consumption of CH_3 for stretched flames and the perfectly stirred reactor, respectively. For the stretched laminar flame, both reactions show limited sensitivity to increasing stretch with a maximum change of 4%. For the PSR, this change is ~25% with decreasing residence times.

The dominant reactions for each species in DNS exhibit a strong qualitative and quantitative similarity with their stretched flame counterparts. For example in Figure 4.31(a), $HCO+M \rightarrow CO+H+M$ consumes ~45% of the total HCO as seen in Figure 4.31(a, top and center) and changes by <1% with increasing turbulence intensity. The maximum change of ~8% is seen for the reaction $HCO+O_2 \rightarrow CO+HO_2$ between Ka=1 and Ka=12. Unlike the stretched, laminar flames, no cross-over is seen by the two dominant reactions. In Figure 4.31(b), the dominant CH_3 consuming reaction of $CH_3+O \rightarrow CH_2O+H$ shows a maximum increase of ~7% with increasing turbulence intensity. The primary difference

between stretched flames and DNS is the appearance of the fuel fragments recombination reactions of $2CH_3 \rightarrow C_2H_5+H$ and $CH_3+C_2H_4 \rightarrow nC_3H_7$ in addition to $2CH_3(+M) \rightarrow C_2H_6(+M)$.

Figure 4.32 plots the consumption rates for OH (high temperature radicals) and HO_2 (low temperature radical). Similar conclusions as discussed above can be drawn here-most notably, the weak effect of Ka on the relative contributions of radical formation/destruction reactions. In general, all reactions for the DNS and the stretched laminar flames show only minor variations with increasing turbulence intensities/ stretch. On the other hand, substantial variation is seen with changing residence times for the PSR. This is likely a thermal effect. Figure 4.33 (a) plots the flame speed and temperature dependence upon the normalized stretch rate. The κ=0 result comes from PREMIX. Figure 4.33(b) plots the temperature variation as a function of residence time. For reference, Figure 4.33(c) plots the temperature variation for the DNS flames with Karlovitz number. This temperature is obtained by taking the mean of the maximum temperature along all flame normals. The error bars indicate one standard deviation from the mean value of this maximum temperature at every *Ka*. This mean changes by ~80K from *Ka*=1 to *Ka*=108 suggesting limited thermal effects with turbulence. Comparing the temperature changes for the three calculations, there is a roughly 300K, 200K, and 80K difference for the PSR, stretched flame, and DNS. In other words, the PSR temperature changes the most and the DNS the least which may be a key driver behind the much larger changes in chemical pathways for the PSR with residence time than is observed for the stretched flames, as well as a possible reason for the near insensitivity of integrated reaction metrics to Karlovitz number for the turbulent flame.

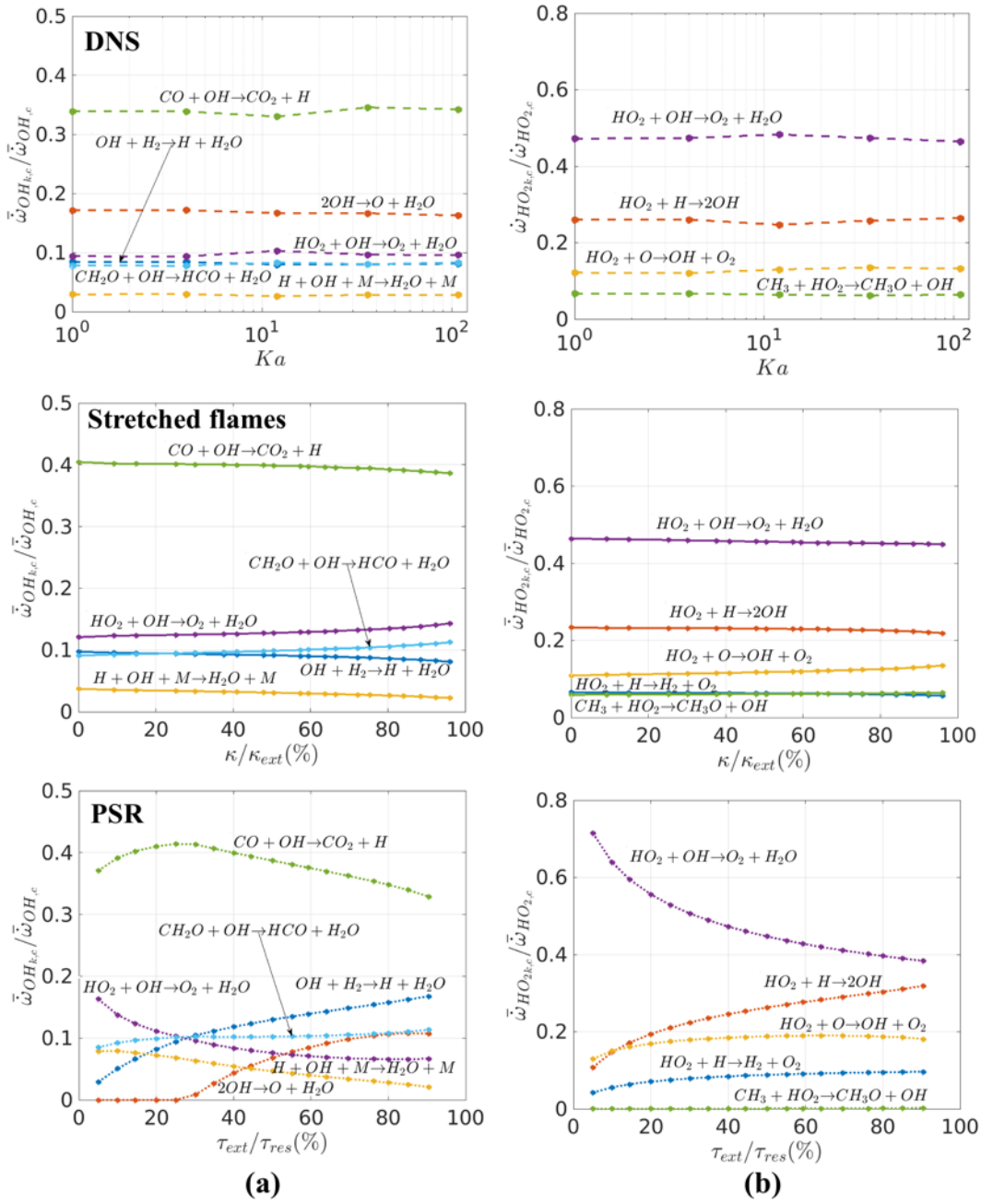

Figure 4.32. Variation of normalized consumption rates for (a) OH and (b) HO_2 with increasing turbulence intensities (left), increasing stretch(center) and decreasing residence time(right).

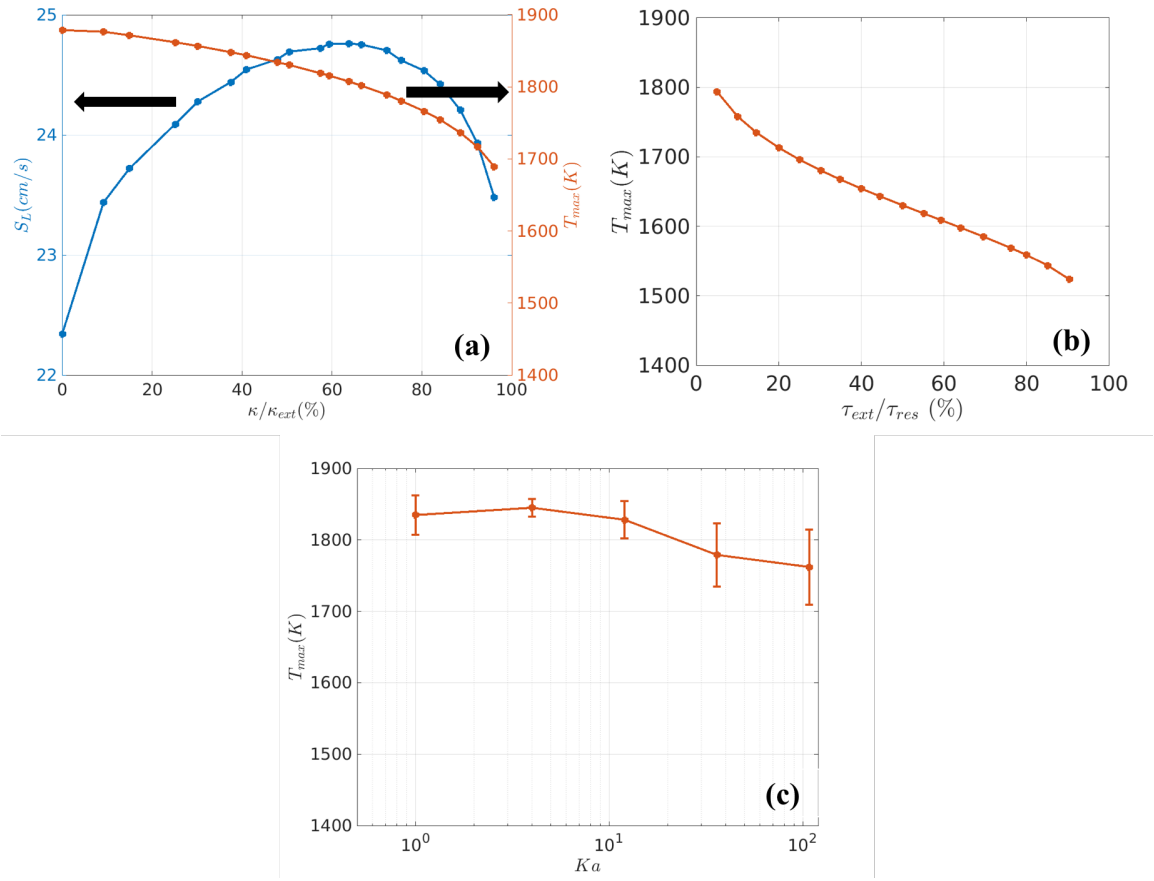

Figure 4.33. (a) Flame speed and maximum temperature variation with increasing stretch rates obtained from OPPDIF(left) (b) max maximum temperature variation with decreasing residence time and (c) maximum temperature variation with increasing turbulence intensities for DNS calculation, ϕ=0.7 n-dodecane/air, T^u=298K, p=1atm.for $\emptyset = 0.7$, T^u=298K, p=1atm.

4.4.4 Global analysis conditioned on curvature

This section focuses on curvature conditioning of the integrated metrics discussed above. Five different topological regions (concave/convex spherical elements, concave/convex cylindrical elements, and saddle points) conditioned on the two principal

components of curvature, $\mathbb{k}_1$ and $\mathbb{k}_2$ are defined. Figure 4.34 below plots the fractional contribution of the different elements to the net heat release.

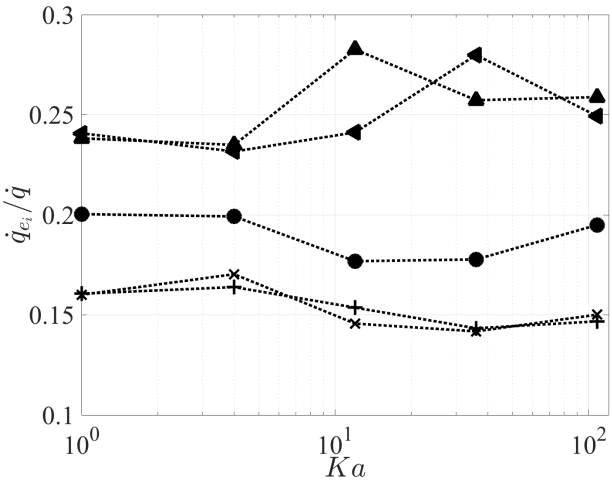

Figure 4.34. Variation of fractional heat release within each element with Karlovitz number. (.▲:Spherical negatively curved, .◀:Cylindrical negatively curved, .●:Saddle points, +:Spherical positively curved, .x: Cylindrical positively curved)

It can be observed that most of the heat release occurs in the negatively curved regions, as expected for this reactant mixture, where *Le*>1 and where burning is enhanced in negatively curved regions. Aspden et al.[68] showed a higher concentration of key species in these regions which in turn leads to increased reaction rates.

Figure 4.35 below plots the fraction heat release contribution of different reactions in each element. The heat release by a reaction is normalized by the total heat release within a certain element. It can be seen that the same reactions dominate the heat release in all 5 elements. The most dominant reaction changes from CO+OH→CO_2+H to HO_2+OH→O_2+H_2O in the positively curved elements with increasing turbulence intensities. Slices of reaction rates suggest a broadened region of reaction rate for CO+OH→CO_2+H which leads to lower overall values of the reaction rates and hence heat

release whereas the reaction $HO_2+OH \rightarrow O_2+H_2O$ occurs in a thin region. This leads to a lowered contribution of the CO_2 formation reaction to the net heat release with increasing turbulence intensities. The most significant change is seen for the reaction $H+OH+M \rightarrow H_2O+M$ with a decrease in contribution of ~50% in the positively curved elements. $H+O_2(+M) \rightarrow HO_2(+M)$ and $HCO+O_2 \rightarrow CO+HO_2$ change by ~40% with increasing turbulence intensities. Additionally, we note the growing contribution of the reaction $CH_2O+OH \rightarrow HCO+H_2O$ in these elements. This reaction has a higher heat release contribution than $H+O_2(+M) \rightarrow HO_2(+M)$ and $H+OH+M \rightarrow H_2O+M$ at higher turbulence intensities suggesting a slight alteration of the heat release pathway at higher Ka for the positively curved elements. One can also note a comparable heat release contribution of the reactions $CH_3+O \rightarrow CH_2O+H$ and $HCO+O_2 \rightarrow CO+HO_2$ to the dominant reactions at a high Ka. These reactions have a relatively lower contribution at lower Ka.

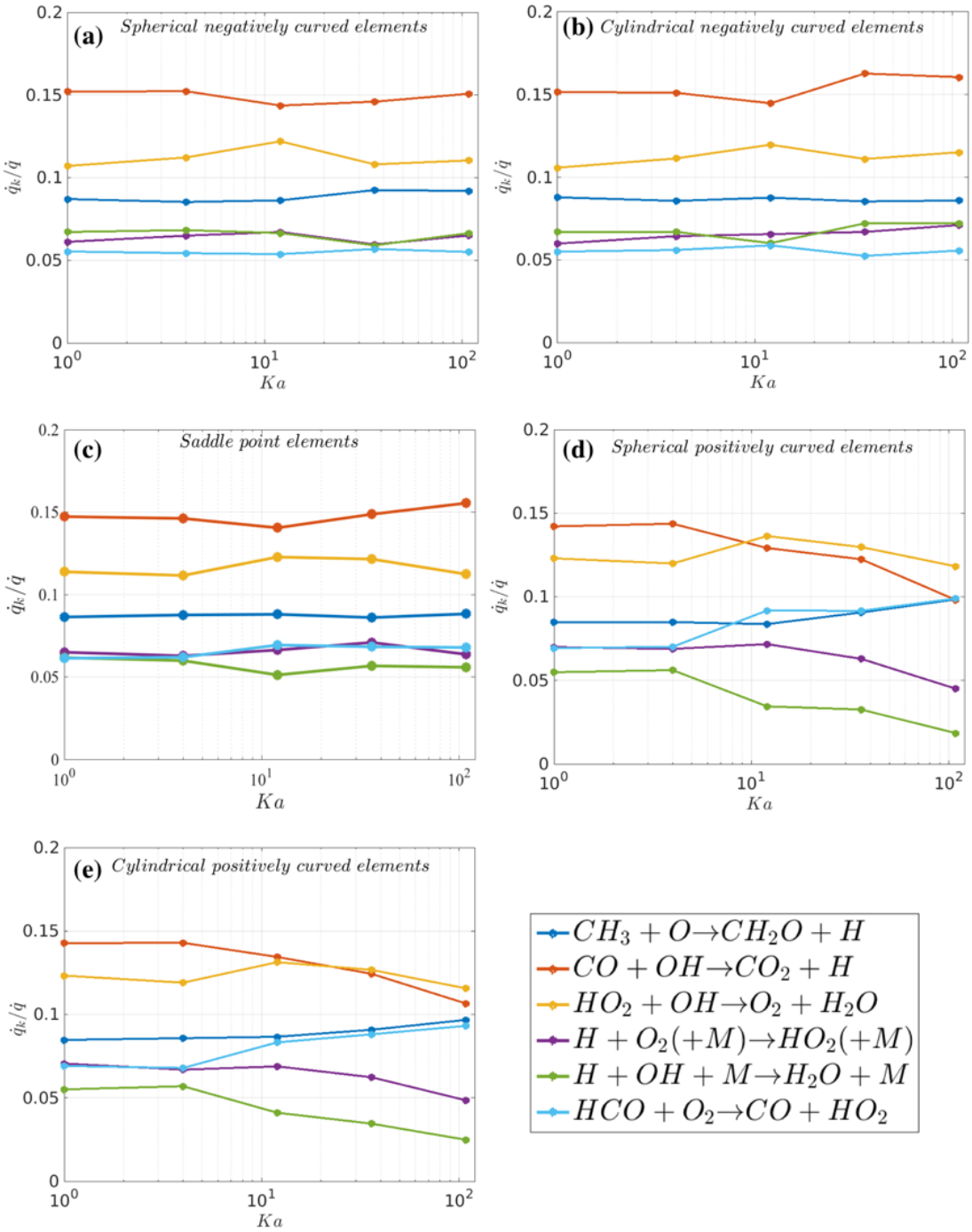

Figure 4.35. Normalized heat release by the dominant reactions in (a) Spherical negatively curved elements (b) Cylindrical negatively curved (c) Saddle point elements (d) Spherical positively curved (e) Cylindrical positively curved elements.

The contribution of the reactions in the negatively curved regions and saddle point elements behave similar to its global counter-part. For example, the contribution of the reaction $CO+OH \rightarrow CO_2+H$ changes by ~6% for the global characteristics and for these three elements.

Figure 4.36 below plots the normalized rate of consumption/production of certain key species. The same dominant reactions for HCO can be observed in Figure 4.36(a). For HCO consumption, it can be noted that $HCO+O_2 \rightarrow CO+HO_2$ is the dominant HCO consuming reaction in the positively curved elements (Figure 4.36 (a, left)) followed by $HCO+M \rightarrow H+CO+M$. The contribution of $HCO+O_2 \rightarrow CO+HO_2$ increases by ~25% with increasing turbulence intensities whereas the contribution of $HCO+M \rightarrow H+CO+M$ decreased by ~25%. The same two reactions are observed for the negatively curved elements and saddle point elements (Figure 4.36 (a, right)). The order of the dominant reactions is reversed for these elements with limited sensitivity to increasing turbulence intensities. For OH we can observe changes in the contributions of the secondary reactions with increasing turbulence intensities for the positively curved elements (Figure 4.36 (b, left)). The consumption of OH by $CO+OH \rightarrow CO_2+H$ decreases by ~15% with increasing turbulence intensities. At higher turbulence intensities, the reactions $HO_2+OH \rightarrow H_2O+O_2$, $OH+H_2 \rightarrow H_2O+H$ and $CH_2O+OH \rightarrow HCO+H_2O$ have a higher consumption rate than $2OH \rightarrow H_2O+O$ which is the second dominant OH consumer at lower turbulence intensities. The contributions of these reactions do not change significantly for the negatively curved and saddle point elements (Figure 4.36 (b, right)).

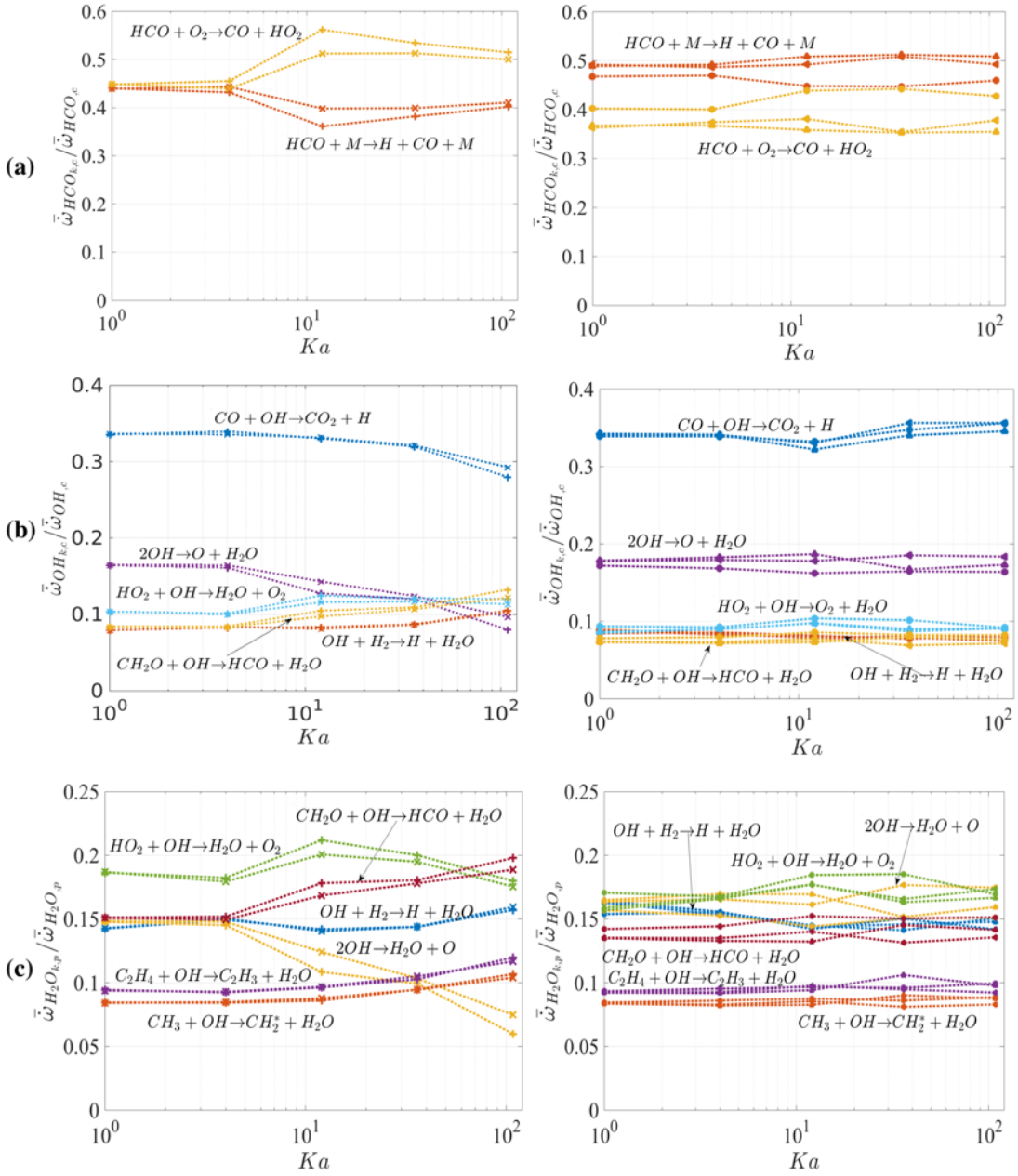

Figure 4.36. Normalized species consumption by the dominant reactions for (a) HCO consumption (b) OH consumption (c) H_2O productions. (.▲:Spherical negatively curved, .◀:Cylindrical negatively curved, .●:Saddle points, +:Spherical positively curved, .x: Cylindrical positively curved).

The pathways for water formation, one of the key products in hydrocarbon combustion, are strongly affected with increasing turbulence intensities for the positively curved elements (Figure 4.36(c, left)). For example, $CH_2O+OH \rightarrow HCO+H_2O$ takes over as the dominant H_2O producing reaction from $HO_2+OH \rightarrow H_2O+O_2$ at higher turbulence intensities. Also, the reactions $C_2H_4+OH \rightarrow C_2H_3+H_2O$ and $CH_3+OH \rightarrow CH_2^*+H_2O$ have a higher contribution to H_2O production than $2OH \rightarrow H_2O+O$ with increasing Ka. These contributions are increased by ~25% from Ka=1 to Ka=108. Other species such as HO_2, CH_3 show limited sensitivity to turbulence and curvature. Figure 4.37 plots the normalized contributions to certain other key species consumption by different reactions.

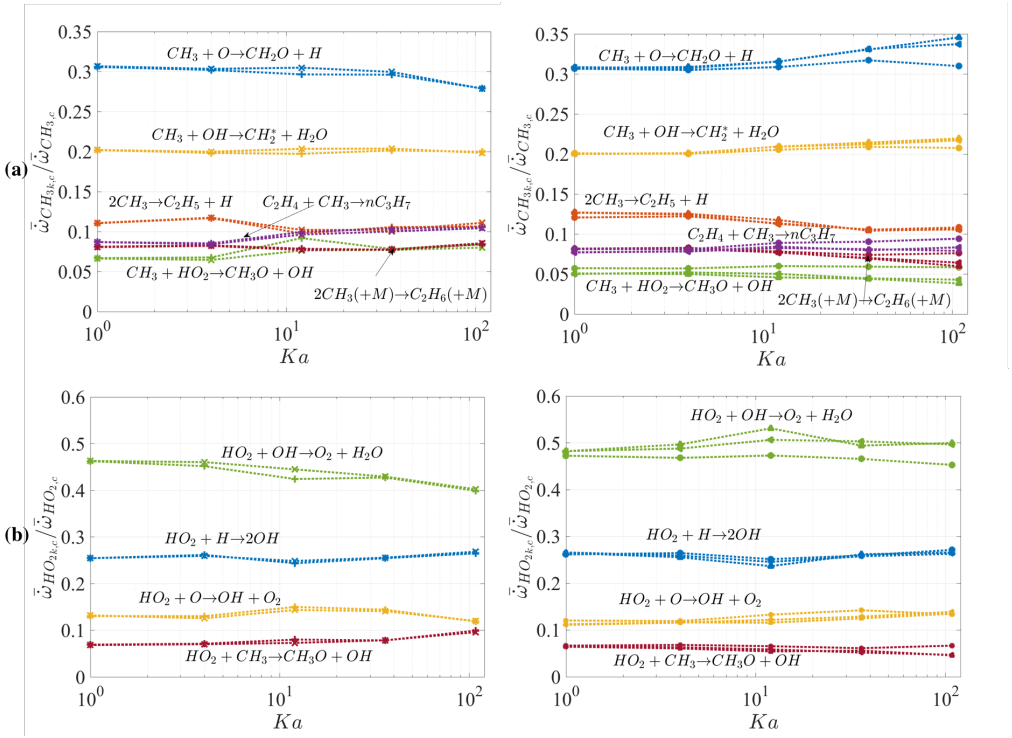

Figure 4.37. Normalized species consumption by the dominant reactions for (a) CH_3 consumption (b) HO_2 consumption. (.▲:Spherical negatively curved, .◄:Cylindrical negatively curved, .●:Saddle points, +:Spherical positively curved, .x: Cylindrical positively curved).

The dominant reactions for CH_3 consumption show limited sensitivity to increasing turbulence intensity (Figure 4.37(a)). The reactions of secondary importance for CH_3 consumption include recombination reactions. At higher turbulence intensities, $C_2H_4+CH_3 \rightarrow nC_3H_7$ has a comparable consumption rate compared to $2CH_3 \rightarrow C_2H_5+H$ for the positively curved elements. We do not observe these changes for the negatively curved elements (Figure A1(a, right)). The limited sensitivity of the HO_2 consumption reactions to increasing turbulence intensities and curvature is evident in Figure 4.37(b).

Overall, the reactions in the positively curved elements show a stronger sensitivity with increasing turbulence intensities compared to the negatively curved elements and saddle point elements.

4.4.5 Global analysis conditioned on progress variable

Figure 4.38 below plots the fractional contribution of the dominant reactions to the total heat release at a given progress variable. It is clear from Figure 4.38 that the same dominant heat release reactions show up at different progress variables. At the leading edge of the flame, i.e. $\bar{c} = 0.1$(in Figure 4.38(a)), the variations in the reactions with increasing Ka are the most significant. At higher Karlovitz numbers, the reaction $HO_2+OH \rightarrow O_2+H_2O$ takes over as the most dominant reaction from $CO+OH \rightarrow CO_2+H$. The heat release contributions of $H+O_2(+M) \rightarrow HO_2(+M)$ and $H+OH+M \rightarrow H_2O+M$ are attenuated by ~50% with increasing turbulence intensity. Additionally, the contribution of the reaction $HCO+O_2 \rightarrow CO+HO_2$ increases by ~35% with increasing turbulence intensities compared to a ~1% change for the global characteristics. The heat release variations for the reactions at the other progress variables (Figure 4.38(b), (c) and (d)), namely $\bar{c} = 0.3, 0.5, 0.7$, is

similar to its global counter-part. For example, the reaction CO+OH→CO_2+H changes by ~6% for the global characteristics. This change is between ~1-6% for the progress variables away from the leading edge of the flame. Similarly, the change in the reaction CH_3+O→CH_2O+H is ~1-2% for the global behavior and these progress variables.

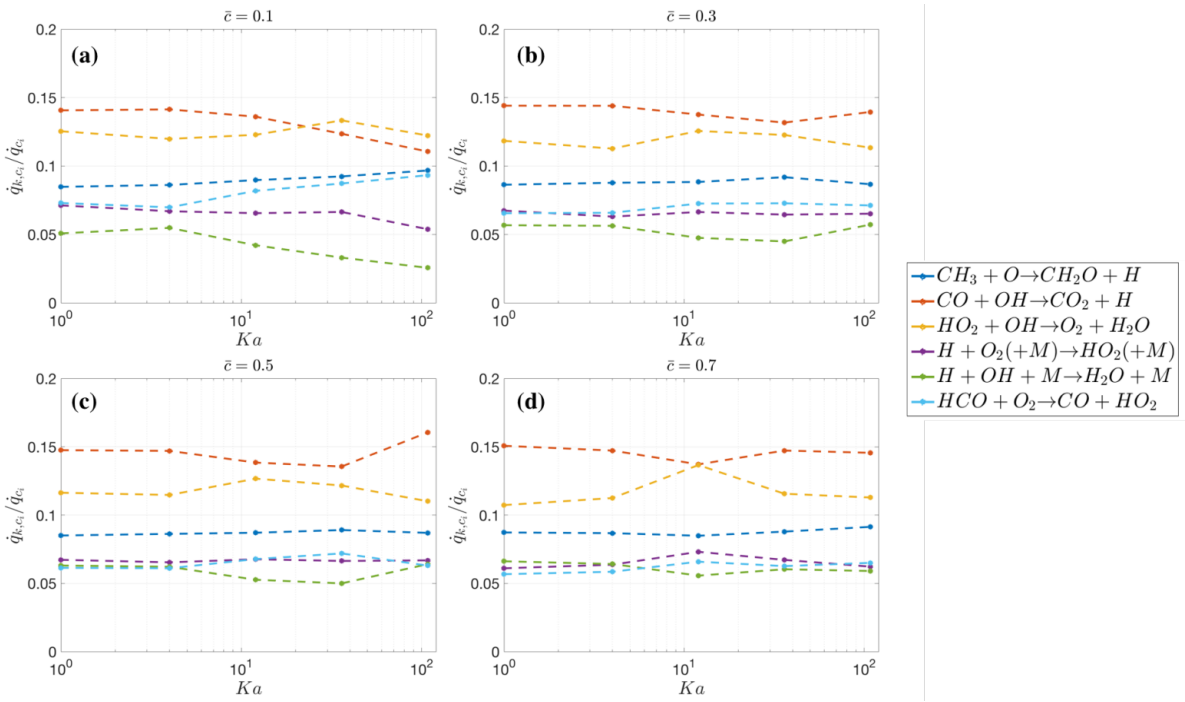

Figure 4.38. Normalized heat release by different reactions at (a) $\bar{c} = 0.1$ (b) $\bar{c} = 0.3$ (c) $\bar{c} = 0.5$ (d) $\bar{c} = 0.7$.

The individual behavior of the reactions at different progress variables are considered and compared with their laminar counterpart. Figure 4.39 shows the variation of the key reactions at different progress variables with increasing turbulence intensities. The quantitative contributions of the reactions are close to the stretched flame calculations. However, certain reactions are relatively better represented than the others. For example, the contribution of the reactions CO+OH→CO_2+H, HO_2+OH→O_2+H_2O and

$H+O_2(+M)\rightarrow HO_2(+M)$ fall outside the bounds of the laminar calculations whereas $CH_3+O\rightarrow CH_2O+H$, $H+OH+M\rightarrow H_2O+M$ and $HCO+O_2\rightarrow CO+HO_2$ are closer to the laminar bounds. The y-axis for the plots covers a relatively small range and hence the changes in variations across the progress variables is of the order of ~10-15% with the maximum change of the order of ~30% for all the reactions. In general, similar to our previous observation, the reactions at $\bar{c} = 0.1$ behave differently compared to other progress variables. For example, the reaction $CO+OH\rightarrow CO_2+H$ shows a ~20% decrease in contribution with increasing Ka at the leading edge whereas it shows a modest change of ~5% for the other progress variables and the global behavior. This stronger increase or decrease in contributions with increasing turbulence intensities at $\bar{c} = 0.1$ can be observed for the others reactions as well such as $HCO+O_2\rightarrow CO+HO_2$ and $H+OH+M\rightarrow H_2O+M$.

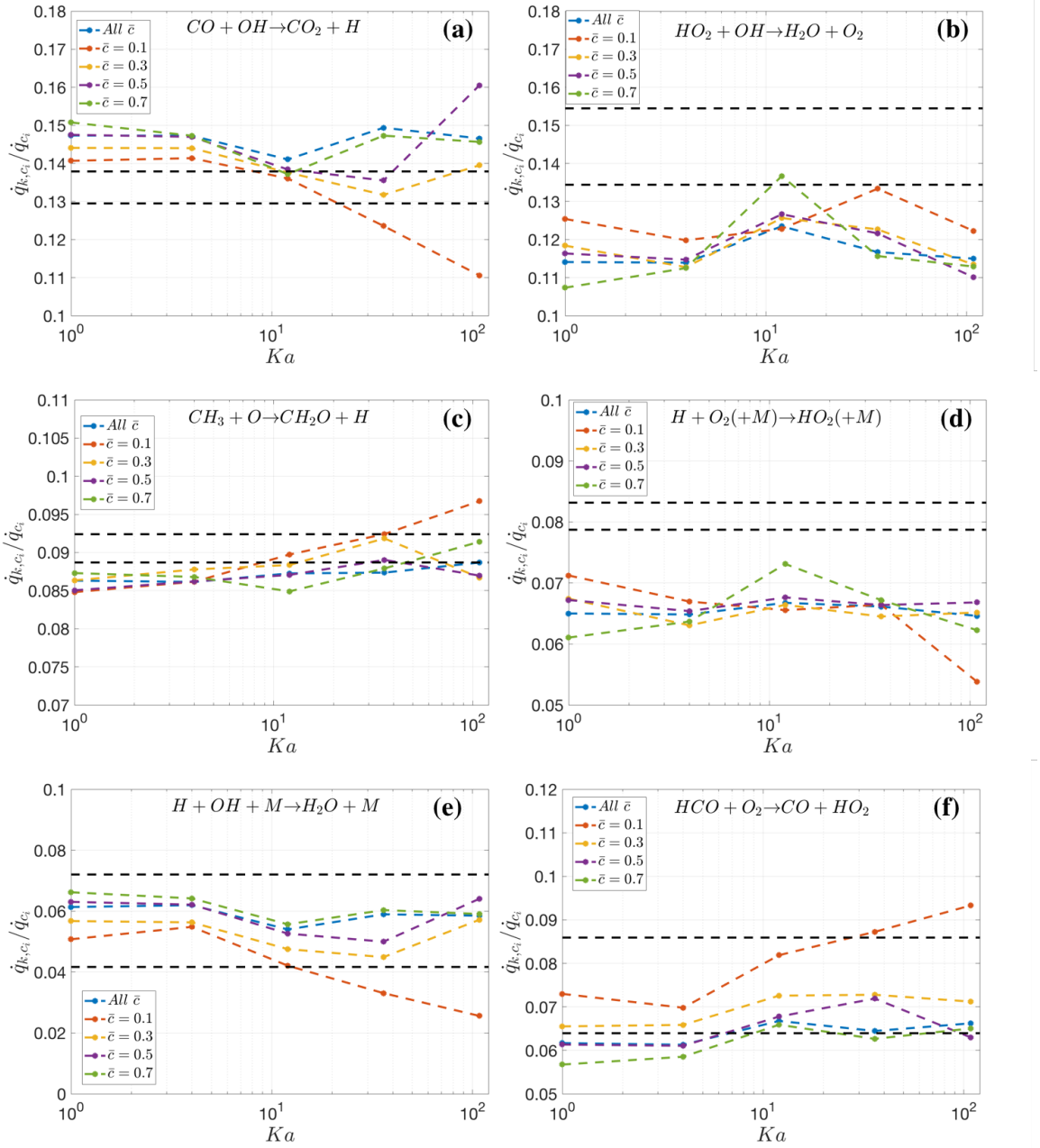

Figure 4.39. Progress variable conditioned heat release for (a)CO+OH→CO_2+H (b)HO_2+OH→O_2+H_2O (c)CH_3+O→CH_2O+H (d)H+O_2(+M)→HO_2(+M) (e)H+OH+M→H_2O+M (f)HCO+O_2→CO+HO_2 ; (Blue: All $\bar{c}$, Orange: $\bar{c}$ = 0.1, Yellow: $\bar{c}$ = 0.3, Purple: $\bar{c}$ = 0.5, Green: $\bar{c}$ = 0.7). Dashed horizontal lines denote range of values from OPPDIF calculations.

Figure 4.40 plots the normalized rates for HCO consumption, OH consumption and H_2O production. At $\bar{c} = 0.1$, the dominant HCO consuming reaction is $HCO+O_2 \rightarrow CO+HO_2$ followed by $HCO+M \rightarrow H+CO+M$. This observation is in line with our observation for the positively curved elements. The ordering of the reactions is flipped for $\bar{c} = 0.7$ similar to our observation for the global properties and the negatively curved conditions. The dominant OH consuming reaction does not change between the different progress variables. The reactions of secondary importance change with increasing turbulence intensities for $\bar{c}$=0.1. For example, the OH consumption by the reaction $2OH \rightarrow O+H_2O$ is comparable to the other secondary reactions at Ka=108. However, this reaction consumes twice as much OH compared with the other reactions at lower turbulence intensities. Pathways for water formation have a stronger sensitivity to turbulence at progress variables closer to the leading edge of the flame compared to the other progress variables. For example, the H_2O production by the reaction $2OH \rightarrow O+H_2O$ decreases by ~50% and by the reaction $CH_2O+OH \rightarrow HCO+H_2O$ increases by ~35% with increasing Ka. These numbers for the other $\bar{c}$ is ~5% for both the reactions.

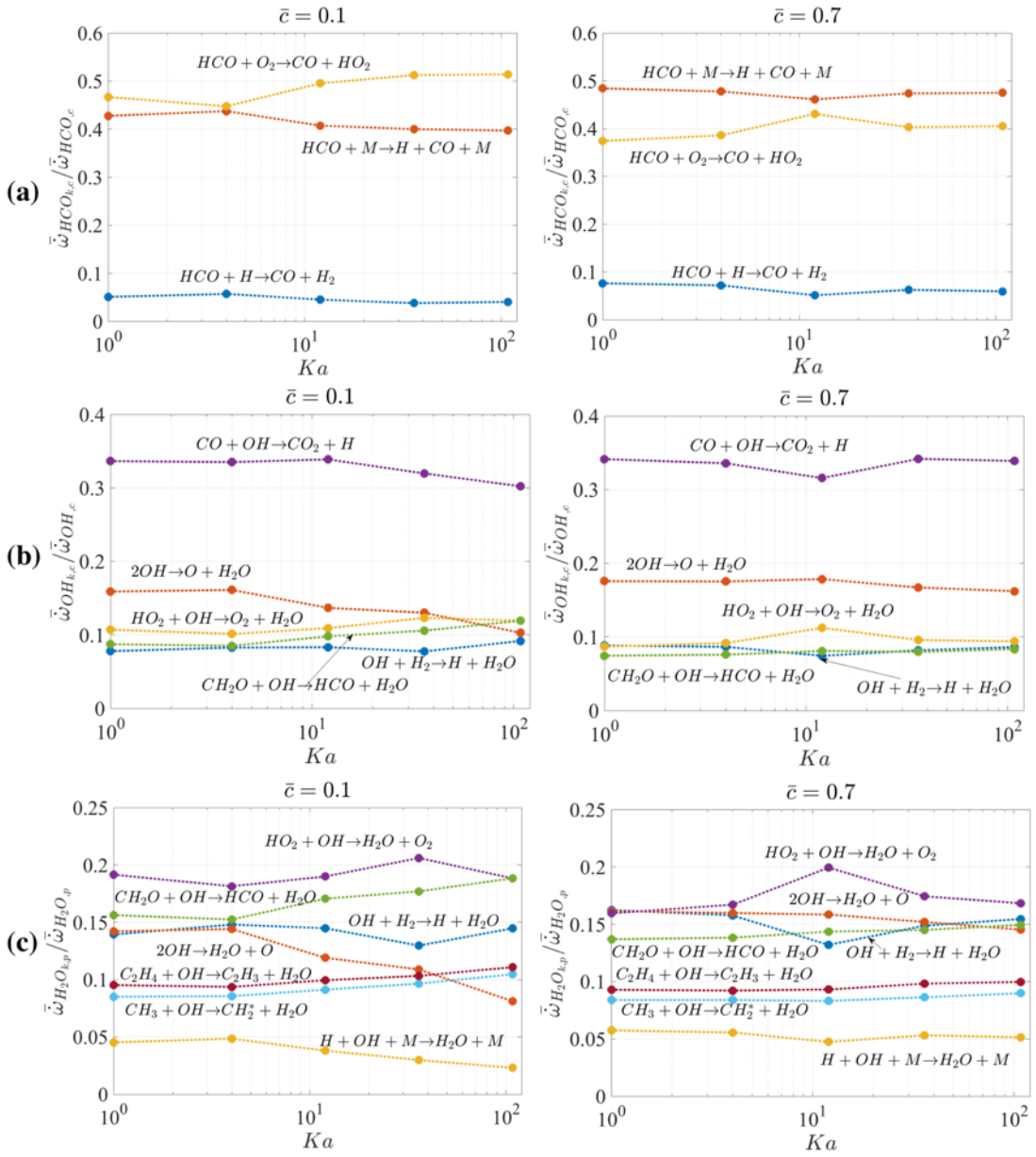

Figure 4.40. Normalized contribution of reactions for (a) HCO consumption (b) OH consumption (c) H_2O production for $\bar{c} = 0.1$ (left), 0.7 (right)

The dominant reactions for CH_3 consumption do not change between the different progress variables as seen in Figure 4.41(b). The reactions of secondary importance have varied contributions at higher turbulence intensities for $\bar{c} = 0.1$. For example, the reaction, C_2H_4+CH_3→nC_3H_7 has a higher rate of consumption at higher turbulence intensities

compared to $2CH_3 \rightarrow C_2H_5+H$. Reactions involved in HO_2 consumption show limited sensitivity to increasing Ka and remain consistent across all the progress variables as seen in Figure 4.41(a).

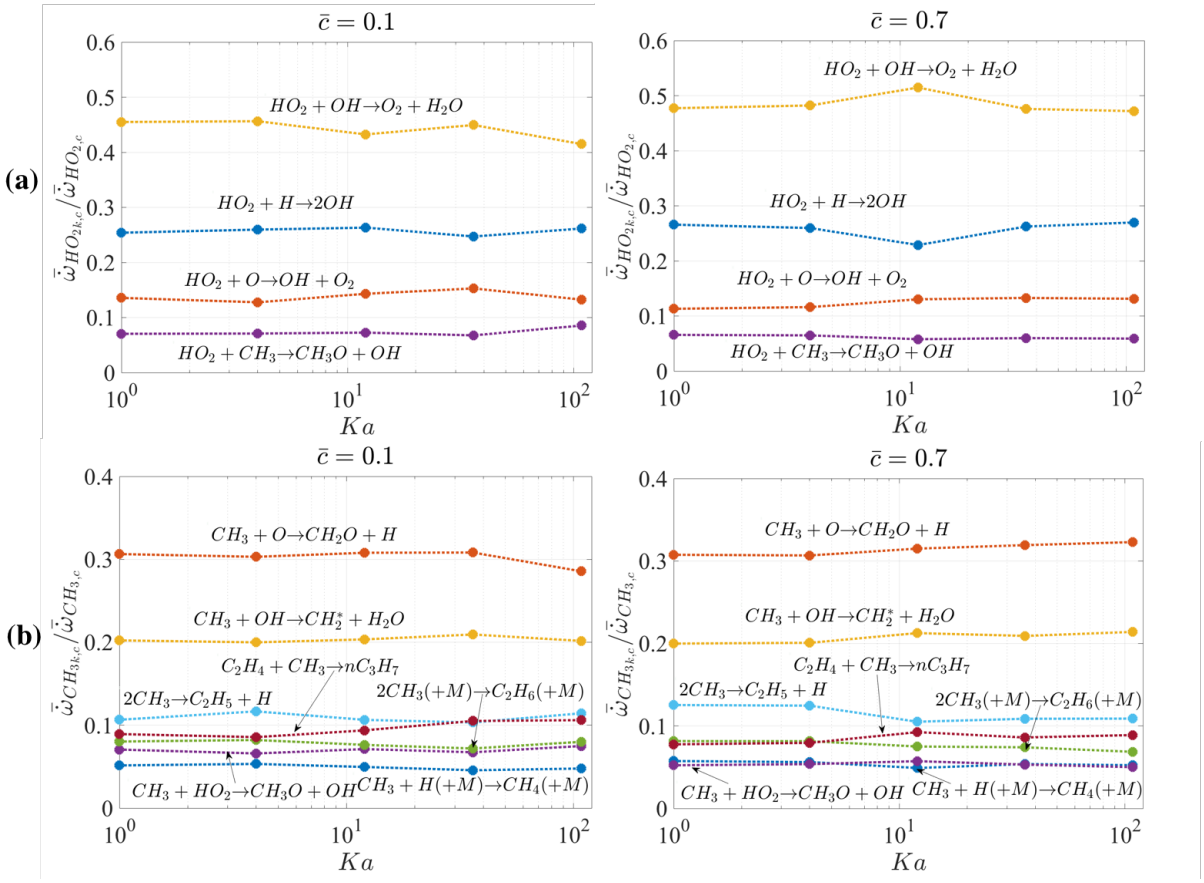

Figure 4.41. Normalized species consumption by different reactions for (a) HO_2 (b) CH_3 for $\bar{c} = 0.1$ (left), 0.7(right).

Overall, we see a stronger dependence of the reactions on Ka for progress variables closer to the leading edge of the flame compared to the rest of the flame. The behavior of the reactions at the other progress variables is closer to the global characteristics and are relatively insensitive to turbulence.

4.5 Conclusions

This chapter discusses modifications to the chemical pathways of lean premixed flames due to turbulence for three different fuels. The results are compared with counter flow flames and perfectly stirred reactors.

It is found that for hydrogen/air flames the spatially integrated contributions of several key reactions to heat release, as well as H, OH, and HO_2 consumption, remain qualitatively similar between a highly turbulent and a steady unstretched flame configurations. For example, the contribution of the dominant exothermic reaction, $H+O_2+M \rightarrow HO_2+M$, to the heat release changes by about 20% between the unstretched, laminar flame and the *Ka*=36 turbulent flame. The importance of the $H+OH+M \rightarrow H_2O+M$ reaction roughly doubles, which is a substantial effect, but its overall contribution to the heat release is only 1/2 to 1/3 of the most exothermic reaction. The dominant heat release reaction is also the dominant consumer of the H radical. However, it shows a decreased consumption from the laminar unstretched case to the *Ka*=36 case. The most significant change between the steady and turbulent cases is associated with the HO_2 consumption by the reaction $HO_2+H \rightarrow OH+OH$, showing an increase by 40%. Its heat release shows minimal changes with increasing *Ka*. Similarly, analysis of the chemical pathways for progress-variable-conditioned results showed strong similarities between the steady unstretched cases and turbulent cases. The largest differences are seen near the leading edge of the brush, at $\bar{c}$=0.1, but even here the relative importance of the dominant exothermic reaction changes by 5% from *Ka*=1 to *Ka*=36. The key implication suggests

that the kinetics of highly turbulent, lean premixed hydrogen-air flames is not markedly different from their steady, unstretched 1D counterparts.

The results for methane/air flames is consistent with the hydrogen/air analysis - namely that the fractional contribution of the dominant heat release reactions changes relatively little between laminar flames and highly turbulent ones; e.g., $O+CH_3 \rightarrow CH_2O+H$ accounts for ~14% of the total heat release and shows limited variation with increasing turbulence intensities. The CO_2 formation reaction of $OH+CO \rightarrow H+CO_2$ contributes about ~12% to the total heat release increasing by ~9% with increasing turbulence. The hydrogen chemistry reactions of $H+O_2(+M) \rightarrow HO_2(+M)$ and $H_2+OH \rightarrow H_2O+H$ follow next with a contribution of ~8-9% each to the total heat release. These reactions also display the maximum fractional change of ~25-30% between Ka=0 and Ka=36. Similar conclusions apply for key reactions involving C-containing species/radicals. The stretched flame results also mirrored the DNS results for the lower stretch rates for the H-containing species. At higher stretch rates however, some species production reactions, such as those producing HO_2 and OH showed cross-over to different reactions that dominated their consumption or production. For example, the dominant producer of HO_2 shifted from $H+O_2(+M) \rightarrow HO_2(+M)$ to $HCO+O_2 \rightarrow HO_2+CO$ with increasing stretch rates. The curvature conditioned data showed different chemistry behavior in the negatively and positively curved elements, as well as significantly more changes in dominant reactions in the positively curved (spherical and cylindrical elements). For example, a shift from $O+CH_3 \rightarrow CH_2O+H$ to $OH+CO \rightarrow H+CO_2$ was observed from the positively curved to the negatively curved elements. The HO_2 production showed a cross-over from $H+O_2(+M) \rightarrow HO_2(+M)$ to $HCO+O_2 \rightarrow HO_2+CO$ from negatively curved to positively

curved elements. At progress variables closer to the leading edge of the flame, the pathways for key species is similar to highly stretched flames whereas for progress variables away from the leading edge of the flame, the pathways are similar to the global characteristics obtained from DNS.

Finally, the changes in chemical pathways for n-dodecane/air premixed turbulent flames are analyzed wherein the metrics are conditioned on local quantities such as curvature and fuel consumption. It is observed that the fractional contribution of the dominant heat release reactions changes very little with increasing turbulence intensity. For example, the reaction, $CO+OH \rightarrow CO_2+H$, accounts for ~15% of the total heat release, and shows limited variation (~6%) for Ka varying from 0 to 108. The H_2O formation reaction, $HO_2+OH \rightarrow O_2+H_2O$, contributes about ~12% to the total heat release, and increases by ~5% over the same range. Flame slices suggest a stronger effect on the reaction rate of $CO+OH \rightarrow CO_2+H$ compared to $HO_2+OH \rightarrow O_2+H_2O$. In fact, in negatively curved regions at Ka=12, $HO_2+OH \rightarrow O_2+H_2O$ is slightly enhanced compared to it values at Ka=4 whereas a significant variation is seen for $CO+OH \rightarrow CO_2+H$. The DNS results mirror closely those of the stretched flame results. For example, the dominant CH_3-consuming reaction, $CH_3+O \rightarrow CH_2O+H$, is responsible for 65% of the total CH_3 consumption, and changes by ~7% with increasing turbulence intensity. The same reaction changes by ~4% from κ/κ_{ext}=0 to $\kappa/\kappa_{ext} = 0.97$ in the steady stretched flames. reactions to increasing turbulence intensities. For the curvature conditioned results, it is observed that the negatively curved elements and the saddle point element behave similar to their global counterpart. For example, the contribution of the reaction $CO+OH \rightarrow CO_2+H$, which accounts for ~15% of the total heat release, changes by ~6% for the global characteristics

and for these three elements. However, on the other hand more significant changes are observed for the positively curved elements. The most dominant reaction changes from $CO+OH \rightarrow CO_2+H$ to $HO_2+OH \rightarrow O_2+H_2O$ in the positively curved elements with increasing turbulence intensities. The most significant change is seen for the reaction $H+OH+M \rightarrow H_2O+M$ with a decrease in contribution of ~50% in the positively curved elements. A stronger sensitivity of the reaction path for different species is observed in these elements as well. For example, the contribution of the second dominant OH consuming reaction of $2OH \rightarrow H_2O+O$ decreases by ~50% with increasing turbulence intensities whereas for the negatively curved elements it changes by ~5%. Certain species show altered pathway between the different elements. For example, the dominant HCO consuming reaction for the positively curved elements is $HCO+O_2 \rightarrow CO+HO_2$. The dominant reaction changes to $HCO+M \rightarrow H+CO+M$ in the saddle point and negatively curved elements. Progress variable based conditioning reveals a slightly different behavior at $\bar{c}$ closer to the leading edge of the flame compared to the rest of the flame. The reaction $HO_2+OH \rightarrow O_2+H_2O$ takes over as the most dominant reaction from $CO+OH \rightarrow CO_2+H$ with increasing turbulence intensities and a nearly 50% drop in the heat release contributions of the reactions $H+O_2(+M) \rightarrow HO_2(+M)$ and $H+OH+M \rightarrow H_2O+M$ at $\bar{c} = 0.1$. This difference in behavior at $\bar{c} = 0.1$ is also observed when we compare individual reactions at different progress variables. We also observe that some reactions, such as $H+OH+M \rightarrow H_2O+M$ and $CH_3+O \rightarrow CH_2O+H$ are bounded within their laminar maxima and minima. In contrast, reactions such as $CO+OH \rightarrow CO_2+H$, $H+O_2(+M) \rightarrow HO_2(+M)$ lie outside these laminar bounds. However, the difference in their contributions with respect to their laminar counter-part is of the order of ~10-30%. The reactions consuming or

producing the species involved are sensitive to turbulence at progress variables closer to the leading edge of the flame compared to the other progress variables. For example, the contribution of the H_2O producing reaction, $2OH \rightarrow H_2O+O$ drops by ~50% from Ka=1 to Ka=108 for $\bar{c} = 0.1$ and by ~5% for $\bar{c} = 0.3,0.7$.

CHAPTER 5. FLAME STRUCTURE - LOCAL ANALYSIS

Local analysis analyzes the conditional means of reaction rates and species concentration for hydrogen, methane and n-dodecane flames. These are compared with unstretched and stretched laminar calculations to understand the applicability of laminar chemistry and tabulation for turbulent flames.

5.1 Hydrogen

As a first look for hydrogen flames, the fuel consumption rate and heat release for different *Ka* are plotted in Figure 5.1. Unstretched and stretched laminar flames using mixture-averaged and *Le*=1 transport are overlaid. An increase in fuel consumption and heat release with increasing turbulence across all temperatures can clearly be observed. The peak temperature for fuel consumption changes from 1065K at *Ka*=1 to 1135K at *Ka*=36 showing a limited change of 70K. The peak temperature for heat release does not change appreciably with increasing turbulence.

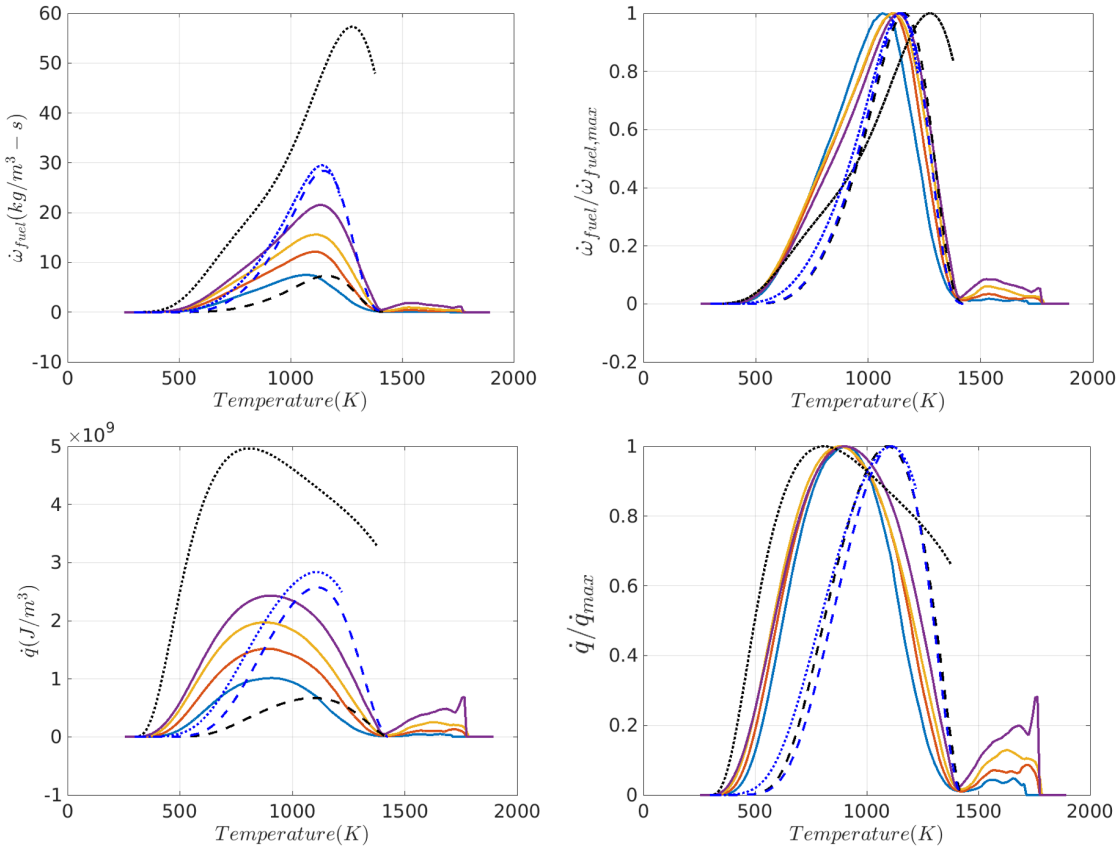

Figure 5.1. Variation of fuel consumption (top, left) normalized fuel consumption (top, right), heat release (bottom, left) and normalized heat release (bottom, right) with temperature for hydrogen/air flames. Black dashed line: Unstretched laminar, Black dotted line: Maximum stretch, Blue dashed line: Unstretched *Le*=1 laminar, Blue dotted line: Stretched *Le*=1 laminar, Blue: *Ka*=1, Orange: *Ka*=4, Yellow: *Ka*=12, Purple: *Ka*=36.

Lean hydrogen flames are susceptible to thermo-diffusive instabilities and hence an unstretched laminar flame for these conditions is a theoretical construct and cannot be realized. This is apparent in the figure wherein the unstretched laminar profile behaves differently compared to the turbulent flame and stretched flame profiles. For example, the unstretched laminar flame profile shows significantly lower fuel consumption and heat release in the low temperature region i.e. T<1000K compared to all the turbulent flames. The stretched flame profile can capture the essential features of turbulent flames i.e.

increasing heat release and fuel consumption across all temperatures with increasing stretch. However, these flames reach a lower equilibrium temperature compared to the adiabatic flame temperature and hence the profiles do not cover the entire expanse of the temperature space. Another feature of lean turbulent hydrogen flames is the appearance of regions of super-adiabatic temperatures due to cellular burning. The adiabatic flame temperature (T_{ad}) for this hydrogen flame is 1426K. Non-zero heat release and fuel consumption can be observed for $T > T_{ad}$. None of the laminar calculations shown here can capture this feature for lean hydrogen flames.

Reaction rates for all the key reactions identified in Section 4.2.3 are plotted in Figure 5.2. The unstretched laminar flame profiles, similar to earlier observation, show a dissimilar behavior compared to the turbulent and stretched flame profiles. Significant increase in reaction rates across all temperatures can be seen for all the reactions. For example, the peak reaction rate for the reaction $HO_2+H \rightarrow OH+OH$ almost triples from Ka=1 to Ka=36.

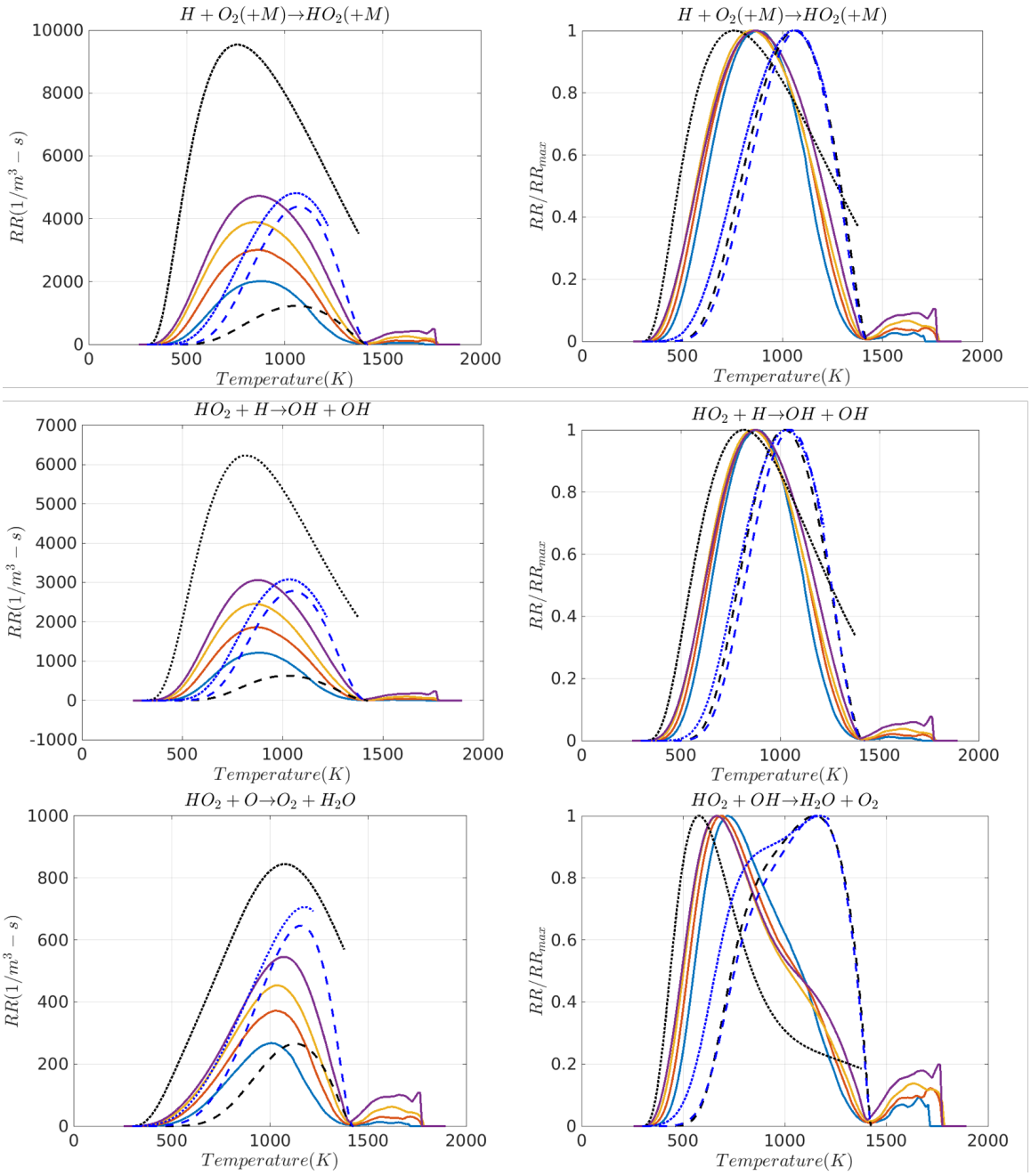

Figure 5.2. Variation of reaction rates (left) and normalized reaction rates (right) for different reactions with temperature for hydrogen flames. Black dashed line: Unstretched laminar, Black dotted line: Maximum stretch, Blue dashed line: Unstretched *Le*=1 laminar, Blue dotted line: Stretched *Le*=1 laminar, Blue: *Ka*=1, Orange: *Ka*=4, Yellow: *Ka*=12, Purple: *Ka*=36.

Additionally, increased rates in the super-adiabatic regions can also be observed. For example, the reaction rate value for the reaction HO_2+O→O_2+H_2O increases from nearly

0 at *Ka*=1 to ~100m^3/s (~20% of the maximum value) at *Ka*=36 for $T > T_{ad}$. This explicit change in reaction rates between *Ka*=1 and *Ka*=36 is shown in Figure 5.3. This change in reaction rate can be interpreted as a measure of the positional shift in the reaction rate profiles in temperature space.

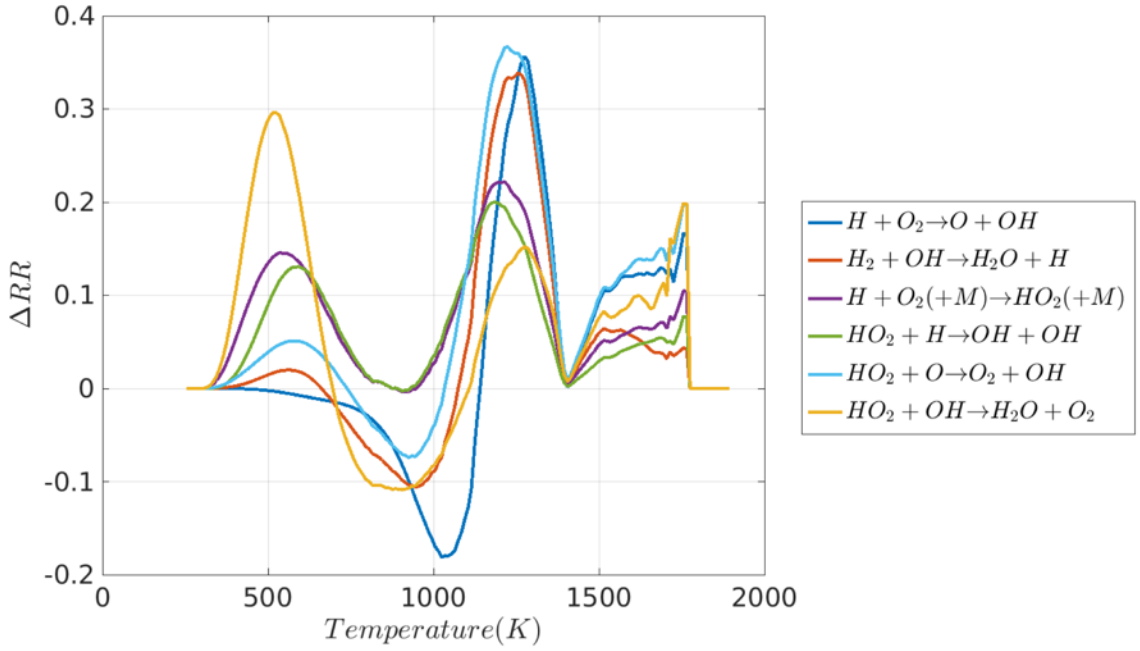

Figure 5.3. Variation of change of reaction rate between *Ka*=1 and *Ka*=36 for different reactions for hydrogen flames.

The reaction rates at *Ka*=36 and *Ka*=1 are normalized by the maximum value of the given reaction's rate at *Ka*=36 and *Ka*=1 respectively. The change in reaction rate (ΔRR) is then calculated by taking the difference of the normalized reaction rate at *Ka*=36 and normalized reaction rate at *Ka*=1. This normalization also removes the effect of increased reaction rates due to larger volumetric burning with increasing turbulence intensity for these lean premixed hydrogen flames. $\Delta RR > 0$ implies increased reaction rate at *Ka*=36 compared to *Ka*=1. All key reactions show a significant increase in reaction rates with

increased turbulence in the low temperature region especially for $T < 800$K. The rates for reactions involving the low temperature radical HO_2, $HO_2+H \rightarrow OH+OH$, $H+O_2(+M) \rightarrow HO_2(+M)$, $HO_2+OH \rightarrow O_2+H_2O$ show a significant increase for $T < 500$K. The peak changes for the other key reactions occur in the higher temperature region i.e. above 1000K. For example, peak ΔRR for $O_2+H \rightarrow O+OH$ and $H_2+OH \rightarrow H+H_2O$ occurs at ~1200K. The relative change in magnitude of the reaction rates in plotted in Figure 5.4.

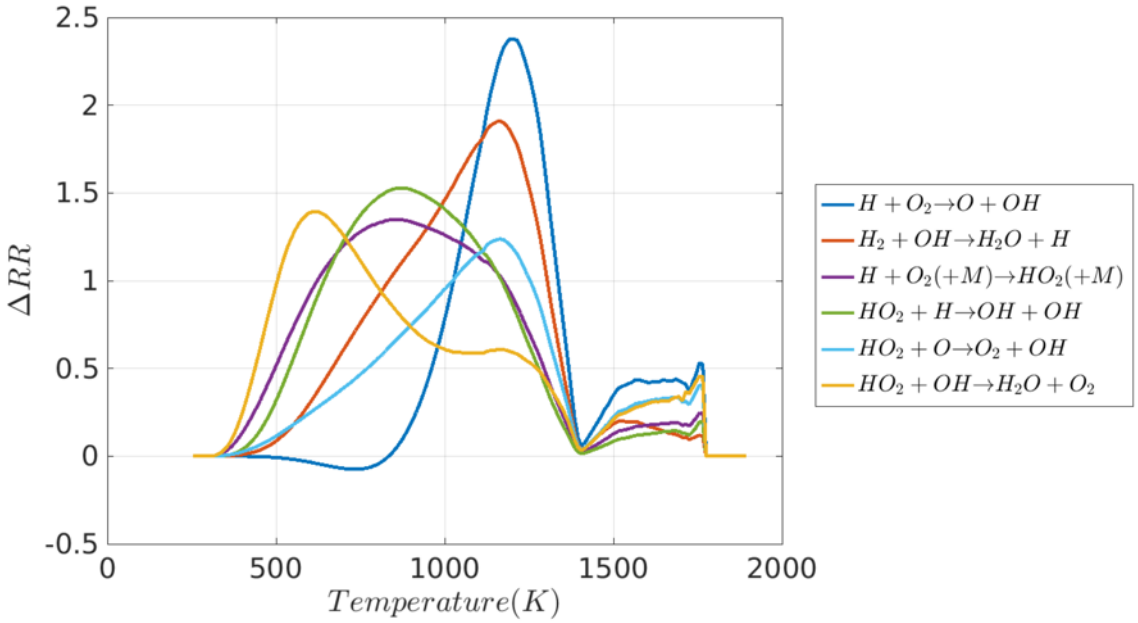

Figure 5.4. Variation of relative difference of reaction rates between *Ka*=1 and *Ka*=36 for different reactions for hydrogen flames.

The change in reaction rate (ΔRR) is calculated by taking the difference of the reaction rate at *Ka*=36 and *Ka*=1 and normalizing this value with the peak value at *Ka*=1. All key reactions show a 1.5-2 times increase in reaction rates with increased turbulence. In general, all reactions are highly sensitive to turbulence with increased rates. Since the reaction rates are a strong function of species concentrations, a plausible explanation for this increase can be attributed to the increased radical pool at lower temperatures. Figure

5.5 plots the conditional means for the concentration of H, HO_2, OH and H_2 for the turbulent, unstretched and stretched flames.

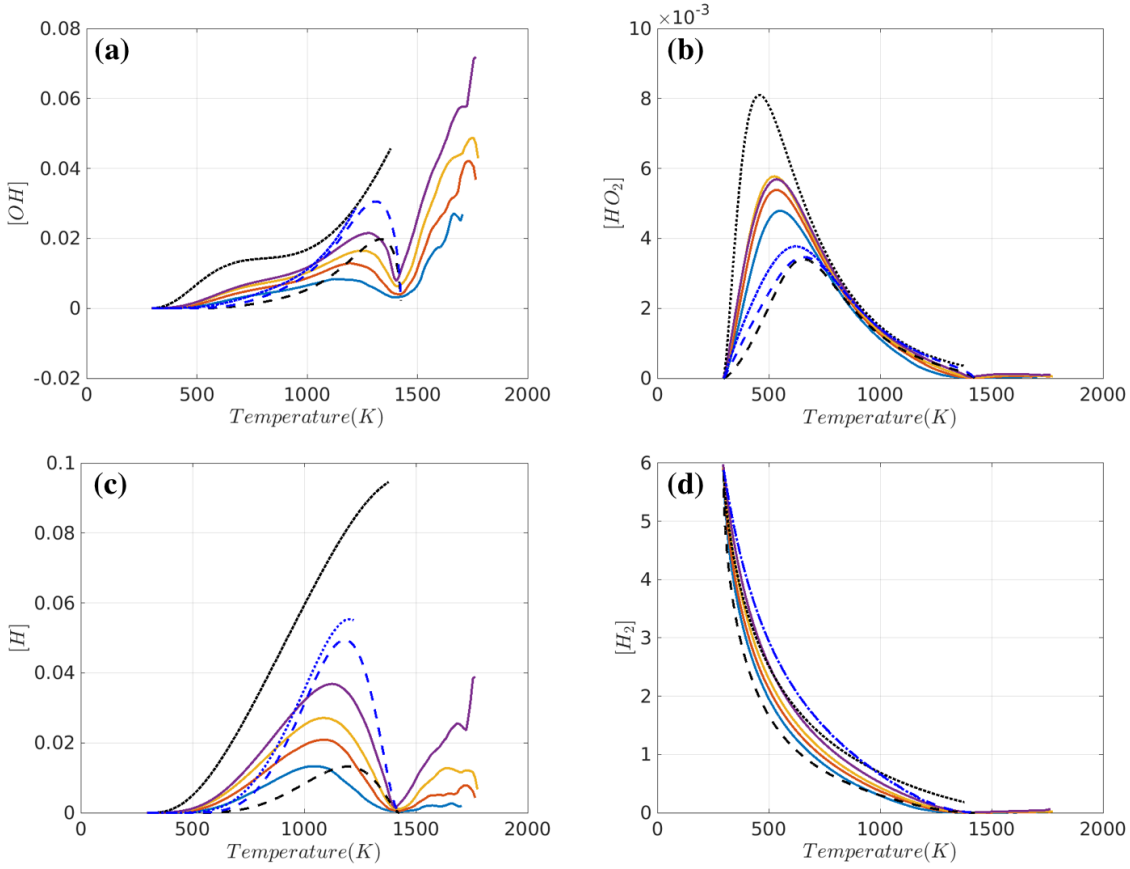

Figure 5.5. Variation of concentration for (a) OH (b) HO_2 (c) H (d) H_2 with temperature. Black dashed line: Unstretched laminar, Black dotted line: Maximum stretch, Blue dashed line: Unstretched *Le*=1 laminar, Blue dotted line: Stretched *Le*=1 laminar, Blue: *Ka*=1, Orange: *Ka*=4, Yellow: *Ka*=12, Purple: *Ka*=36.

For the species shown here, it can be observed that the turbulent flame trends align well with the stretched flame calculations. Increasing stretch leads to increased radical and species concentrations in the low temperature. In the context of turbulent flames, increasing turbulence increases the stretch experienced by the flame. This explains the increased reaction rates of the turbulent flame profiles at lower temperatures similar to that for highly stretched flames.

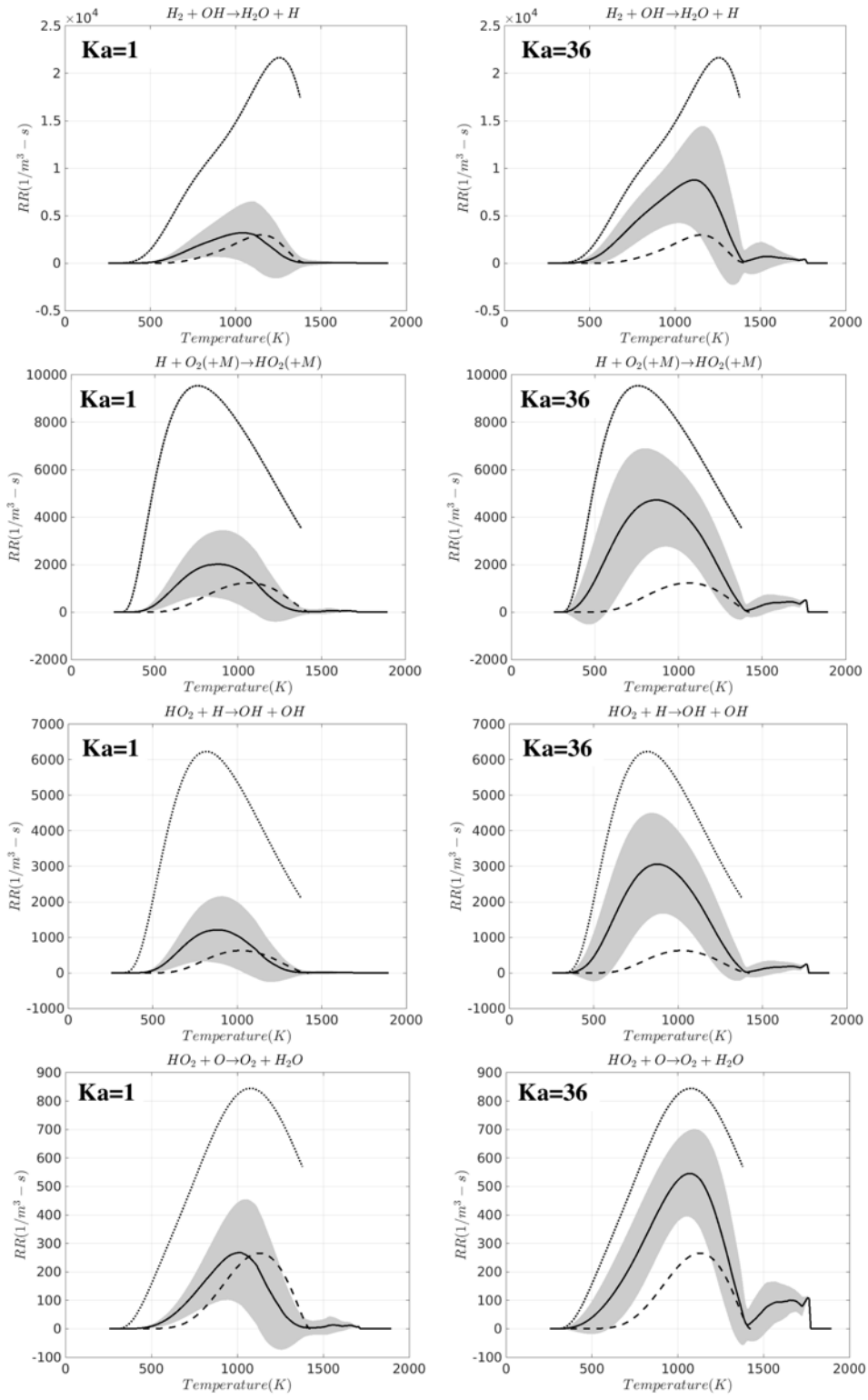

Figure 5.6. Variation of reaction rates with temperature for different Karlovitz number. Black solid line: DNS mean, Black dashed line: Unstretched laminar, Black dotted line: Maximum stretch, Grey region: mean± one standard deviation.

It is imperative to note here that the means are a representation of the behavior of the different quantities such as reaction rates and concentrations and in general for turbulent flames there is a spread in data. Figure 5.6 plots the mean with one standard deviation (denoted by the grey area) around the mean for the *Ka*=1 and *Ka*=36 cases. For *Ka*=36, the highly stretched flame seems to provide an upper bound for the spread in the data. In general, for these thermo-diffusively unstable flames, the standard deviation about the mean is large even for the least turbulent flame i.e. *Ka*=1. For example, for the reaction $H+O_2(+M)\rightarrow HO_2(+M)$, the peak standard deviation is 1.4786×10^3 $1/m^3$-s. At the same temperature, the reaction rate is 1.8755×10^3 $1/m^3$-s and hence the standard deviation is ~80% of the mean. With increasing turbulence intensities, the spread across the mean does not change significantly. For the same reaction at *Ka*=36 the standard deviation and mean are 2.605×10^3 and 3.6135×10^3 respectively leading to a standard deviation that is ~75% of the mean. The spread in data is much lower at lower turbulence intensity cases for the methane and n-dodecane/air flames which will be noted in the subsequent sections.

5.2 Methane

First the heat release rate and the fuel consumption rate for *Ka*=1 and 36 are plotted in Figure 5.7. The laminar profiles for unstretched and maximum stretched flames (i.e. $\kappa/\kappa_{ext} \approx 0.96$) are overlaid on the same plots in Figure 5.7 as well. *Ka*=4 profiles are similar to the *Ka*=1 profiles and hence are not shown here explicitly.

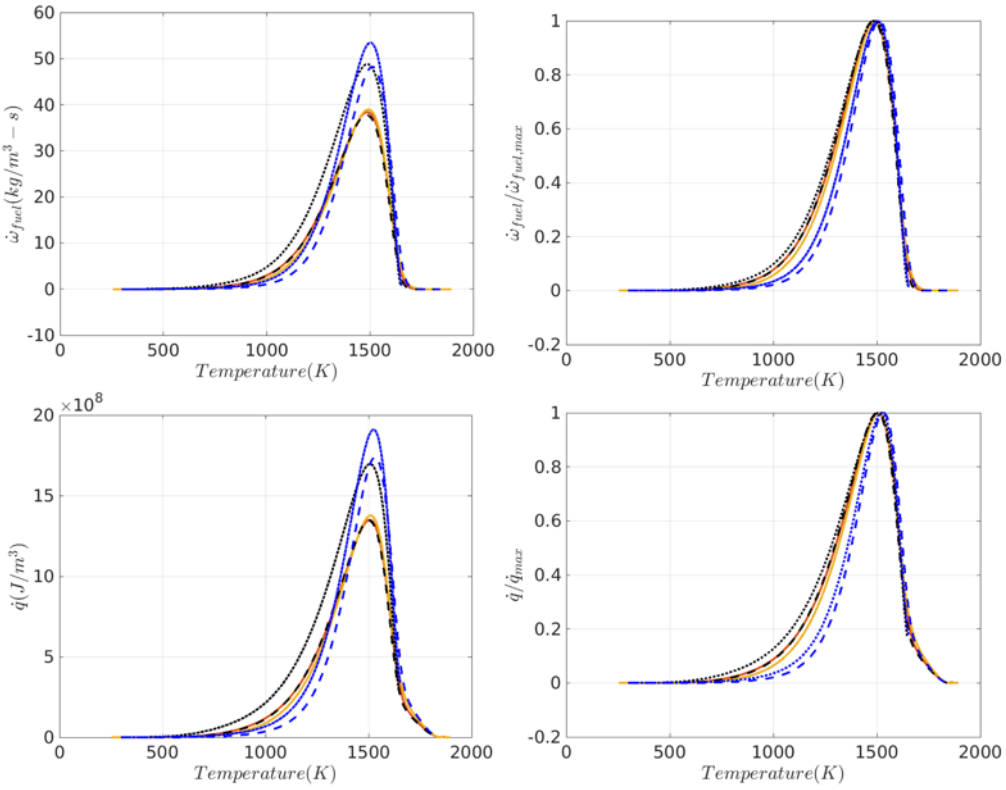

Figure 5.7. Variation of fuel consumption (top, left) normalized fuel consumption (top, right), heat release (bottom, left) and normalized heat release (bottom, right) with temperature for methane/air flames. Black dashed line: Unstretched laminar, Black dotted line: Maximum stretch, Blue dashed line: Unstretched *Le*=1 laminar, Blue dotted line: Stretched *Le*=1 laminar, Orange: *Ka*=1, Yellow: *Ka*=36.

For the turbulence intensities considered here, the conditional means are fairly invariant with increasing turbulence. The conditional mean profiles for both heat release and fuel

consumption are well represented by the unstretched laminar flame profile. The peak temperature for heat release and fuel consumption is 1500K and 1460K for the unstretched laminar flame. These values remain unchanged for the turbulent flame profiles.

Mean reaction rate profiles for key reactions identified in 4.4.3 are plotted in Figure 5.8. The lower turbulence intensities i.e. *Ka*=1 (and 4) align well with the unstretched laminar flame profile for all the reactions. With increasing stretch, the laminar profiles show increased reaction rate at lower temperature (i.e. $T < 1200$K) for all the key reactions. On the other hand, increasing turbulence leads to slightly reduced means at these lower temperatures thus portraying a behavior different from stretched flames. For example, increasing stretch almost doubles the reaction rate at lower temperatures (i.e. below 1200K) for $H+O_2(+M) \rightarrow HO_2(+M)$. However, with increasing turbulence intensities this reaction shows a slight drop in reaction rate at the same temperatures. However, this difference is not significant as the percentage change between the unstretched profile and the *Ka*=36 profile at these lower temperatures is below 5%. Overall, all the turbulent profiles align closely with the unstretched laminar flame profile. In general, all the reactions show very limited sensitivity to increasing turbulence intensities at all temperatures. For example, the maximum change between *Ka*=1 and *Ka*=36 for $OH+CO \rightarrow CO_2+H$ is ~7% at a temperature of ~1600K. The average change across all temperatures for this reaction is ~4%. A higher sensitivity of ~13% is seen for the reaction $H+O_2(+M) \rightarrow HO_2(+M)$ at ~1645K. The dominant heat release reaction of $O+CH_3 \rightarrow CH_2O+H$ remains fairly invariant with increasing turbulence intensities with a maximum change of ~2% across all temperatures.

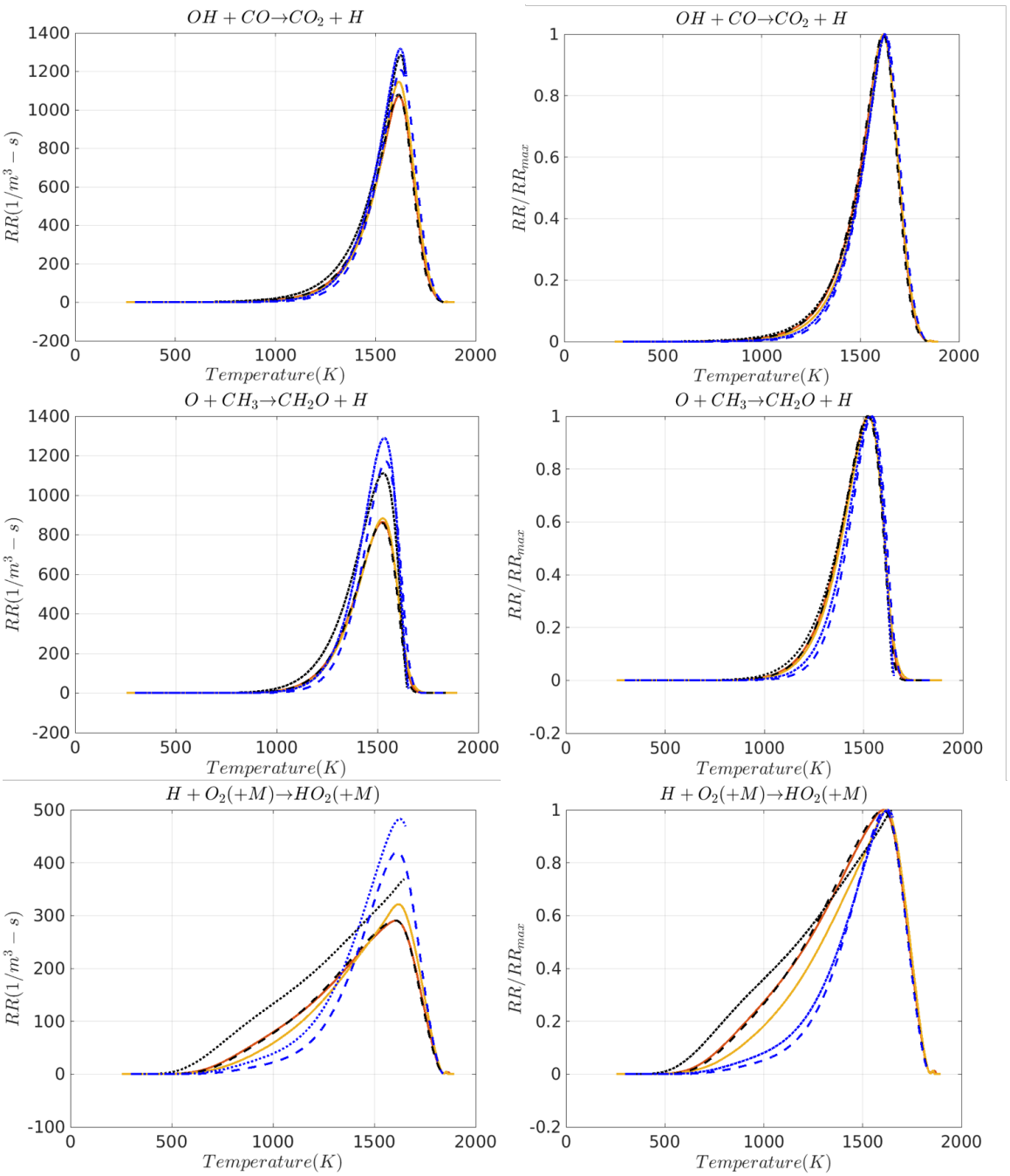

Figure 5.8. Variation of reaction rates (left) and normalized reaction rates (right) for different reactions with temperature. Black dashed line: Unstretched laminar, Black dotted line: Maximum stretch, Blue dashed line: Unstretched *Le*=1 laminar, Blue dotted line: Stretched *Le*=1 laminar, Orange: *Ka*=1, Yellow: *Ka*=36.

To quantify the changes in reaction rates between *Ka*=36 and *Ka*=1, the fractional change of these reaction rates (ΔRR) is calculated by taking the difference between the normalized reaction rates at *Ka*=36 and *Ka*=1. This is plotted in Figure 5.9.

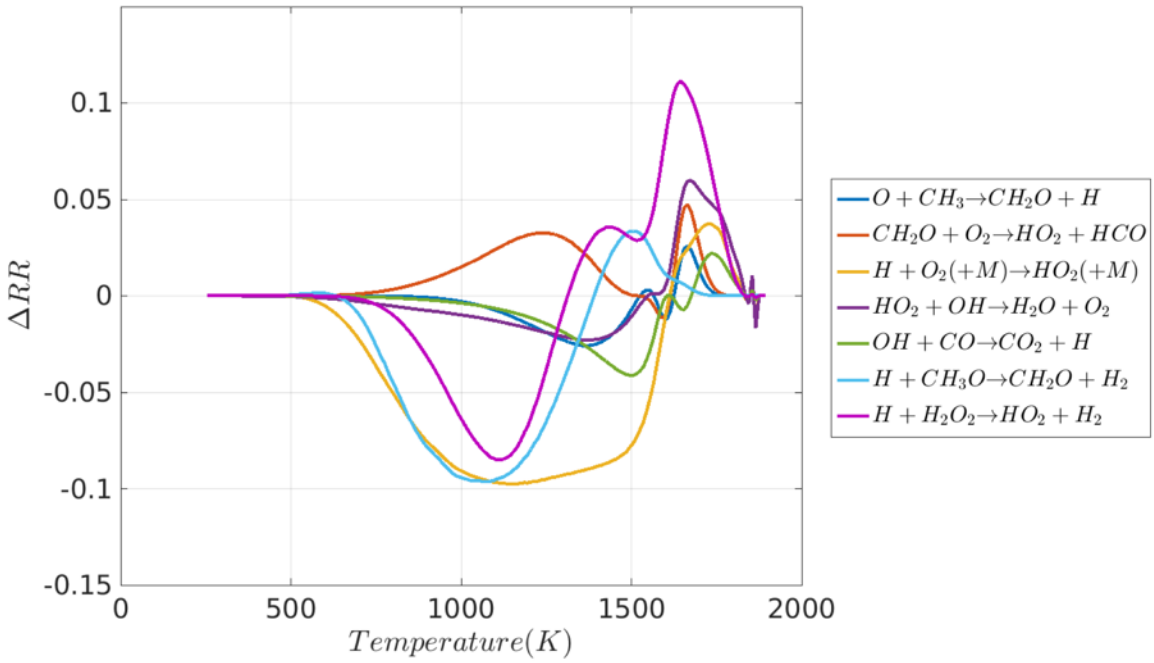

Figure 5.9. Variation of change of reaction between *Ka*=1 and *Ka*=36 for different reactions for methane flames.

The strongest sensitivity is shown by the reaction $H+O_2(+M) \rightarrow HO_2(+M)$ wherein the low temperature reaction rate is reduced by ~10% and the high temperature reaction rate is accentuated by ~4%. All the reactions show increased activity for temperatures greater than 1500K with increased turbulence intensities. Most of the reactions show slightly reduced reaction rates for temperatures less than 1500K. The plot suggests that the HCO forming reaction of $CH_2O+O_2 \rightarrow HCO+HO_2$ shows an increased reaction rate at temperatures less than 1500K. This reaction has a negative reaction rate for T < 1200K. The reaction rate is slightly reduced at these temperatures with increasing turbulence and

hence "less negative" leading to a net positive value for ΔRR. Reactions of secondary importance such as $CH_3O+H \rightarrow CH_2O+H_2$ (a key reaction in the secondary pathway for CH_2O formation) and $H+H_2O_2 \rightarrow HO_2+H_2$ (a key H_2O_2 consuming reaction leading to a secondary pathway for H_2O formation) have a strong response to turbulence which can be seen in Figure 5.9. Both reactions have a lower reaction rate at Ka=36 till T~1400K. Their reaction rates are reduced by ~9-10% in this region. The relative change in magnitude of the reaction rates in plotted in Figure 5.10.

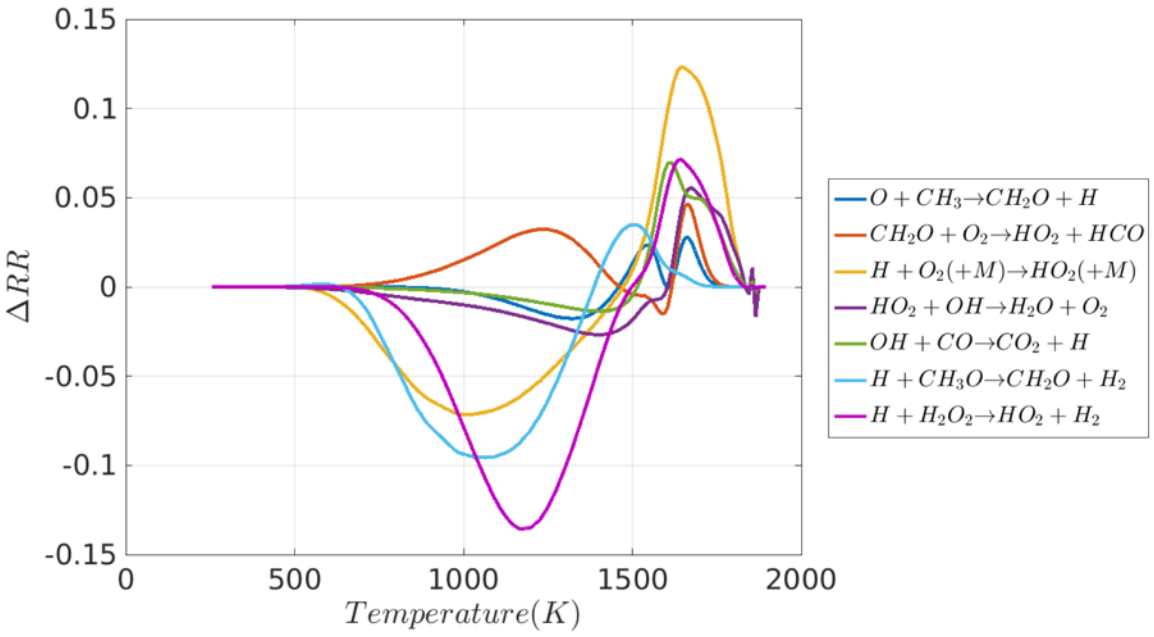

Figure 5.10. Variation of relative difference of reaction rates between *Ka*=1 and *Ka*=36 for different reactions for methane flames.

This plot also emphasizes the limited sensitivity of the reaction to increasing turbulence intensities. As a comparison, the change in reaction rates is an order of magnitude higher in hydrogen flames as shown in Figure 5.4.

The relative insensitivity of the reactions can be attributed to the limited change in the species response with increasing turbulence intensities as shown in Figure 5.11. It can be observed that key species such as fuel(CH_4), stable product(CO), high temperature radical(OH, H), high temperature stable species (CH_2O, CH_3) shown in Figure 5.11(a)-(f) have a reduced response to turbulence with a maximum variation of <6% at higher temperatures between the *Ka*=1 and *Ka*=36 cases. These limited responses manifest themselves as limited responses in the reaction rates. For example, for the reaction $CH_3+O \rightarrow CH_2O+H$, the profiles for CH_3 and O (not shown here but similar to high temperature radicals) do not change significantly with turbulence leading to a <3% change in the reaction rate as seen in Figure 5.9.

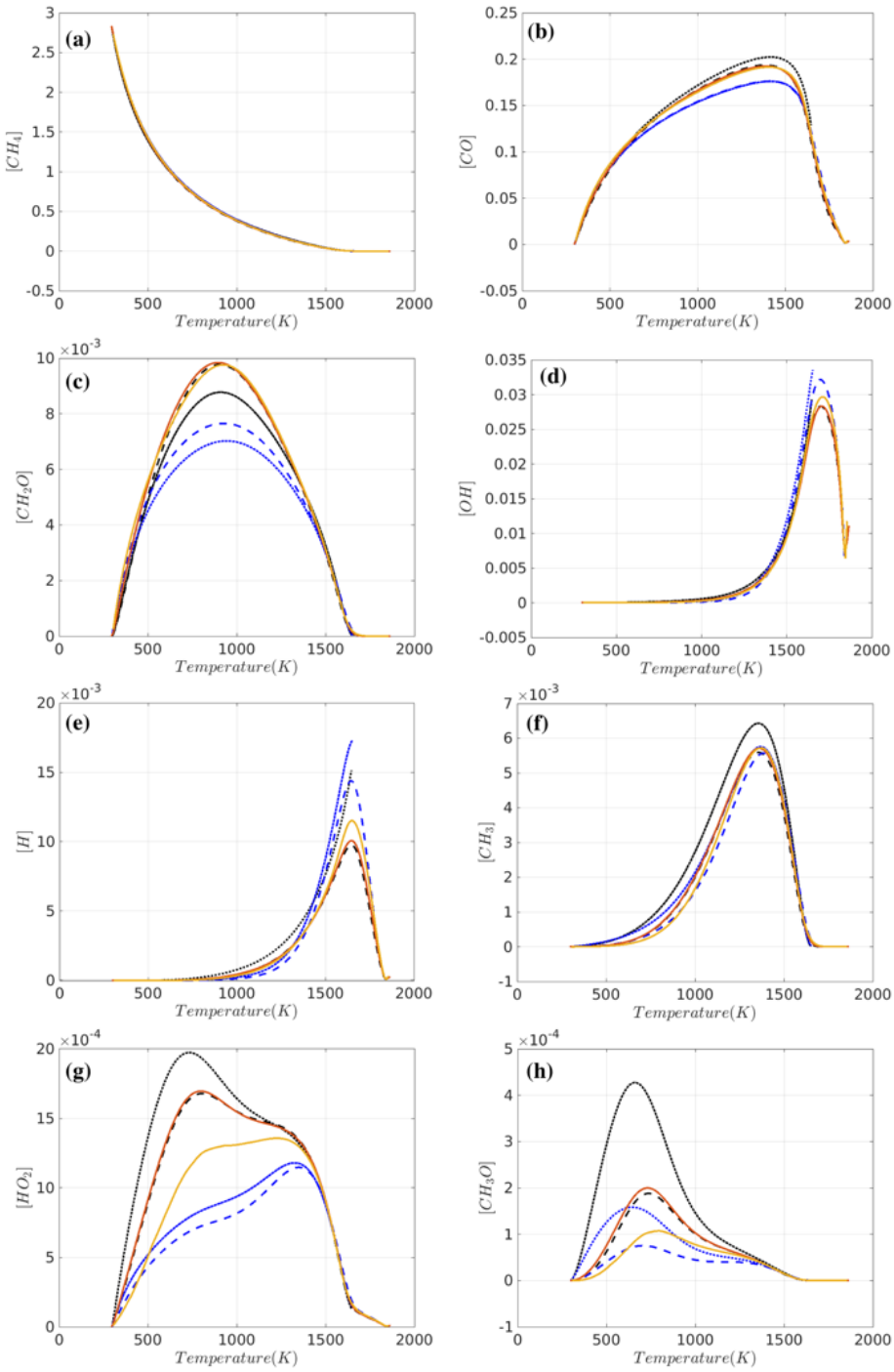

Figure 5.11. Variation of concentration for (a) CH_4 (b) CO (c) CH_2O (d) OH (e) H (f) CH_3 (g) HO_2 (h) CH_3O with temperature. Black dashed line: Unstretched laminar, Black dotted line: Maximum stretch, Blue dashed line: Unstretched *Le*=1 laminar, Blue dotted line: Stretched *Le*=1 laminar, Orange: *Ka*=1, Yellow: *Ka*=36.

For most of the species, the unstretched and stretched laminar flame profiles provide a good quantitative estimate of the species concentration at all temperatures. For example, for CO, the peak deviation between the laminar and turbulent profiles occurs at ~1450K and this deviation is ~10% from the stretched flame profile and ~12% from the unstretched flame profile. For the H radical, the peak deviation occurs at ~1600K. The quantitative deviation between *Ka*=1 and the unstretched and stretched flame profiles is ~15% and ~30% respectively. The deviation between *Ka*=36 and the unstretched and stretched flame profiles is ~30% and ~15% respectively. This also suggests a closer alignment of the lower turbulence intensity profiles with unstretched flames and with the stretched flame profile for the higher turbulence intensity cases. However, for certain species such as HO_2 and CH_3O, this alignment is not evident. There are significant qualitative and quantitative variations in the concentrations of these species with turbulence as shown in Figure 5.11 (g)-(h). For HO_2, the peak HO_2 concentration occurs at ~900K for *Ka*=1 whereas it occurs at ~1400K for the *Ka*=36 case. The peak values are reduced by ~20% between the two cases. Even though the quantitative reduction is captured by the two laminar flame profiles, their behaviors are significantly different from the *Ka*=36 case. For the CH_3O profiles, there is a qualitative similarity in the laminar and turbulent profiles. However, with increasing turbulence, the CH_3O concentrations are reduced whereas with increasing stretch its concentration is seen to increase which displays a significant change in behavior. The physics behind these changes are discussed in details in the next chapter wherein altered effects of transport on reactions rates are analyzed. Even though some of the species show significant changes, the reactions involving them may not mirror these changes since reaction rates depend on the correlation of the concentration of the involved

species and not a single species concentration. For example, the reaction $HO_2+OH \rightarrow H_2O+O_2$ does not change significantly with turbulence as shown in Figure 5.8 even though HO_2 displays a more dynamic behavior with increasing turbulence (Figure 5.11(g)). This can be partly attributed to the limited change in OH concentrations which exists only at higher temperatures (Figure 5.11(d)). As a result, the species correlation is zero at low temperatures and is non-zero at higher temperatures leading to limited variation of the overall reaction rates.

As pointed out earlier, for turbulent flames the means are a representation of the physics and there is a variation in data about this mean. Conditional means of reaction rates of some key reactions with one standard deviation across the mean (denoted by the grey region) are plotted in Figure 5.12. It can be observed that unlike the hydrogen flames, the *Ka*=1 methane/air flames have a much smaller deviation about the mean. For example, for the reaction $H+O_2(+M) \rightarrow HO_2(+M)$, the peak standard deviation of 30.5 $1/m^3$-s occurs at ~1600K. This value is 10% of the mean value of reaction rate at the same temperature. For the same reaction in hydrogen flames the maximum standard deviation was 80% of the mean for *Ka*=1. With increased turbulence, the standard deviations increase especially for temperatures below 1500K suggesting a slight disturbance of the low temperature regions compared to the higher temperature region. However, this disturbance is not significant enough to alter the flame structure when compared to laminar flames resulting in a close alignment of the means with the laminar flame profiles. For *Ka*=36, the maximum standard deviation for the reaction $H+O_2(+M) \rightarrow HO_2(+M)$ is 56.6 $1/m^3$-s and is ~17% of the mean at the same temperature. This variation is also significantly smaller compared to the variation for hydrogen flames at higher turbulence intensities.

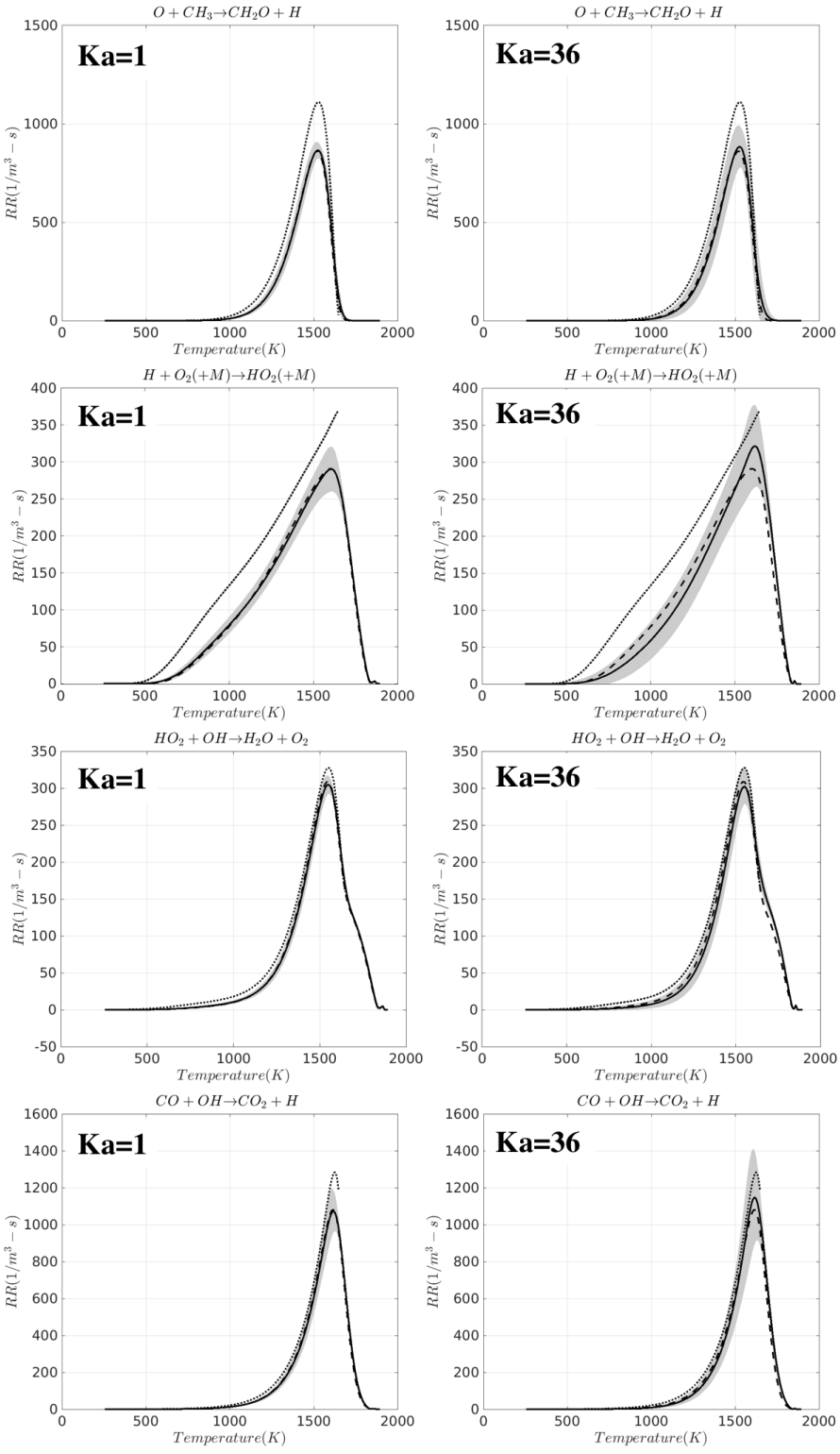

Figure 5.12. Variation of reaction rates with temperature for different Karlovitz number. Black solid line: DNS mean, Black dashed line: Unstretched laminar, Black dotted line: Maximum stretch, Grey region: mean± one standard deviation

5.3 n-dodecane

Figure 5.13 plots the net heat release and fuel consumption as a function of temperature for *Ka*=1, 12 and 108. The behavior of *Ka*=4 is similar to *Ka*=1 and *Ka*=36 is similar to *Ka*=12 and hence only these three cases are plotted for clarity. The profiles for unstretched laminar and the maximum stretched laminar case (i.e. $\kappa/\kappa_{ext} \approx 0.97$) are overlaid for comparison.

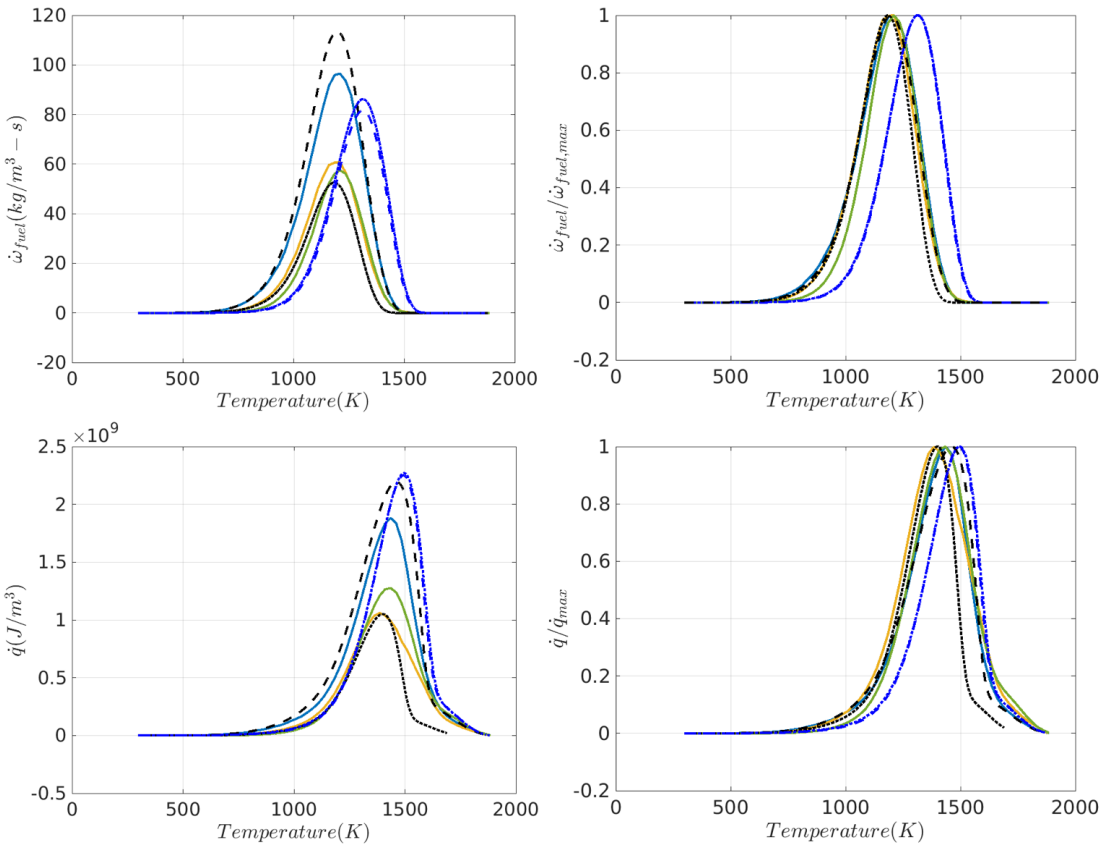

Figure 5.13. Variation of fuel consumption (top, left) normalized fuel consumption (top, right), heat release (bottom, left) and normalized heat release (bottom, right) with temperature for n-dodecane/air flames. Black dashed line: Unstretched laminar, Black dotted line: Maximum stretch, Blue dashed line: Unstretched *Le*=1 laminar, Blue dotted line: Stretched *Le*=1 laminar, Blue: *Ka*=1, Yellow: *Ka*=12, Green: *Ka*=108.

The figure indicates that the peak temperature for fuel consumption and heat release are not significantly affected by increased turbulence intensity. However, there is a slight shift towards high temperature with increasing turbulence intensities suggesting a shift in chemistry towards higher temperatures. For heat release, the DNS profiles are well represented by the extreme laminar cases as seen in Figure 5.13(right). As expected, the *Ka*=1,4 cases are closer in behavior to the unstretched laminar flame profile. The higher turbulence cases (*Ka*=12-108) behave similar to the highly stretched laminar flame up to a temperature of ~1200K. The highly stretched laminar flame reaches a lower equilibrium temperature than the unstretched/DNS cases, resulting in its deviation from the *Ka*=12-108 results at temperatures beyond 1400K.

Figure 5.14 plots the variation of reaction rates of some of the key reactions identified in Section 4.4.3. The lower turbulence intensities of *Ka*=1,4 follow the unstretched laminar profile well. With increasing turbulence intensities, however the trend is not obvious. Response of certain reactions such as $HCO+O_2 \rightarrow CO+HO_2$, $HO_2+OH \rightarrow O_2+H_2O$, $CH_3+O \rightarrow CH_2O+H$ is similar to the highly stretched laminar flame whereas, the other reactions $H+OH+M \rightarrow H_2O+M$, $H+O_2(+M) \rightarrow HO_2(+M)$, $CO+OH \rightarrow CO_2+H$ have a qualitatively similar response to the unstretched laminar flame (peak temperature, slope of the curves). A shift of reaction rate profiles towards higher temperatures can also be observed. This is more clearly illustrated in Figure 5.15.

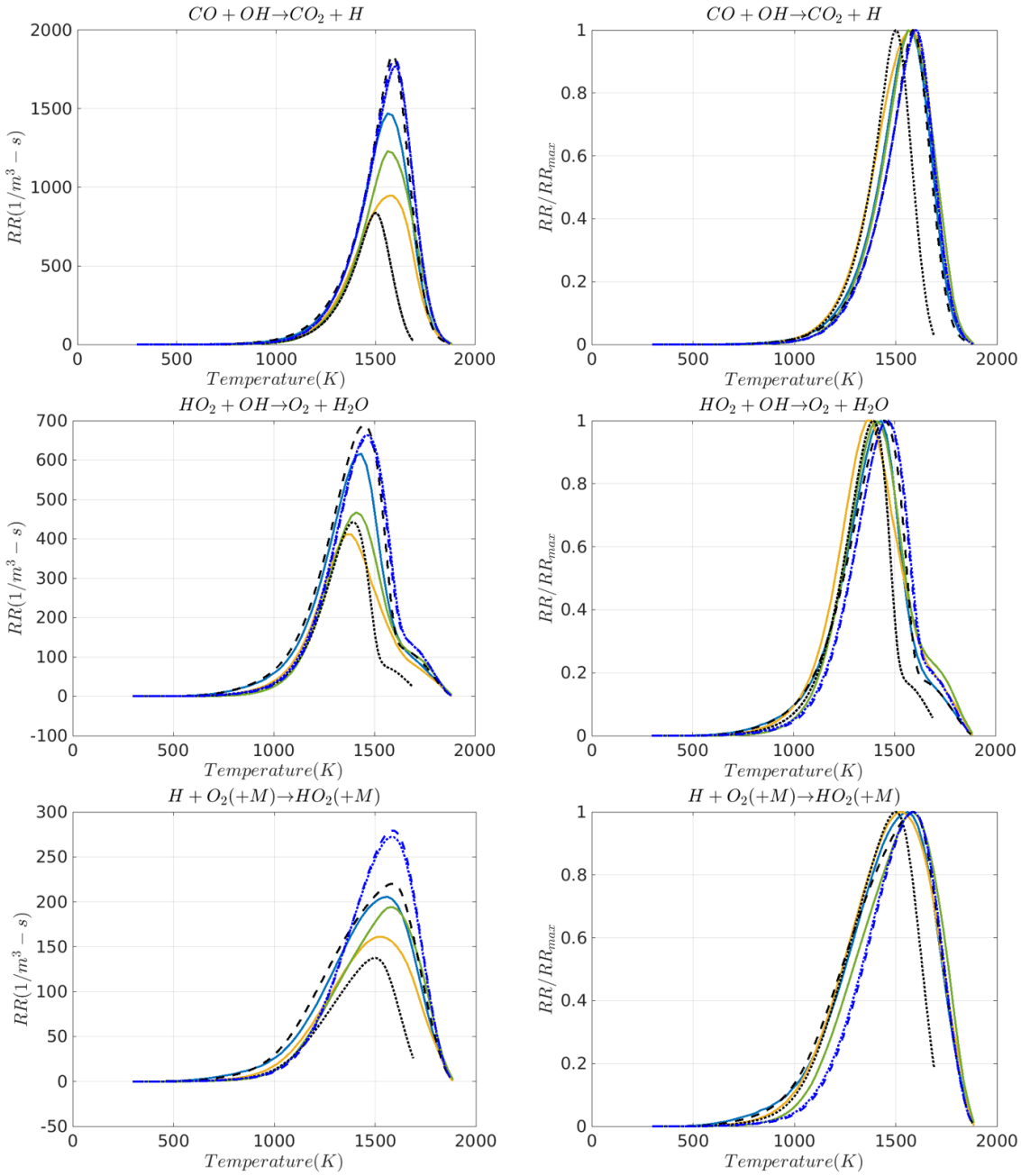

Figure 5.14. Variation of reaction rates (left) and normalized reaction rate (right) for different reactions with temperature for n-dodecane/air flames. Black dashed line: Unstretched laminar, Black dotted line: Maximum stretch, Blue dashed line: Unstretched *Le*=1 laminar, Blue dotted line: Stretched *Le*=1 laminar, Blue: *Ka*=1, Yellow: *Ka*=12, Green: *Ka*=108.

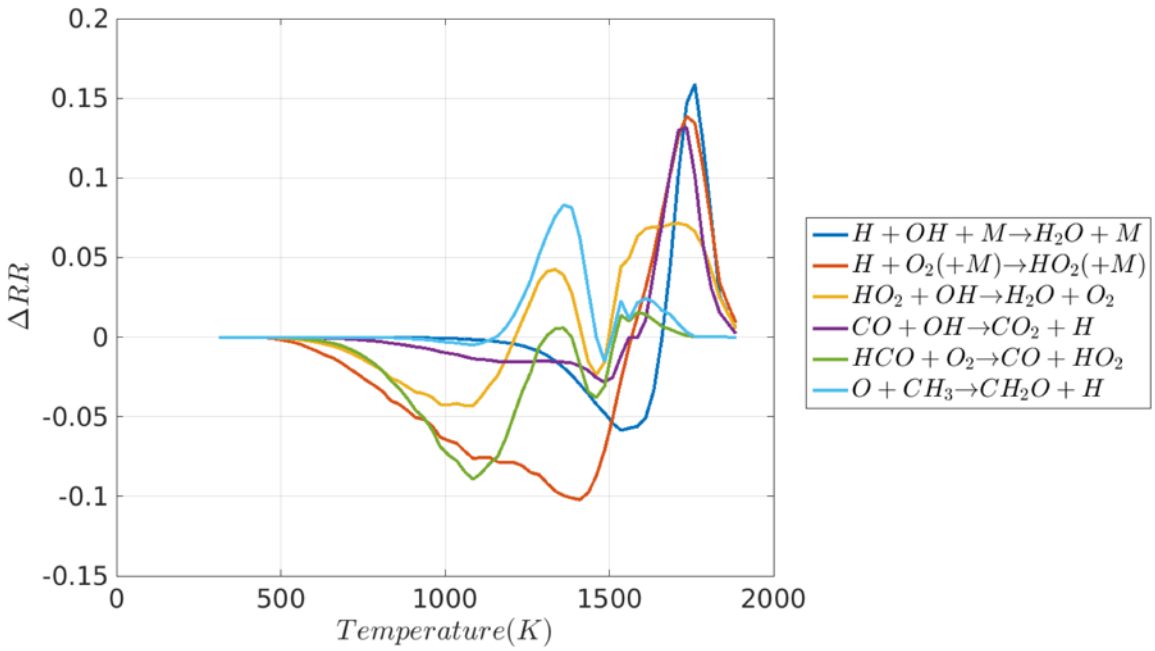

Figure 5.15. Variation of change of reaction between *Ka*=1 and *Ka*=108 for different reactions for n-dodecane flames.

Figure 5.15 plots the change in reaction rates(ΔRR) between the two extreme turbulent cases i.e. *Ka*=1 and *Ka*=108. ΔRR is calculated by subtracting the normalized reaction rate profile of *Ka*=1 from the normalized reaction rate profile of *Ka*=108. This shows a positional shift of the profiles in temperature space i.e. if the profiles shift towards higher or lower temperatures with increasing turbulence intensities. Thus, $\Delta RR < 0$ indicates higher normalized reaction rates for *Ka*=1 than for *Ka*=108. The reactions that are active below 1200K (i.e. have a non-zero reaction rate at these temperatures), such as $HCO+O_2 \rightarrow CO+HO_2$, $HO_2+OH \rightarrow O_2+H_2O$, and $H+O_2(+M) \rightarrow HO_2(+M)$, show relatively reduced activity in this temperature range at higher turbulence intensities. These same reactions have a relatively stronger high temperature sensitivity i.e. $\Delta RR > 0$ indicating increased activity in this region. On the other hand, the reactions which are active above 1200K, show very little deviation below 1200K. For example, the high-temperature

reaction, CO+OH→CO_2+H, shows much higher rates above 1500K. This behavior is also seen for the other high-temperature reaction, H+OH+M→H_2O+M. The reaction, CH_3+O→CH_2O+H, exhibits an increased activity in the interim range, between 1200-1500K. It also shows increased rates above 1500K (though not as strong as in the interim region). The relative change in magnitude of the reaction rates in plotted in Figure 5.16.

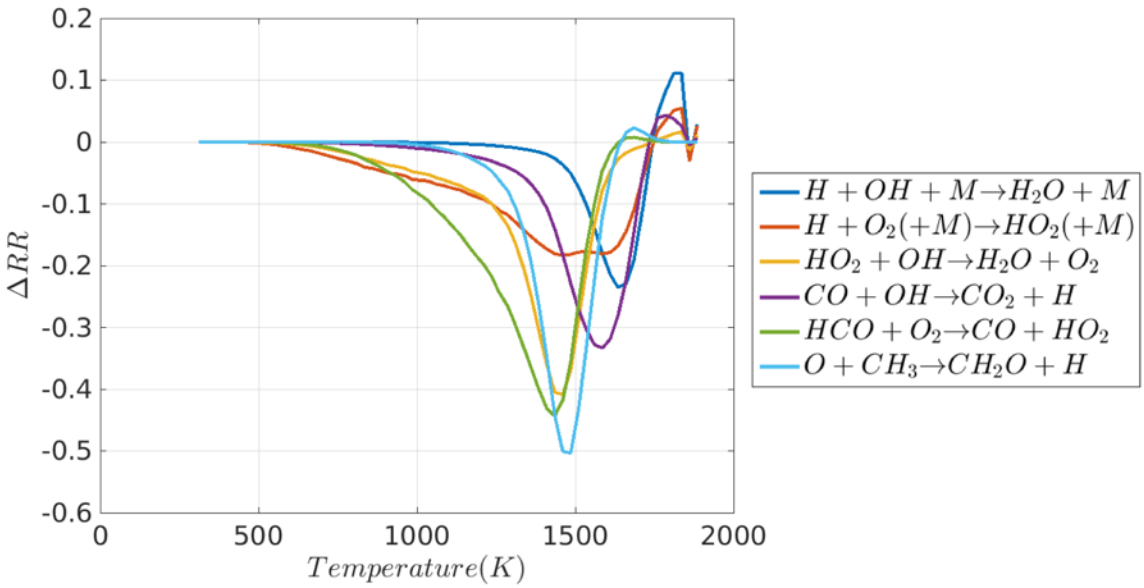

Figure 5.16. Variation of relative difference of reaction rates between *Ka*=1 and *Ka*=36 for different reactions for n-dodecane flames.

All the reactions show reduced reaction rates with increased turbulence for temperatures below 1500K. The strongest responses are seen for the reactions HCO+O_2→CO+HO_2, O+CH_3→CH_2O+H and HO_2+OH→O_2+H_2O. The contribution of these reactions reduces by ~25-30% for temperatures below 1500K. ~10-15% decrease in reaction rates is seen for the reactions H+O_2(+M)→HO_2(+M) and CO+OH→CO_2+H. All the dominant reactions involve atleast one high temperature species/radical and show an increase in reaction rate at higher temperatures for *Ka*=108 compared to *Ka*=1 suggesting a strengthening of the

high temperature chemistry with increased turbulence intensities. An interesting feature is observed for reactions involving fuel fragments whose rates peak in the low temperature region (i.e. below 1200K). Figure 5.17 plots the variation of reaction for two representative reactions involving fuel fragments, pC$_4$H$_9$ and nC$_3$H$_7$.

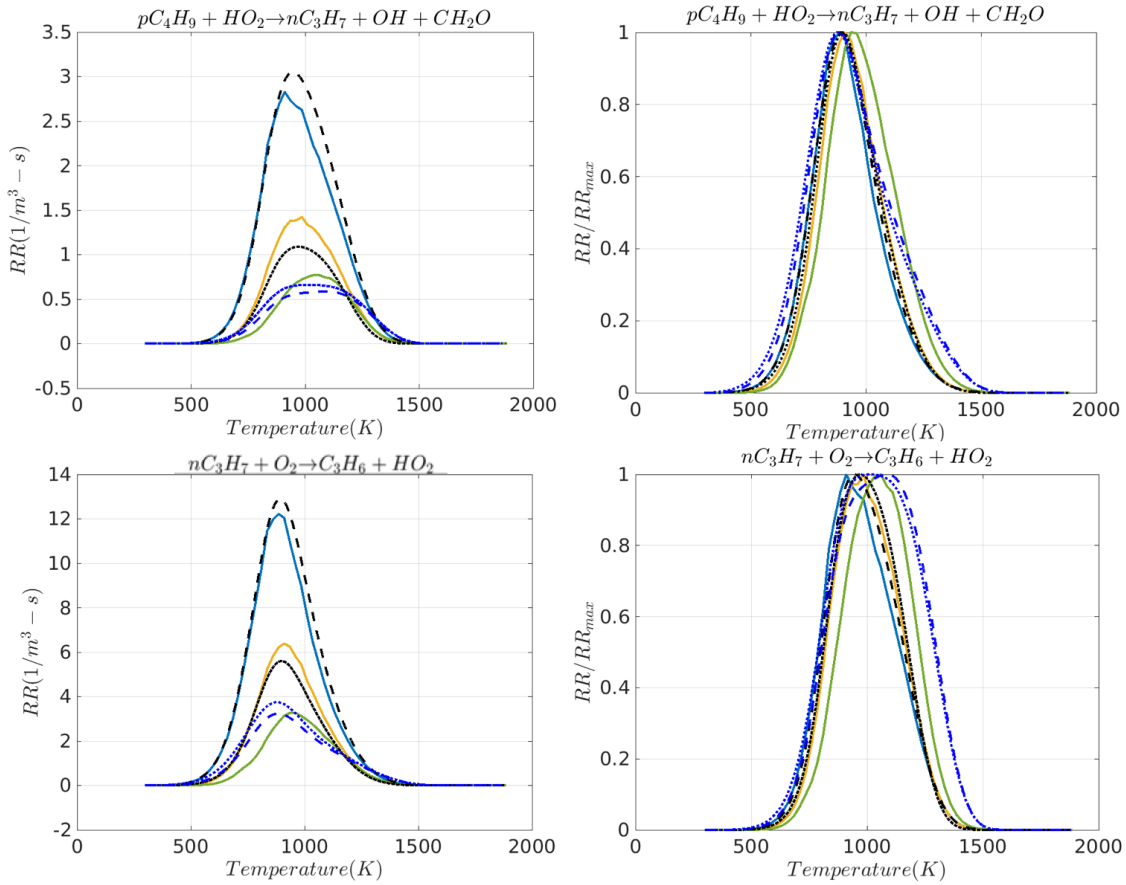

Figure 5.17. Variation of reaction rates (left) and normalized reaction rate (right) for different reactions with temperature for n-dodecane/air flames. Black dashed line: Unstretched laminar, Black dotted line: Maximum stretch, Blue dashed line: Unstretched *Le*=1 laminar, Blue dotted line: Stretched *Le*=1 laminar, Blue: *Ka*=1, Yellow: *Ka*=12, Green: *Ka*=108.

A clear systematic shift of the reaction rate profiles towards higher temperature region and a reduction in reaction rates can be observed in Figure 5.17. This behavior is consistent for all the reactions whose rates peak below 1200K (the temperature of peak fuel

consumption). Overall, the response of the reactions to increased turbulence intensities is well represented by the two extreme cases of laminar stretched flames, namely the unstretched laminar case and the most stretched case ($\kappa/\kappa_{ext} \approx 0.97$) when plotted in temperature space. With increasing turbulence intensities all reactions show a movement towards higher temperature, particularly those with peak rate occurring in the low temperature region. A potential reason for this shift can be explained through the altered species concentration with increasing turbulence intensities since the reaction rates depend on the correlation between the reactant species concentrations. Figure 5.18 plots the conditional concentration means for species involved in the fuel oxidation process. These species include the fuel($n$$C_{12}H_{26}$), high temperature radicals (CH_3, OH, H), low temperature species (CH_2O, HO_2) and high temperature stable species (CO). For most of the species, a shift towards higher temperature can be observed. For species which are dominantly produced in the high temperature region, the temperature of peak concentration does not change with turbulence. For example, for CH_3 the temperature corresponding to peak concentration for *Ka*=1 is ~1300K. This remains unchanged for *Ka*=12 and *Ka*=108. For OH the peak concentration occurs at ~1600K and for *Ka*=12 and *Ka*=108 occurs at a slightly higher value of ~1625K. The laminar profiles bound the turbulent means well for these high temperature species. However, for low temperature (HO_2) and highly diffusive species(H_2) the laminar profiles cannot capture the turbulent flame trends with increasing turbulence. For HO_2, the unstretched laminar flame can represent the *Ka*=1 behavior and the highly stretched flame can, to some extent, predict the *Ka*=12 profile qualitatively and quantitatively. However, the *Ka*=108 cannot be represented by either profile. The same observation can be made for H_2. A repercussion of this cannot be seen in the reaction rates,

which remain bounded by the laminar profiles, since most of the reactions involving these species also include a high temperature species. Since the reaction rates depends on the correlations of the species and not on the species concentration itself, the reaction rates do not show significant changes. As an example, the reaction involving HO_2 and OH, $HO_2+OH \rightarrow H_2O+O_2$ remains bounded as can be seen in Figure 5.14 even though the HO_2 profile does not.

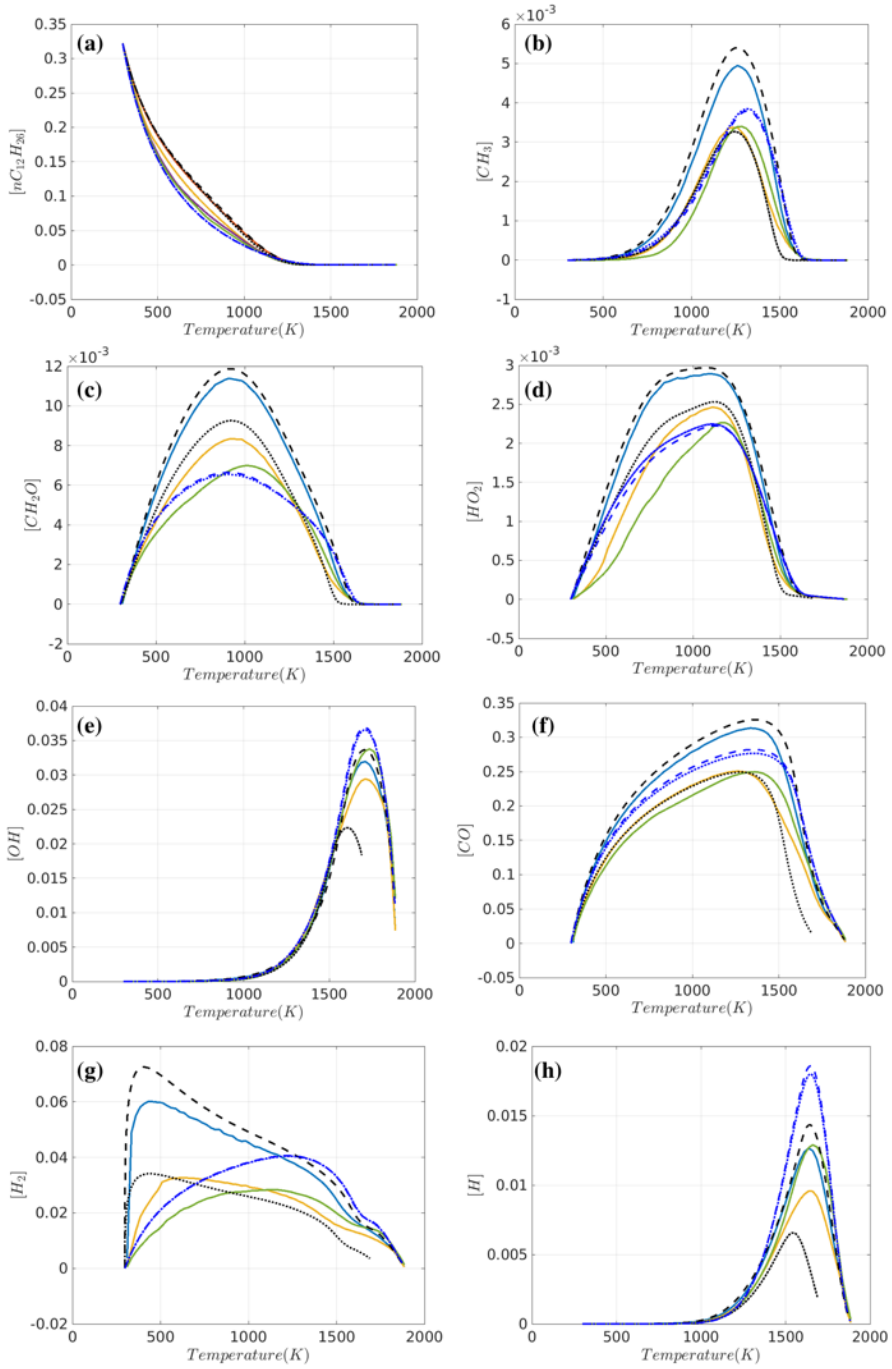

Figure 5.18. Variation of concentration for (a) $nC_{12}H_{26}$ (b) CH_3 (c) CH_2O (d) HO_2 (e) OH (f) CO (g) H_2 (h) H with temperature. Black dashed line: Unstretched laminar, Black dotted line: Maximum stretch, Blue dashed line: Unstretched *Le*=1 laminar, Blue dotted line: Stretched *Le*=1 laminar, Blue: *Ka*=1, Yellow: *Ka*=12, Green: *Ka*=108.

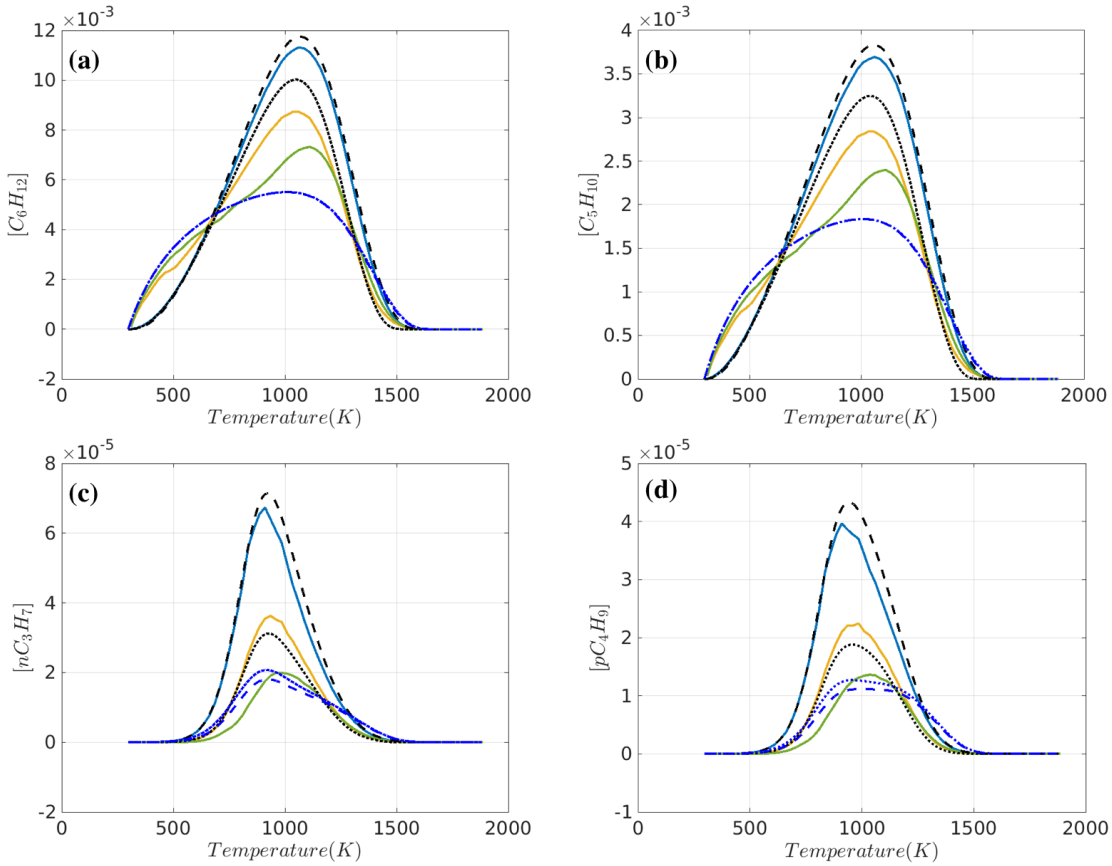

Figure 5.19. Variation of concentration of fuel fragments (a) C_6H_{12} (b) C_5H_{10} (c) nC_3H_7 (d) pC_4H_9 with temperature. Black dashed line: Unstretched laminar, Black dotted line: Maximum stretch, Blue dashed line: Unstretched *Le*=1 laminar, Blue dotted line: Stretched *Le*=1 laminar, Blue: *Ka*=1, Yellow: *Ka*=12, Green: *Ka*=108.

It can be observed in Figure 5.19 that the concentration profiles of nC_3H_7 and C_3H_6 shift towards higher temperatures with increased turbulence intensities which directly influences the behavior of the reactions involving these species. For example, for the reaction $nC_3H_7+O_2 \rightarrow C_3H_6+HO_2$, since O_2 concentration profile (not shown here) shows limited sensitivity to turbulence and exists across the entire temperature space (since the reactant mixture is lean), a direct correlation can be seen between the reaction rate profile in Figure 5.17 and the species concentration profile for nC_3H_7 in Figure 5.19(c). It can also be noted that for larger fuel fragments which are the first products in the pyrolysis process

in this mechanism have an increased concentration at lower temperature which cannot be captured by the laminar profiles. This can partly be attributed to the increased fuel concentration at lower temperatures with increasing turbulence as shown in Figure 5.18(a). The movement of the species profile and the reaction rate towards higher or lower temperatures can potentially be understood using altered transport models which is discussed in the next chapter.

To investigate the behavior of the conditional means and its standard deviation, Figure 5.20 plots the conditional means with one standard deviation for the heat release at the lower and higher Karlovitz number.

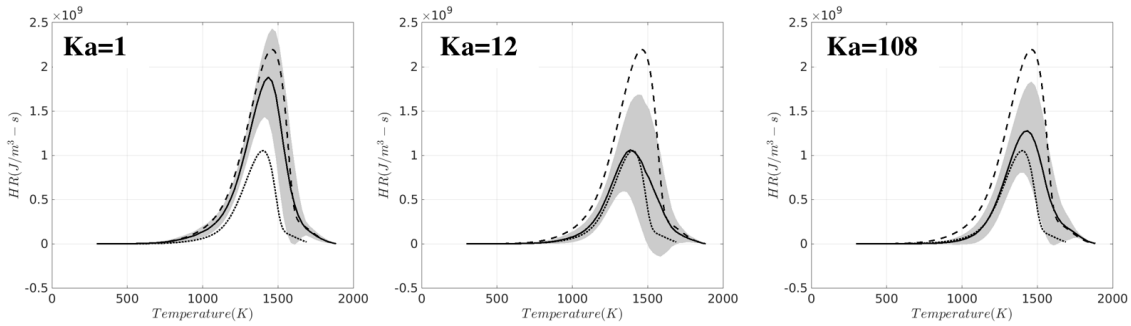

Figure 5.20. Variation of heat release with temperature for different Karlovitz number. Black solid line: DNS mean, Black dashed line: Unstretched laminar, Black dotted line: Maximum stretch, Grey region: mean± one standard deviation.

Clearly, the spread in the data increases with turbulence intensities. Additionally, there are regions in the temperature space wherein values of the heat release cannot be captured using the two extreme laminar bounds. For example, at *Ka*=1, the upper bound of the heat release lies outside the unstretched laminar flame bound. However, this difference between the unstretched profile and the turbulent flame upper bound is ~8%. This increased

spread with increasing turbulence can be seen for different reactions as well. Figure 5.21 plots some of the mean and the standard deviation about the mean for selected reactions.

A similar increase in spread with turbulence intensities can be seen for the reaction rates as well. For example, for the reaction $H+O_2(+M) \rightarrow HO_2(+M)$ the peak standard deviation of 38.7 $1/m^3$-s occurs at ~1685K at *Ka*=1. This value is ~26% of the mean value of reaction rate at the same temperature. For the same reaction in hydrogen flames the maximum standard deviation was 80% of the mean for *Ka*=1 and ~10% for the methane flames at *Ka*=1. For *Ka*=108, the maximum standard deviation is 34.8 $1/m^3$-s and is ~27% of the mean at the same temperature. These variations are significantly smaller compared to the variation for hydrogen flames are higher turbulence intensities. These flame however, do show a larger variation compared to the methane flames.

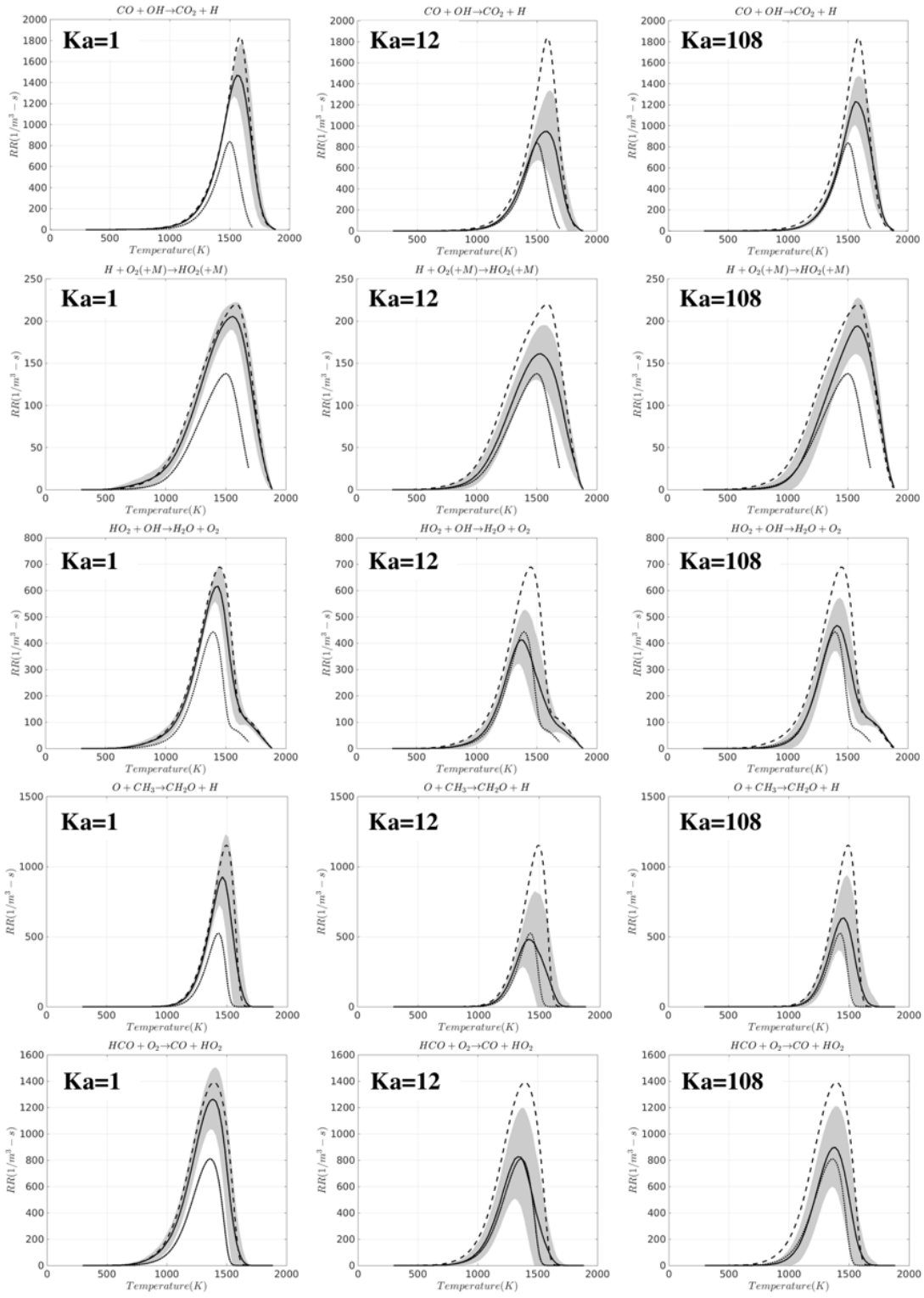

Figure 5.21. Variation of reaction rates with temperature for different Karlovitz number. Black solid line: DNS mean, Black dashed line: Unstretched laminar, Black dotted line: Maximum stretch, Grey region: mean± one standard deviation.

5.4 Conclusions

This chapter discusses a local analysis of the behavior of the reactions involved in the oxidation process for three fuels: hydrogen, methane and n-dodecane. This is accomplished by comparing the conditional mean of reaction rates with those obtained from equivalent laminar and stretched flame calculations.

For the hydrogen flames it is observed that the unstretched laminar flames cannot represent the behavior for the turbulent flames since lean premixed hydrogen flames are thermo-diffusively unstable. For all the reactions, the reaction rates showed an increase with increasing turbulence intensity. Additionally, they also showed increased low temperature rates for all reactions leading to higher low temperature heat release which has been noted in literature by Aspden et al.[12] and Carlsson et al.[14]. For example, the reaction $H_2+O\rightarrow OH+H$, which is a dominant OH producing reaction, shows a 2.5 times increase in reaction rate between the Ka=1 and Ka=36 cases. Similarly, the reaction rate of the dominant H_2O producing reaction. $H_2+OH\rightarrow H_2O+H$ almost doubles with increasing turbulence intensities. The stretched flame profile represents the increasing turbulence trends well and form the upper bound for the reaction rates for the highly turbulent flames. These laminar flame calculations however, cannot capture the super-adiabatic temperatures reached in the turbulent flames. This occurs due to the enhanced burning in the cellular burning regions formed due to the instability. The reaction rates of all the reactions grow with turbulence in these super-adiabatic regions. The species response aids in interpreting the changes in the reaction rates. All species showed elevated concentration at lower temperature leading to higher reaction rates. Finally, the instability also leads to large spread in the data even for the weakly turbulent flames. The standard deviations are

comparable to the value of the mean and can be as high as 80% of the mean for these hydrogen flames.

For the methane flames, no significant change in reaction rates was observed with increasing turbulence intensity. For example, the maximum deviation is observed for the reaction $H+O_2(+M) \rightarrow HO_2(+M)$. At ~1000K, the reaction rate for *Ka*=36 is reduced by ~5% from the reaction rate for *Ka*=1. At ~1600K, the reaction rate for *Ka*=36 is ~10% higher than that for *Ka*=1. This may be due to the unity global Lewis number of the flame. Typically, unity Lewis number flames are not significantly affected due to stretch. However, the effects of differential diffusion exist and maybe the reason for the changes noted. The response of all the reactions closely resembles the unstretched laminar flame. The limited sensitivity of the reactions is replicated by most of the species response wherein the maximum change is observed for the H radical. Its concentration is augmented by ~20% at higher temperatures for *Ka*=36 compared to *Ka*=1. Species with low temperature activity such as HO_2 and CH_3O however show significantly different behavior at higher turbulence intensities compared to their laminar counterparts. For example, for HO_2 the peak concentration for *Ka*=1 occurs at 900K whereas for *Ka*=36 it occurs at ~1400K. For CH_3O, laminar flame calculations suggest increasing stretch leads to increased concentration across all temperature range. However, the highly turbulent flames show an opposite trend. The *Ka*=36 has lower values of peak concentrations and is shifted towards higher temperatures compared to the *Ka*=1 profile. It is stipulated that an altered transport due to turbulence may cause this altered behavior of the species and is further investigated in the next chapter. Overall, the rate response of the reactions involving these species is not dramatic since the reaction rates are a function of the correlation between the

species concentration. The spread in the data for these flames is also much lower compared to their hydrogen counterpart. The standard deviations are much smaller compared to the value of the mean and is generally ~20% of the mean for these methane flames.

For the n-dodecane flames, the unstretched and stretched flame profiles well represent the turbulent flame means for most of the key reactions. All the reactions portray a shift towards higher temperature with increasing turbulence intensities. A maximum reduction of ~30% between the *Ka*=1 and *Ka*=108 is seen for $HCO+O_2 \rightarrow CO+HO_2$ and $CH_3+O \rightarrow CH_2O+H$. Beyond 1500K all reactions have an elevated reaction rate at *Ka*=108. Reactions with low temperature activity i.e. the reactions for which the peak reaction rate occurs at temperatures less than 1200K show a drastic shift towards higher temperature with increasing turbulence intensities. These reactions are also not well represented by the two laminar extremes and generally include fuel fragments as reactants. The behavior of the fuel fragments mirrors the behavior of the reactions involving them i.e. their profiles move towards higher temperatures explaining the reaction rate behavior. The standard deviation about the mean is the smallest for the *Ka*=1 case and increases with increasing turbulence intensity. The maximum deviation between ~15-27% can be seen for the turbulence cases. These deviations are smaller than the hydrogen flames but larger than the methane flames.

It has been well established here that the response of the reactions is closely tied to the response of the species. Turbulence is known to alter scalar diffusivity and transport which in turn may lead to altered transport of species and hence altered reaction rates. Even though some of the features of the means are captured by simple stretched flame calculations, many responses are not understood with this comparison. For example, the

altered response of HO_2 for methane flames or for the fuel fragments for the $n C_{12}H_{26}$ flames are not explained by the stretched flame calculations. Altered transport models can potentially explain these responses and are discussed in details in the next chapter.

CHAPTER 6. TRANSPORT MODEL COMPARISON

A well-known effect of turbulence on the flow field is an increased scalar diffusivity. Different models for transport are tested here to understand the influence of transport characteristics on the reaction rates for laminar unstretched and stretched flames. Thus understanding is then applied to explain the behavior of turbulent flames.

6.1 Discussion of models

Three categories of models are tested

(a) Mixture-averaged transport

(b) Unity Lewis number transport

(c) Mixture-averaged transport with an additional constant diffusivity

6.1.1 Mixture-averaged transport model

Multicomponent diffusion transport model is the most detailed transport model[92]. This model, however, is computationally expensive for the calculation of diffusive fluxes. Using Hirschfelder-Curtiss[93] approximation for this multicomponent diffusion leads to a simplified transport model called the mixture-averaged diffusion transport model[94]. In this model, the transport coefficients, heat conductivity, dynamic viscosity and species diffusion coefficients are calculated using an averaging procedure. A significant advantage of this model over the multi-component diffusion transport is reduced computational costs for the calculation of diffusive fluxes which appears in the species and energy equations.

This makes the inclusion of detailed chemistry in simulations tractable. The diffusivity of species, *i*, w.r.t the mixture, *m* ($D_{i,m}$)is given by:

$$D_{i,m} = \frac{1 - Y_i}{\sum_{j \neq i} \frac{X_j}{D_{ji}}} \tag{6.1}$$

where, Y_i is the mass fraction of species, *i*, X_j is the mole fraction of species, *j*, D_{ji} is the binary diffusion coefficient of species, *j,* relative to species, *i.*

The thermal diffusivity of the mixture, α_{mix} is calculated from the mixture-averaged thermal conductivity k_{mix}, mixture-averaged density, ρ_{mix} and mixture-averaged specific heat $c_{p_{mix}}$ as:

$$\alpha_{mix} = \frac{k_{mix}}{\rho_{mix} c_{p_{mix}}} \tag{6.2}$$

This model is implemented in CHEMKIN[74].

6.1.2 Unity Lewis number transport model

This is a simplified model for the calculation of $D_{i,m}$ and leads to the elimination of terms in the energy and species equations. Lewis number of a species, *i*, (Le_i) is defined as the ratio of the thermal diffusivity of the mixture (α_{mix}) to the mixture-averaged mass diffusivity of species, *i*($D_{i,m}$). For $Le_i = 1$, $D_{i,m}$ is computed from α_{mix} as:

$$D_{i,m} = \alpha_{mix} \tag{6.3}$$

This definition removes the effect of preferential diffusion of heat and mass and differential diffusion of species (since all the diffusivities are the same). This is hypothesized to represent the limit where turbulent mixing overwhelms molecular transport and as a result, all scalars are transported in the same way[67, 68]. This model is implemented in CHEMKIN[74].

6.1.3 Mixture-averaged transport model with an additional constant

This transport models uses the same basis as the mixture-averaged transport discussed earlier. An additional constant, D_T is added to $D_{i,m}$ to mimic the effect of increased diffusivity due to turbulence. Since, turbulence moves all scalars the way, a turbulent Lewis number ($Le_T = \alpha_T / D_T$) can be set to 1. This implies that the turbulent thermal diffusivity, α_T can be set equal to D_T, This leads to an altered value for the mixture thermal conductivity given by:

$$k_{mix,T} = k_{mix} + \rho_{mix} c_{p_{mix}} D_T \tag{6.4}$$

The typical value for mass diffusivity is O (10^{-4}) m^2/s for most species and O (10^{-3}) m^2/s for lighter species such H_2, H. The constant values chosen for D_T are 10^{-2}, 10^{-3}, 10^{-4}, 10^{-5}, 10^{-6}. These values span multiple orders of magnitude such that the smaller values act as a tiny perturbation on $D_{i,m}$ and the larger values supersede the value of $D_{i,m}$. This is implemented in Cantera[95] by adding a new transport class. The inlet flow details for the stretched flame calculations are detailed in Appendix B.

6.2 Hydrogen

This section compares the unstretched and stretched laminar flame profiles for the different transport models with the turbulent flame profiles for lean hydrogen/air flames. The value of mass diffusivity using mixture-averaged transport for some key species is tabulated in Table 6.1.

Table 6.1. Mass diffusivity for key species for hydrogen flames

Species	Maximum $D_{i,m}$ (x10^{-4} m^2/s)	$Le_{D_{i,m},max}$	Minimum $D_{i,m}$ (x10^{-4} m^2/s)	$Le_{D_{i,m},min}$
O_2	3.02	1.09	0.22	1.48
H_2O	4.11	0.8	0.25	1.32
H_2	11.19	0.29	0.91	0.36
H_2O_2	3.04	1.08	0.23	1.44
H	19.02	0.17	1.31	0.25
OH	4.65	0.7	0.35	0.93
HO_2	3.06	1.07	0.23	1.44
O	4.74	0.69	0.36	0.92

The minimum and maximum value of the mass diffusivity of H_2 and H is an order of magnitude higher for the other species. The maximum value of the constant D_T is an order of magnitude higher than the mass diffusivity of these light species. The minimum value

is two orders of magnitude smaller than the diffusivity for most species and hence represents a limit fairly close to the mixture-averaged transport.

First, the effect of the transport models on heat release is plotted in Figure 6.1. The profiles for unstretched and stretched flames are plotted separately to understand the effect of altered transport on heat release. The DNS means are then plotted and overlaid with two limits: mixture-averaged and *Le*=1.

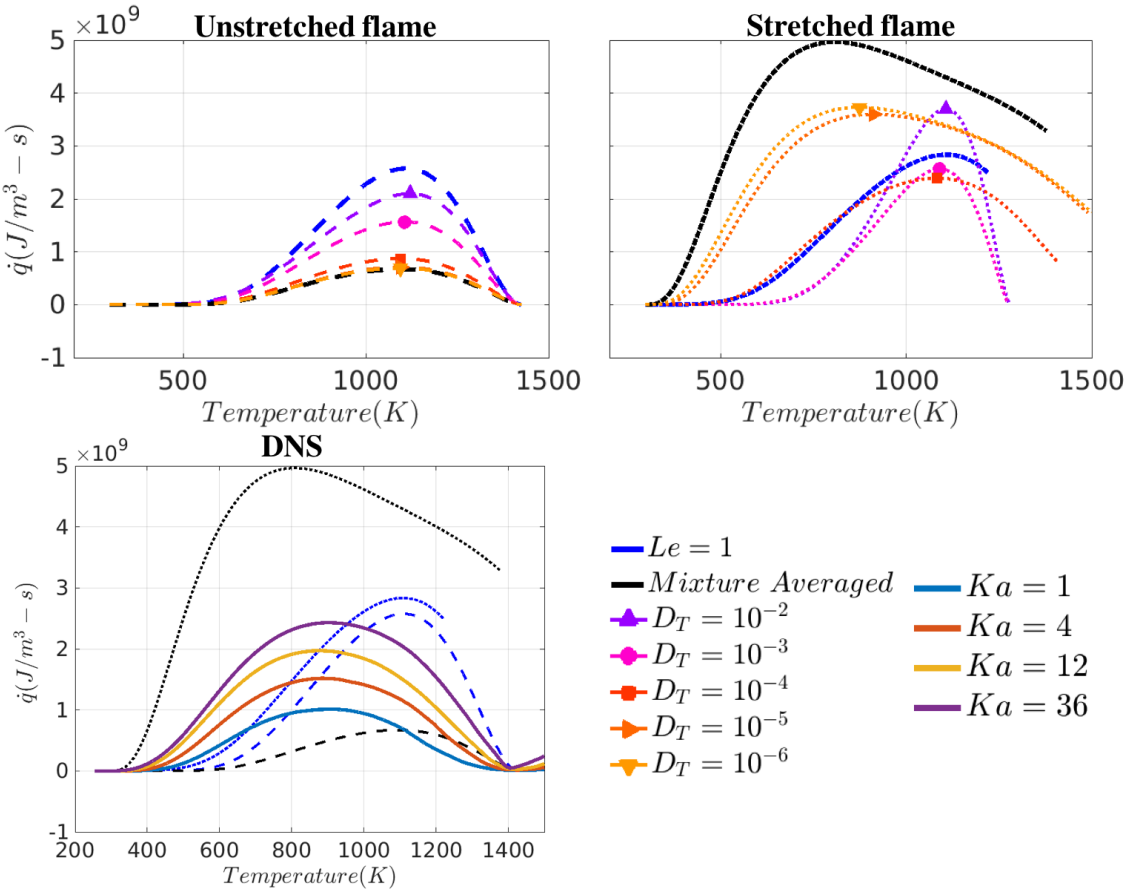

Figure 6.1. Variation of heat release with temperature for different transport models for unstretched flames, stretched flames and DNS.

Unstretched flames for lean hydrogen flames cannot be achieved due to thermo-diffusive instability. The profiles for the unstretched flames have been shown here for

completion. For the unstretched flames, it can be observed that the profile with $D_T = 10^{-6}$ is fairly close to the mixture-averaged transport. This is not surprising since this constant is two orders of magnitude lower than the maximum mass diffusivity and one order of magnitude smaller than the minimum mass diffusivity of the key species. With increasing diffusivity, the unstretched profiles seem to move towards higher values of heat release over the entire temperature range ultimately moving closer to Le=1(in blue) profile. For the highly stretched flame profiles, the mixture-averaged transport (in black) has a higher heat release, compared to the other transport models, at all temperatures. Increasing diffusivity pushes the profiles towards higher temperatures (and towards Le=1 profile, in blue). This can be seen up to $D_T = 10^{-4}$. A further increase in diffusivity leads to a significant change in the profile behavior. For $D_T = 10^{-3}$ (pink) the profile shows negligible low temperature heat release with a peak heat release occurring at a higher temperature of ~1150K (compared to ~900K for $D_T = 10^{-5}, 10^{-6}$). For the DNS means, with increasing turbulence, an increase in heat release is observed at all temperatures. This response is different from the behavior of stretched flames with increasing diffusivity. Comparing unstretched and stretched flames, it is observed that increasing stretch increases the low temperature heat release. For example, For the mixture-averaged transport, non-negligible heat release can be seen starting at ~600K whereas for the mixture-averaged stretched flame heat release occurs at a temperature as low as 300K. The response of the reactions can be dictated by the species response. Figure 6.2 plots the variation of the fuel, H_2 and a high temperature (and highly diffusive) radical, H with temperature for the different transport models.

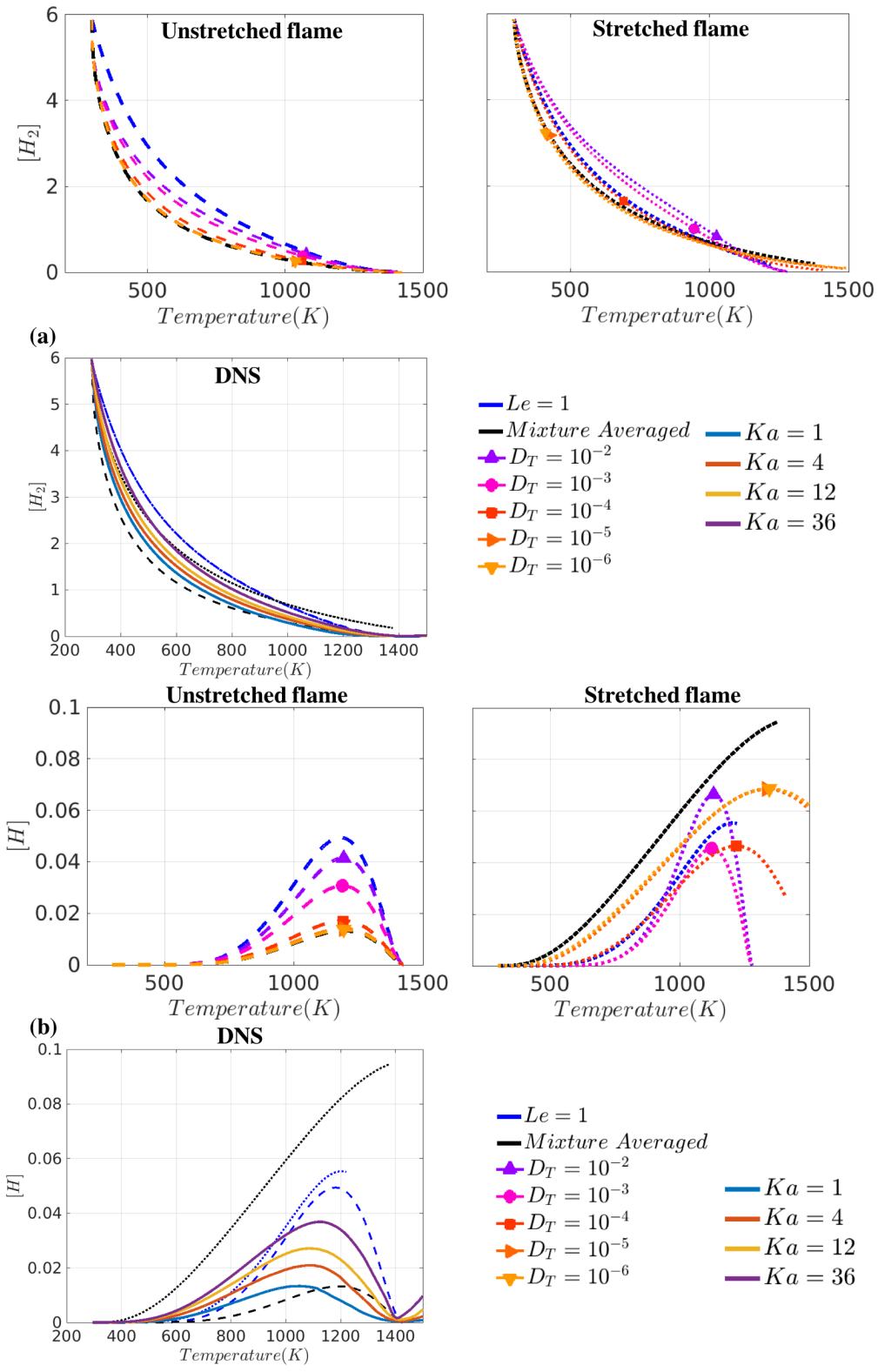

Figure 6.2. Variation of concentration for (a) H_2 and (b) H with temperature for different transport models for unstretched flames, stretched flames and DNS.

For the unstretched flame, increasing diffusivity pushes the fuel concentration profiles towards Le=1(in blue) profile. For the stretched flame profiles, increasing diffusivity (till $D_T = 10^{-4}$) moves the profiles towards the stretched flame Le=1(in blue) profile and $D_T = 10^{-4}$ shows a good agreement with this profile. With further increase, the profiles move past the $Le = 1$ profile. The DNS means move towards higher temperatures with increasing turbulence intensities. The Ka=36 profile sits close to the stretched mixture-averaged profile. For the high temperature radical, H, increasing diffusivity pushes the stretched flame profiles towards higher temperatures leading to reduced H concentrations in the low temperature regions. For a given transport model, increasing stretch, in general, pushes the profiles towards lower temperature. For example, for the mixture-averaged transport (in black), the unstretched profile shows a non-zero H concentration starting at ~700K whereas for the equivalent stretched flame, non-zero H concentration is seen at ~400K. Similarly, for $D_T = 10^{-4}$ non-zero H concentrations for unstretched and stretched flames are seen for temperatures greater than 700K and 450K respectively. Increasing turbulence intensity has a two-fold effect on the flame; firstly, increased wrinkling of the flame and hence increased stretch and secondly, increased scalar diffusivity. These two effects have an opposite effect on the concentration profiles i.e. increasing stretch leads to increased low temperature activity whereas increased diffusivity pushes the profiles towards higher temperatures. With increasing turbulence, the DNS profiles show increased H concentration in the low temperature region. For the turbulence intensities considered here, thus, the effect of stretch overpowers the effect of increased diffusivity leading to increased H concentration at lower temperatures.

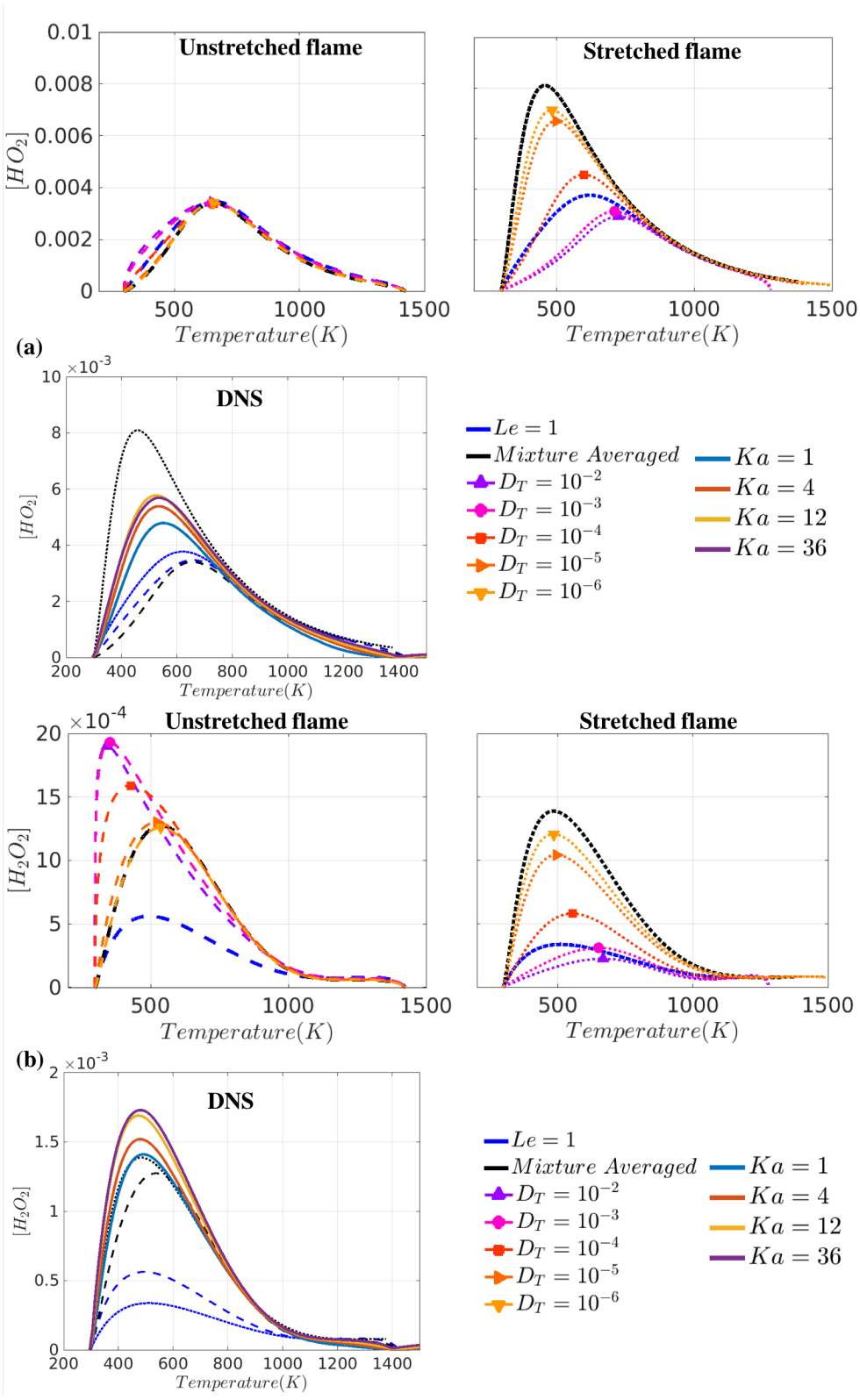

Figure 6.3. Variation of concentration for (a) HO_2 and (b) H_2O_2 with temperature for different transport models for unstretched flames, stretched flames and DNS.

Figure 6.3 plots the concentration variation of low temperature species HO_2 and H_2O_2 with temperature. For both the species, increasing diffusivity shifts the profiles towards lower temperatures for the unstretched flames. For the stretched flames, increasing diffusivity shifts the profiles towards higher temperatures leading to lower concentrations at lower temperatures. For example, for stretched flames, at ~400K, the HO_2 concentration is ~0.006 mol/m^3 and ~0.002 mol/m^3 for $D_T = 10^{-6}$ and $D_T = 10^{-4}$ respectively. Unlike the high temperature species, increasing stretch does not have a significant effect on the range of temperatures over which these species have a non-zero concentration. For example, HO_2 concentration start increasing from zero at temperatures ~300K for the unstretched and stretched flames for all the transport models. Increasing stretch leads to increased concentrations across all temperatures for the different transport models. For example, for the mixture-averaged transport and for models with $D_T = 10^{-6}, 10^{-5}, 10^{-4}$, the HO_2 concentrations for stretched flames are 2-4 times higher than the unstretched flame concentrations till ~800K. For higher values of D_T, the concentrations are comparable between the two profiles. For HO_2, increasing turbulence leads to increased concentrations at lower temperatures similar to an increasing stretch behavior.

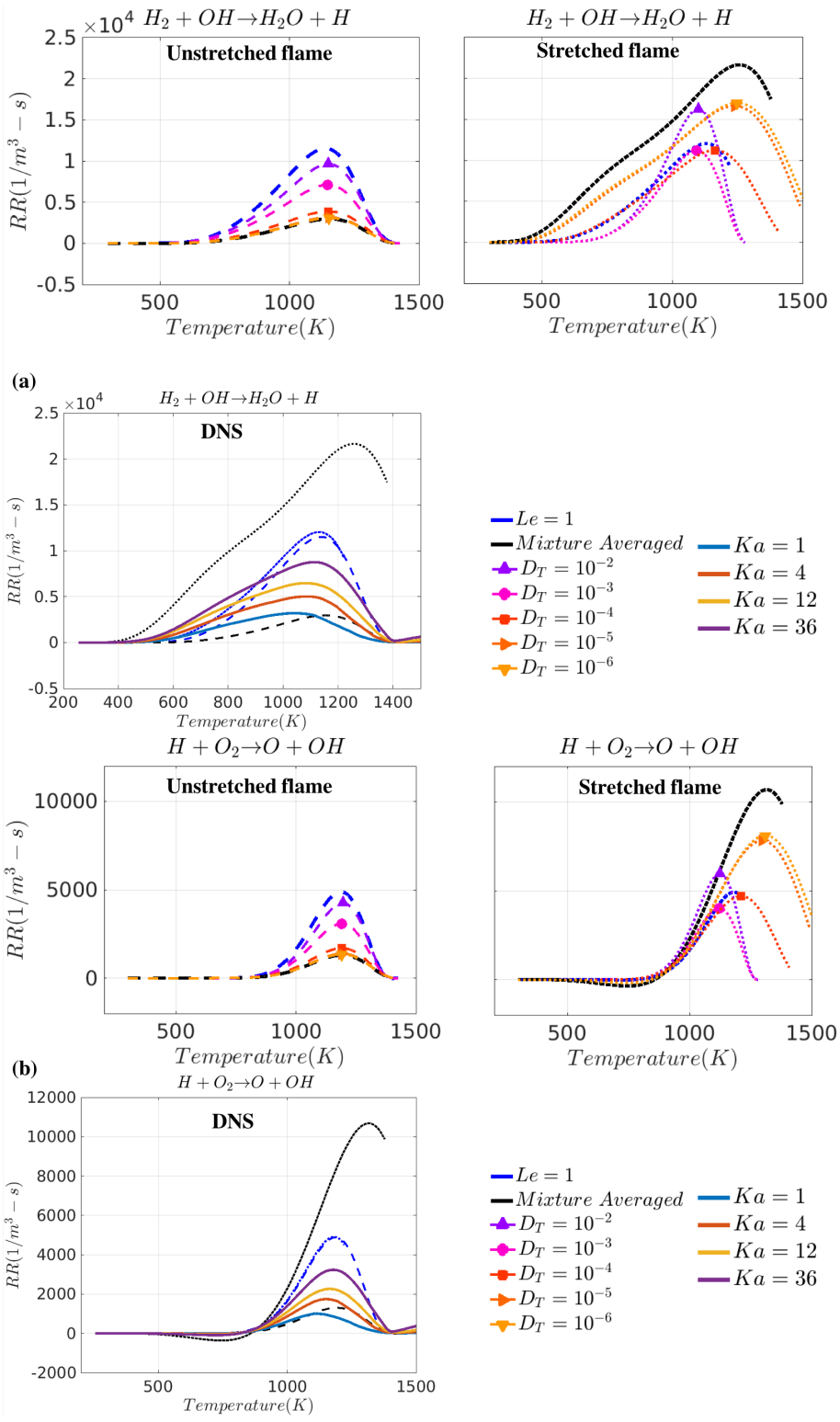

Figure 6.4. Variation of reaction rate for (a) H_2+OH→H_2O+H and (b) H+O_2→O+OH with temperature for different transport models for unstretched flames, stretched flames and DNS.

Focusing specifically on the key reactions, Figure 6.4 plots the reaction rate variation of H_2+OH→H_2O+H (dominant reaction in fuel oxidation) and H+O_2→O+OH(a key OH forming reaction). For both these reactions, $D_T = 10^{-4}$ profile is close to the $Le = 1$ profile for stretched flames. For highly stretched flames, increasing diffusivity moves the profiles towards higher temperature. Increasing turbulence increases the low temperature reaction rates for both the reactions and, in general, increases the reaction rates over the entire temperature range. This behavior is similar to the response of the involved species i.e. H_2, OH (similar to H), H, O_2(similar to H_2) wherein the effect of increasing stretch dominates over changes due to altered transport. Rates for reactions involving low temperature radicals are shown in Figure 6.5 and Figure 6.6. Similar observations can be made for these reactions i.e. increasing diffusivity leads to reduced reaction rates across the entire temperature range for stretched flames and, increasing stretch leads to increased low temperature reaction rates for a given transport model. This latter behavior is shown by the turbulent flame profiles suggesting a stronger effect of stretch on the chemistry of hydrogen flames compared to altered transport due to increased diffusivity. The global Lewis number for this flame is 0.36, leading to enhanced thermo-diffusive effects. Differential diffusion is also enhanced due to the high concentration of lighter species such as H_2. For the turbulent flames considered here, the increased diffusivity, due to increased turbulence, cannot overshadow the effect of molecular diffusivity and hence the profile behaviors are better represented by the stretched flame mixture-averaged profiles.

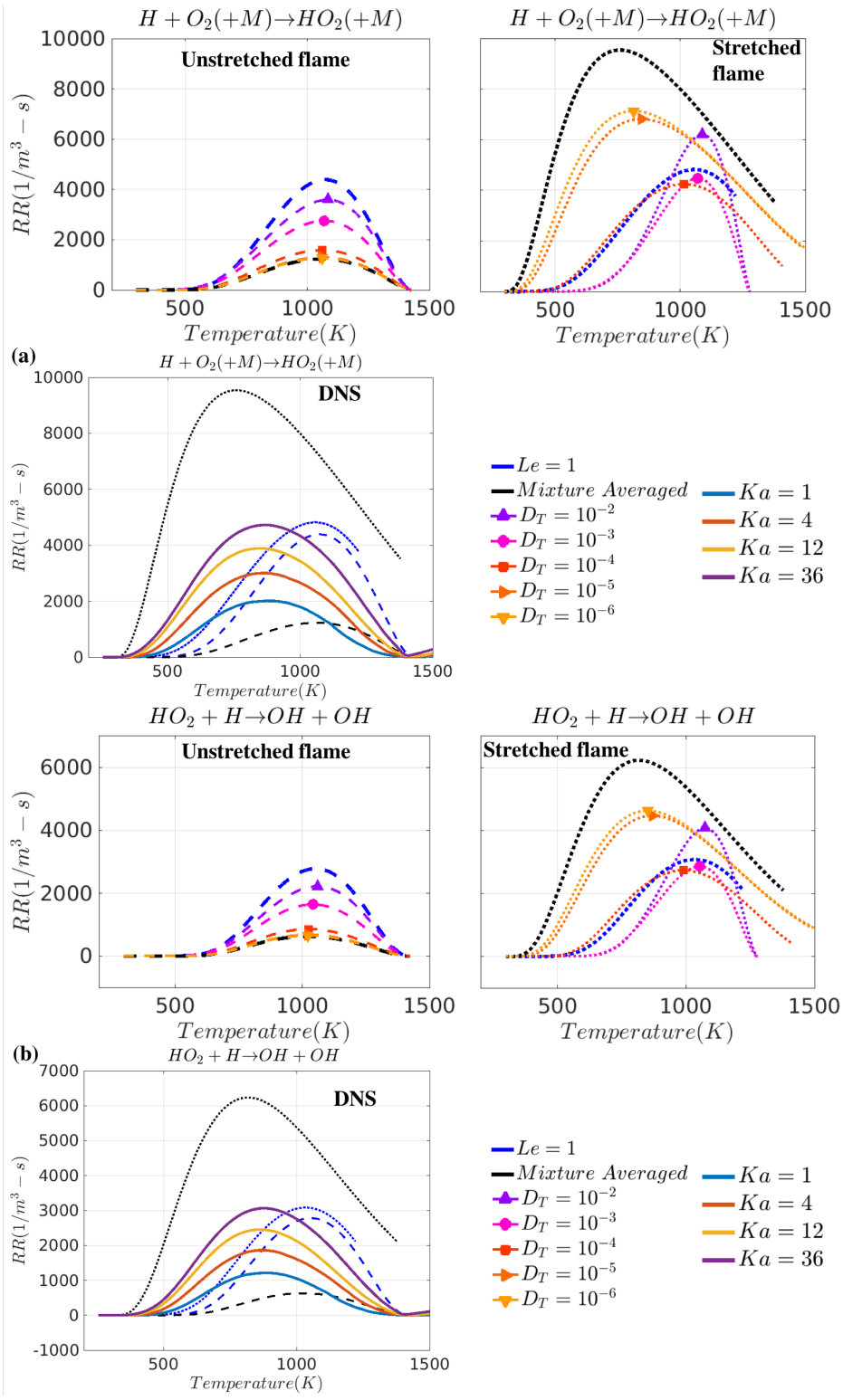

Figure 6.5. Variation of reaction rate for (a) H+O₂(+M)→HO₂(+M) and (b) HO₂+H→OH+OH with temperature for different transport models for unstretched flames, stretched flames and DNS.

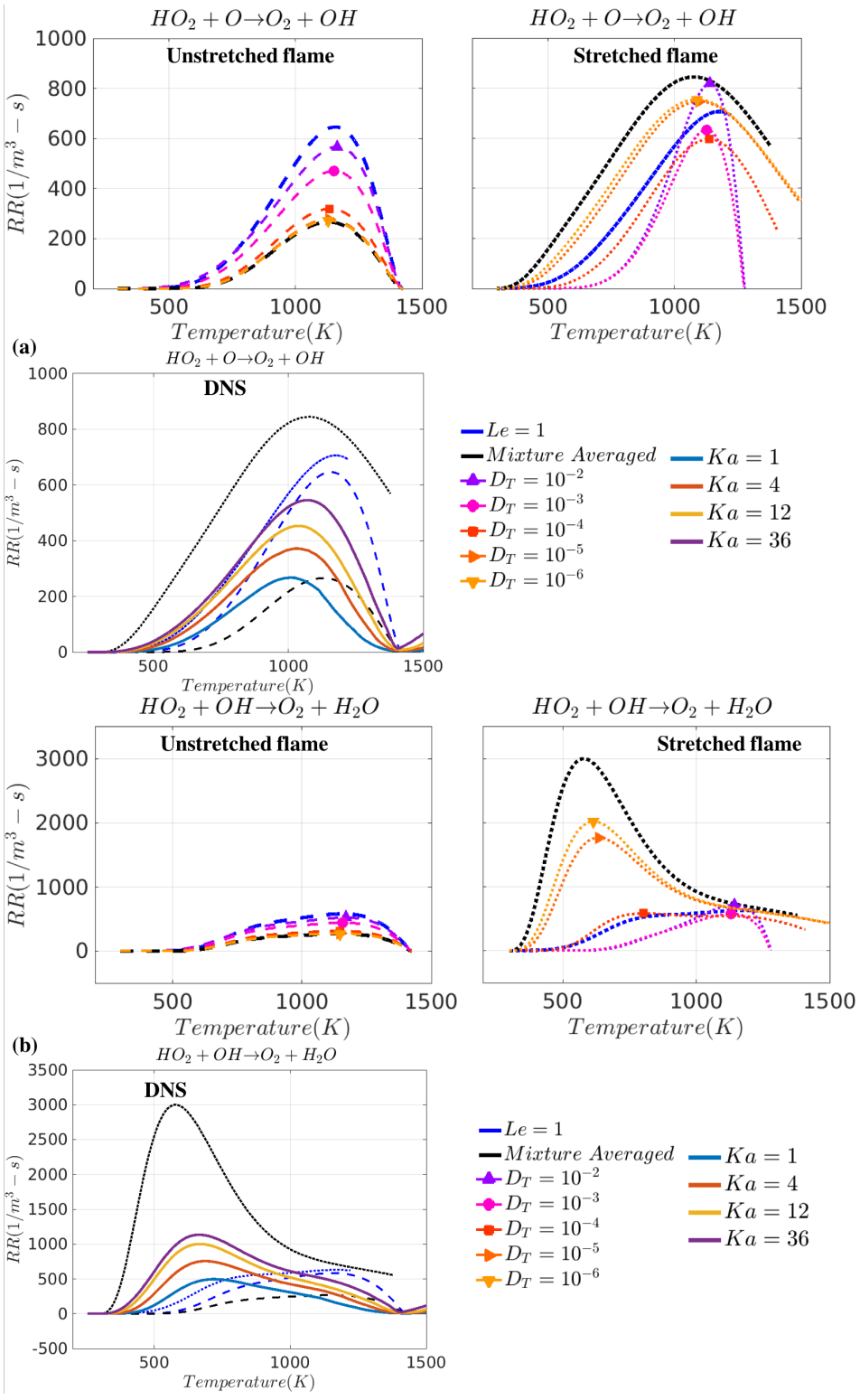

Figure 6.6. Variation of reaction rate for (a) HO_2+O→O_2+OH and (b) HO_2+OH→H_2O+O_2 with temperature for different transport models for unstretched flames, stretched flames and DNS.

6.3 Methane

This section compares the behavior of stretched and unstretched flame using the different transport models for lean methane/air flames. Typical values of mass diffusivity of key species are listed in Table 6.2. The maximum and minimum mass diffusivity of H_2 and H is an order of magnitude higher than the other involved species. Note the limited variation in the Lewis numbers for a given species based on these diffusivity values.

Table 6.2. Mass diffusivity for key species for methane flames

Species	Maximum $D_{i,m}$ (x10^{-4} m^2/s)	$Le_{D_{i,m},max}$	Minimum $D_{i,m}$ (x10^{-4} m^2/s)	$Le_{D_{i,m},min}$
H_2	16.81	0.29	0.79	0.28
H	28.61	0.17	1.22	0.18
O_2	4.56	1.06	0.2	1.1
OH	6.96	0.69	0.32	0.7
H_2O	6.18	0.78	0.22	0.99
HO_2	4.57	1.06	0.21	1.07
CH_3	5.05	0.95	0.22	0.99
CH_4	5.03	0.96	0.23	0.96
CO	4.53	1.06	0.21	1.07
CO_2	3.62	1.33	0.16	1.42
HCO	3.98	1.21	0.16	1.42
CH_2O	3.95	1.22	0.15	1.43
CH_3O	3.86	1.25	0.15	1.44

The global Lewis number for this flame is 0.96 (i.e. close to unity), calculated using the thermal diffusivity and mass diffusivity of the deficient fuel at inlet conditions. For most of the other species, the Lewis number is close to unity

The variations in heat release for the different models for unstretched, stretched and turbulent flames are plotted in Figure 6.7.

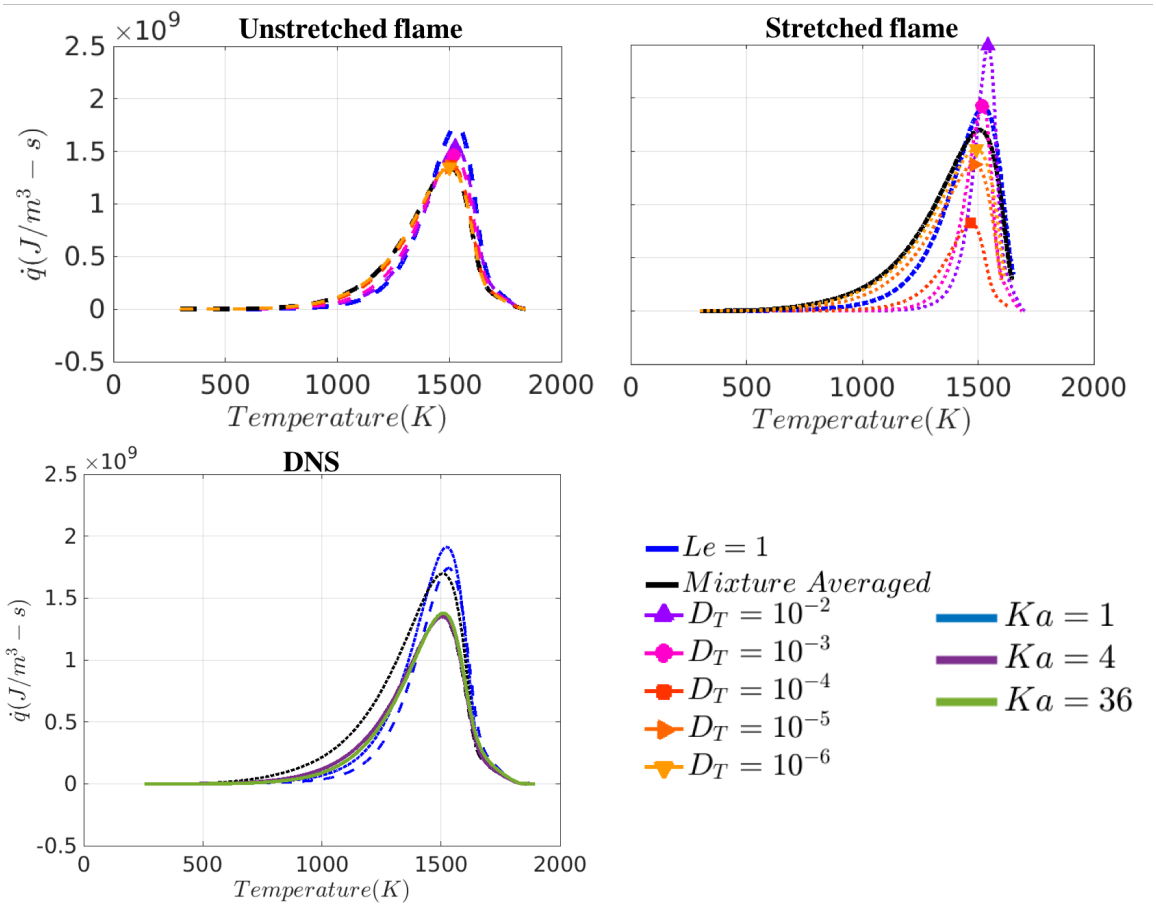

Figure 6.7. Variation of heat release with temperature for different transport models for unstretched flames, stretched flames and DNS.

Increasing diffusivity moves the heat release towards higher temperatures and progressively towards $Le = 1$ profile for the unstretched flames. $D_T = 10^{-6}$ profile is close in behavior to the unstretched flame profile. This is expected since this value is two orders of magnitude lower than typical mass diffusivity values. For the stretched flames, increasing diffusivity shifts the highly stretched flame profiles towards higher temperatures. The $D_T = 10^{-6}, 10^{-5}$ profiles move towards the $Le = 1$ profile. Higher values of diffusivity show a further decrease in low temperature heat release and move beyond the $Le = 1$ profile towards higher temperatures. This observation emphasizes the importance of the absolute value of the diffusivity constant, even though the ratio of the thermal and mass diffusivity at these higher values of D_T leads to a unity Lewis number. In general, significant variation in behavior is observed when the diffusivity of all species is an order of magnitude higher than the mass diffusivity obtained from mixture-averaged transport. Comparing the unstretched and stretched flame profiles, for the mixture-averaged, $D_T = 10^{-6}, 10^{-5}$ and $Le = 1$, an increased heat release at all temperatures can be observed. For example, for the mixture-averaged transport, the net heat release rate for the unstretched flame at 1000K is ~0.15x10^9 J/m^3-s, whereas for the stretched flame this value is ~0.25x10^9 J/m^3-s. For the turbulent flame, a significant change in heat release cannot be observed. The *Ka*=36 shifts slightly towards higher temperatures and potentially towards $Le = 1$ profile. This behavior is consistent with the behavior of highly stretched flames with increasing diffusivity highlighting the importance of increased scalar diffusivity for these flames.

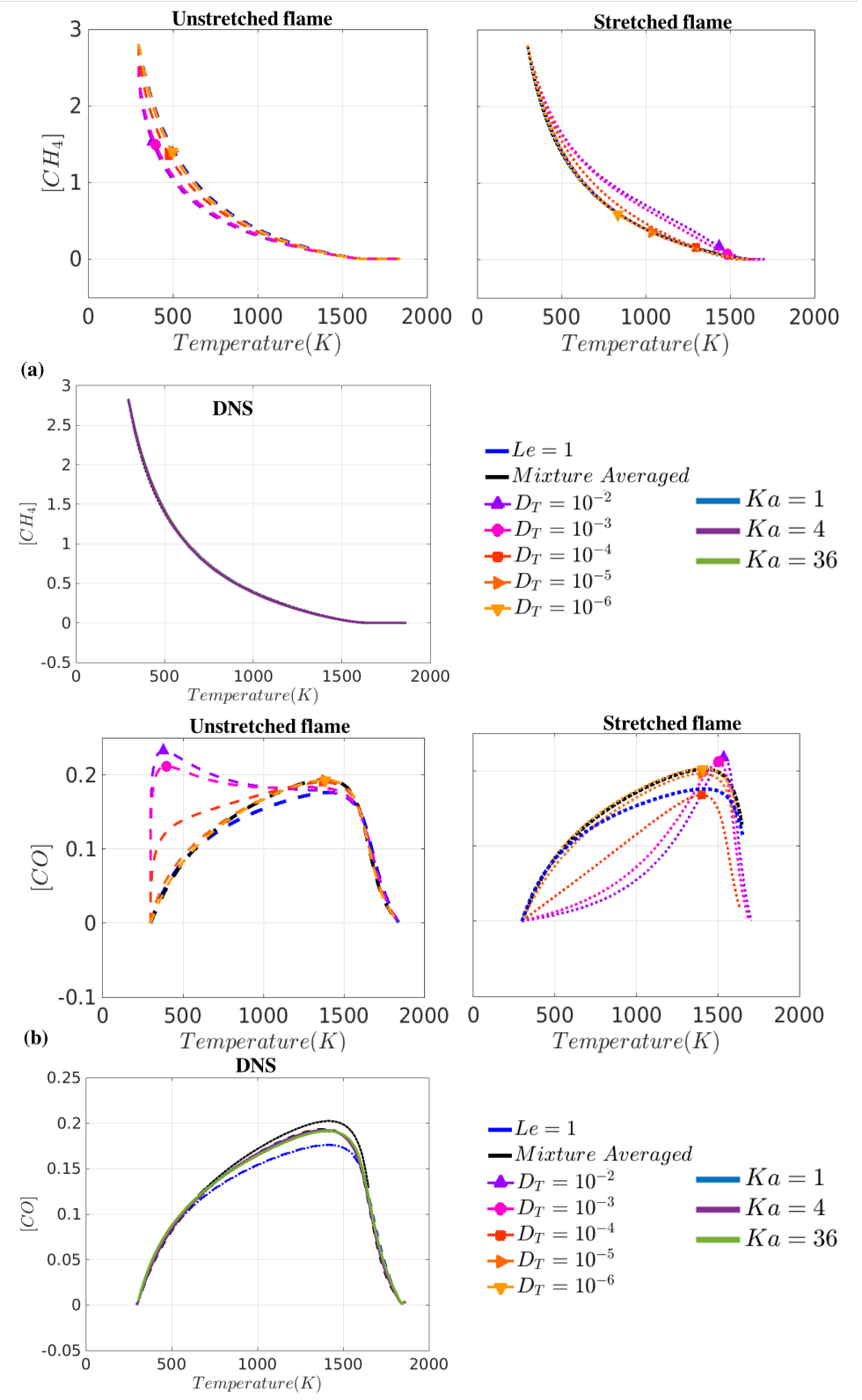

Figure 6.8. Variation of concentration for (a) CH_4 and (b) CO with temperature for different transport models for unstretched flames, stretched flames and DNS.

The effect of the altered transport on fuel and CO concentration is presented in Figure 6.8. For unstretched flames, increasing diffusivity moves the fuel concentration profiles towards slightly lower temperatures eventually moving towards $Le = 1$ profile. For the stretched flames, The $Le = 1$, $D_T = 10^{-6}, 10^{-5}$ and the mixture-averaged profiles are indecipherable from each other. Higher diffusivities shift the profiles towards higher temperatures. For the turbulent flames, there is no noticeable change in the fuel concentration profiles and they match well with the mixture-averaged and $Le = 1$ profiles. For a stable high temperature species such as CO, increasing diffusivity has a similar effect on the concentration profiles for the laminar flames as CH_4. For the turbulent flames, there is an insignificant change in the concentration profile and they align well with the unstretched laminar flame profile. Figure 6.9 plots the concentration profiles for high temperature radicals CH_3 and H. For CH_3, for unstretched flames, increasing diffusivity moves the profiles slightly towards higher temperatures without appreciable change in the peak concentration. This behavior is seen for the turbulent profiles as well. For H concentration, increasing diffusivity, for unstretched flames, pushes the profiles towards higher temperatures leading to lower concentrations for T<1300K. For higher temperatures, an increase in peak concentration (by ~50%) can be observed with increasing diffusivities. On the other hand, comparing unstretched and stretched flames, increasing stretch leads to higher concentration H concentrations in the low temperature regions. For example, for the mixture-averaged transport, there is a ~50% increase in H concentration at ~1000K between the unstretched and stretched flame profile. However, for the turbulent flames, there is a slight reduction in concentrations at lower temperatures and increased peak concentrations at higher temperatures. These observations are consistent with those

for unstretched flames with increasing diffusivity. In general, there is a strong correlation between the behavior of unstretched flames with increasing diffusivity and the turbulent flames with increasing turbulent intensity.

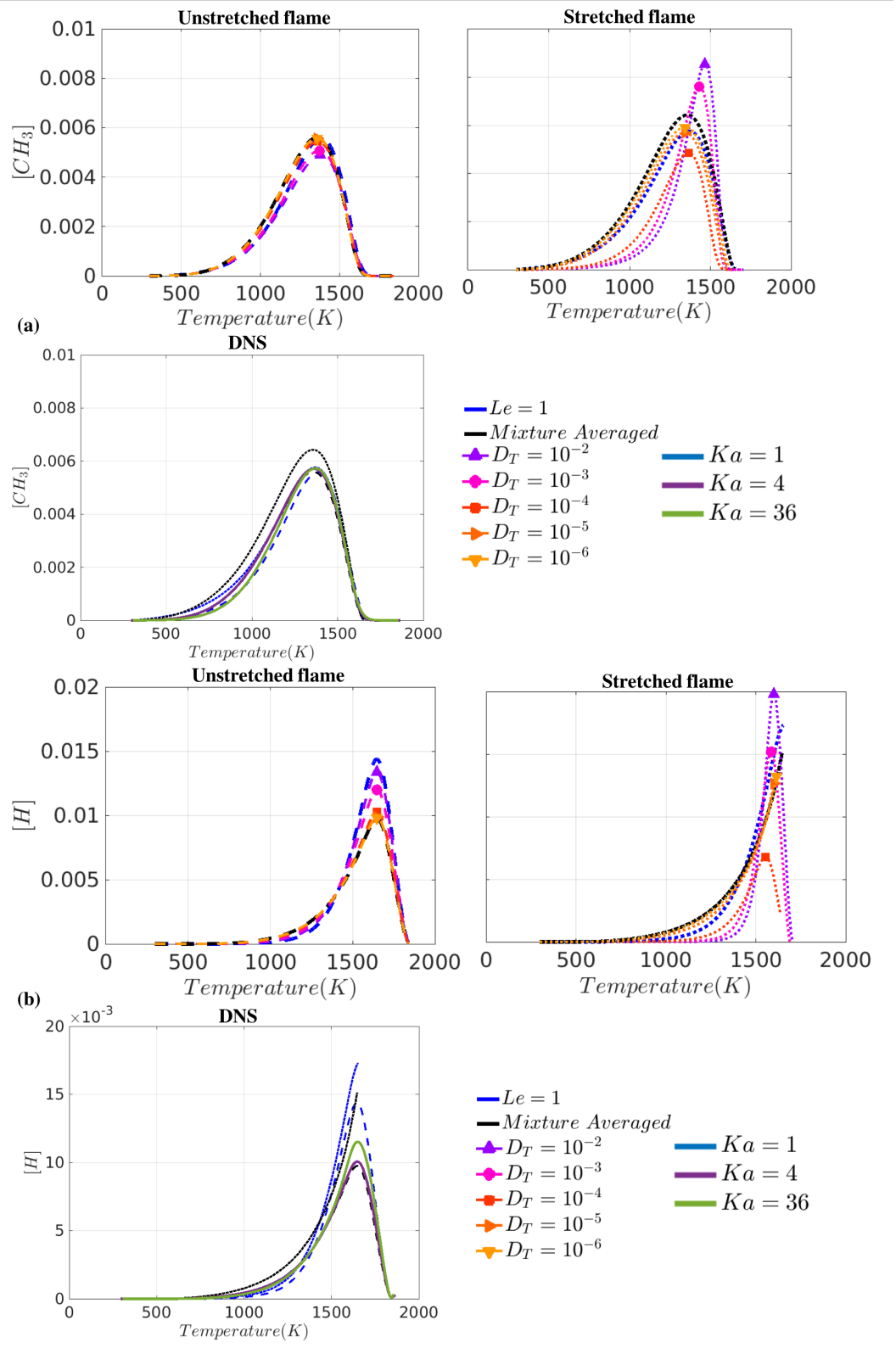

Figure 6.9. Variation of concentration for (a) CH_3 and (b) H with temperature for different transport models for unstretched flames, stretched flames and DNS.

A much more significant impact of turbulence can be seen for the low temperature species as shown in Figure 6.10. For both the species, with increasing diffusivity, the unstretched and stretched flame profiles move higher temperatures leading to reduced concentrations at lower temperatures. For HO_2, the peak concentration value occurs at ~750K for the mixture-averaged stretched and unstretched flame profiles. However, for the $Le = 1$ profile there is a reduction in concentration in the low temperature region with the peak occurring at ~1300K for both the laminar flames. This same behavior is shown by the turbulent flames, wherein increasing turbulence shifts the profiles towards higher temperatures with a reduction in concentration in the low temperature region in addition to shifting the peak concentration to higher temperatures. Comparing the impact of increasing flame stretch, an increase in concentration can be seen for the mixture-averaged, $Le = 1$ and $D_T = 10^{-6}, 10^{-5}$ between the stretched and unstretched profiles whereas for $D_T = 10^{-4}, 10^{-3}, 10^{-2}$, there is a significant reduction in concentrations for T <1400K. This latter observation is seen for turbulent flames as well. Concentrating specifically in regions where T<500K, it can be observed that the Ka=36 concentrations are lower than that predicted by $Le = 1$ profile. This shift beyond the $Le = 1$ further towards higher temperatures can be seen for the stretched flames with increased diffusivity. For CH_3O, similar conclusions can be drawn as HO_2 i.e. reduced concentrations and shift towards higher temperatures due to increased diffusivity for both laminar models. Thus, at lower temperatures (T<700K), these profiles correlate well with stretched flames with high diffusivity.

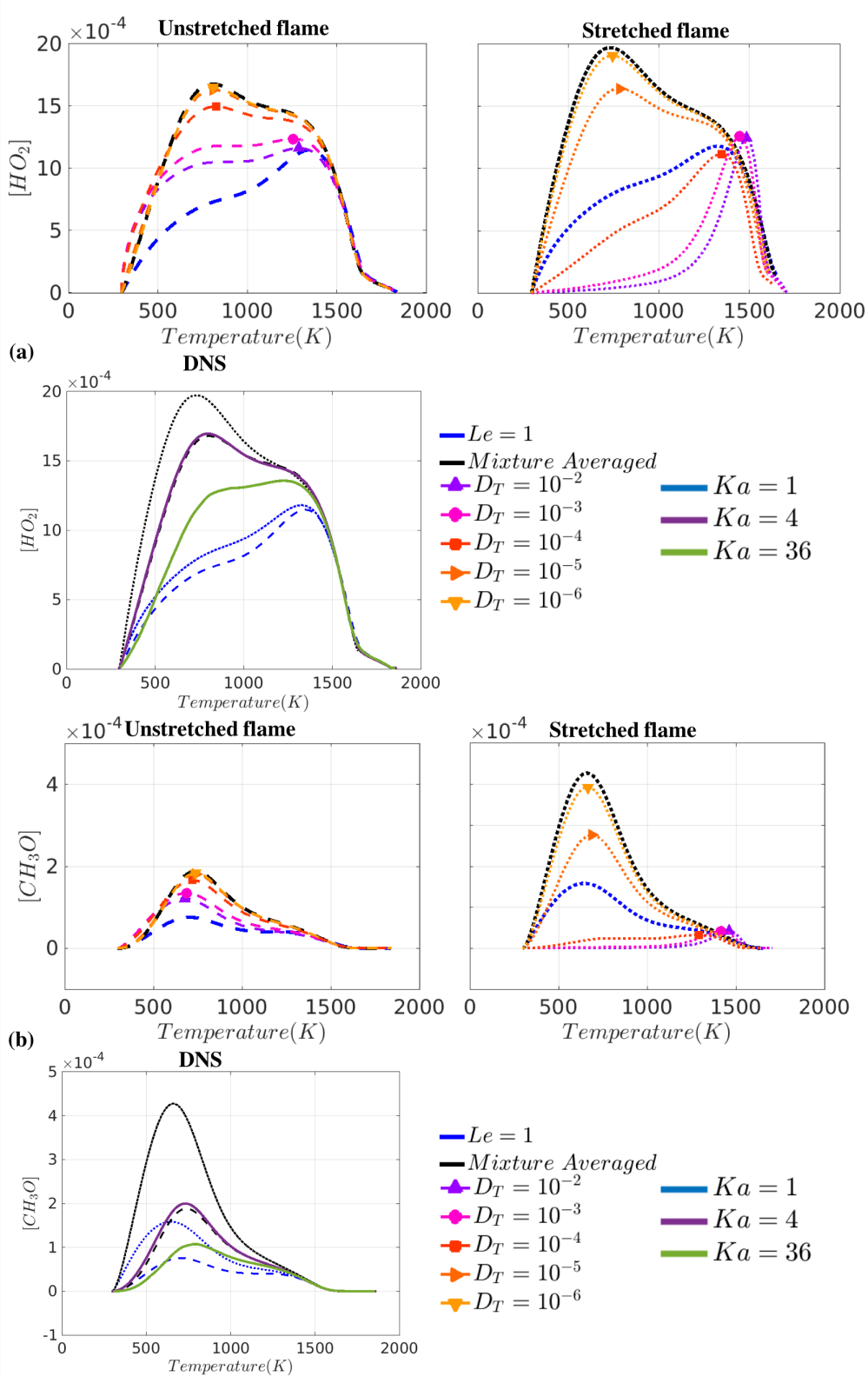

Figure 6.10. Variation of concentration for (a) HO_2 and (b) CH_3O with temperature for different transport models for unstretched flames, stretched flames and DNS.

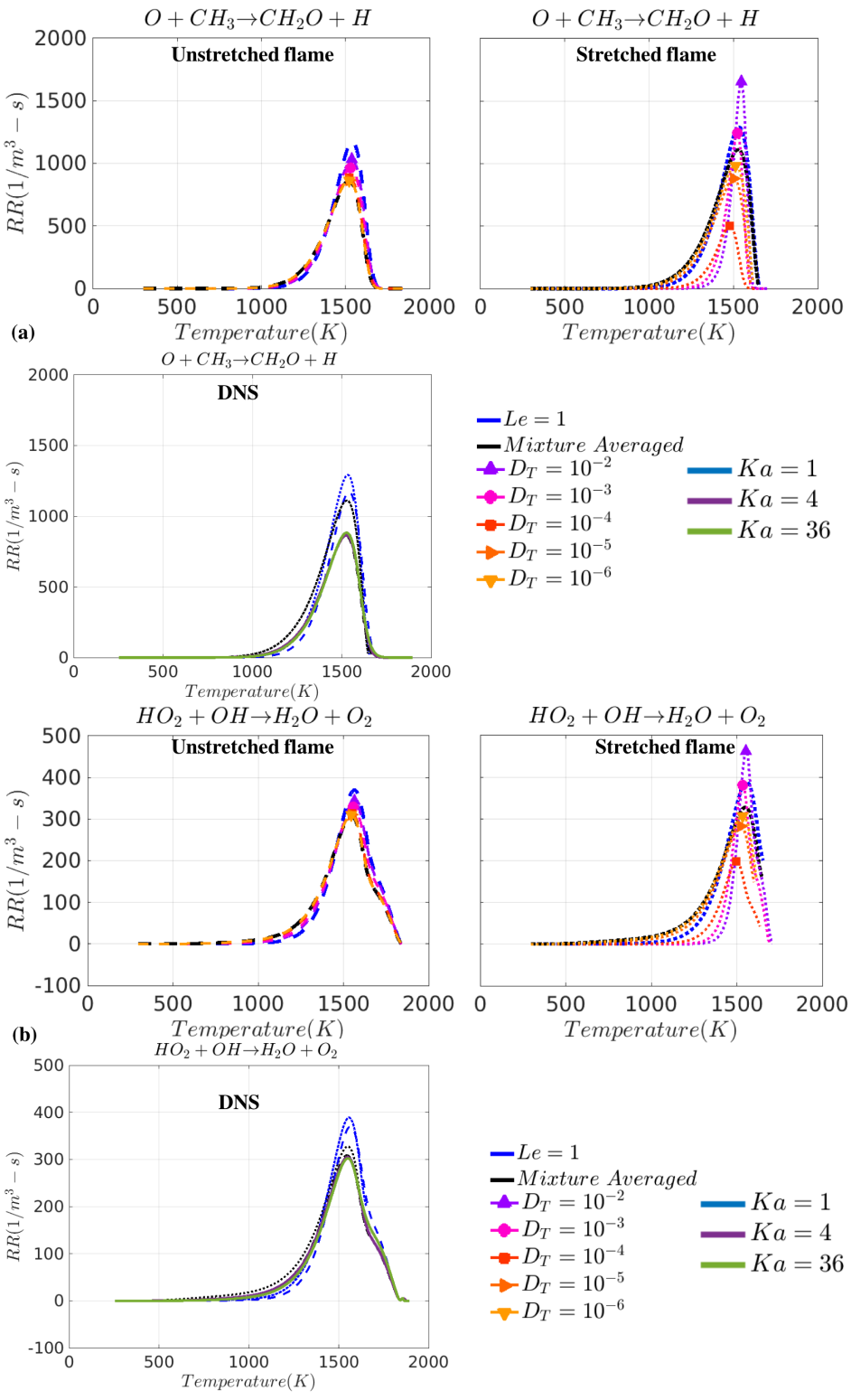

Figure 6.11. Variation of reaction rate for (a) $O+CH_3 \rightarrow CH_2O+H$ and (b) $HO_2+OH \rightarrow H_2O+O_2$ with temperature for different transport models for unstretched flames, stretched flames and DNS.

Figure 6.11 plots the reaction rate variation for two key reactions involved in methane oxidation. For the dominant heat release reaction, $O+CH_3 \rightarrow CH_2O+H$, the laminar profiles move slightly towards higher temperatures with ~50% increase in the peak reaction rate between the mixture-averaged and $Le = 1$ profile for both the stretched and unstretched flames. The turbulent profiles are not significantly impacted by turbulence potentially due to the negligible impact of turbulence on the CH_3 profiles. In general, for both the reactions, increasing diffusivity has a fairly limited impact on the reaction rate profiles and aids in pushing the profiles marginally towards higher temperatures. Even though the reaction $HO_2+OH \rightarrow H_2O+O_2$ involves HO_2, which is significantly impacted by turbulence, the reaction rate remains invariant due to the presence of OH. OH is produced at higher temperatures and is not significantly affected by increased diffusivity. Figure 6.12(a) plots the other key heat release reaction $OH+CO \rightarrow CO_2+H$ which involves CO and OH which are not impacted significantly by diffusivity for the turbulence intensities considered. Figure 6.12(b) plots the reaction rate for $H+O_2(+M) \rightarrow HO_2(+M)$,which was identified as a key player in the hydrogen oxidation process as well. At lower temperatures, the shift towards higher temperatures and hence towards $Le = 1$ can be explained by the increased diffusivity seen in this temperature regime. Note in this regime, increasing stretch should have led to increased reaction rate but, this is not observed for the turbulent flames. An increase in the reaction rate at temperatures greater than 1500K can be attributed to the increasing diffusivity which leads to increased reaction rates for the unstretched laminar flames. Overall, for these reactions, a stronger correlation can be seen between the unstretched profiles with increasing diffusivity and the turbulent profiles with increasing intensity.

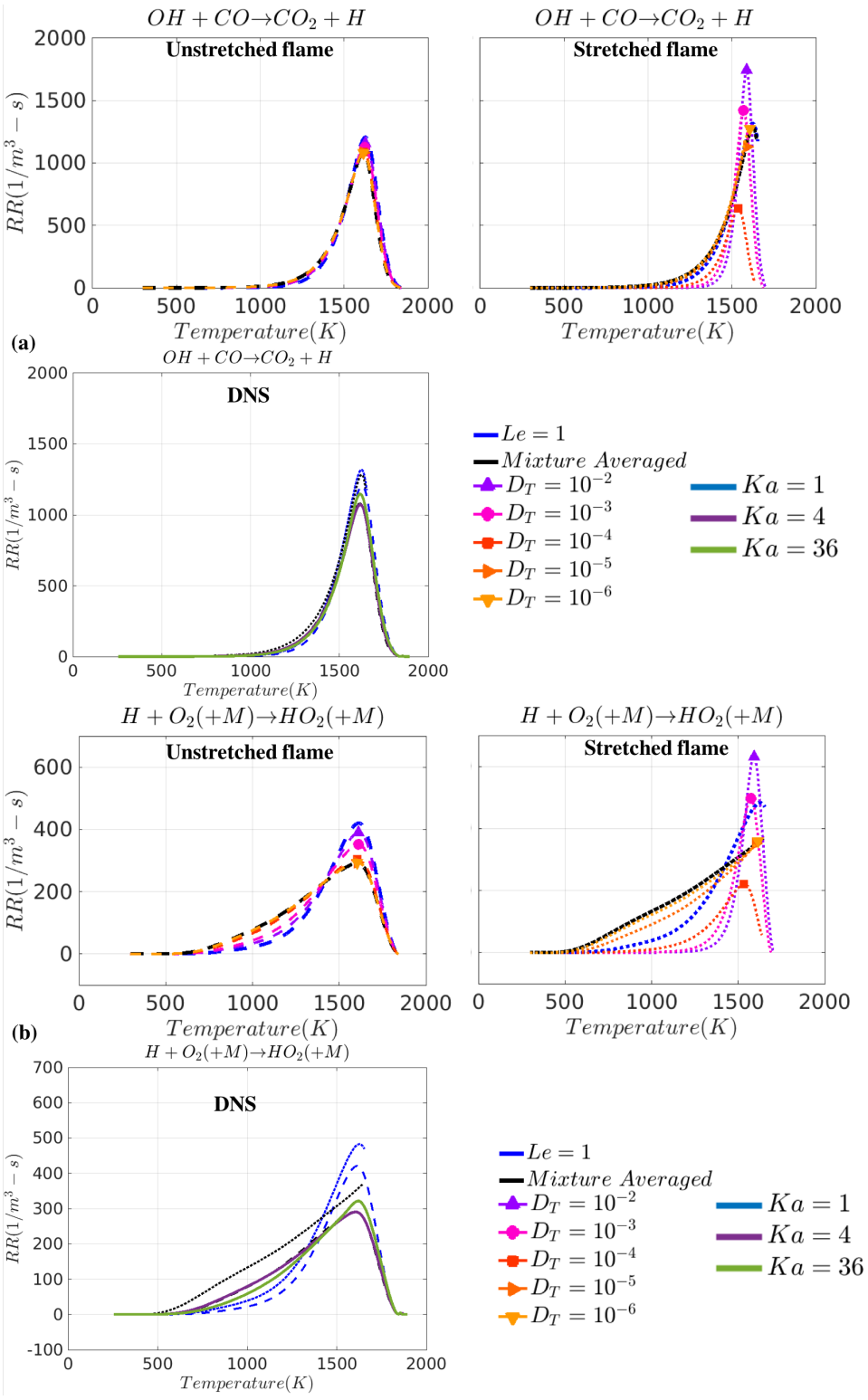

Figure 6.12. Variation of reaction rate for (a) OH+CO→CO_2+H and (b) H+O_2(+M)→HO_2(+M) with temperature for different transport models for unstretched flames, stretched flames and DNS.

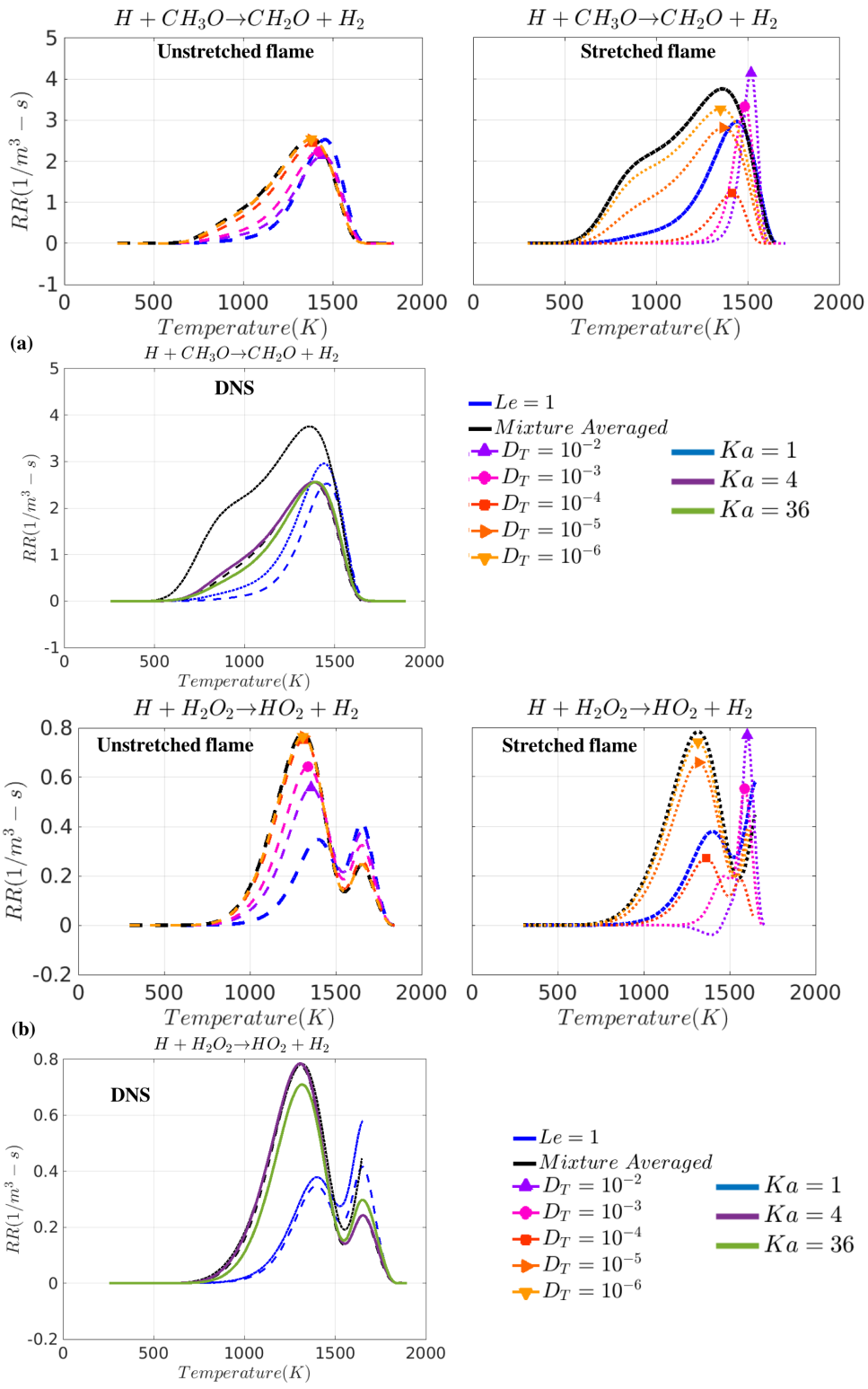

Figure 6.13. Variation of reaction rate for (a) $H+CH_3O \rightarrow CH_2O+H_2$ and (b) $H+H_2O_2 \rightarrow HO_2+H_2$ with temperature for different transport models for unstretched flames, stretched flames and DNS.

Reactions of secondary importance are affected by these altered transport models similar to the dominant reactions. The dominant path for CH_2O formation is via CH_3. A secondary pathway is through CH_3O. The reaction $H+CH_3O \rightarrow CH_2O+H_2$ is a dominant player in this pathway. The effect of increased diffusivity on the turbulent flames mimics the behavior of unstretched flames with increasing diffusivity in the lower temperature regime. A similar response can be seen for $H+H_2O_2 \rightarrow HO_2+H_2$ (a secondary pathway for HO_2 formation).

For the close to unity Lewis number flames, stretch plays a limited role in determining species concentrations and reaction rates for turbulent flames. The only species which show a finite stretch response are the low temperature species such as HO_2 for $T<700K$. In general, all the other species and reaction rates profiles for turbulent flames bear a strong resemblance to the behavior of unstretched flames with increasing diffusivity.

6.4 n-dodecane

This section compared the behavior of stretched and unstretched flame using the different transport models for lean n-dodecane/air flames. Typical values of mass diffusivity of key species are listed in Table 6.3. The global Lewis number for this flame is 4.36 and is calculated using the thermal diffusivity and mass diffusivity of the deficient fuel at inlet conditions. This flame is thus, susceptible to thermo-diffusive effects.

Table 6.3. Mass diffusivity for key species for n-dodecane flames

Species	Maximum $D_{i,m}$ (x10^{-4} m^2/s)	$Le_{D_{i,m},max}$	Minimum $D_{i,m}$ (x10^{-4} m^2/s)	$Le_{D_{i,m},min}$
H	29.34	0.17	1.2	0.17
OH	7.11	0.68	0.31	0.66
HO_2	4.66	1.04	0.2	1.02
H_2	17.25	0.28	0.78	0.26
CH_3	5.17	0.94	0.22	0.94
HCO	4.07	1.19	0.15	1.36
CH_2O	4.04	1.2	0.15	1.37
CH_3O	3.95	1.23	0.15	1.38
CO	4.63	1.05	0.2	1.02
CO_2	3.67	1.32	0.15	1.36
nC_3H_7	2.77	1.76	0.11	1.86
C_5H_{10}	2.25	2.16	0.08	2.45
$nC_{12}H_{26}$	1.39	3.48	0.05	4.36

Pyrolysis breaks down the fuel into fuel fragments. These species are generally large and have low diffusivity. Their maximum and minimum mass diffusivity are almost 1-3 orders of magnitude smaller than the other involved species. On the other hand, lighter species such as H_2 and H have a much higher diffusivity (almost an order of magnitude higher) compared to most of the other species involved.

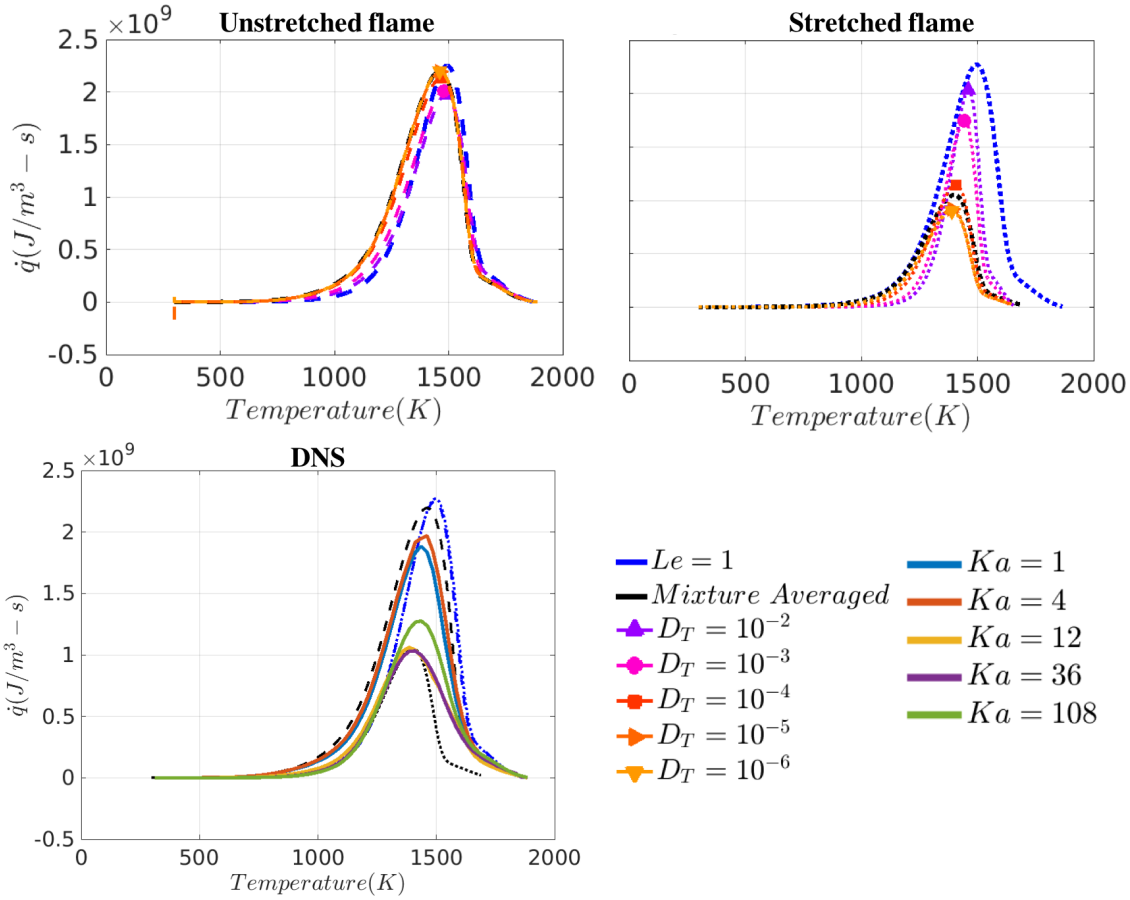

Figure 6.14. Variation of heat release with temperature for different transport models for unstretched flames, stretched flames and DNS.

Figure 6.14 plots the variation of heat release for unstretched, stretched for different transport models and compares them with turbulent flames. Mixture-averaged transport and $Le = 1$ are overlaid with the turbulent profiles. For the unstretched flames, increasing

diffusivity moves the heat release towards higher temperatures eventually towards $Le = 1$ profile. For the stretched flames, increasing diffusivity shifts the profiles towards higher temperatures as well. Unlike unstretched flames, these stretched flames have a significant increase in heat release rates with increasing diffusivity. For example, the peak heat release for the stretched mixture-averaged flame is ~1x10^9 J/m^3-s whereas the peak heat release for $D_T = 10^{-2}$ is ~2x10^9 J/m^3-s. Finally, increasing stretch, pushes the profiles towards higher temperatures. For example, for the unstretched mixture-averaged transport, non-zero heat release can be at ~750K whereas for the equivalent stretched flame, this temperature is close to ~900K. Comparing the different turbulent flame profiles, many interesting observations can be made. Firstly, *Ka*=1 and *Ka*=4 align well with the unstretched laminar flame profile. Secondly, between *Ka*=1 and *Ka*=4, a slight increase in heat release can be seen for *Ka*=4 compared to *Ka*=1. The flame topology does not change significantly between these two turbulent flames which can be seen in Figure 4.28. An increased turbulence intensity leads to a slightly higher diffusivity leading to the marginal increase in heat release. The *Ka*=12 and 36 profiles move towards higher temperatures, have reduced peaks and align well with the mixture-averaged stretched flame calculation. This change can be attributed to increased stretched from *Ka*=1,4 profiles. Another point to note here is the alignment of *Ka*=12, 36,108 profiles with $Le = 1$ and stretched flame profiles for T<1200K suggesting a combined influence of diffusivity and stretch in this region. Finally, for *Ka*=108 an increase in peak heat release compared to *Ka*=12,36 can be seen. This observation can be attributed to the effect of increased diffusivity on stretched flames wherein increasing diffusivity leads to increased heat release for the highly stretched flames.

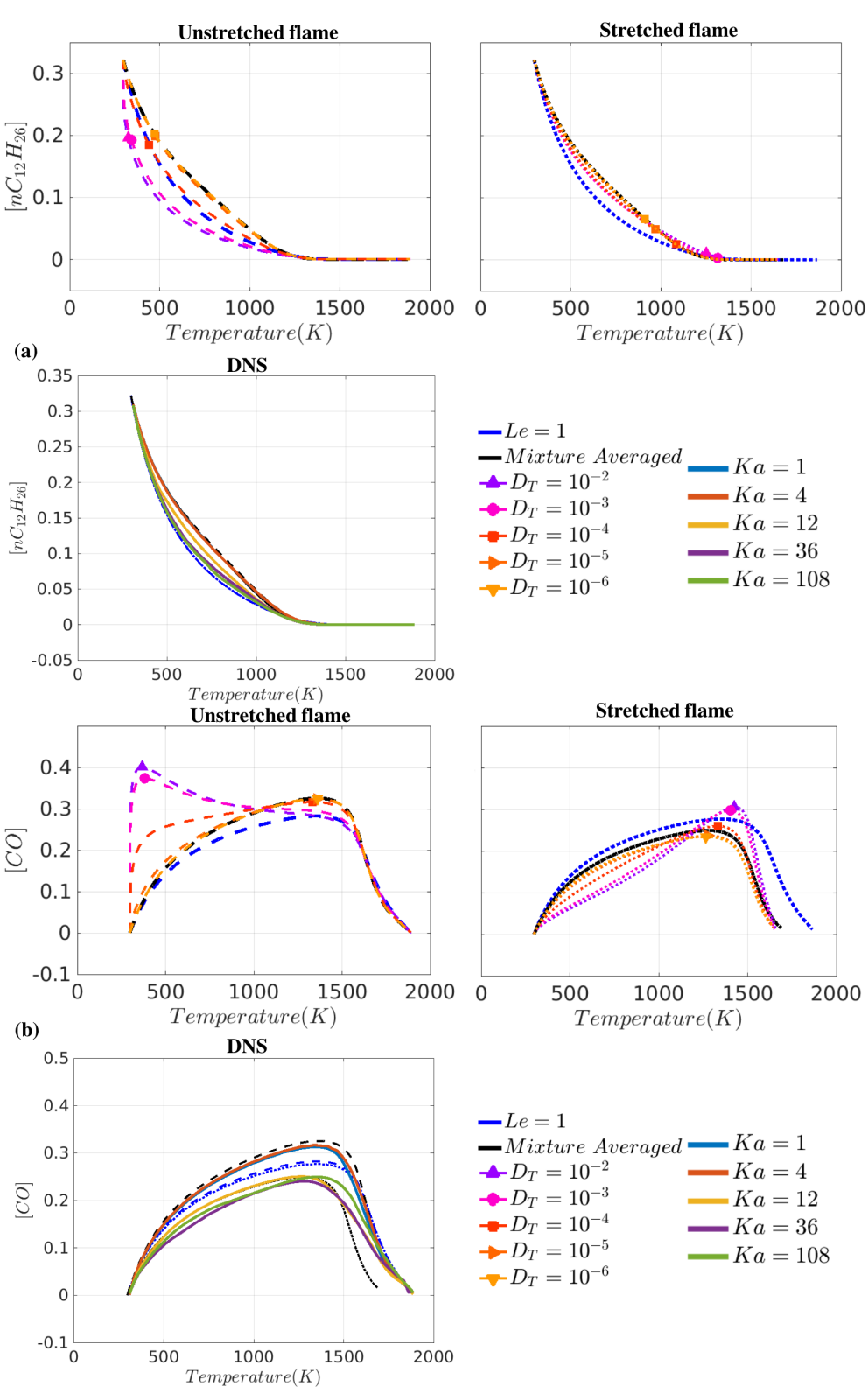

Figure 6.15. Variation of concentration for (a) nC$_{12}$H$_{26}$ and (b) CO with temperature for different transport models for unstretched flames, stretched flames and DNS.

Figure 6.15 plots the variation of fuel concentration and a stable high temperature species, CO for the different transport models. For the fuel concentration, increasing diffusivity, in general, tends to shift the profiles towards lower temperatures. *Ka*=1,4 profiles align closely with the mixture-averaged profiles (note the stretched and unstretched flame profiles do not significantly change for the fuel concentration). Increasing turbulence pushes the profiles towards lower temperatures moving towards $Le = 1$ emphasizing the importance of increased diffusivity. For CO, the unstretched profile move towards lower temperatures with increased diffusivity. At higher turbulence intensities (and hence diffusivity) the flames are seldom unstretched and hence the high diffusivity profiles ($D_T = 10^{-2}, 10^{-3}$) are not physically achievable in turbulent flames. For stretched flames, the profiles move to higher temperatures with increasing D_T. The $Le = 1$ for CO shows an increased low temperature concentration compared to stretched flame for mixture-averaged transport i.e. the stretched flame profiles do not move towards $Le = 1$ profile. With increasing turbulence, the turbulent flame profiles move towards higher temperatures. This feature is captured by the highly stretched flame profiles with increasing diffusivity. *Ka*=12,36,108 also show a reduced concentration compared to *Ka*=1,4 at higher temperatures. This behavior is consistent with the change from unstretched to stretched flames. For example, for the unstretched mixture-averaged transport, the peak concentration of CO is 0.32 mol/m^3 whereas, for the stretched flame it is 0.25 mol/m^3. Thus, stretch and diffusivity play a role in determining the behavior of the CO concentration profiles. A strong correlation can be seen in the behavior of these species in turbulent flames with stretched flames with increasing diffusivity.

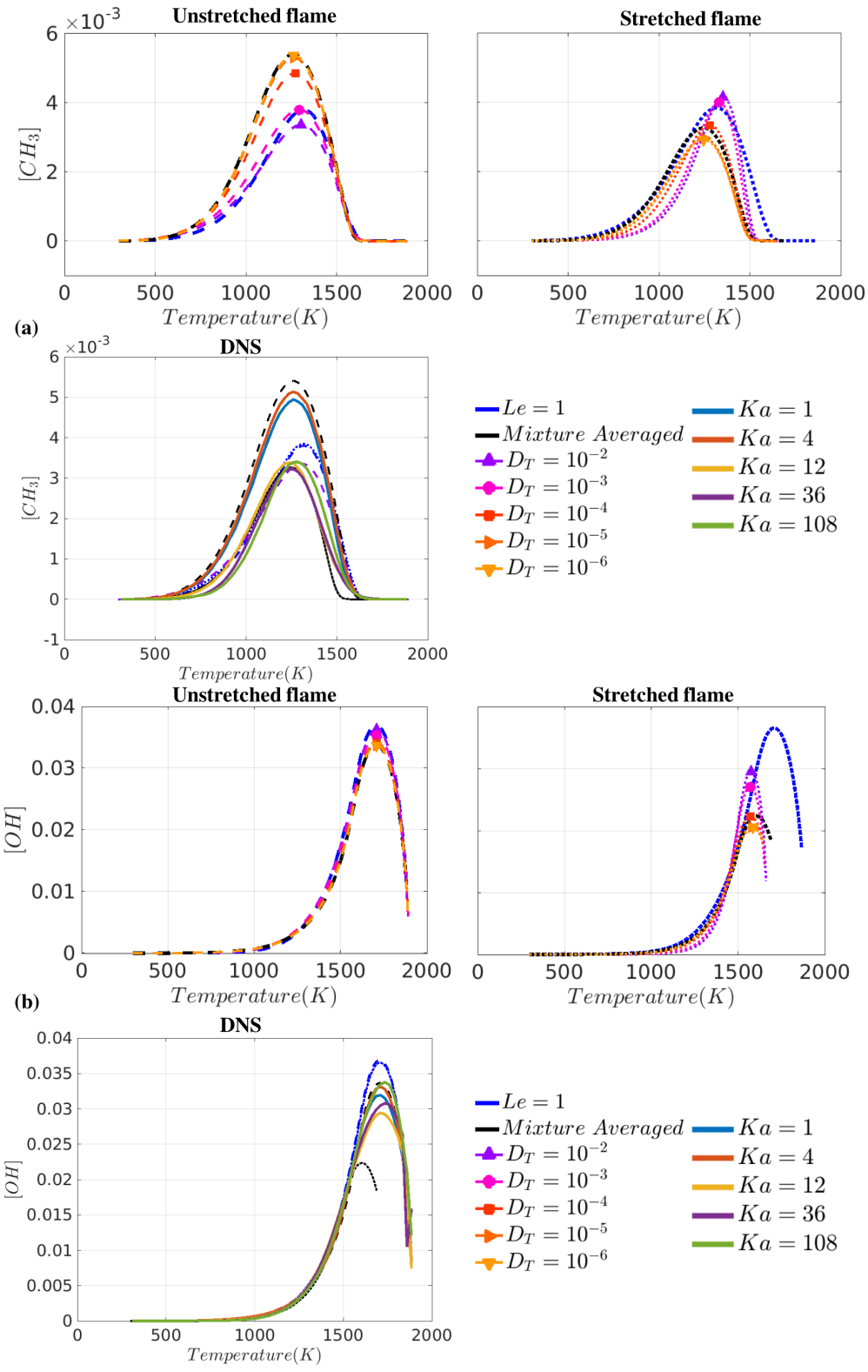

Figure 6.16. Variation of concentration for (a) CH_3 and (b) OH with temperature for different transport models for unstretched flames, stretched flames and DNS.

CH_3 shows a similar behavior as CO as seen in Figure 6.16(a). The CH_3 concentration turbulent flame profiles are influenced by stretch which is indicated by the reduced peak concentration in addition to the reduced low temperature concentration. These profiles are influenced by diffusivity as well. It can be observed that Ka=36,108 move beyond the $Le = 1$ profile with a reduced low temperature concentration. This is consistent with the behavior of highly stretched flames subjected to increasing diffusivity. The turbulent flame profiles for OH concentrations show a similar story wherein the profiles are affected by stretch leading to a reduction in the peak concentrations (from *Ka*=1, 4 to *Ka*=12, 36) followed by a coupled effect of stretch and diffusivity which leads to an increase in the peak concentrations (from *Ka*=36 to *Ka*=108). The non-monotonicity in the change in peak concentrations is captured by these stretched flames with high diffusivity.

These non-unity Lewis number flames are strongly affected by stretch. Increased diffusivity does not overshadow the influence of stretch but couples with it leading to concentration profiles that can deviate from $Le = 1$ profile. This is considered the limit wherein turbulent mixing takes over molecular transport and the effective thermal and mass diffusivity are the same. It should be emphasized here that the value of the diffusivities is equally important. A high value of diffusivity, such as $D_T = 10^{-2}, 10^{-3}$, are 1-2 orders of magnitude higher than the typical values of mass diffusivity and in this high diffusivity limit the overall mass diffusivity ($D_{i,m} + D_T$) and thermal diffusivity ($\alpha_{i,m} + D_T$) tend to D_T leading to $Le = 1$ for all species. But the profiles for stretched flames for $Le = 1$ compared to $D_T = 10^{-2}, 10^{-3}$ are significantly different. This point is further emphasized by the concentration profiles for low temperature species such as CH_2O and HO_2 in Figure 6.17 and selected fuel fragments in Figure 6.18.

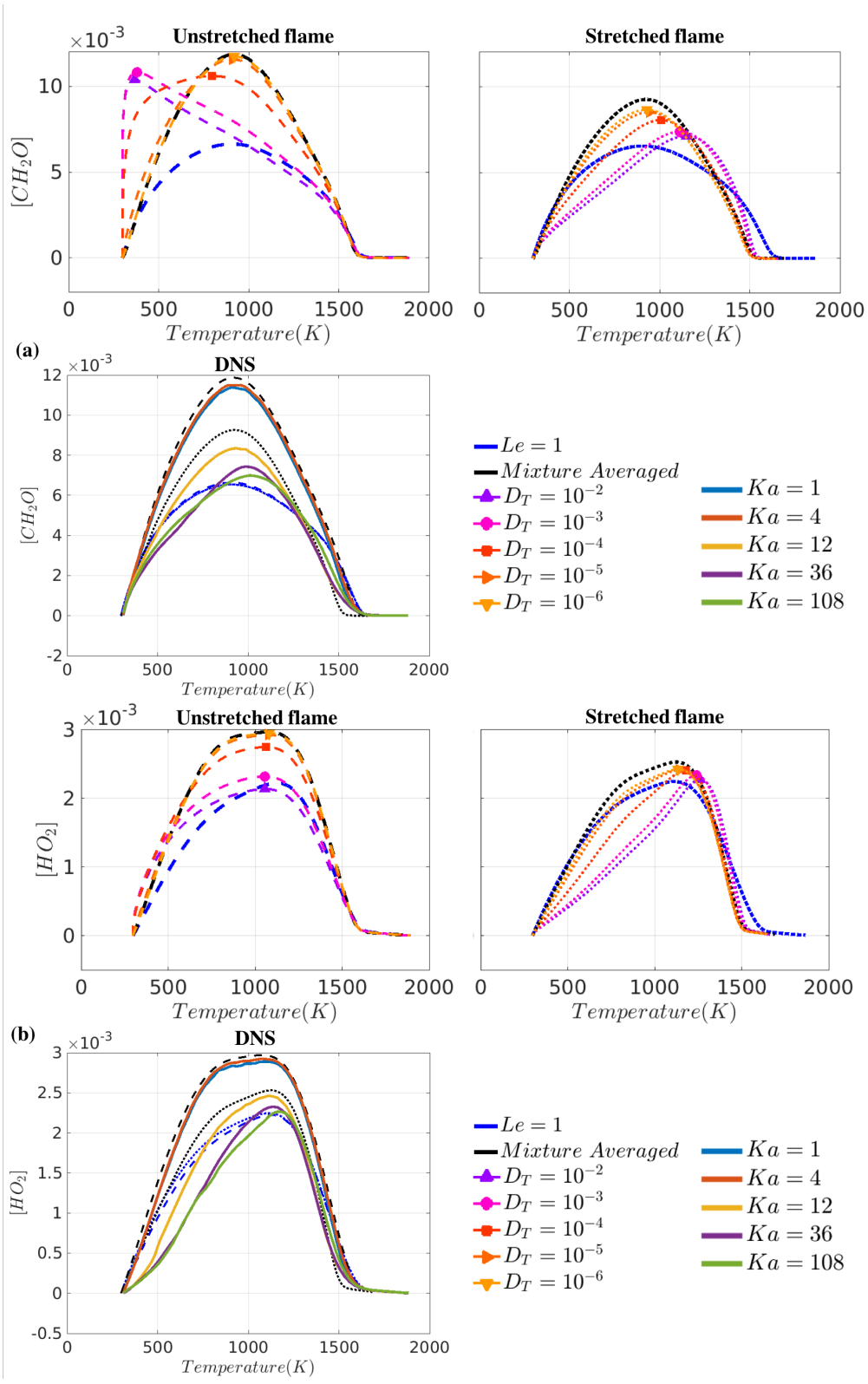

Figure 6.17. Variation of concentration for (a) CH_2O and (b) HO_2 with temperature for different transport models for unstretched flames, stretched flames and DNS.

For the highly stretched flame profiles, increasing diffusivities moves the profiles towards higher temperatures and reduced concentration are lower temperatures. For example, at ~700K, the CH_2O concentration for the mixture-averaged transport is $8x10^{-3}$ mol/m^3 whereas for $D_T = 10^{-2}$ this value is $5x10^{-3}$ mol/m^3. The profiles also significantly deviate from the $Le = 1$ profile as can be seen in Figure 6.17(a). For the turbulent flames, as expected the lower turbulent intensities of *Ka*=1,4 align closely with the unstretched profile. Increasing turbulence intensities first leads to a drop in peak concentration (for *Ka*=12 compared to *Ka*=1,4) which is explained by the enhanced effect of stretch, since there is a dip in concentration for all transport models between the stretched and unstretched flame profiles. Finally, for the higher turbulence intensities (*Ka*=36,108) the concentration profiles move further towards higher temperature regions; a phenomenon not captured by the $Le = 1$ profile but clearly shown by the stretched flames with high diffusivity. This same conclusion can be drawn for HO_2 profiles. The *Ka*=36,108 profiles show a stronger resemblance with the high diffusivity stretched flames profiles opposed to the $Le = 1$ profile. For the fuel fragments in Figure 6.18 there is a strong similarity in the response of nC_3H_7 compared with these low temperature species/radicals. Increasing turbulence intensities shifts to the profiles towards higher temperatures and leads to reduced peak concentrations; all features captured by stretched flames with increasing diffusivity. An interesting feature can be observed for C_5H_{10}. Increasing turbulence leads to increased concentrations at *T*<500K for *Ka*=12,36,108. This feature is also shown by the $Le = 1$ profile. However, the overall response of the profiles closely follows the stretched flames which also show this increased low temperature concentration with increasing diffusivity.

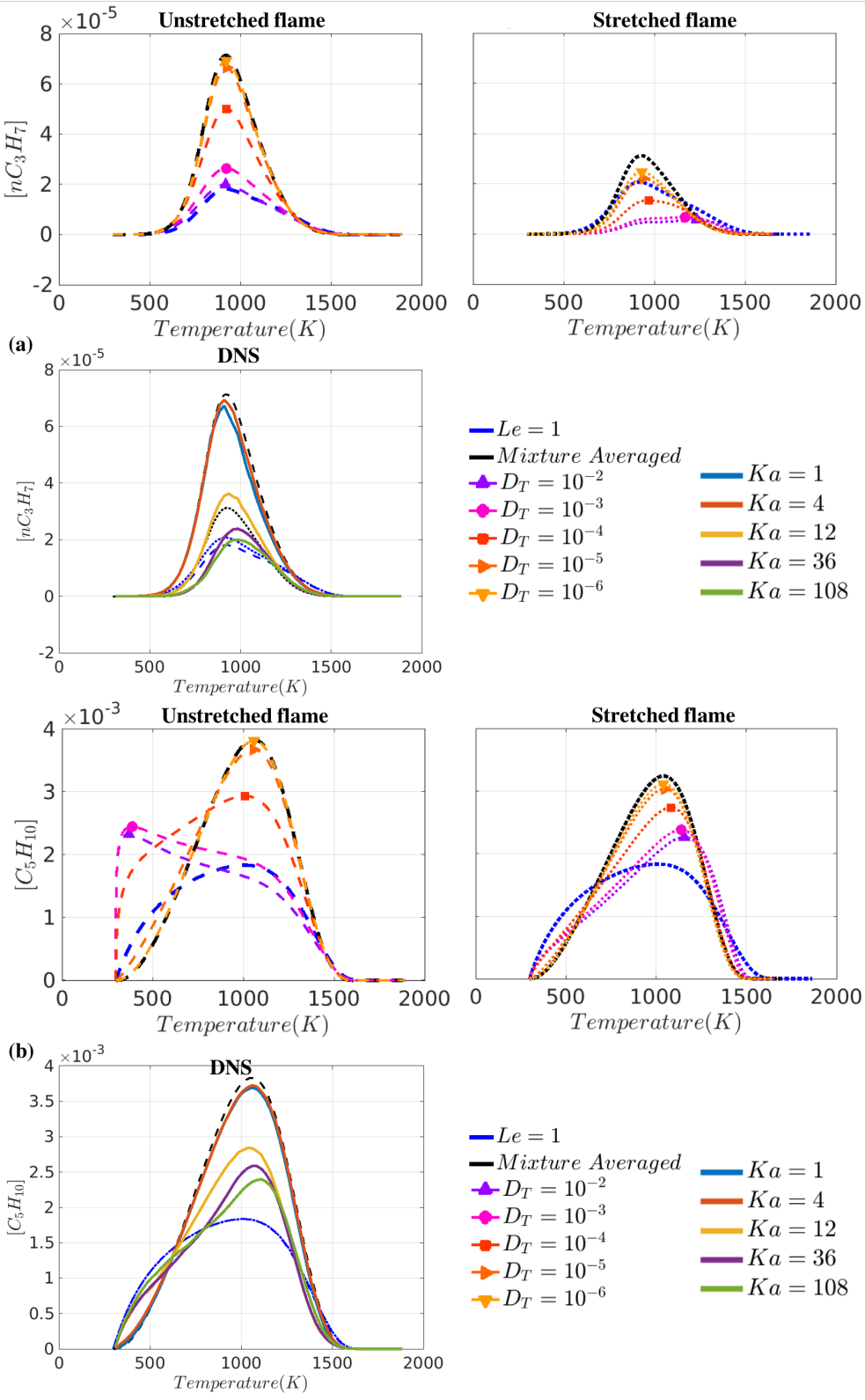

Figure 6.18. Variation of concentration for (a) nC$_3$H$_7$ and (b) C$_5$H$_{10}$ with temperature for different transport models for unstretched flames, stretched flames and DNS.

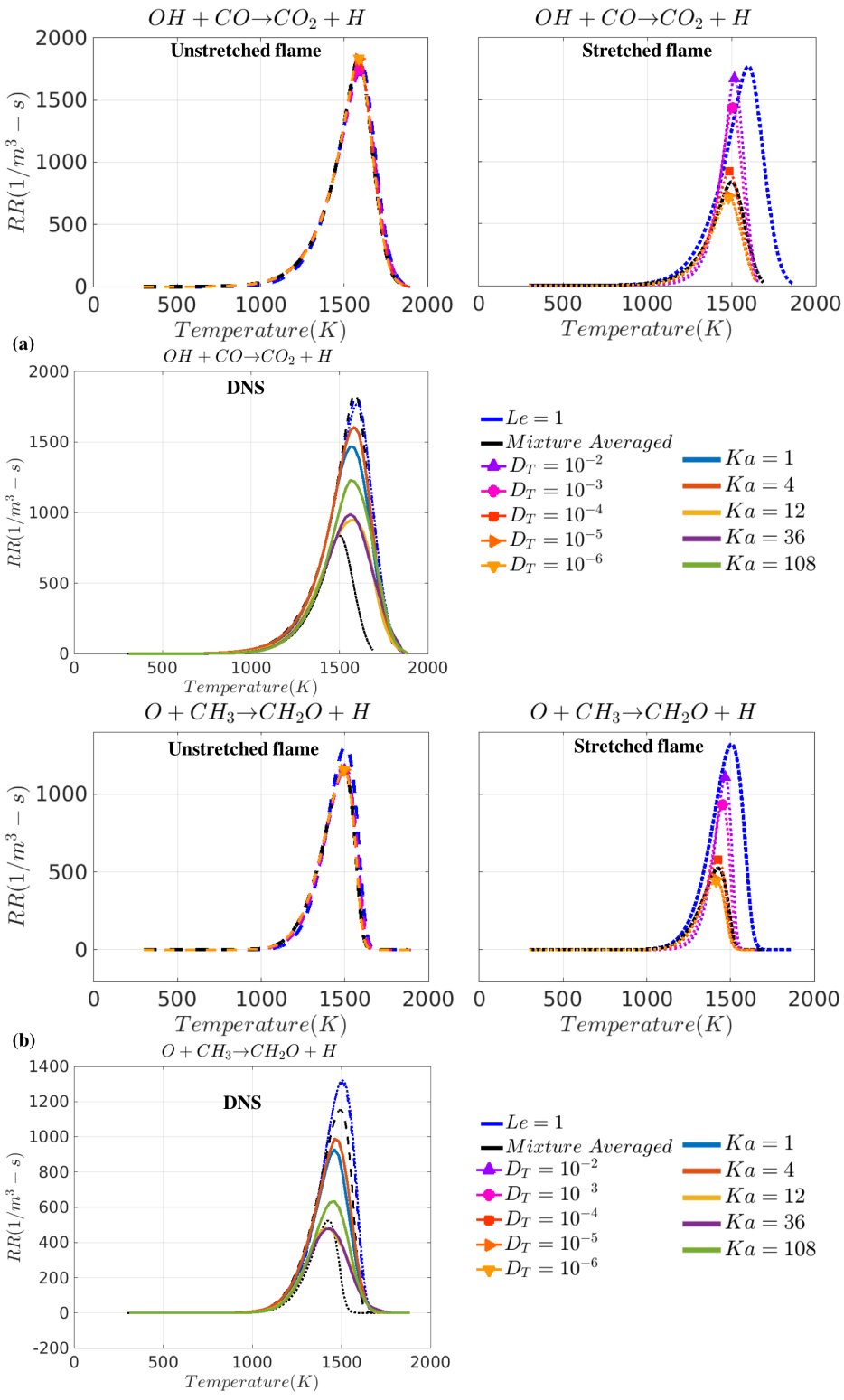

Figure 6.19. Variation of reaction rate for (a) OH+CO→CO_2+H and (b) O+CH_3→CH_2O+H with temperature for different transport models for unstretched flames, stretched flames and DNS.

Focusing on reactions, Figure 6.19, Figure 6.20 and Figure 6.21 plot the variation of key reactions with altered transport model. Three common observations for the unstretched and stretched flames can be made for $OH+CO \rightarrow CO_2+H$ (Figure 6.19(a)),$O+CH_3 \rightarrow CH_2O+H$ (Figure 6.19(b)), $HO_2+OH \rightarrow H_2O+O_2$ (Figure 6.20(a)), $HCO+O_2 \rightarrow CO+HO_2$ (Figure 6.20(b)) and $H+O_2(+M) \rightarrow HO_2(+M)$ (Figure 6.21(a)). Firstly, increasing diffusivity pushes the rates towards higher temperatures. Secondly, for lower values of diffusivity ($D_T = 10^{-6} - 10^{-4}$), increasing stretch reduced the peak reaction rates. For higher values of diffusivity, the peak rates are comparable. Thirdly, increasing diffusivity first reduces the reaction rate (for $D_T = 10^{-5}, 10^{-5}$) and then increases the reaction rates for highly stretched flames. Turbulent flame profile associate with each of these observations. The first observation supports the reduced low temperature reaction rates. For example, for $HO_2+OH \rightarrow H_2O+O_2$ the reaction rate at 1000K is ~70% lower for *Ka*=12,36, 108 compared to *Ka*=1,4. The second and third observations explain the reduced peak reaction rates for *Ka*=12,36 compared to *Ka*=1,4. Finally, the non-monotonic increase in the reaction rate for *Ka*=108 compared to *Ka*=12,36 can be explained by the effect of increased diffusivity on highly stretched flames. These observations are in line with the behavior of the involved species discussed earlier. $H+OH+M \rightarrow H_2O+M$ (Figure 6.21(b)) slightly deviates in behavior compared to the other reactions. With increasing diffusivity, the unstretched flame profiles move towards lower temperatures and the stretched flame profile do not shift considerably in temperature space. This latter observation manifests itself as a limited impact on the reaction rate profiles across all turbulent intensities at T<1400K. The second and third observations, discussed earlier, hold for this reaction as well.

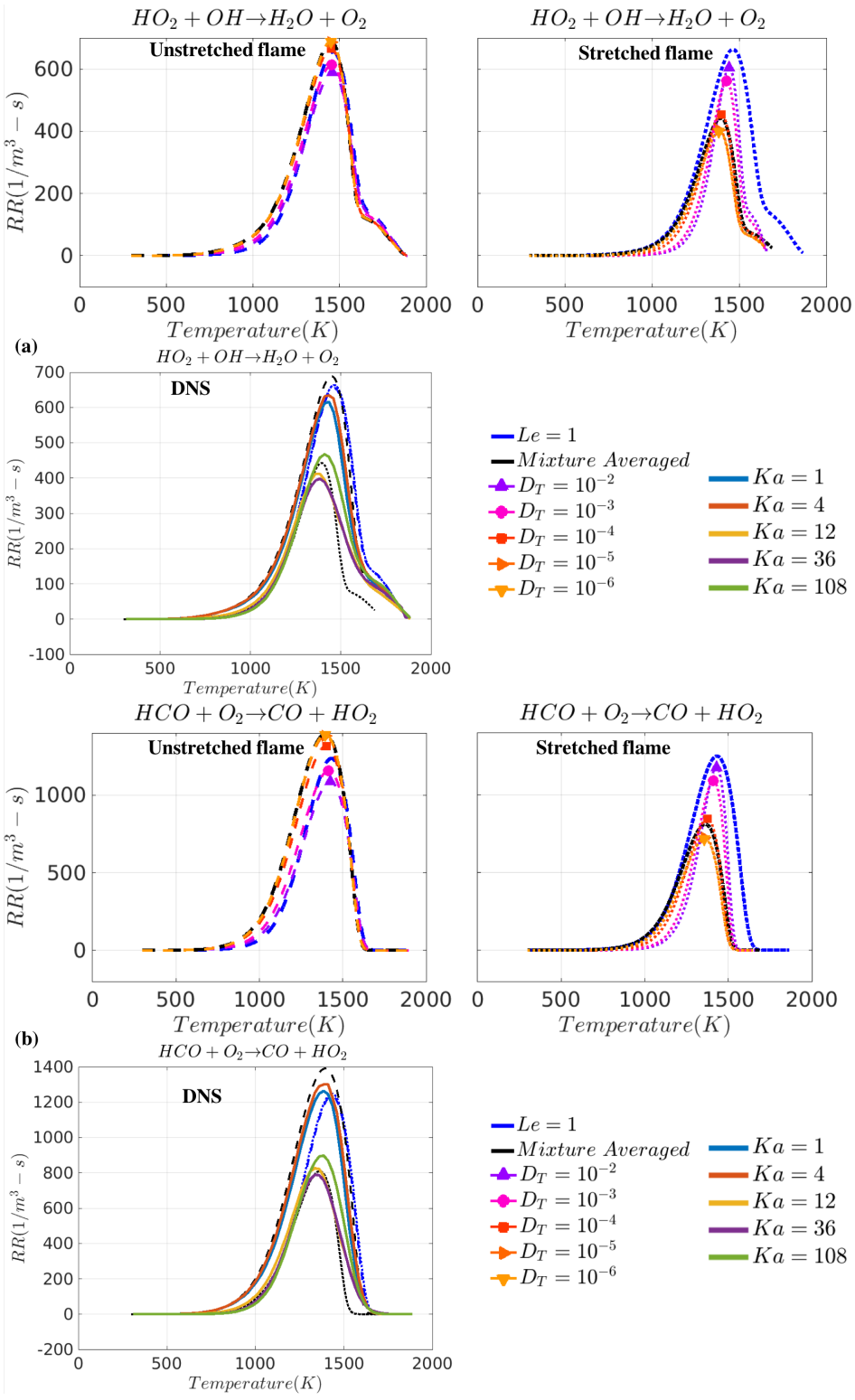

Figure 6.20. Variation of reaction rate for (a) HO_2+OH→H_2O+O_2 and (b) HCO+O_2→CO+HO_2 with temperature for different transport models for unstretched flames, stretched flames and DNS.

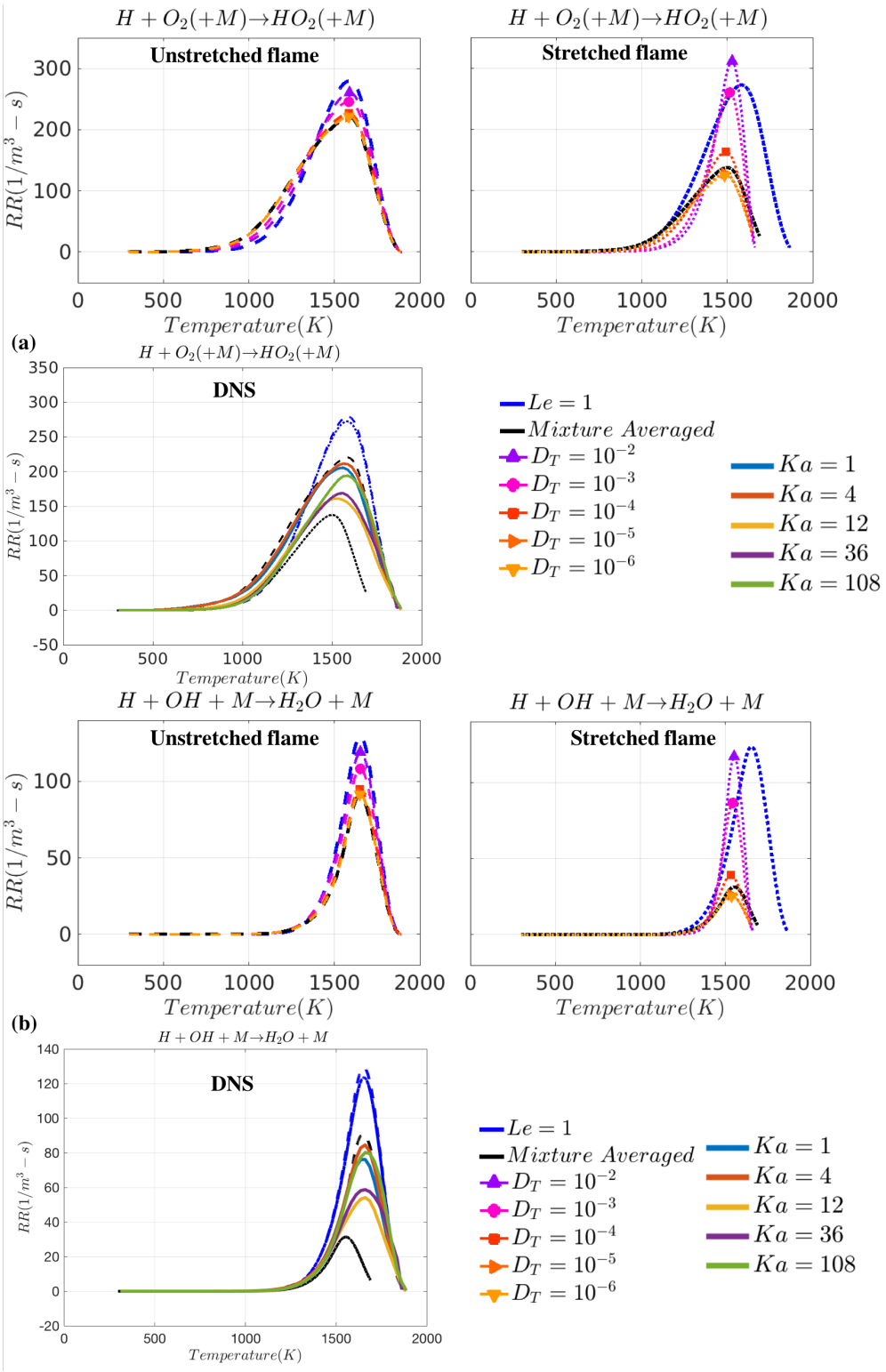

Figure 6.21. Variation of reaction rate for (a) H+O₂(+M)→HO₂(+M) and (b) H+OH+M→H₂O+M with temperature for different transport models for unstretched flames, stretched flames and DNS.

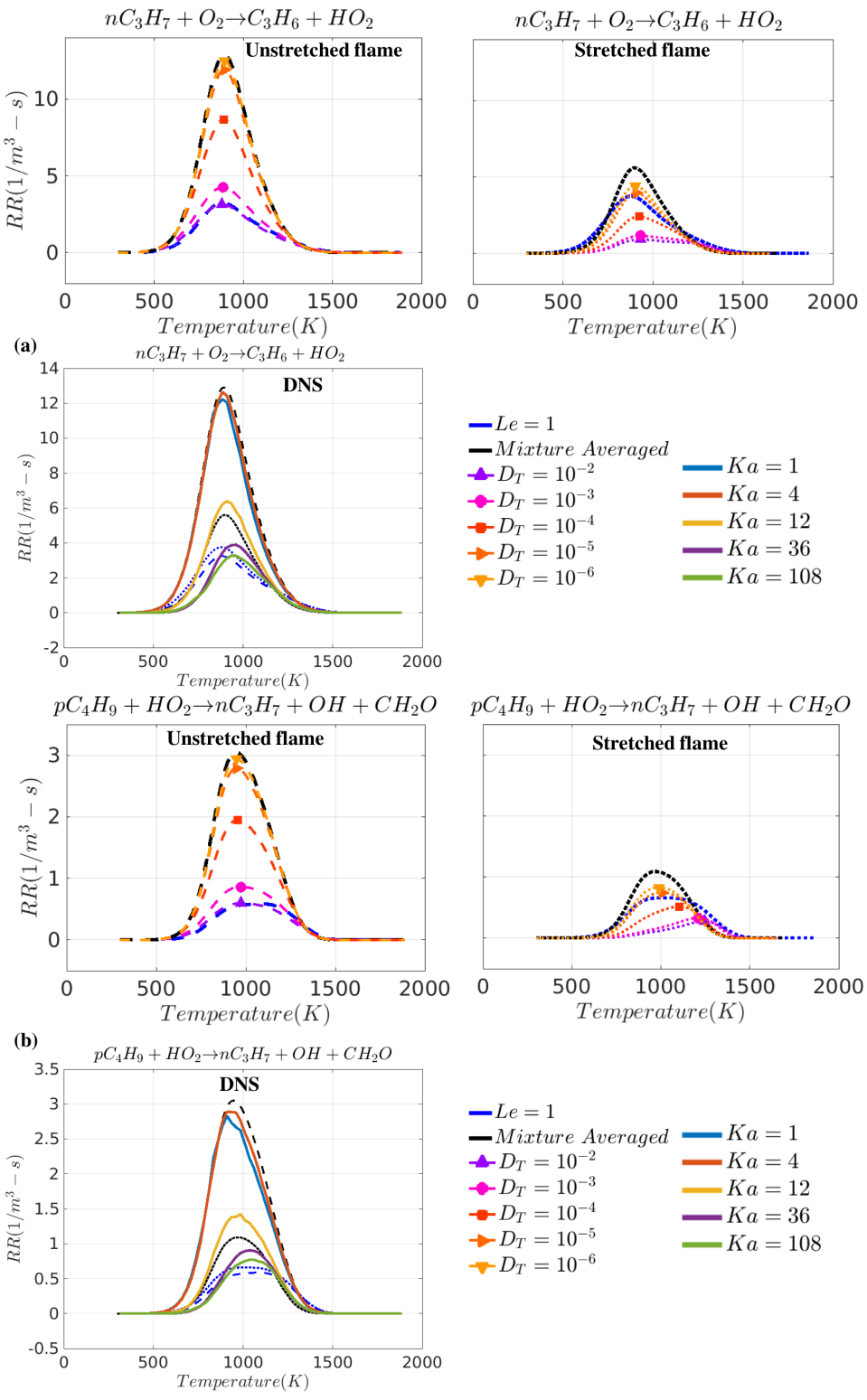

Figure 6.22. Variation of reaction rate for (a) nC$_3$H$_7$+O$_2$→C$_3$H$_6$+HO$_2$ and (b) pC$_4$H$_9$+HO$_2$→nC$_3$H$_7$+OH+CH$_2$O with temperature for different transport models for unstretched flames, stretched flames and DNS.

Figure 6.22 plots the variation of reaction rates for reactions involving fuel fragments using different transport models. For these reactions, increasing diffusivity shifts the profiles towards higher temperatures for unstretched and stretched flames. Additionally, the peak reaction rates are significantly reduced with increasing diffusivity for both the laminar flame models unlike the reactions discussed above. In general, for stretched flames, the high D_T profiles show a very different behavior compared to the $Le = 1$ profile. The change in the turbulent flame profiles with increasing turbulence replicates the behavior of stretched flame with increasing diffusivity i.e. reduced low temperature reaction rates and reduced peak reaction rate across the entire temperature space.

Overall, for these n-dodecane flames, the turbulent flames strongly resemble the stretched flame behavior with increasing diffusivity.

6.5 Conclusions

This chapter discusses the effect of altered transport model on simple laminar models: unstretched and stretched flames. The transport models are implemented using the basic mixture-averaged transport model with an additional constant D_T. This D_T is intended to mimic the effect of enhanced diffusivity due to increasing turbulence. This understanding is then extrapolated to understand the behavior of the turbulent flame profiles with increasing turbulence intensities for three fuels: hydrogen, methane, n-dodecane.

The lean hydrogen flames considered have a global Lewis number of 0.36 and are thermo-diffusively unstable. As a result, the unstretched laminar profiles cannot represent the physics of these flames. In general, increasing diffusivity leads to a reduction in low

temperature activity for highly stretched flames. For example, for the reaction $H+O_2(+M)\rightarrow HO_2(+M)$, at 500K the reaction rate for the mixture-averaged transport is ~6000 1/m^3-s whereas for $D_T = 10^{-5}$ it is ~2250 1/m^3-s and for $D_T = 10^{-4}$ it is ~200 1/m^3-s. Additionally, increasing diffusivity also leads to reduced peak reaction rates for stretched flames. For instance, the peak reaction rate for $H_2+OH\rightarrow H_2O+H$ for the mixture-averaged transport is 2.2x10^4 1/m^3-s compared to 1.7x10^4 1/m^3-s for $D_T = 10^{-5}$ and 1.1x10^4 1/m^3-s for $D_T = 10^{-4}$. Considering only the effect of stretch, an increase in reaction rates across all temperatures can be seen with increasing stretch for a given model. For example, the reaction $HO_2+OH\rightarrow O_2+H_2O$ has a nearly zero reaction rate at 500K for the mixture-averaged unstretched flame whereas for the equivalent stretched flame, the reaction rate at 500K is 2250 1/m^3-s. Focusing on the turbulent flames, all the reaction rate profiles display an enhanced reaction rate with increasing turbulence intensity. This observation is consistent with that for laminar flames with increasing stretch. Increased diffusivity due to turbulence does not seem to play a role in determining the behavior of these lean hydrogen flames. These flames have a high concentration of light species such as H_2 and H. These species are highly diffusive and potentially control the transport dynamics. This is also evidenced by the fact that none of the species or reaction rate profiles tends towards $Le = 1$ suggesting that molecular diffusivity still holds its character in determining the chemistry and chemical pathways for these flames. Thus, the dominant effect of turbulence on chemistry is through flame stretch.

The lean methane flames considered have a global Lewis number of 0.96 (close to 1). In general, for the species and reactions, increasing diffusivity moves the profiles towards higher temperatures for the unstretched and stretched flames. For example, for the

reaction OH+CO→CO_2+H, the reaction rate for stretched flames with mixture-averaged transport at ~1300K is ~300 1/m^3-s compared to ~100 1/m^3-s for $D_T = 10^{-4}$. Increasing stretch for a given transport model shifts the profiles towards lower temperatures. For example, the reaction rate for H+O_2(+M)→HO_2(+M) at 1000K for unstretched mixture-averaged flame is ~90 1/m^3-s whereas the corresponding value for the stretched flame is ~125 1/m^3-s. Increasing turbulence shows a very limited effect on the reaction rate and species concentration profile. Marginal changes are observed for reactions such as H+O_2(+M)→HO_2(+M), H+CH_3O→CH_2O+H_2 wherein increasing turbulence moves the profiles towards higher temperatures and possibly towards $Le = 1$. Relatively stronger effects are seen for low temperature species such as HO_2 and CH_3O wherein the turbulent flame profiles show a substantial shift towards higher temperatures and mimic the behavior of stretched flames with increasing diffusivity. However, the behavior of all the reactions and most other species is similar to the behavior of unstretched flames with increasing diffusivity. Thus, for these flames, diffusivity, as opposed to stretch, drives the chemistry and chemical pathways.

For the lean n-dodecane flames considered here, the global Lewis number is 4.36 and these flames are hence prone to thermo-diffusive effects. Increasing diffusivity, similar to the observation for hydrogen and methane flames, moves the species concentration and reaction rate profiles towards higher temperatures. Increasing diffusivity also affects the peak concentrations and reaction rates. For example, increasing diffusivity in highly stretched flames leads to reduced concentrations for low temperature species such as HO_2, CH_2O, C_5H_{10}, nC_3H_7 and reduced reaction rates for low temperature reactions such as nC_3H_7+O_2→C_3H_6+HO_2, pC_4H_9+HO_2→nC_3H_7+OH+CH_2O. For high temperature species,

such as H, CH_3, and high temperature reactions, such as OH+CO→CO_2+H, O+CH_3→CH_2O+H, an increase in concentration/reaction rates is observed with increasing diffusivity ($D_T \geq 10^{-4}$) for highly stretched flames. Increasing stretch for a given model, in general, leads to a reduced concentration or reaction rate for all considered species and reactions. The turbulent flame profiles respond to a coupled influence of stretch and diffusivity. The lower turbulent profiles are close in response to the unstretched mixture-averaged profiles. A further increase in turbulence leads to a reduction in concentration and reaction rates similar to an increased stretch response for the laminar flame models. Further increasing the turbulence leads to an increase (decrease) in peak concentrations and reaction rates for high(low) temperature species and reactions, again consistent with the behavior of highly stretched flame with increasing diffusivity. Another point to note here is the difference in behavior of the highly turbulent flames with $Le = 1$ transport model. Even though this predicts the shift towards higher temperature, it cannot predict the qualitative and quantitative changes in the species and reaction rate profiles. As pointed out in the text, a high value of the diffusivity compared to species mass (and thermal) diffusivity produces an effective Lewis number of unity but the individual values of the diffusivity play a role in determining the behavior of the profiles leading to a significantly different behavior between the $Le = 1$ and $D_T = 10^{-2}, 10^{-3}$ profiles. Thus, the turbulent flame profiles show a stronger correlation with the behavior of highly stretched flames with high diffusivity as opposed to $Le = 1$.

Aspden et al. [67, 68] noted the transition of the species profiles towards unity Lewis number for lean methane flames which has been noted here and suggested a potential transition of species for n-dodecane flames towards unity Lewis number. Lapointe et al.

[71] also noted a movement of the fuel and fuel fragments towards unity Lewis number for n-heptane flames. This analysis suggests that these observations may not be entirely correct for all the involved species and reactions rates for all turbulent premixed flames. For flames with global Lewis number close to unity, these observations hold true for the flame structure and chemical pathways. However, a deviation from unity global Lewis number leads to an intertwined effect of stretch and increased scalar diffusivity

CHAPTER 7. CONCLUSIONS AND FUTURE WORK

This chapter summarizes the results and key findings presented in this thesis. Additionally, several avenues of future work are proposed which include continuations of the current work and new topics rooted in the lessons learnt from this work.

7.1 Conclusions

The primary focus of this thesis has been to investigate the effects of turbulence on chemistry through chemical pathways and flame structure for lean premixed flames. Investigating this piece of the puzzle is essential, not only for a better understanding of the interaction, but also for improving and potentially developing new models for turbulence-chemistry interactions. With significant improvements in supercomputing facilities, it is now possible to perform fully resolved three dimensional simulations of turbulent reacting flows with detailed chemistry allowing for the investigation of the influence of turbulence on chemistry.

Three fuels: hydrogen, methane and *n*-dodecane are chosen. These fuels are fundamentally different in behavior; hydrogen is highly diffusive compared to air, methane and air are (almost) equally diffusive and *n*-dodecane is a large chain hydrocarbon with significantly lower diffusivity compared to air. Datasets generated using direct numerical simulations are used to investigate the effects of turbulence. These results are compared and contrasted with simplified laminar models such as unstretched flames, stretched flames and perfectly stirred reactors.

Chapter 4 discusses a "bird's eye view" on the effects of turbulence on chemical pathways. A "global" analysis for the chemical pathways, for different metrics such as heat release rates and key species consumption and production rates, is performed. The integrated reaction rates for turbulent flames are first averaged across the entire "flame" surface to provide a single value to represent every Karlovitz number. These are compared with integrated reaction rates for stretched flames (zero stretch corresponds to unstretched laminar flame) and reaction rates for perfectly stirred reactors. For hydrogen and methane flames, there is a strong similarity in the qualitative and quantitative prediction of the chemical pathways for the different metrics for all three simulations. For n-dodecane flames, the turbulent flame predicted pathways are in close agreement with the stretched flame calculations. The PSR predicted pathways are quantitatively different from those predicted by the laminar stretched flames and turbulent flames. Qualitatively, the behavior of the reactions is consistent with the other two models i.e. for a given reaction, all models predict an increasing (or decreasing) trend with increasing stretch, decreasing residence time and increasing turbulence. Conditioning of the integrated reaction rates on local features such as curvature and fuel consumption reveal a different story. Even though the same dominant reactions are observed for these local conditioning, their qualitative and quantitative behaviors can be significantly different from their global counterpart. For example, for hydrogen flames, the largest differences are seen at progress variables close to the leading edge of the flame whereas the pathways at other progress variables behave similar to the global characteristics. For methane flames, different pathways and their sensitivity is observed for the negatively curved vs the positively curved elements. For example, there is a shift of the dominant heat release reaction from $O+CH_3 \rightarrow CH_2O+H$

(predicted by the global characteristics) to $OH+CO \rightarrow CO_2+H$ in the negatively curved elements. Although these elements show an altered pathway, the integrated heat release rates do not change significantly with increasing turbulence. On the other hand, the positively curved elements display the same pathways with considerably higher sensitivity to turbulence compared to the global characteristics. This higher sensitivity of reactions in the positively curved elements is portrayed by n-dodecane flames as well. These local effects on chemical pathways is a direct manifestation of the effects of stretch, leading to focusing and defocusing of scalars locally and hence altering the local reaction rates. This explanation is supported by the strong correlation between the integrated chemical pathways for turbulent and stretched flames. Overall, the key finding here is that the laminar models (stretched flames in particular) can predict the chemical pathways (from integrated rates) for turbulent flames. It cannot predict the local variations in pathways but can provide a good quantitative ballpark for the relative contribution of reaction to heat release or species consumption/production.

Chapter 5 "zooms in" on the effects of turbulence on chemistry and discusses a local analysis of the chemical flame structure using conditional means of reaction rates and species for the different fuels. The conditional means are compared with the equivalent stretched and unstretched flame profiles. For hydrogen flames, the unstretched flame cannot represent the turbulent flames since these flames are thermo-diffusively unstable and form highly curved cellular flames. The stretched flames can predict the increased reaction rate of turbulent flames with increasing turbulence intensity. However, the reactant-to-reactant opposed flow configuration cannot predict the super-adiabatic temperatures characteristic of the leading edge of these hydrogen flames. The stretched

flame can predict the increased radical concentration in the low temperature region which leads to the elevated rates with increasing turbulence. The reaction rate profiles for the methane flames, on the other hand, do not show a significant change with increasing turbulence and move slightly towards higher temperatures. In general, the turbulent profiles are close to the unstretched flame profiles. However, low temperature species display a more dynamic response to turbulence and these effects cannot be captured by the unstretched or stretched flame profiles. For n-dodecane flames, all reactions show reduced low temperature activity. The most drastic impact of turbulence is seen by the reactions with peak activity in the low temperature regions (i.e. below 1200K). The rate profiles for these reactions are not bounded by the unstretched and stretched flame profiles. From a modeling standpoint, for flames with a global Lewis number close to unity, this analysis suggests that's mean quantities such as heat release, fuel consumption rate, mass fractions of major species can be calculated using tabulated chemistry without the usage of detailed chemistry in simulations. However, for flames with non-unity Lewis numbers (and hence susceptible to thermo-diffusive effects) this may not suffice necessitating the development of reduced order models for accurately predicting source terms.

Chapter 6 extends the results obtained in Chapter 5 to identify potential parameters necessary for reduced order modeling. The key idea is to isolate the impacts of increased stretch and diffusivity on the reaction rates and species concentration profiles for the three fuels. In addition to the unstretched and stretched flame profiles obtained using mixture-averaged transport, these laminar flame results are obtained for different transport models namely, unity Lewis number transport and mixture-averaged transport with an additional constant to mimic the effect of increased scalar diffusivity due to turbulence. The chosen

constants span multiple orders of magnitude. The thermo-diffusively unstable lean hydrogen flames are not significantly affected by increased diffusivity primarily due to the high concentration of light species. These species can diffuse very easily and do not need the "aid" of turbulence to effectuate changes. Flame stretch enhances the effects of differential and preferential diffusion and plays a key role in determining the behavior of the reaction rates and species concentration profiles for hydrogen flames primarily leading to elevated rates and concentrations over the entire temperature range. The lean methane flames considered here do not seem to affected by flame stretch. This may be due to the unity Lewis number of the reactant mixture which suppresses the effects of differential and preferential diffusion. The movement of the turbulent flame profiles towards higher temperatures is similar to the effect of increased diffusivity on the laminar flame models. Thus, for these flames, turbulent diffusivity is the leading factor in determining the response of the reaction rate and species profiles. The modification of the reaction rate and species concentration for n-dodecane turbulent flames is explained through a combined effect of stretch and diffusivity. Thermo-diffusive effects play a role for these flames as well, since the global Lewis number is greater than 1. Stretch tends to enhance these effects and, hence, with increasing turbulence the profile behavior mimics the response of stretched flames with mixture-averaged transport. A further increase in turbulence introduces the effects of increased diffusivity and the turbulent flame profiles respond to both: stretch and diffusivity. Overall, from this analysis it can be concluded that stretch effects cannot be neglected for lean premixed flames with global Lewis numbers not equal to unity. Additionally, increased diffusivity is an important factor in determining the behavior of highly stretched flame which is replicated in the response of turbulent flames.

Another key finding from this analysis is the lack of unity Lewis number profile to provide a good estimate for the species and reaction rates. It can, to some extent, predict the behavior of flames with a global unity number close to one. However, for non-unity Lewis number the turbulent flame profiles do not correlate with the unity Lewis number profiles. This observation is particularly relevant, since, typically in turbulent-chemistry interactions literature, this is considered the theoretical limit wherein turbulent mixing is the dominant player in scalar transport. This analysis emphasizes that, even though higher values of diffusivity (compared to the mass diffusivity) lead to an effective unity Lewis number, the value of the diffusivity is equally important in determining the behavior of the flames subjected to these high diffusivities and is potentially an important parameter to consider for reduced-order modeling.

The work presented here is an important piece in understanding turbulence-chemistry interactions and providing insight into improvement of the existent turbulent-chemistry models implemented in LES and RANS. This is particularly relevant in combustion modeling where the flame needs to be resolved correctly to effectively simulate engine combustion in highly turbulent environment.

7.2 Future Work

This works adds to the relatively new body of work emerging in turbulent-chemistry interactions. Several interesting questions still remain open in understanding the complete physics governing this interaction:

1. **Isolating the impact of H and H_2 diffusion**

   Clearly, these highly diffusive species affect the diffusivity effects on the flame and its chemistry especially when present in higher concentrations. It will be interesting to isolate their impact to understand their influence on the diffusivity of the entire mixture. This could potentially be achieved by performing more DNS simulations with a fixed unity Lewis number for these species and allowing the other species to evolve with mixture-averaged transport and vice-versa for the different fuels with varying turbulence intensities.

2. **3D simulations for *Le*=1 turbulent flames**

   The *Le*=1 is a popular transport model in understanding the turbulent mixing limited species transport. It will be interesting to compare the detailed transport simulations with those from *Le*=1 transport models and see if the behavior of the three-dimensional flames is similar to their *Le*=1 counterpart. This analysis will also help isolate the impacts of increased scalar diffusivity since *Le*=1 flames show limited stretch sensitivity.

3. **Understanding the impact of turbulence on chemistry during transient phenomenon**

   The analysis presented in this thesis uses statistically steady, nominally 1D turbulent flames and compares their behavior with steady laminar flames. Phenomenon such as auto-ignition or blow-off are not steady state phenomenon and the chemical pathways analysis should be extended for such transient occurrences. These unsteady phenomena may be more susceptible to effects of turbulence especially due to increased diffusivity potentially resulting in altered chemical pathways for fuel oxidation.

From a modeling standpoint, an interesting extension of this work is:

1. **Development of reduced-order models**

   Chapter 5 and Chapter 6 illustrate that for unity Lewis number flames, unstretched and stretched flame can predict most of the reaction rate and species concentrations profiles well allowing for the usage of tabulated chemistry for determining mean quantities. However, for non-unity Lewis number flames, the strong thermo-diffusive effects lead to additional effects of stretch and diffusivity on the flames. It would be useful to develop a reduced order model that can capture these effects since most of the fuels such as Jet-A, Jet-B, Diesel, Kerosene etc. used in gas turbine and internal combustion engines have characteristics similar to n-dodecane.

   For instance, one of the common models used for turbulence-chemistry interactions is the thickened flame model developed by Colin et al.[44] which uses a constant multiplier, $\mathcal{F}$, to thicken the flame leading to an altered species diffusivity given by $\mathcal{F}D_i$. This model has been extended to allow a dynamic calculation of the thickening factor, $\mathcal{F}$ using a flame sensor function, Ω which is based on a progress variable [96].

The studies in this thesis suggest, for highly turbulent flames, it is essential to incorporate the effect of increased diffusivity due to increased turbulence, in addition to stretch effects, providing a new approach for modeling $\mathcal{F}$ rooted in the physics of the problem. The effective diffusivity $D_{i,eff} = D_i + D_T = D_i(1 + D_T/D_i)$ allowing $\mathcal{F}$ to be modeled as $(1 + D_T/D_i)$. However, the value of D_T cannot be treated as a constant (unlike in the simplified model presented here) since, the effective turbulence intensity drops through the flame due to increased viscosity with increasing temperature. Effective methodology needs to be developed to capture this variation of D_T and incorporate it in a model.

This D_T (accounting for variation across the flame) can be used as another dimension for chemistry tabulation, in addition to the other existent dimensions namely , a progress variables (defined based on temperature or product mass fraction, strain, enthalpy etc. [50].

Accommodating the effect of increased diffusivity in these models will help in providing better estimates of the flame structure and, in turn, help in capturing its behavior in highly turbulent environments for realistic combustor configurations using LES and/or RANS.

APPENDIX A. REACTION MODEL SENSITIVITY FOR N-DODECANE/AIR FLAMES

Three reaction mechanisms are tested for n-dodecane/air flames to compare the sensitivity of the chemical pathways to the choice of the model. These mechanisms include You et al.[89], Luo et al.[90] and Narayanswamy et al.[91].

A.1 Mechanism details

You et al. [89] which consists of 56 species and 289 reactions. It is compared with those of the more detailed mechanisms of Luo et al. [90] consisting of 106 species and 420 reactions, and of Narayanswamy et al. [91] consisting of 255 species and 1509 reactions. You et al.[89]'s model is derived by appending the USC mechanism[97] for C_1-C_4 hydrocarbons with reactions to describe high temperature pyrolysis and oxidation of *n*-alkanes. Luo et al.[90] is derived from the detailed LLNL mechanism[98]. Narayanswamy et al.[91] is also derived from the same LLNL mechanism[98]. This reduced mechanism they obtained is appended with their older base model for the oxidation of substituted aromatic species[99]. Henceforth, we will use the following shorthand for the mechanisms: Y1 for You et al.[89], L2 for Luo et al.[90] and NS3 for Narayanswamy et al.[91]. The results from the laminar configurations using the three different kinetics mechanisms listed above are compared.

A.2 Results and Discussions

A.2.1 Key Parameters

The key parameters for the different laminar models are the extinction strain rate, κ_{ext}, the minimum PSR residence time for ignition, τ_{ext}, and unstretched laminar flame speed, S_{L_O}. Table A.1 below summarizes the values obtained using the different mechanisms.

Table A.1. Summary of the key parameters and their deviation from the reference mechanism.

Mechanism (see text)	S_{L_O} **(cm/s)**	$\Delta\varepsilon_{S_{L_O}}$	κ_{ext} **(1/s)**	$\Delta\varepsilon_{\kappa_{ext}}$	τ_{ext} **(ms)**	$\Delta\varepsilon_{\tau_{ext}}$
Y1	22.3	-	244.4	-	0.16	-
L2	17.9	19.8%	160.9	34.2%	0.18	12.5%
NS3	23.7	6.3%	232.9	4.7%	0.15	6.3%

The deviation for a parameter is calculated with respect to the Y1 mechanism as:

$$\Delta\varepsilon_{S_{L_O}} = \left|\frac{S_{L_O} - S_{L_{O,Y1}}}{S_{L_{O,Y1}}}\right| \tag{A.1}$$

A similar deviation can be defined for κ_{ext} and τ_{ext}.

It can be observed that the smaller Y1 mechanism captures the values of these key laminar parameters very well when compared to the more detailed mechanism of NS3. There are higher deviations for the intermediate L2 mechanism.

A.2.2 Mechanism Sensitivity

Heat release and its sensitivity to increasing stretch or residence time are discussed for the different mechanisms. Figure A.1 below compares the dominant heat release reactions obtained from OPPDIF calculations.

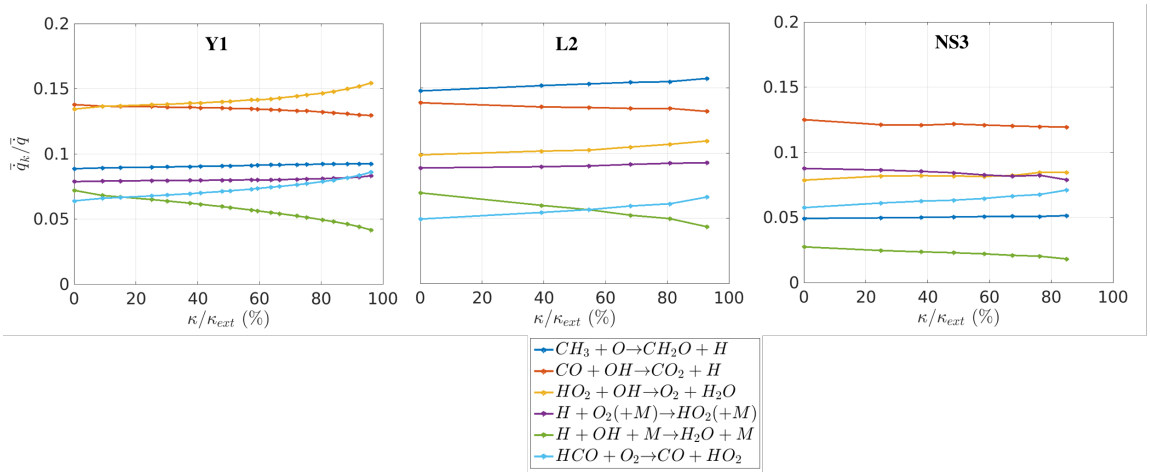

Figure A.1. Variation of normalized heat release with increasing stretch for three mechanisms. All three plots have the same y-scale.

The first clear observation is that the same set of reactions show up as the dominant 6 heat release reactions. However, within these top 6 heat release producing reactions, the relative order varies between mechanisms. For example, in the case, of Y1 the reaction HO_2+OH→O_2+H_2O is the dominant heat release reaction. However, this reaction is the third dominant reaction for L2 and changes from third to second dominant reaction for NS3 with increasing stretch rates. Similarly, the reaction of CO+OH→CO_2+H is the second largest contributor to heat release for L2 and Y1 but is identified as the most dominant heat release contributor for NS3.

The next interesting observation is the sensitivity of these dominant reactions with increasing stretch for the three mechanisms. The trends of the reactions i.e. increasing or decreasing and percentage changes with stretch remain fairly consistent across the three mechanisms. For example, the fractional change in heat release with increasing stretch for the reaction H+OH+M→H_2O+M changes by ~40% for L2, Y1 and 35% for NS3. These numbers for the reaction CO+OH→CO_2+H are ~5% and ~6% respectively.

Figure A.2 presents this same heat release metric, calculated for the PSR.

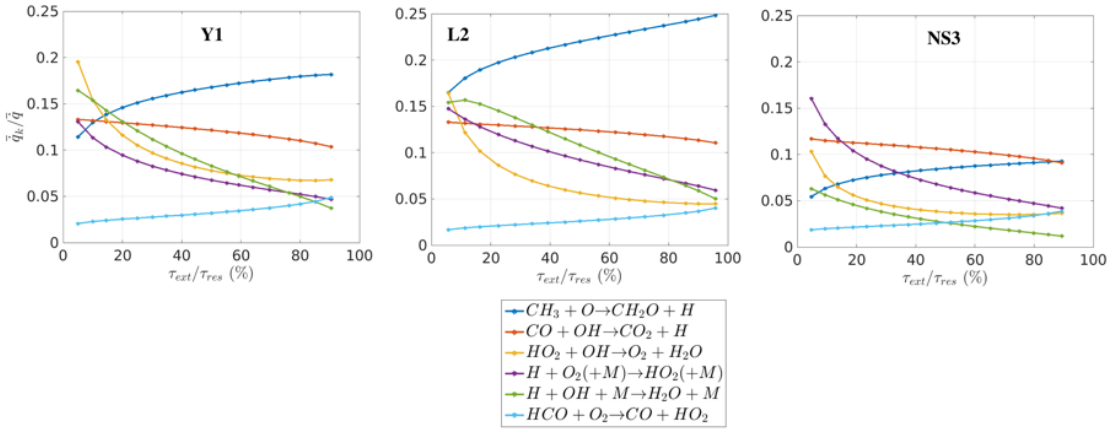

Figure A.2. Variation of normalized heat release with decreasing residence time for three mechanisms. All three plots have the y-scale.

Similar to stretched flames, it is observed that the same reactions are responsible for majority of the heat release. However, the dominant reactions have varied contributions to heat release with respect to mechanisms. For example, the reaction CH_3+O→CH_2O+H is the dominant heat release reaction for the L2 and Y1 mechanisms. However, this is the third (or second) dominant heat release reaction at higher (or lower) residence times for NS3. For PSR as well, there is a good qualitative match in the behavior of the reactions across the three mechanisms. For example, the reaction CH_3+O→CH_2O+H shows a wide

quantitative variation in its contribution to heat release. Its increase in contribution to heat release however is fairly consistent across the three mechanisms varying from ~55% for Y1 and L2 to ~65% for NS3. $H+O_2(+M) \rightarrow HO_2(+M)$ shows a smaller quantitative spread and its change in contribution is around ~60% for Y1 and L2 to ~70% for NS3. In general, it is observed that Y1 and NS3 have different reaction pathways(quantitatively) but they provide similar results for flames speeds, extinction strain rates, auto-ignition delays and qualitative behavior of pathways.

A.3. Conclusions

The You et al.[89] mechanism used in a DNS dataset is compared with other detailed mechanisms of Luo et al.[90] and Narayanswamy et al.[91]. Even though the dominant heat release reactions remain the same across the three mechanisms, we observe quantitative changes in their contributions with increasing stretch and residence times. However, the qualitative response of the reactions is fairly consistent for all the mechanisms. For example, the dominant heat release reaction for Y1, $HO_2+OH \rightarrow O_2+H_2O$, is the third dominant reaction for L2 and second dominant for NS3 for stretched flames but shows a consistent increase of ~10% each mechanism. These results set a solid basis for the comparison of the laminar flame results with the DNS data set using You et al.[89]'s mechanism. Qualitatively, we can understand how turbulence will affect the reactions and their contributions to heat release and key species' production and consumption.

APPENDIX B. INLET CONDITIONS FOR STRETCHED FLAME CALCULATIONS IN CANTERA

The inlet conditions for the stretched flame calculations presented in Chapter 6 are summarized here.

B.1. Hydrogen

The inlet conditions are ϕ = 0.4, T^u = 298K, p = 1atm, domain length = 0.2m

Table B.1. Inlet velocities for stretched flames for hydrogen flames

Diffusivity value (m^2/s)	Inlet velocity (cm/s)
$D_T = 10^{-6}$	57400 cm/s
$D_T = 10^{-5}$	57400 cm/s
$D_T = 10^{-4}$	30800 cm/s
$D_T = 10^{-3}$	14500 cm/s
$D_T = 10^{-2}$	14000 cm/s

B.2. Methane

The inlet conditions are ϕ = 0.7, T^u = 298K, p = 1atm, domain length = 0.02m

Table B.2. Inlet velocities for stretched flames for methane flames

Diffusivity value (m^2/s)	Inlet velocity (cm/s)
$D_T = 10^{-6}$	1170 cm/s
$D_T = 10^{-5}$	990 cm/s
$D_T = 10^{-4}$	257 cm/s
$D_T = 10^{-3}$	120 cm/s
$D_T = 10^{-2}$	110 cm/s

B.3. n-dodecane

The inlet conditions are ϕ = 0.7, T^u = 298K, p = 1atm, domain length = 0.02m

Table B.3. Inlet velocities for stretched flames for n-dodecane flames

Diffusivity value (m^2/s)	Inlet velocity (cm/s)
$D_T = 10^{-6}$	256 cm/s
$D_T = 10^{-5}$	254 cm/s
$D_T = 10^{-4}$	261 cm/s
$D_T = 10^{-3}$	260 cm/s
$D_T = 10^{-2}$	258 cm/s

APPENDIX C. CONVERGENCE TEST FOR UNSTRETCHED FLAMES IN CHEMKIN

The unstretched flame speed and the maximum temperature are plotted as a function of the solution curvature and gradient for convergence testing.

C.1. Hydrogen

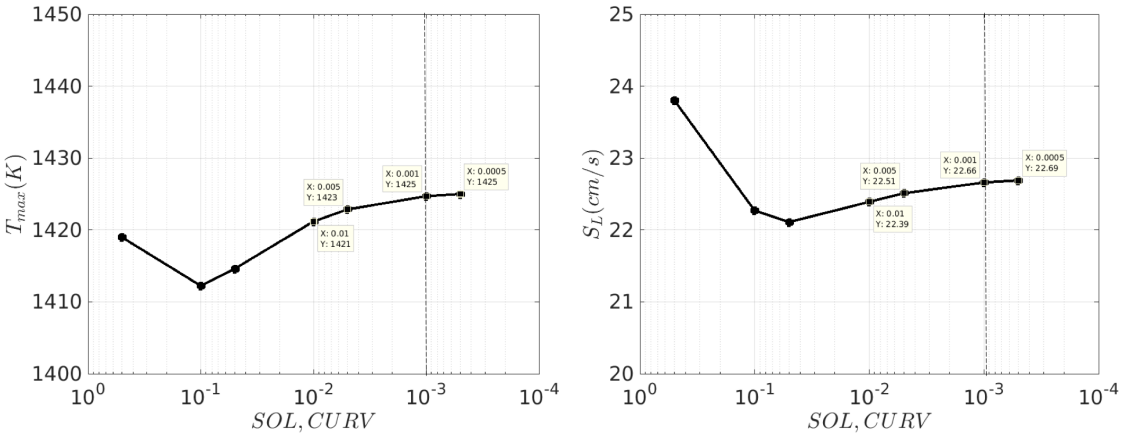

Figure C.1. Variation of maximum temperature (left) and flame speed (right) as a function of solution curvature and gradient for lean hydrogen flames.

Solution convergence is obtained for CURV, GRAD = 0.001 and is used for all unstretched and stretched flame calculations.

C.2. Methane

Solution convergence is obtained for CURV, GRAD = 0.001 and is used for all unstretched and stretched flame calculations.

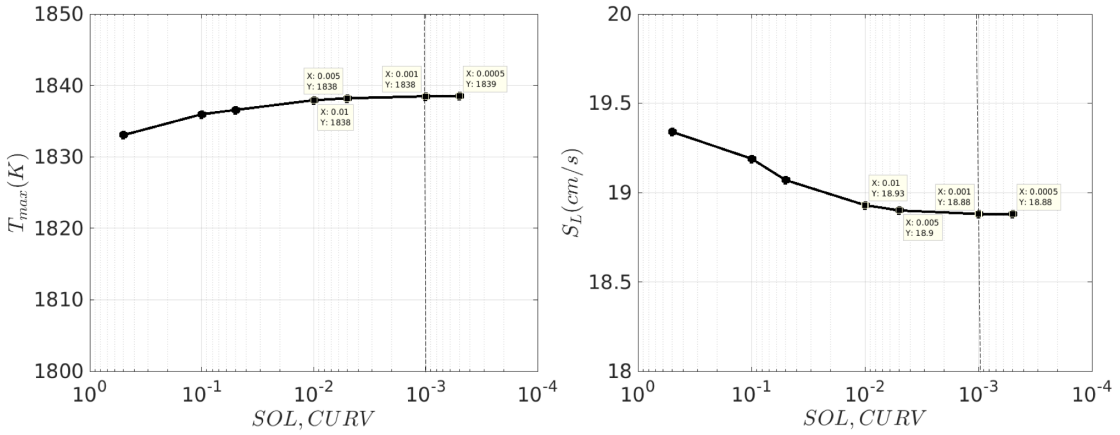

Figure C.2. Variation of maximum temperature (left) and flame speed (right) as a function of solution curvature and gradient for lean methane flames.

C.3. n-dodecane

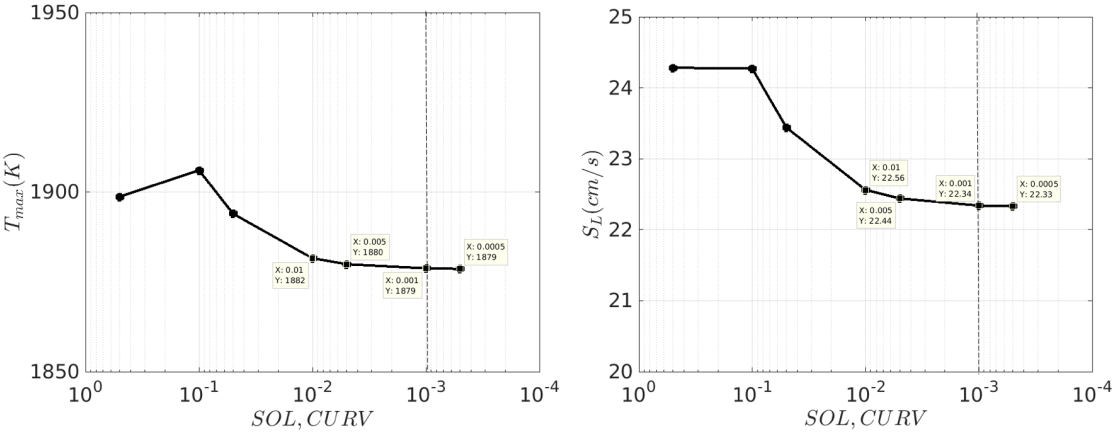

Figure C.3. Variation of maximum temperature (left) and flame speed (right) as a function of solution curvature and gradient for lean n-dodecane flames.

Solution convergence is obtained for CURV, GRAD = 0.001 and is used for all unstretched and stretched flame calculations.

APPENDIX D. OPPDIF INLET CONDITIONS IN CHEMKIN

The inlet conditions, stretch rate are summarized here.

D.1. Hydrogen

The inlet conditions: ϕ = 0.4, T^u = 298K, p = 1atm, domain = 0.02m, κ_{ext}=10170 1/s.

Table D.1. Inlet conditions for stretched hydrogen flames

Case	Inlet Velocity	Stretch rate	$\frac{\kappa}{\kappa_{ext}}(\%)$	Case	Inlet Velocity	Stretch rate	$\frac{\kappa}{\kappa_{ext}}(\%)$
1	284	577.5	5.68	10	2635	5257.7	51.7
2	540	1087.6	10.69	11	2900	5784.6	56.88
3	800	1605.1	15.78	12	3160	6301.86	61.96
4	1060	2122.7	20.87	13	3420	6818.8	67.05
5	1325	2650.3	26.06	14	3680	7335.8	72.13
6	1590	3177.9	31.25	15	3945	7862.9	77.31
7	1850	3695.5	36.34	16	4205	8379.8	82.4
8	2110	4213.1	41.43	17	4470	8905.7	87.57
9	2375	4740.6	46.61	18	4730	9420.7	92.63

D.2. Methane

The inlet conditions: ϕ = 0.7, T^u = 298K, p = 1atm, domain = 0.02m, κ_{ext}=1213 1/s.

Table D.2. Inlet conditions for stretched hydrogen flames

Case	Inlet Velocity	Stretch rate	$\frac{\kappa}{\kappa_{ext}}(\%)$	Case	Inlet Velocity	Stretch rate	$\frac{\kappa}{\kappa_{ext}}(\%)$
1	30	49.41	4.07	10	330	645.48	53.21
2	54	107.73	8.88	11	364	711.59	58.66
3	89	178.48	14.71	12	399	779.68	64.28
4	123	244.66	20.17	13	433	845.84	69.73
5	158	312.29	25.74	14	468	913.98	75.35
6	192	377.96	31.16	15	502	980.16	80.80
7	227	445.66	36.74	16	537	1048.2	86.42
8	261	511.51	42.17	17	571	1114.3	91.86
9	296	579.43	47.77	18	605	1180.1	97.29

D.3. n-dodecane

The inlet conditions: ϕ = 0.7, T^u = 298K, p = 1atm, domain = 0.02m, κ_{ext}=244 1/s.

Table D.3. Inlet conditions for stretched hydrogen flames

Case	Inlet Velocity	Stretch rate	$\frac{\kappa}{\kappa_{ext}}(\%)$	Case	Inlet Velocity	Stretch rate	$\frac{\kappa}{\kappa_{ext}}(\%)$
1	25	22.47	9.19	11	77	155.81	63.74
2	27.5	36.59	14.97	12	80.6	162.63	66.53
3	34.2	61.45	25.14	13	88	176.48	72.2
4	38.5	73.72	30.16	14	92.2	184.2	75.35
5	45.8	91.68	37.5	15	99	196.67	80.45
6	49.5	100.15	40.97	16	103.8	205.32	84
7	57.4	116.96	47.85	17	110	216.35	88.51
8	60.5	123.41	50.48	18	115.4	225.73	92.34
9	69	140.28	57.39	19	121	234.86	96.08
10	71.5	145.23	59.41				

REFERENCES

[1] S.R. Turns, An Introduction to Combustion: Concepts and applications, 2 ed., McGraw Hill Book Co2000.

[2] S.B. Pope, Turbulent Flows, Cambridge: Cambridge University Press 2000.

[3] T. Echekki, J.H. Chen, Unsteady Strain Rate and Curvature Effects in Turbulent Premixed Methane-Air Flames Combustion and Flame 106 (1996) 184-202.

[4] J.H. Chen, H.G. Im, Stretch effects on the burning velocity of turbulent premixed hydrogen/air flames, Proceedings of the Combustion Institute 28 (2000) 211-218.

[5] N. Chakraborty, R.S. Cant, Effects of strain rate and curvature on surface density function transport in turbulent premixed flames in the thin reaction zones regime, Physics of Fluids 17 (2005) 065108.

[6] N. Chakraborty, R.S. Cant, Influence of Lewis number on curvature effects in turbulent premixed flame propagation in the thin reaction zones regime, Physics of Fluids 17 (2005) 105105.

[7] N. Chakraborty, S. Cant, Unsteady effects of strain rate and curvature on turbulent premixed flames in an inflow–outflow configuration, Combustion and Flame 137 (2004) 129-147.

[8] H.G. Im, J.H. Chen, Preferential Diffusion Effects on the Burning Rate of Interacting Turbulent Premixed Hydrogen-Air Flames, Combustion and Flame 131 (2002) 246-258.

[9] J.B. Bell, R.K. Cheng, M.S. Day, I.G. Shepherd, Numerical simulation of Lewis number effects on lean premixed turbulent flames, Proceedings of the Combustion Institute 31 (2007) 1309-1317.

[10] W. Kollmann, J.H. Chen, Pocket formation and the flame surface density equation, Symposium (International) on Combustion 27 (1998) 927-934.

[11] J.H. Chen, T. Echeckki, W. Kollmann, The mechanism of two-dimensional pocket formation in lean premixed methane-air flames with implications to turbulent combustion, Combustion and Flame 116 (1999) 15-48.

[12] A.J. Aspden, M.S. Day, J.B. Bell, Turbulence-chemistry interaction in lean premixed hydrogen combustion, Proceedings of the Combustion Institute 35 (2015) 1321-1329.

[13] B. Savard, B. Bobbitt, G. Blanquart, Structure of a high Karlovitz n-C7H16 premixed turbulent flame, Proceedings of the Combustion Institute 35 (2015) 1377-1384.

[14] H. Carlsson, R. Yu, X.-S. Bai, Direct numerical simulation of lean premixed CH4/air and H2/air flames at high Karlovitz numbers, International Journal of Hydrogen Energy 39 (2014) 20216-20232.

[15] C.K. Law, Combustion Physics, Cambridge University Press, New York2006.

[16] K.K. Kuo, Principles of Combustion, John Wiley &n Sons, Inc.2005.

[17] J. Li, Z. Zhao, A. Kazakov, F.L. Dryer, An Updated Comprehensive Kinetic Model of Hydrogen Combustion International Journal of Chemical Kinetics 36 (2004) 566-575.

[18] G.P. Smith, D.M. Golden, M. Frenklach, N.W. Moriarty, B. Eiteneer, M. Goldenberg, C.T. Bowman, R.K. Hanson, S. Song, J. William C. Gardiner, V.V. Lissianski, Z. Qin, GRI Mech 3.0.

[19] J.M. Simmie, Detailed chemical kinetic models for the combustion of hydrocarbon fuels, Progress in Energy and Combustion Science 29 (2003) 599-634.

[20] J.A. van Oijen, A. Donini, R.J.M. Bastiaans, J.H.M. ten Thije Boonkkamp, L.P.H. de Goey, State-of-the-art in premixed combustion modeling using flamelet generated manifolds, Progress in Energy and Combustion Science 57 (2016) 30-74.

[21] C.K. Law, C.J. Sung, Structure, aerodynamics, and geometry of premixed flamelets, Progress in Energy and Combustion Science 26 (2000) 459–505.

[22] T. Lieuwen, Unsteady Combustor Physics, Cambridge University Press2012.

[23] D.C. Haworth, T. Poinsot, Numerical simulations of Lewis number effects in turbulent premixed flames, Journal of Fluid Mechanics 244 (1992) 405-436.

[24] N. Peters, P. Terhoeven, J.H. Chen, T. Echekki, Statistics of Flame Displacement speeds from computations of 2-D unsteady methane-air flames, Symposium (International) on Combustion 27 (1998) 833-839.

[25] M. Baum, T. Poinsot, D.C. Haworth, N. Darabiha, Direct numerical simulation of H2/02/N2 flames with complex chemistry in two-dimensional turbulent flows Journal of Fluid Mechanics 281 (1994) 1-32.

[26] S.H. Kim, H. Pitsch, Scalar gradient and small-scale structure in turbulent premixed combustion, Physics of Fluids 19 (2007) 115104.

[27] P. Clavin, G. Joulin, High-frequency response of premixed flames to weak stretch and curvature: a variable-density analysis, Combustion Theory and Modelling 1 (1997) 429-446.

[28] H.G. Im, J.H. Chen, Effects of flow transients on the burning velocity of laminar hydrogen/air premixed flames, Proceedings of the Combustion Institute 28 (2000) 1833-1840.

[29] R. Borghi, On the Structure and Morphology of Turbulent Premixed Flames, in: C. Casci (Ed.), Recent Advances in the Aerospace Sciences, Plenum, New York1985, pp. 117-138.

[30] P.A. Libby, F.A. Williams, Structure of Laminar Flamelets in Premixed Turbulent Flames Combustion and Flame 44 (1982) 287-303.

[31] N. Peters, The turbulent burning velocity for large-scale and small-scale turbulence, Journal of Fluid Mechanics 384 (1999) 107-132.

[32] C. Meneveau, T. Poinsot, Stretching and Quenching of Flamelets in Premixed Turbulent Combustion, Combustion and Flame 86 (1991) 311-332.

[33] W.L. Roberts, J.F. Driscoll, M.C. Drake, L.P. Goss, Images of the Quenching of a Flame by a Vortex--To Quantify Regimes of Turbulent Combustion, Combustion and Flame 94 (1993) 58-69.

[34] T.M. Wabel, A.W. Skiba, J.E. Temme, J.F. Driscoll, Measurements to determine the regimes of premixed flames in extreme turbulence, Proceedings of the Combustion Institute 36 (2017) 1809-1816.

[35] E.R. Hawkes, J.H. Chen, Direct numerical simulation of hydrogen-enriched lean premixed methane–air flames, Combustion and Flame 138 (2004) 242-258.

[36] E.R. Hawkes, J.H. Chen, Comparison of direct numerical simulation of lean premixed methane–air flames with strained laminar flame calculations, Combustion and Flame 144 (2006) 112-125.

[37] M. Day, J. Bell, P.T. Bremer, V. Pascucci, V. Beckner, M. Lijewski, Turbulence effects on cellular burning structures in lean premixed hydrogen flames, Combustion and Flame 156 (2009) 1035-1045.

[38] R. Sankaran, E.R. Hawkes, J.H. Chen, T. Lu, C.K. Law, Structure of a spatially developing turbulent lean methane–air Bunsen flame, Proceedings of the Combustion Institute 33 (2007) 1291-1298.

[39] A. Trouve, T. Poinsot, The evolution equation for the flame surface density in turbulent premixed combustion, Journal of Fluid Mechanics 278 (1994) 1-31.

[40] C.J. Rutland, A. Trouve, Direct simulations of premixed turbulent flames with nonunity Lewis numbers, Combustion and Flame 94 (1993) 41-57.

[41] T. Poinsot, D. Veynante, Theoretical and Numerical Combustion, third ed., Poinsot and Veynante2012.

[42] S. Cant, RANS and LES Modelling of Premixed Turbulent Combustion, in: T. Echekki, E. Mastorakos (Eds.), Turbulent Combustion Modeling Advances, New Trends and Perspectives, Springer2011.

[43] D.B. Spalding, Mixing and chemical reaction in steady confined turbulent flames, Symposium (International) on Combustion 13 (1971) 649-657.

[44] O. Colin, F. Ducros, D. Veynante, T. Poinsot, A thickened flame model for large eddy simulations of turbulent premixed combustion, Physics of Fluids 12 (2000).

[45] T.D. Butler, P.J. O'Rourke, A numerical method for two dimensional unsteady reacting flows, Symposium (International) on Combustion 16 (1977) 1503-1515.

[46] N. Peters, Turbulent Combustion, Cambridge University Press2000.

[47] H. Pitsch, Large-Eddy Simulation of Turbulent Combustion, The Annual Review of Fluid Mechanics 38 (2006) 453-482.

[48] E.R. Hawkes, R.S. Cant, A flame surface density approach to large-eddy simulation of premixed turbulent combustion, Proceedings of the Combustion Institute 28 (2000) 51-58.

[49] M. Boger, D. Veynante, H. Boughanem, A.Trouvé, Direct numerical simulation analysis of flame surface density concept for large eddy simulation of turbulent premixed combustion, Symposium (International) on Combustion 27 (1998) 917-925.

[50] B. Fiorina, R. Vicquelina, P. Auzillon, N. Darabiha, O. Gicquel, D.Veynante, A filtered tabulated chemistry model for LES of premixed combustion, Combustion and Flame 157 (2010) 465-475.

[51] P. Auzillon, O. Gicquel, N. Darabiha, D. Veynante, B. Fiorina, A Filtered Tabulated Chemistry model for LES of stratified flames, Combustion and Flame 159 (2012) 2704-2717.

[52] A.Y. Klimenko, R.W. Bilger, Conditional moment closure for turbulent combustion, Progress in Energy and Combustion Science 25 (1999) 595-687.

[53] O. Gicquel, N. Darabiha, D. Thevenin, Laminar premixed hydrogen/air counterflow flame simulations using flame prolongation of ILDM with differential diffusion Proceedings of the Combustion Institute 28 (2000) 1901-1908.

[54] F.A. Williams, Combustion Theory, CRC Press: Boca Raton1985.

[55] K.N.C. Bray, M. Champion, P.A. Libby, The Interaction Between Turbulence and Chemistry in Premixed Turbulent Flames., in: R. Borghi, S.N.B. Murthy (Eds.), Turbulent Reactive Flows. Lecture Notes in Engineering, Springer, New York, NY1989.

[56] S.B. Pope, PDF methods for turbulent reactive flows, Progress in Energy and Combustion Science 11 (1985) 119-192.

[57] D. Veynante, L. Vervisch, Turbulent combustion modeling, Progress in Energy and Combustion Science 28 (2002) 193-266.

[58] J.F. Driscoll, Turbulent premixed combustion: Flamelet structure and its effect on turbulent burning velocities, Progress in Energy and Combustion Science 34 (2008) 91–134.

[59] T. Poinsot, S. Candel, A. Trouve, Applications of Direct Numerical Simulation to Premixed Turbulent Combustion, Progress in Energy and Combustion Science 21 (1996) 531-576.

[60] R. Sankaran, E.R. Hawkes, C.S. Yoo, J.H. Chen, Response of flame thickness and propagation speed under intense turbulence in spatially developing lean premixed methane–air jet flames, Combustion and Flame 162 (2015) 3294-3306.

[61] A.J. Aspden, M.S. Day, J.B. Bell, Characterization of low Lewis number flames, Proceedings of the Combustion Institute 33 (2011) 1463-1471.

[62] A.J. Aspden, M.S. Day, J.B. Bell, Turbulence–flame interactions in lean premixed hydrogen: transition to the distributed burning regime, Journal of Fluid Mechanics 680 (2011) 287-320.

[63] J. Savre, H. Carlsson, X.S. Bai, Tubulent Methane/Air Premixed Flame Structure at High Karlovitz Numbers, Flow, Turbulence and Combustion 90 (2013) 325-341.

[64] J.H. Chen, Petascale direct numerical simulation of turbulent combustion-fundamental insights towards predictive models, Proceedings of the Combustion Institute 33 (2011) 99-123.

[65] M.S. Day, X. Gao, J.B. Bell, Properties of lean turbulent methane-air flames with significant hydrogen addition, Proceedings of the Combustion Institute 33 (2011) 1601-1608.

[66] H. Carlsson, R. Yu, X.-S. Bai, Flame structure analysis for categorization of lean premixed CH4/air and H2/air flames at high Karlovitz numbers: Direct numerical simulation studies, Proceedings of the Combustion Institute 35 (2015) 1425-1432.

[67] A.J. Aspden, M.S. Day, J.B. Bell, Three- dimensional direct numerical simulation of turbulent lean premixed methane combustion with detailed kinetics, Combustion and Flame 166 (2016) 266–283.

[68] A.J. Aspden, J.B. Bell, M.S. Day, F.N. Egolfopoulos, Turbulence-Flame Interactions in Lean Premixed Dodecane Flames, Proceedings of the Combustion Institute 36 (2017) 2005-2016.

[69] T. Nilsson, H. Carlsson, R. Yu, X.-S. Bai, Structures of turbulent premixed flames in the high Karlovitz number regime – DNS analysis, Fuel 216 (2018) 627-638.

[70] A.Y. Poludnenko, E.S. Oran, The interaction of high-speed turbulence with flames: Global properties and internal flame structure, Combustion and Flame 157 (2010) 995-1011.

[71] S. Lapointe, B. Savard, G. Blanquart, Differential diffusion effects, distributed burning, and local extinctions in high Karlovitz premixed flames, Combustion and Flame 162 (2015) 3341-3355.

[72] B. Zhou, C. Brackmann, Q. Li, Z. Wang, P. Petersson, Z. Li, M. Alden, X. Bai, Distributed reactions in highly turbulent premixed methane/air flames Part I. Flame structure characterization, Combustion and Flame 162 (2015) 2937-2953.

[73] H. Wang, E.R. Hawkes, B. Zhou, J.H. Chen, Z. Li, M. Alden, A comparison between direct numerical simulation and experiment of the turbulent burning velocity-related statistics in a turbulent methane-air premixed jet flame at high Karlovitz number, Proceedings of the Combustion Institute 36 (2017) 2045-2053.

[74] R.J. Kee, F.M. Rupley, J.A. Miller, M.E. Coltrin, J.F. Grcar, E. Meeks, H.K. Moffat, A.E. Lutz, G.D.-. Lewis, M.D. Smooke, J. Warnatz, G.H. Evans, R.S. Larson, R.E. Mitchell, L.R. Petzold, W.C. Reynolds, M. Caracotsios, W.E. Stewart, P. Glarborg, C. Wang, O. Adigun, CHEMKIN Collection, Release 3.6, Reaction Design, Inc., San Diego, CA, 2000.

[75] A.E. Lutz, R.J. Kee, J.F. Grcar, F.M. Rupley, OPPDIF: A Fortran Program for Computing Opposed-Flow Diffusion Flames, Sandia National Laboratories, Livermore, CA, 1996.

[76] P. Glarborg, R.J. Kee, J.F. Grear, J.A. Miller, PSR: A FORTRAN Program for Modelling Well-Stirred Reactors, Sandia National Laboratories, Livermore, CA, 1986.

[77] R.G. Rehm, H.R. Baum, The Equations of Motion for Thermally Driven, Buoyant Flows, JOURNAL OF RESEARCH of the Notional Bureau of Standards 83 (1978) 297-308.

[78] G.I. Sivashinsky, Hydrodynamic theory of flame propagation in an enclosed volume, Acta Astronautica 6 (1979) 631-645.

[79] A. Majda, J. Sethian, The Derivation and Numerical Solution of the Equations for Zero Mach Number Combustion, Combustion Science and Technology 42 (1985) 185-205.

[80] A. Ern, V. Giovangigli, Multicomponent Transport Algorithms, Springer- Verlag, Berlin, 1994.

[81] M.S. Day, J.B. Bell, Numerical simulation of laminar reacting flows with complex chemistry, Combustion Theory and Modelling 4 (2000) 535-556.

[82] A.S. Almgren, J.B. Bell, P. Colella, L.H. Howell, M.L. Welcome, A Conservative Adaptive Projection Method for the Variable Density Incompressible Navier–Stokes Equations, Journal of Computational Physics 142 (1998) 1-46.

[83] A.S. Almgren, J.B. Bell, W.Y. Crutchfield, Approximate Projection Methods: Part I. Inviscid Analysis, SIAM Journal on Scientific Computing 22 (2000) 1139–1159.

[84] A.S. Almgren, J.B. Bell, W.G. Szymczak, A Numerical Method for the Incompressible Navier-Stokes Equations Based on an Approximate Projection, SIAM Journal on Scientific Computing 17 (1996) 358–369.

[85] A.J. Aspden, J.B. Bell, M.S. Day, S.E. Woosley, M. Zingale, Turbulence-Flame Interactions in Type Ia Supernovae, The Astrophysical Journal 689 (2008) 1173-1185.

[86] A.J. Aspden, N. Nikiforakis, S. Dalziel, J.B. Bell, Analysis of implicit LES methods, Communications in Applied Mathematics and Computer Science 3 (2008) 103-126.

[87] X. Gao, M.S. Day, J.B. Bell, Characterization of Freely Propagating Hydrogen Flames, Fall Technical Meeting of the Western States Section of the Combustion Institute, University of California, Irvine, 2009.

[88] M. Garland, Quadric-Based Polygonal Surface Simplification, Carnegie Mellon University, 1999.

[89] X. You, F.N. Egolfopoulos, H. Wang, Detailed and simplified kinetic models of n-dodecane oxidation: The role of fuel cracking in aliphatic hydrocarbon combustion, Proceedings of the Combustion Institute 32 (2009) 403-410.

[90] Z. Luo, S. Som, S.M. Sarathy, M. Plomer, W.J. Pitz, D.E. Longman, T. Lu, Development and validation of an n-dodecane skeletal mechanism for spray combustion applications, Combustion Theory and Modelling 18 (2014) 187-203.

[91] K. Narayanswamy, P. Pepiot, H. Pitsch, A chemical mechanism for low to high temperature oxidation of n-dodecane as a component of transportation fuel surrogates, Combustion and Flame 161 (2014) 866-884.

[92] M.D. Smooke, The computation of laminar flames, Proceedings of the Combustion Institute 34 (2013) 65-98.

[93] J.O. Hirschfelder, C.F. Curtiss, R.B. Bird, Molecular theory of gases and liquids, Wiley, New York1954.

[94] R.B. Bird, W.E. Stewart, E.N. Lightfoot, Transport phenomena, John Wiley and Sons Inc., New York1960.

[95] D.G. Goodwin, H.K. Moffat, R.L. Speth, Cantera: An object- oriented software toolkit for chemical kinetics, thermodynamics, and transport processes, 2017, pp. http://www.cantera.org/.

[96] L. Durand, W. Polifke. Implementation of the Thickened Flame Model for Large Eddy Simulation of Turbulent Premixed Combustion in a Commercial Solver. In: editor^editors. Turbo Expo: Power for Land, Sea, and Air; 2007. p. 869-878.

[97] H. Wang, X. You, A.V. Joshi, S.G. Davis, A. Laskin, F. Egolfopoulos, C.K. Law, USC Mech Version II. High-Temperature Combustion Reaction Model of H2/CO/C1-C4 Compounds. http://ignis.usc.edu/USC_Mech_II.htm, .

[98] S.M. Sarathy, C.K. Westbrook, M. Mehl, W.J. Pitz, C. Togbe, P. Dagaut, H. Wang, M.A. Oehlschlaeger, U. Niemann, K. Seshadri, P.S. Veloo, C. Ji, F.N. Egolfopoulos, T. Luf, Comprehensive chemical kinetic modeling of the oxidation of 2-methylalkanes from C7 to C20, Combustion and Flame 158 (2011) 2338-2357.

[99] K. Narayanaswamy, G. Blanquart, H. Pitsch, A consistent chemical mechanism for oxidation of substituted aromatic species, Combustion and Flame 157 (2010) 1879-1898.